

THE COMPUTER AIDED DESIGN OF
ELECTRON DETECTORS FOR THE
SCANNING ELECTRON MICROSCOPE.

by

A Khursheed, BSc

A thesis submitted to the Faculty of Science
of the University of Edinburgh,
for the degree of Doctor of Philosophy

University of Edinburgh

1983



ABSTRACT

The scanning electron microscope is now an important means for measuring voltages at internal points in very-large-scale integrated circuits in order to verify that new designs are operating as predicted and to locate defects in malfunctioning devices. The technique has the advantages that the smallest known structures can be probed, there is no mechanical damage to the specimen and, provided the correct conditions are observed, the electrical loading on the circuit is negligible.

Reliable quantitative voltage information requires precise measurement of the energies of secondary electrons, having energies below 15 eV, which leave the surface at the point under investigation. In the past, a number of different detector structures have been used to attempt to achieve accurate measurements, but in most cases their design has been largely empirical with little theoretical justification because of the great complexity of the electric fields and electron trajectories in these devices.

This work was first aimed at providing a computer-based interactive method for the calculation and visualisation of fields and trajectories in the case of systems with two-dimensional planar symmetry. The method was applied to detectors and to electron trajectories immediately above a realistic representation of an integrated circuit surface. Programs were then developed to investigate the properties of certain detectors which have been described in the literature, where three-dimensional methods had to be employed. This expedient had to be adopted because it was otherwise impossible to compare their performances because of the non-standard operating conditions employed by the various workers. The results of these

computations showed that all these devices had some shortcomings in one or both of the areas of collection efficiency and linear response to specimen voltage.

In the light of the experience gained in the above work, a new detector was designed which was predicted to have both a very high collection efficiency and a linear voltage response. This detector has been constructed at British Telecom Research Laboratories at Martlesham; initial tests confirmed its predicted performance and it is now the subject of a patent application.

ACKNOWLEDGEMENTS

I would like to thank Dr A R Dinnis for his help with experimental work and general guidance throughout the period of this work. I would also like to thank J M Hannah for his advice on computing matters and Mr Alan Walker for his help on the analytical solutions to some field problems.

Thanks are due to the British Telecom Research group concerned with using the S.E.M for voltage contrast purposes. In particular I would like to thank Mr Gary Proctor, Mr Donald Ranasinghe and Mr Tony Barrow for their part in developing a practical prototype of the electron detector designed in this thesis.

Finally I would like to thank the Science and Engineering Research Council for the financial support for this work.

DECLARATION OF ORIGINALITY

I declare that this thesis has been composed by me and that the work it contains is my own

(A Khursheed)

to my mother

CONTENTS

	Page	
CHAPTER 1	INTRODUCTION TO THESIS	1
CHAPTER 2	REVIEW OF PAST WORK ON	
	VOLTAGE CONTRAST	3
2.1	Past Detectors	3
2.1.1	The First Detector	3
2.1.2	Band-Pass Detectors	4
2.1.3	Retarding Field Detectors	4
2.1.4	Performance of Past Detectors	6
2.1.5	General Considerations on Different	
	Types of V.C Detectors	8
2.2	Review of Theoretical and Computational	
	Work on Past Detectors	10
2.2.1	Analysis of Different Detectors	10
2.2.2	Criticisims on Munro's Work	12
2.2.3	Work on Surface Fields	13
2.2.4	Grid Non-Linearities	15
	Summary	16
CHAPTER 3	PROGRAMS	18
3.1	Intoduction	18
3.2	Solving Potential Field Distributions	20
3.2.1	Finite-Difference Methods	22
3.2.2	Electron Trajectory Plots	25
3.2.3	Calculation of Electric Fields for the	
	Electron Trajectory	27

	Page	
3.3	Program Options	28
3.3.1	Simulation of Secondary Electrons	
	Leaving a Specimen	28
3.3.2	Overall Transport Efficiency	30
3.3.3	Filter Response	30
3.3.4	Collected S-curves	31
3.3.5	Error Option	32
3.4	Detector Design Programs	34
3.4.1	Computer Graphics in Specifying	
	Detector Design	35
3.4.2	Instruction Characters	36
3.4.3	Relaxation Mesh	36
3.5	Trajectory Plotting for Design Programs	39
3.5.1	Interpolation	39
3.5.2	Electron Field Step near Boundary	42
3.5.3	Turning Points in the	
	Electron's Trajectory	43
3.5.4	Grids	44
3.6	Applications of 2-D Design Programs	45
3.6.1	Different Detector Designs	45
3.6.2	Dinnis Detector	47
3.6.2	Detector Curves	49
3.6.4	Lintech Detector	51
3.6.5	Transport Efficiency	52

	Page	
3.6.6	Comparison of Computing Results with Practical Results	53
	Summary	54
CHAPTER 4	SIMULATION OF PARTICULAR DETECTORS	55
4.1	Introduction	55
4.2	Potential Field Distributions for Hemispherical Detectors	57
4.2.1	The Analytical Approach to Fentem's Detector	57
4.2.2	The Hemispherical Shell	57
4.2.3	Inner Hemisphere	58
4.2.4	Solving Field A	59
4.2.5	Solving Field B	60
4.3	Numerical Methods for Solving Fields in a Hemispherical Detector	62
4.4	Trajectory Plotting	64
4.4.1	Interpolation	64
4.4.2	Preventing the Electron from Stepping across a Grid	64
4.4.3	Calculating Electric Fields near Grids	66
4.4.4	Modifying Electric Fields	67
4.5	The Feuerbaum Detector	70
4.5.1	Introduction	70
4.5.2	Field Distributions for the Feuerbaum Detector	70

	Page	
4.5.3	Deflection Field Distribution Solved by the Relaxation Method	72
4.5.4	Trajectory Calculations	72
4.6	Results on the Hemispherical Detectors	73
4.6.1	Electrons Leaving Specimen Centre	73
4.6.2	Off-axis Electrons	74
4.7	Results on the Feuerbaum Detector	75
4.7.1	Electrons Leaving Specimen Centre	75
4.7.2	Off-axis Electrons	77
	Summary	77
CHAPTER 5	SURFACE FIELDS	78
5.1	Introduction	78
5.2	Field Distributions near a Specimen	78
5.2.1.	Introduction	79
5.2.2	Techniques of Graded Meshes in the Finite-Difference Method	80
5.2.3	Surface Mesh	81
5.2.4	Fields F2 and F3	83
5.2.5	Relaxation at Field Boundaries	83
5.3	Trajectory Plotting in Surface Fields	84
5.4	Results on Surface Fields	85
5.4.1	Two Electrode Structure with a 3 micron Gap	85
5.4.2	Positive Neighbouring Conductor	85
5.4.3	Varying the Extraction Field for the 3 micron Single Gap Layout	86

	Page	
5.4.4	Measurements near the 3 micron Gap Edge	87
5.4.5	A 9 micron Single Gap Layout	88
5.4.6	Different Extraction Fields for a 9 micron Single Gap Layout	89
5.4.7	Measurements near a 9 micron Gap Edge	90
5.4.8	21 micron Single Gap Layout	90
5.4.9	Different Extraction Fields for a 21 micron Gap Layout	91
5.4.10	Near a 21 micron Gap	91
5.4.11	Single Gap Layout with a Negative Neighbouring Conductor	93
	Three Conductor Layouts	94
5.4.12	A Positive Central Track between two Earthed Conductors	94
5.4.13	An Earthed Track between Two Large Positive Conductors	95
5.4.14	An Earthed Track between Two Negatively Biased Conductors	96
5.5	Surface Fields in Hemispherical Detectors	97
5.5.1	Introduction	97
5.5.2	Results	97
5.6	Surface Fields in the Feuerbaum Detector	100
	Summary	101

	Page	
CHAPTER 6	DESIGN OF A NEW	
	VOLTAGE CONTRAST DETECTOR	103
6.1	Introduction	103
6.2	Program Model to Simulate a	
	Curved Tube Detector	104
6.2.1	The Potential Distribution in the	
	Deflection Field	105
6.2.2	Boundary and Mesh Line Intersections	105
6.3	Initial Detector Design	107
6.4	Practical Construction of the	
	Curved Tube Detector	108
6.5	Computer Simulation of the	
	Practical Design	108
6.5.1	Optimum Voltage Configuration	109
6.5.2	Off-axis Positions	110
6.5.3	Surface Field Effects in the New	
	Detector Design	111
6.6	Design and Construction of a	
	Test Specimen	113
6.7	Provisional Experimental Results from	
	the New Detector	114
	Summary	115
CHAPTER 7		116
7.1	CONCLUSIONS	116
7.2	FUTURE WORK	120
APPENDIX 1	Hemispherical Shell	122

	Page
APPENDIX 2	Inner Hemisphere Problem
	Problem A 128
APPENDIX 3	The Inner Hemisphere Problem
	Problem B 130
APPENDIX 4	Analytical Solution to Potential Field
	Inside the Feuerbaum Detector 133
APPENDIX 5	Residual Equation at a Silicon
	Dioxide/Air Interface 135
REFERENCES	138
PATENT APPLICATION FOR THE NEW DETECTOR	142

CHAPTER 1INTRODUCTION

The Scanning Electron Microscope (S.E.M.) has become a powerful and versatile tool in testing and diagnostic work on Integrated Circuits. The work described in this thesis is concerned with using the S.E.M as a voltage probe on Integrated Circuits (ICs). The advantages of the S.E.M in this field, known as voltage contrast (VC) are well known (Gopinath(1978)). Such a contact-free method provides less damage to an I.C and greater spatial resolution in the measurement than is possible with mechanical probing. The aim of the work in this thesis is to improve the methods of making voltage contrast measurements and provide greater understanding of the technique in general.

Chapter 2 consists of a review of past work in voltage contrast, both experimental and theoretical. The survey includes the development of electron energy detectors, work on surface fields and grid non-linearities.

Chapter 3 introduces the computational techniques used in developing programs to design and simulate electron detectors, these programs are restricted to a two-dimensional analysis. At the end of this chapter the performance of two existing detectors are simulated and the theoretical results compared with experimental results.

Chapter 4 describes the development of computer programs for a three-dimensional analysis of two specific detectors. Chapter 5 investigates the characteristics of surface fields above MOS circuits. This chapter describes the development of computer programs which analyse these surface fields. Results are then given which show the extent to which surface fields can affect voltage contrast measurements. The performance of two electron detectors under strong surface fields is also investigated.

Chapter 6 traces the development and design of a new electron energy detector, giving a detailed description of the three-dimensional analysis of this detector. Details of the practical construction of this detector are also presented and provisional experimental results are reported. In Chapter 7 overall conclusions are made and future extensions to the work in this thesis are suggested.

CHAPTER 2REVIEW OF PAST WORK ON VOLTAGE CONTRAST2.1 Past Detectors2.1.1 The First Detector

The first published work on voltage contrast detectors is generally recognised to have been made by Wells and Bremer(1968), although suggestions of their possible use had been made previously by Everhart. Wells and Bremer used an 84 degree cylindrical mirror detector, essentially a band pass detector. The specimen was fixed at -17 volts to maximise the output signal and detector output curves were produced by varying potentials on the detector plates. Shifts in some output curves were demonstrated and attributed to different surface voltages present on different parts of a silicon/silicon dioxide specimen. The detector curves, however, were mainly of a qualitative nature and no definite voltage resolution was reported. Many sources of error were noted, amongst these were cross-field errors, insulating errors and peak position errors (effect of detector's finite resolution). A drop in signal to noise ratio of an order of magnitude was also observed. Wells and Bremer later(1969) published a modified version of their initial detector. The detector had been changed to a 63 degree deflection cylindrical detector, apart from a 1 volt resolution no other results were reported.

Since the initial work of Wells and Bremer, many other voltage

contrast detectors have been proposed and tested. These detectors or electron energy filters can be divided into two basic categories, the band-pass type or the retarding grid type.

2.1.2 Band-Pass Detectors

As the name suggests these detectors collect electrons whose energies lie in a narrow energy range, much less than the typical secondary electron energy spread (0-50eV). An approximate form of the secondary energy distribution curve is produced by varying the specimen voltage and plotting the video signal; obviously errors are introduced due to the finite pass-band width of the detector. The detector of Wells and Bremer, as already described, is of the band-pass type. Another detector based on the improved detector of Wells and Bremer was made by Hannah (1974), Figure 2.1 shows its basic geometry. When the specimen voltage is changed the surrounding electric fields change and impose a linear shift on the electron energy distribution, Figure 2.2 shows this effect.

2.1.3 Retarding Field Detectors

These detectors are variable high-pass filters and an integrated form of the secondary electron energy distribution is produced from the detector. An electrode or grid is appropriately biased so that electrons below a chosen energy are rejected and are not collected. This electrode or grid provides a retarding field. The retarding electrode voltage is usually time-varying and can be biased

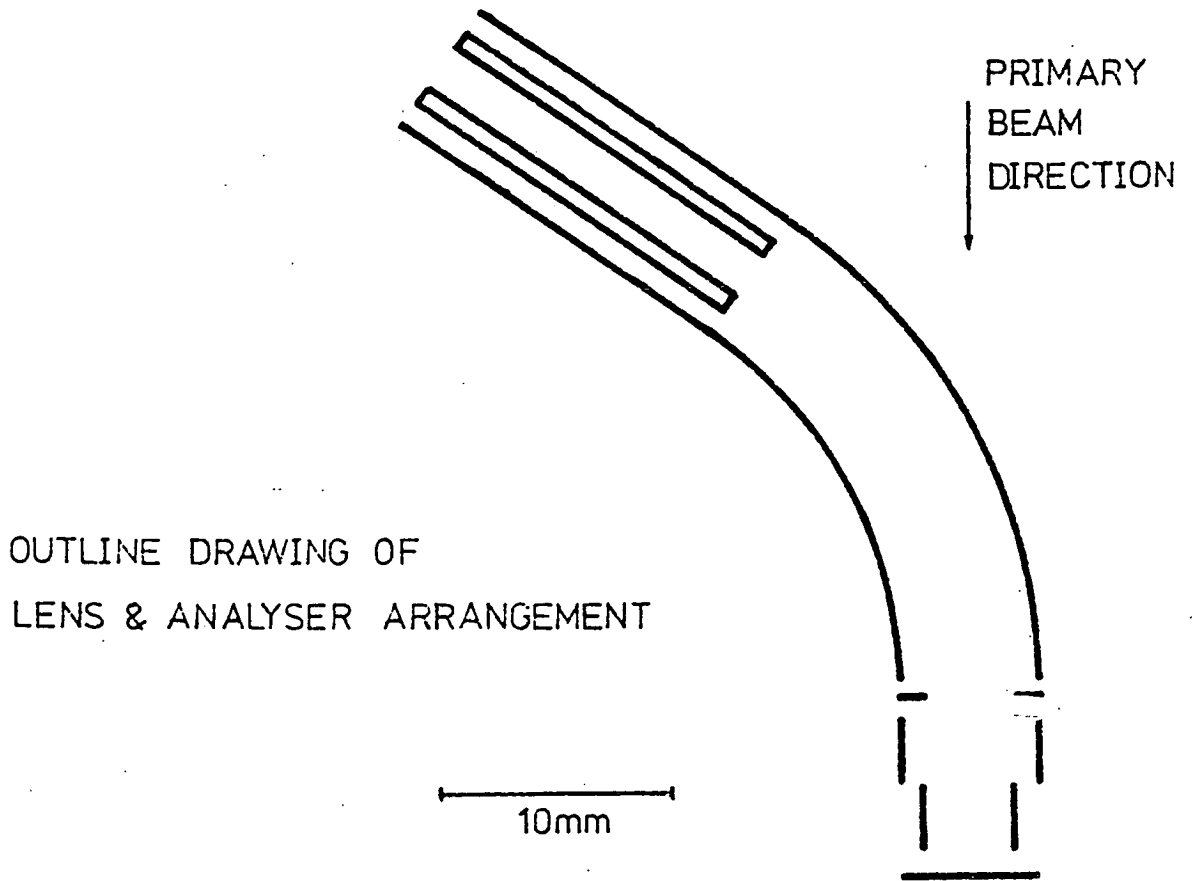


Figure 2.1 Hannah(1974)

Y - 0.5V/DIV. X - ~5V/DIV. → INCREASING ENERGY

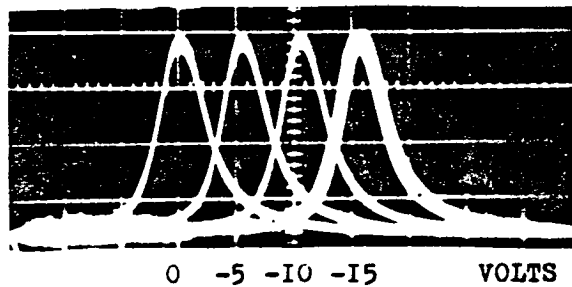


Figure 2.2
Hannah (1974)

appropriately so that at one extreme it rejects all secondary electrons. Hence an S-curve output results from the detector which represents an integrated form of the secondary electron energy distribution at the specimen. When the specimen voltage alters the electric fields above the specimen, the secondary energy distribution is shifted by a linear amount, causing a linear shift in the final S-curve (Figure 2.3).

Within the category of retarding field detectors there are two types; direct retarding field detectors where electron energies are analysed immediately after they have been attracted away from the specimen; and post deflection detectors where electrons are deflected away in a preferred direction and then their energies are analysed by a retarding field. Examples of detectors in the first category are shown in Figures 2.4(a-c), while detectors of the second type are shown in Figures 2.5(a) and 2.5(b). Note a grid in Figure 2.4(a) is placed very close to the specimen, this is to attract all electrons away from the specimen surface. It is also used to overcome surface fields, this will be examined later. Figure 2.4(a) depicts a linear retarding field, the retarding field is perpendicular to the specimen, and a scintillator/photomultiplier collection system is used at the exit of the voltage detector. Detectors in Figures 2.4(b) and 2.4(c) are also of the direct retarding field type but have spherical geometry. The output signal is generated from current collected on an outer grid or plate.

Figure 2.5(a) illustrates a rectangular target cage which

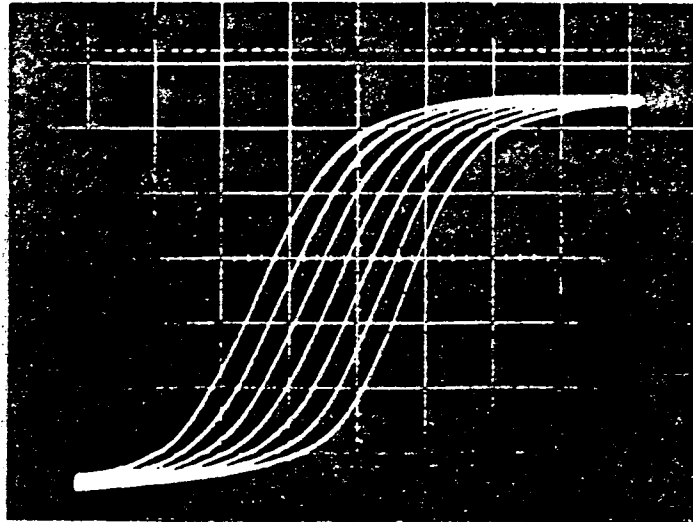


Figure 2.3
Typical S-curves

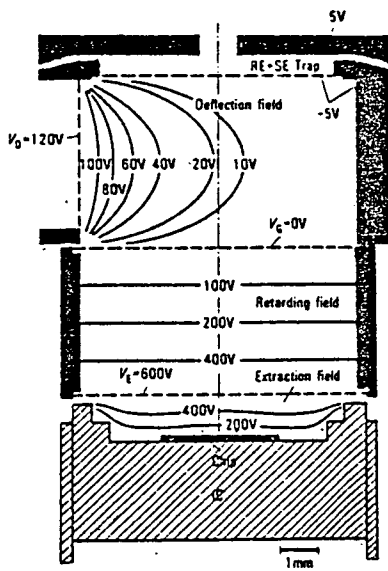


Figure 2.4(a) Feuerbaum(1979)

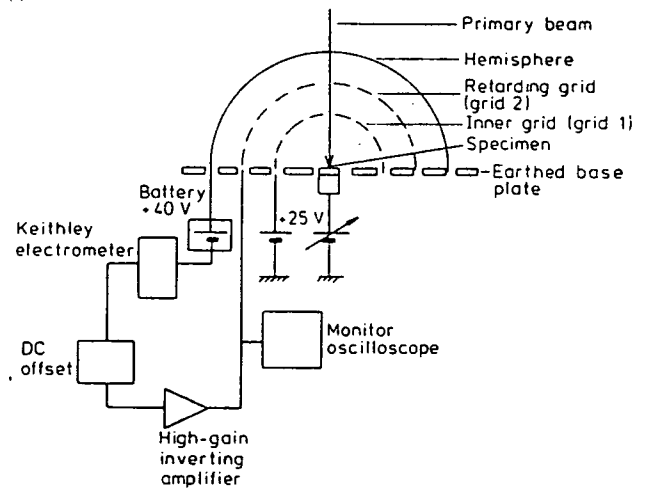


Figure 2.4(b) Fentem and
Gopinath(1974)

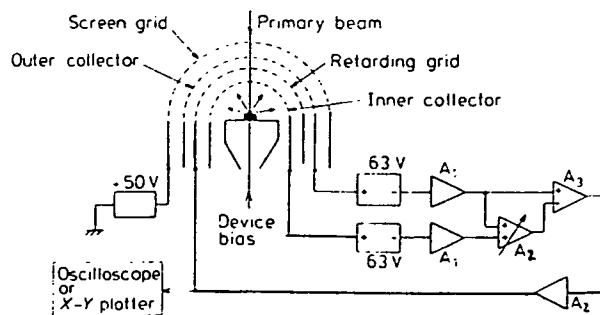


Figure 2.4(c) Tee and Gopinath(1976)

achieves the deflection while Figure 2.5(b) shows a cylindrical capacitor deflecting electrons to a scintillator cage. Detectors which do not fall into any of the afore-mentioned categories are shown in Figures 2.6(a) and 2.6(b). The detector in Figure 2.6(a) consists of a cylindrical cage in which electrons are attracted to a grid exit and are collected by a scintillator. The detector in Figure 2.6(b) is cylindrically symmetric and the output signal is collected on the outer walls of the cylinder. Voltage measurements from both detectors in Figures 2.6(a) and 2.6(b) rely upon varying the specimen voltage and looking for a linear region in the resulting variation. The technique is similar to that used for band-pass detectors only in this case an integrated form of the electron distribution is obtained (S-curves).

2.1.4 Performance of Past Detectors

It is difficult to make a comparative study on the performance of past voltage contrast detectors. Two main reasons account for this; firstly there is a lack of detailed information in published work; and secondly different experiments, specimens and S.E.M operating conditions were used for each detector.

Although voltage resolutions for some detectors were measured; 1mV by Feuerbaum(1979), 10mV by Tee and Gopinath(1976), 80mV by Fentem and Gopinath(1974) and 250mV by Fleming and Ward(1970), they do not necessarily give a figure of merit for the detector's voltage sensitivity. The minimum measurable voltage is largely dependent on

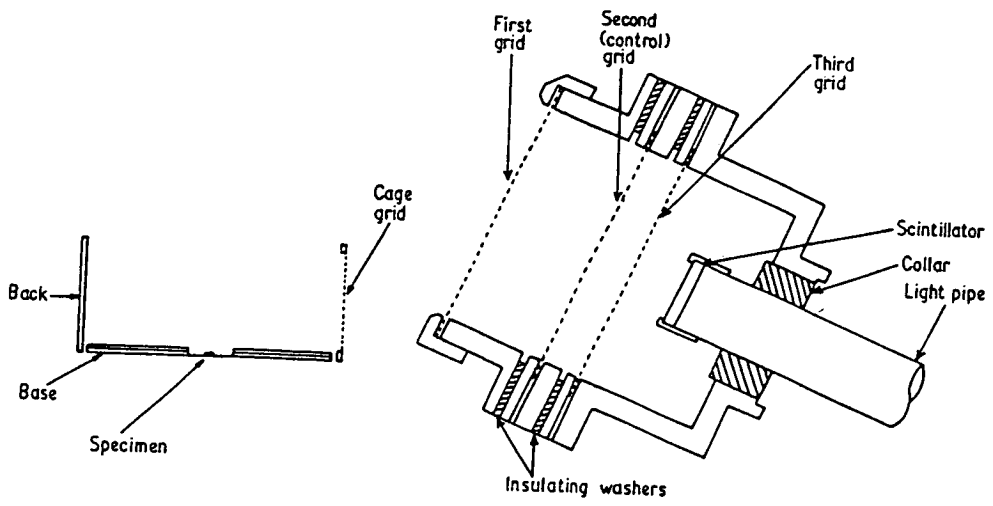


Figure 2.5(a) Gopinath and Sanger(1971)

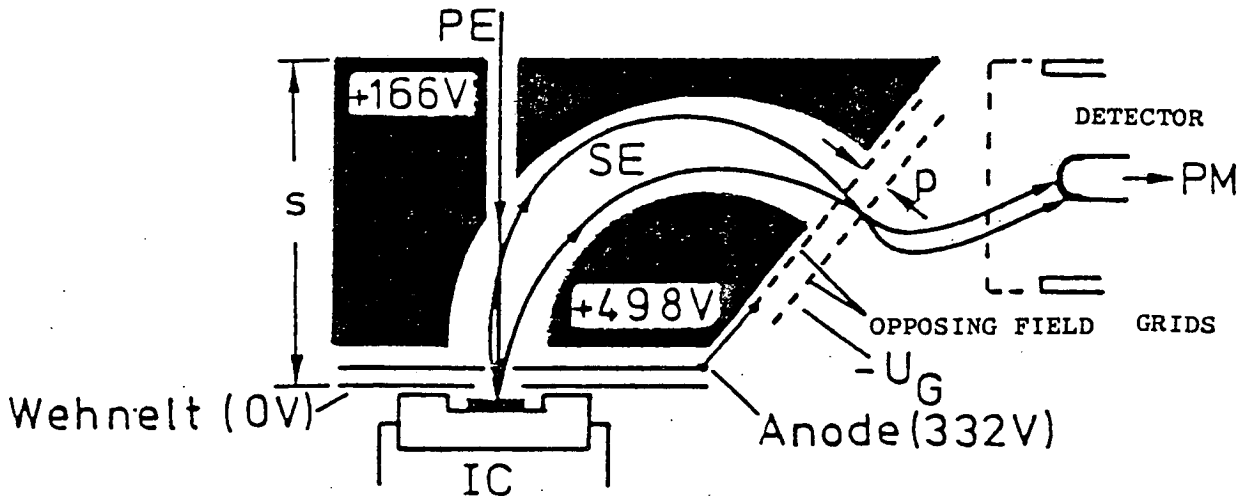


Figure 2.5(b) Balk et al(1976)

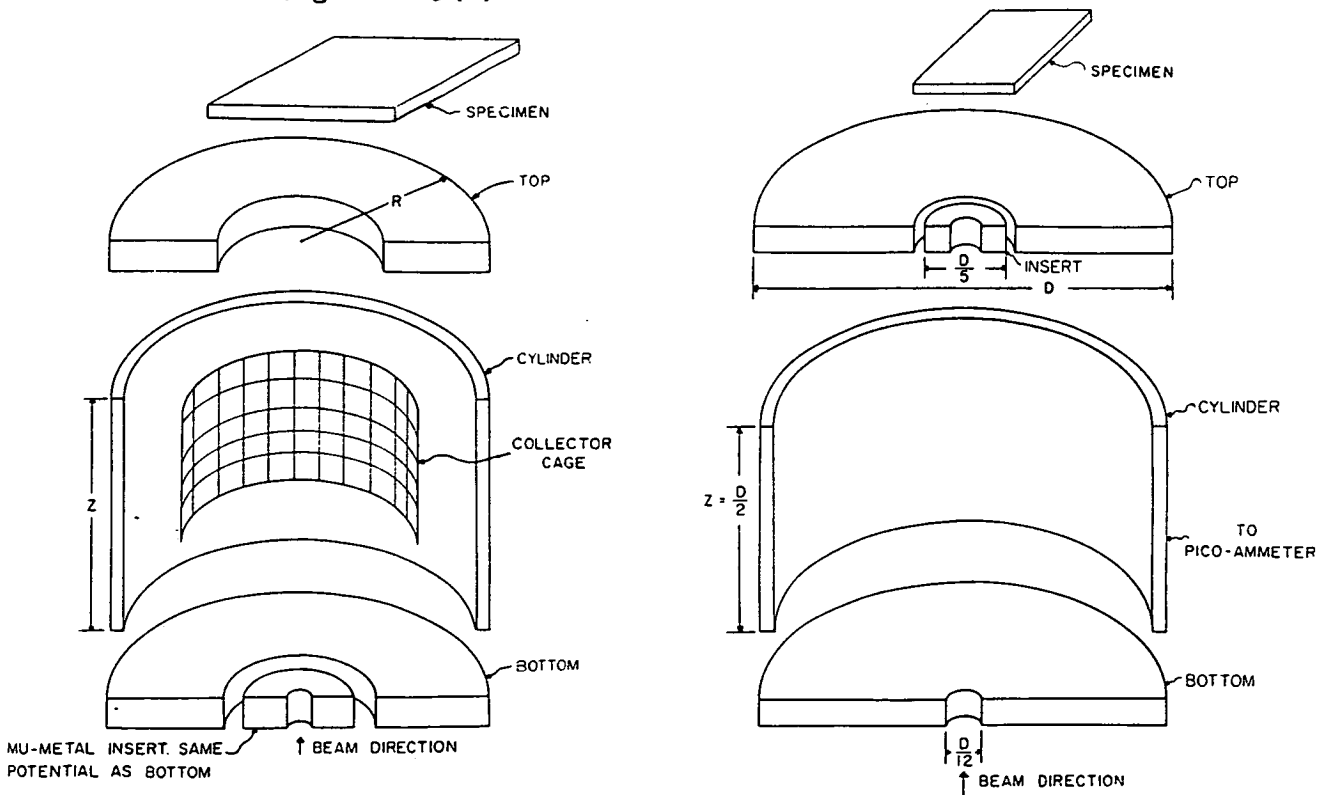


Figure 2.6(a) Banbury and Nixon(1970)

Figure 2.6(b) Yakowitz et al(1972)

the noise present in the output signal, this noise in turn mostly emanates from the shot noise in the primary electron beam. Hence the detector's voltage resolution varies according to the beam current used. The beam currents used for each detector were different, 0.3-3.0 μA by Fentem and Gopinath, 0.1 μA by Feuerbaum. The output noise is also affected by the photomultiplier, head amplifier and any signal processing used on the output, these parameters again were different for each detector.

Although line scans were presented for many detectors, different specimens were used in each case, Tee and Gopinath used a Gallium Arsenide F.E.T and Bipolar transistor, Sanger used a transverse Gunn diode, Hannah used aluminium tracks on silicon-dioxide on silicon substrate. The line scans served only to illustrate improvements on the same detector and could not compare between detectors. In some cases energy distribution curves were given, S-curves in the case of a retarding field detector and peak-curves for a band-pass detector. Fujioka et al (1981) presented S-curves as part of an investigation into surface fields and used a specimen having aluminium tracks on p-type silicon substrate. Although Hannah also provided detailed energy distribution curves for his detector, as already mentioned, he made measurements on aluminium tracks on silicon-dioxide on silicon and hence the two results cannot be directly compared. In general most results, while useful in validating improvements and adjustments on a particular detector, were of a non-standard nature.

2.1.5 General Considerations on different types of V.C Detectors

Band-Pass detectors have some undesirable features. They may reduce the signal/noise ratio at least by an order of magnitude, as reported by Wells and Bremer, the finite pass-band width also degrades the voltage measurement. They may also be sensitive to position and angle variations of electrons at their entrance, a feature reported by Hannah from computational results on his detector.

Detectors which do not use the normal scintillator and photomultiplier arrangement but collect their output signal on a plate or grid will suffer from low signal/noise ratios. Estimated currents as low as 0.1-10nA were collected by the hemispherical detector used by Fentem and Gopinath. Yakowitz et al had to bias their specimen by approximately -130V to obtain collected currents of the order of 2.0nA from their modified cylindrical detector.

Detectors which have a retarding field after the deflecting field like those of C.C.Sanger or Balk et al will experience inaccuracies in their voltage measurement. This is due to the non-linear change imposed on the electron energy distribution as electrons pass through the deflection field. The electrons on reaching the retarding field will no longer have the same energy characteristics as when leaving the specimen. Since the voltage contrast phenomenon essentially takes place just above the specimen, valuable information

could be lost.

2.2 Review of Theoretical and Computational Work on Past Detectors

2.2.1 Analysis of Different Detectors

Significant contributions in this field have been made by Hannah(1974), Munro(1971) and Menzel(1982).

Munro considered a range of detectors all of the Banbury and Nixon type or the Yakowitz type, shown in Figures 2.6(a) and 2.6(b). Surface fields are not taken into account in his analysis and all secondary electrons are assumed to be emitted at 4eV, also the cosine distribution is assumed on an electron's initial direction (Bruining(1954)). He derives an expression for the collected current based on these assumptions, starting with Equation(2.1).

$$I_C = \frac{I_0}{\pi} \int \int \underline{m} \cdot \underline{n} \, d\Omega \quad 2.1$$

If θ represents the azimuth angle and ϕ denotes the off-axis angle, $m(\phi, \theta)$ is the emission direction, $n(\phi_N, \theta_N)$ is the direction normal to specimen surface, I_0 denotes total emitted secondary current and Ω is the solid angle. From this he arrived at ,

$$I_C(\phi_N, \theta_N) = I_0(k_1 \cdot \sin\phi_N \cdot \cos\theta_N + k_2 \cdot \cos\phi_N) \quad 2.2$$

where

$$k_1 = \frac{2}{\pi} \int \int_{D^*} \sin^2\phi_0 \cdot \cos\theta \cdot d\phi \cdot d\theta$$

$$k_2 = \frac{2}{\pi} \int \int_{D^*} \sin\phi \cdot \cos\phi \cdot d\phi \cdot d\theta$$

D^* denotes a collection domain.

Munro defined collection domains for 2-D cylindrically-symmetric detectors (Figure 2.7), like the detector used by Yakowitz. The cut-off angles ϕ_c, ϕ_0 and θ_0 are found by computing many electron trajectories through the detector and noting the collected ones. Munro did this by firstly finding an analytical solution of the electrostatic field distribution within the detector and then using the Runge-Kutta method to numerically plot electron trajectories. Munro also defined a potential contrast figure of merit C_p as

$$C_p = \left(\frac{1}{k_2} \cdot \frac{dk_2}{dV_s} \right)_{V_s=0} \quad 2.3$$

contrast produced by ΔV_s is

$$\frac{I_C}{I_{CO}} = C_p \cdot \Delta V_s \quad \text{where } I_{CO} = I_0 \cdot k_2(0) \quad 2.4$$

where V_s denotes specimen voltage. Equation 2.3 gives the voltage sensitivity of the detector, since k_2 was computed for a variety of different geometrical and voltage configurations, C_p was also found for these conditions. Munro concludes from his results that a contrast stop be used with rotationally symmetric detectors; that 3-D detectors are more efficient but give less potential contrast than for 2-D symmetric detectors; that a retarding field in the form of a negatively biased ring around the specimen would improve potential contrast.

2.2.2 Criticisms on Munro's work

Munro's work is obviously limited to a narrow class of detector types. The omission of surface field effects makes the work valid for only ideal specimens. The assumption that electrons are emitted at 4eV is invalid, results from other sources (Bruining (1954)) show the existence of an energy distribution. Hence the expression for the collected current, Equation (2.1) should be extended to

$$I_C = \frac{I_0}{\pi} \iiint (\underline{m} \cdot \underline{n}) \cdot N(E) \cdot dE \cdot d\Omega \quad 2.5$$

where $N(E)$ is the initial energy distribution, $N(E)$ can easily be obtained from empirical results (Bruining (1954)). This would modify the collection domains to 3-D domains and hence make it much more difficult to find cut-off angles and cut-off energies. The technique of using collection domains is also seen to be limited in three dimensions, since for more complex detectors simple well defined boundaries will not exist in the collection domain. In these cases computing for k_1 and k_2 would require more difficult integrations. Analytical solutions for a detector's electrostatic field distribution do not exist for more complex detector geometries and numerical methods would be required.

Hannah restricted his computational analysis to his own detector. Electrostatic voltage distributions of surface fields, extraction lens and band-pass detector were solved by numerical techniques. Electron trajectories were calculated by linearization

techniques which assume constant electric fields in a small neighbourhood of the electron. Many distinct electrons were generated all with different initial energies and angles, their energy and angular distributions were taken into account. Overall peak energy curves were obtained for different surface fields, these results compared favourably with practical results. Although the computing results of Hannah showed the limitations of his own band-pass detector, the computational techniques are of a more powerful and general nature than those used by Munro. The work of Hannah also provided results for much more realistic conditions than those of Munro.

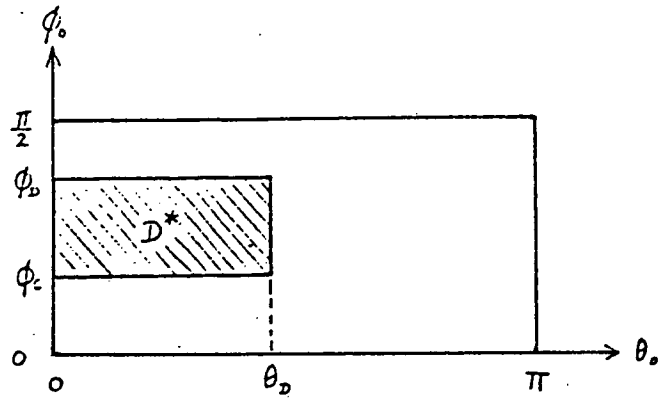
2.2.3 Work on Surface Fields

The type of surface fields that are present on a specimen obviously depend largely on the nature of the specimen. Wells in reviewing Macdonald (1970) calculated an approximate electrostatic field distribution above a P-N junction (Figure 2.8), he assumed no depletion layer and also assumed infinite boundary conditions at either side of the P-N junction. The expression is

$$V(x,y) = (E/\pi) \cdot \tan^{-1}(x/y) + Fy \quad 2.6$$

where F is the electric field above the P-N junction

Wells concluded there was a retarding field on the positive side of a P-N junction. Spivak and Rau (1979) assumed this voltage distribution and found the resulting deviations in electron energies



The collection domain D^* for a detector with a rotationally-symmetric potential distribution

Figure 2.7 (Munro(1971))

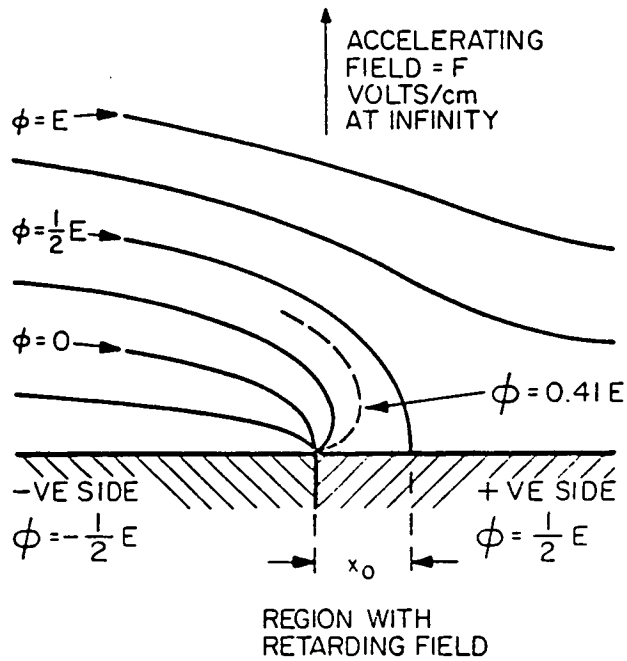


Figure 2.8
Surface Fields Above a P-N junction
(Wells reviewing Macdonald(1970))

through a linear retarding field above the P-N junction. They did not however show how their own detector coped with such deviations and how their final S-curves were affected.

Fujioka et al(1981) presented an analysis on surface fields created by inter-digitated tracks of aluminium on silicon, linear boundary conditions were assumed between tracks. Acceptance diagrams were presented of electron energy against acceptance angle, a two-dimensional field model was used. From these acceptance diagrams S-curves were constructed. No details as to how the acceptance diagrams were calculated is given. There are no results to show how a particular detector will respond to the effect of the surface fields considered.

Hannah modelled surface fields created by silicon-dioxide on silicon, the electrostatic fields were calculated by numerical techniques. The influence of surface fields on Hannah's narrow band-pass detector were investigated and corresponded well with practical results. A recursive matrix reduction method was used to find surface potential distributions, this will be discussed later in greater depth. A general study of surface fields was not made and results were only presented for his particular detector. Figure 2.9 shows a typical equipotential plot of the type of surface fields considered.

Menzel (1982) made a study on surface fields affecting planar retarding field detectors. Only one specimen layout was

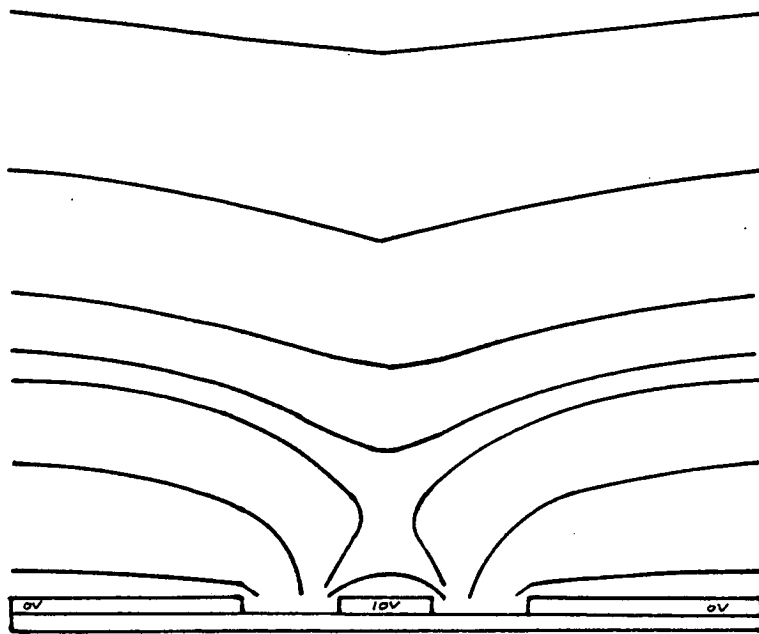


Figure 2.9 Surface Equipotentials
(Hannah(1974))

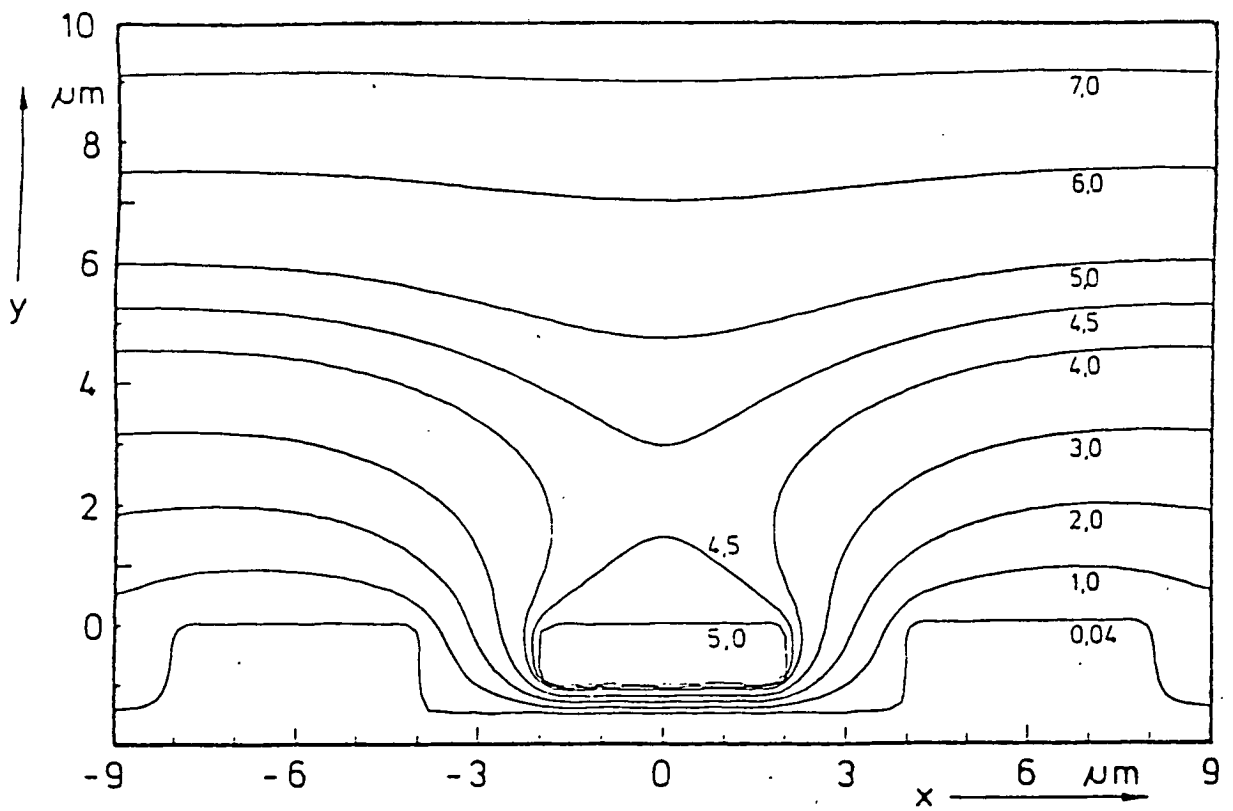


Figure 2.10 Surface Equipotentials (Menzel(1982))

considered, namely a positively biased central conductor placed between two earthed conductors with widths of 4 microns. The gaps between these conductors were set to be 2 microns. This surface model however was not a realistic representation of an I.C specimen, since the central conductor seemed to be suspended above an earthed substrate. In a real specimen all conductors lie on a dielectric, silicon dioxide for MOS devices, which in turn lies on a silicon substrate. This limitation on Menzel's work can be observed when comparing his equipotential lines in Figure 2.10 to those of Hannah in Figure 2.9 who assumed a 1 micron layer of silicon dioxide in the specimen.

Menzel uses the charge replacement method to calculate his surface field distribution. Some electron paths are calculated and the existence of a retarding field above the central conductor is shown. Effects of the surface fields are seen to change the initial electron angular distribution and hence alter the emitted secondary spectrum. The secondary emission curve is shown to drop in height from the presence of the surface fields considered. The effects of these surface fields on a specific detector are not considered and hence their effects on final S-curves are not given.

2.2.4 Grid Non-linearities

The importance of grid non-linearities in electron optics is already well known (Verster (1963)), their study however in voltage contrast detectors has only been recent. To date the only detailed

analysis of grids in voltage contrast detectors has been made by Menzel (1982).

Menzel considered a planar retarding field and found that the transmission through a grid has an angular dependence. Figure 2.11(a) shows his results on the nature of this dependence, and illustrates its cosine form,

$$T \cong T_0 \cdot \cos \alpha$$

T is the overall transmission while T_0 is the transmission through an ideal retarding field and α is the emission angle of the electron. From this expression Menzel predicted a reduction in the overall height of the normal S.E spectra shown here by Figure 2.11(b).

Menzel also investigated energy resolutions of different grids, only electrons perpendicularly incident to the grids were considered. Figures 2.12(a) and 2.12(b) show electron energy/transmission curves for electrons with an energy of 500eV. Figure 2.12(a) shows the effect of varying mesh density while Figure 2.12(b) shows the effect of varying grid spacing. From these results Menzel concluded that the energy resolution of a grid is improved for finer grid meshes and for grids spaced further apart.

Summary

This chapter has shown that previous work on Voltage Contrast is confined to particular detector types and that both theoretical and

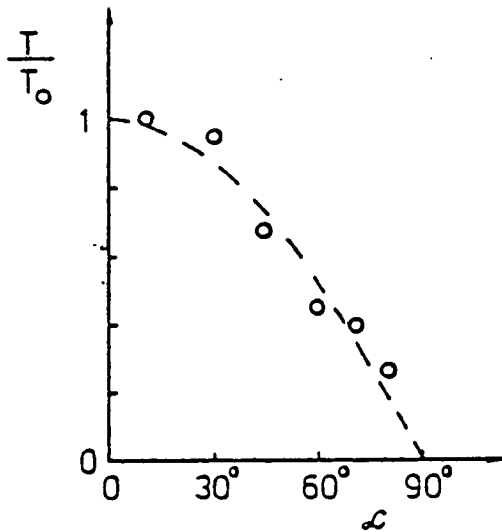


Figure 2.11(a)

Dependence of the transmission on the emission angle of the electrons. (Menzel(1982))

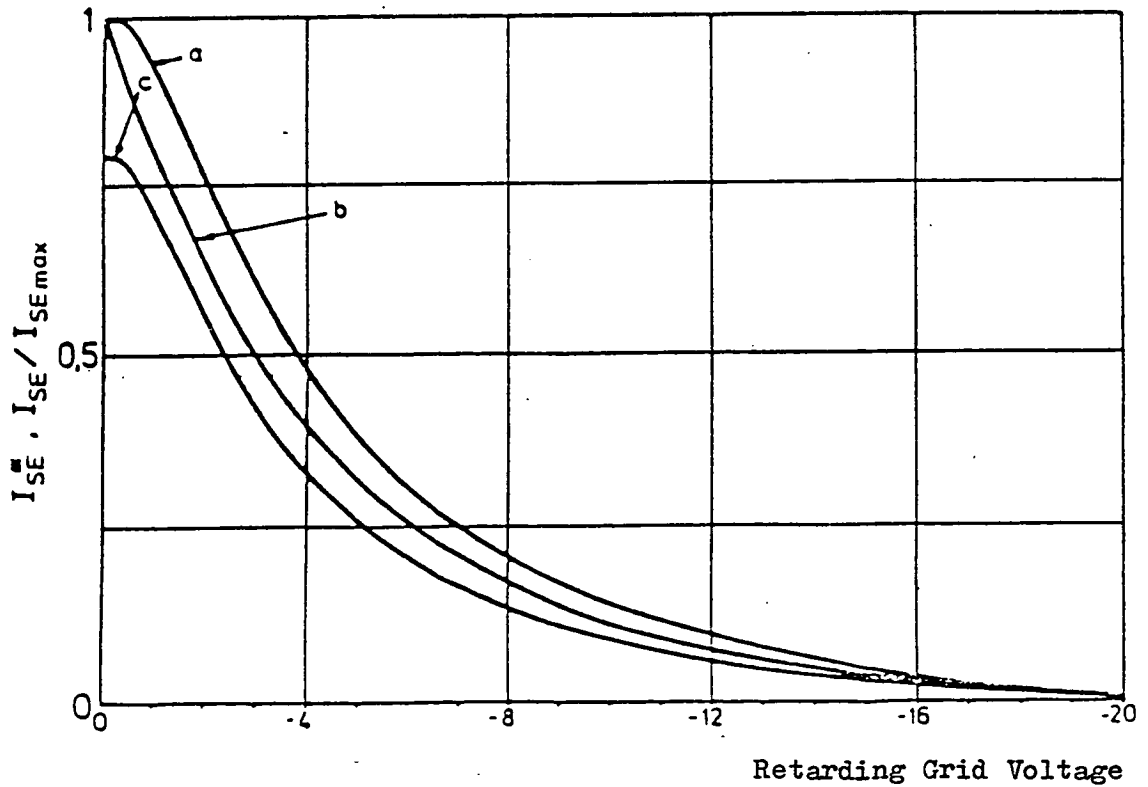


Figure 2.11(b)

Effect of Grid Non-Linearities on Secondary Electron Spectra (Menzel(1982))

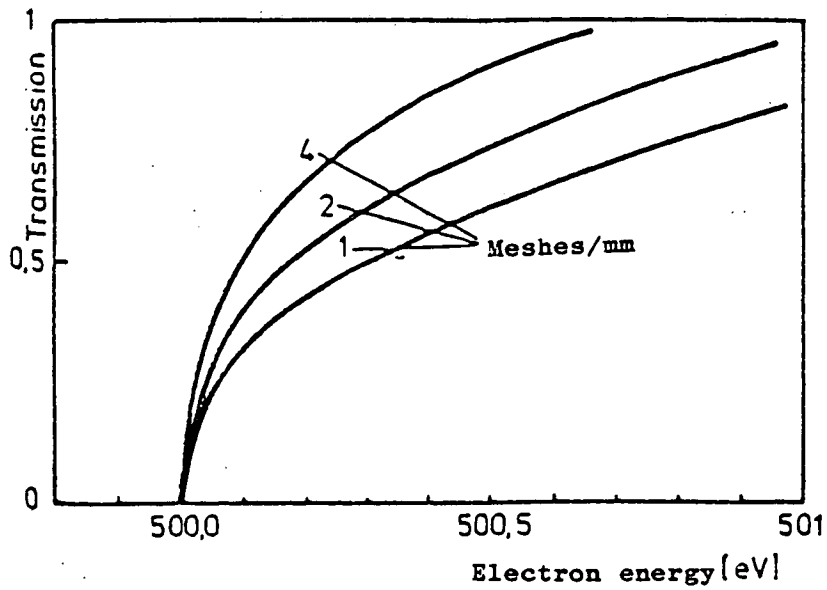


Figure 2.12(a) (Menzel(1982))

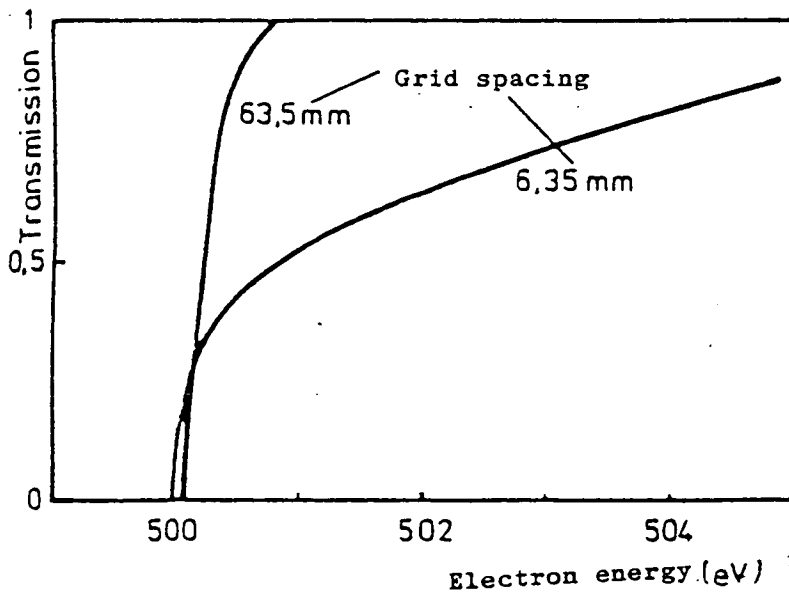


Figure 2.12(b) (Menzel(1982))

experimental results presented are of a non-standard nature. As a result general comparisons between detectors are not possible and hence it is difficult to assess the performance of any one detector. The aim of the following work is to provide a 'design tool' from which the performance of past detectors can be gauged and at the same time provide the design of a new improved detector. It was decided to develop Computer Aided Design techniques to achieve these aims since they have the flexibility to specify a wide variety of detector types. The practical alternative of making a standard electrode structure in the S.E.M from which many different detectors can be built and tested presents many difficult mechanical problems.

CHAPTER 3PROGRAMS3.1 Introduction

As mentioned in the last chapter Computer Aided Design techniques were chosen to help design and simulate voltage contrast detectors. This decision was based on their advantage of being able to specify and analyse a wide range of detector types. Hence program requirements are that they should be versatile enough to model a wide variety of detector types, and at the same time give realistic simulations of each detector. A large number of different results should be presented to give a complete assessment of a detector's performance. Prescription of a detector's electrode-geometry should be simple.

The computer simulation work is divided into three categories; programs which aid the design of detectors possessing two-dimensional symmetry; programs to model the performance of detectors which are described by three-dimensional fields; and programs which model surface fields. The first category consists of two program types, one for a two-dimensional rectilinear field and the other for a cylindrically symmetric field. The second and third categories will be discussed in Chapters 4 and 5 respectively. All programs are based on specifying an electrode geometry and voltage configuration of the field, solving the resulting electric potential distribution and then plotting electron trajectories through the field. The programs were written in Fortran and run on an ICL 2972

main-frame computer. Most results are based on the plotting of electron trajectories, this will be discussed in detail later. The following effects were neglected:

- 1) Charging of dielectrics
- 2) Contamination effects
- 3) Tertiary electrons
- 4) Backscattered electrons
- 5) Electron-electron interactions, quantum and relativistic effects

3.2 Solving Potential Field Distributions

The description of any electrostatic field distribution is governed by Laplace's equation

$$\nabla^2 V = 0$$

where V denotes the electric potential distribution, Equation (3.1) assumes no charge in the field. Laplace's equation holds for many orthogonal coordinate systems. The standard established techniques for solving Laplace's equation are:

- 1) Analytical methods
- 2) Numerical methods
- 3) Electrolytic tank
- 4) Impedance network
- 5) Conductive paper
- 6) Rubber membrane model

(3-6) are experimental methods of solving Laplace's equation and generally unsuitable for large simulation work. Analytical methods are restricted to only simple electrode geometries, among the most powerful techniques within this class of problems are conformal transforms (Gibbs(1958)). The transformation equation however, in many cases may be extremely difficult or impossible to find. Since the design of electron detectors requires great versatility in solving a wide range of field problems analytical methods were found to be unsuitable.

Numerical methods for solving electrostatic field problems are

not restricted to a narrow class of field types as with analytical methods. There are three main types of numerical technique for solving Laplace's equation,

- a) Finite-Difference Methods
- b) Finite-Element Methods
- c) Charge Replacement Methods

The finite-element and charge replacement methods have only been applied to electron optics relatively recently by Munro(1970) and Cruise(1963) respectively. The relaxation method has been applied to electron optics for much longer. Hannah(1974) used finite-difference methods to solve field distributions on his voltage contrast detector, apart from this none of the above methods have been applied to voltage contrast detectors. To date the main applications of the finite-element and charge replacement methods in electron optics have been in electron lenses (Mulvey and Wallington(1973)). Finite-difference methods were chosen for the foregoing simulation of voltage contrast detectors primarily because they had been applied to a limited degree for this purpose before and also since they are generally much simpler to program than the other two methods. It must be acknowledged however that finite-element methods have advantages over finite-difference methods in certain situations. One major advantage is that chosen areas of the field can be specified to a greater accuracy than other areas, the full implications of which will be discussed later. Both methods can specify electrodes of any shape although finite-difference methods are generally more cumbersome in this

respect. However this can be overcome by careful programming and does not pose a serious problem.

3.2.1 Finite-Difference Methods

The normal procedure is to impose a square mesh on the field, Laplace's equation applies to each node of the mesh. The standard finite-difference form of Laplace's equation is used (Vitkovitch(1966))

$$V_1 + V_2 + V_3 + V_4 - 4*V_0 = 0 \quad 3.2$$

Figure 3.1 shows a typical two-dimensional star for which Equation (3.2) holds. Initial potential values are assigned to each node, in which case Equation (3.2) will be modified to

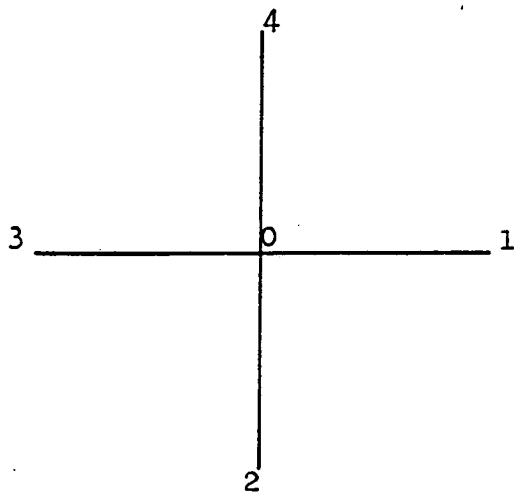
$$V_1 + V_2 + V_3 + V_4 - 4*V_0 = \text{Res} \quad 3.3$$

where Res denotes a residual value. Obviously potential values must be changed so the residual value is zero at each node. This is done by a convergence technique called Over-Relaxation (Vitkovitch(1966)), V_0 is altered according to the residual and a convergence factor, this process is repeated for every mesh point, the algorithm used is

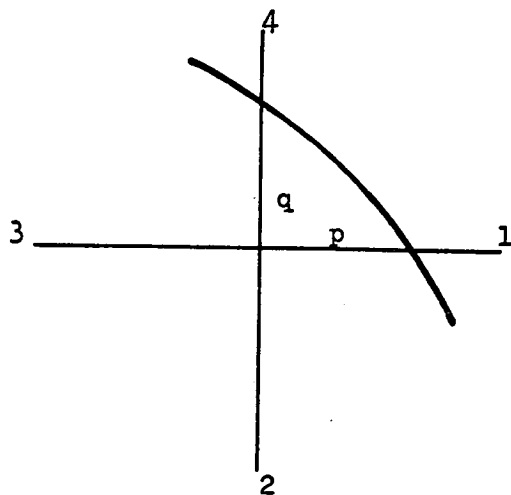
$$V_0 = V_0 + \text{Res} \cdot \alpha / 4 \quad 3.4$$

where α is the convergence factor and lies between 1 and 2.

This algorithm is applied to the mesh in an iterative manner,



Symmetrical Star
Figure 3.1



Asymmetrical Star
Figure 3.2

until the maximum residual in the field falls below a preset limit specified by the user. The convergence factor can either retard or accelerate the whole process, careful choice of the convergence factor is important in greatly reducing computational time.

In the case of curved boundaries, Figure 3.2, a different residual is required (Vitkovitch(1966)),

$$\text{Res} = \frac{2*V_1}{p(p+1)} + \frac{2*V_3}{p+1} + \frac{2*V_2}{q+1} + \frac{2*V_4}{q(q+1)} - 2*\left(\frac{1}{p} + \frac{1}{q}\right) \quad 3.5$$

$$V_0 = V_0 - \frac{\text{Res}*\alpha}{2(1/p+1/q)} \quad 3.6$$

The residual also changes according to the coordinate system, the three most commonly used in electron optics are, rectilinear cylindrical and spherical coordinates. Equation (3.3) applies to a two-dimensional rectilinear case where Laplace's equation takes the form

$$\frac{\partial^2 V}{\partial x^2} + \frac{\partial^2 V}{\partial y^2} = 0 \quad 3.7$$

In the cylindrically symmetric coordinate system Laplace's equation is given by

$$\frac{1}{\rho} \frac{\partial V}{\partial \rho} + \frac{\partial^2 V}{\partial \rho^2} + \frac{\partial^2 V}{\partial z^2} = 0 \quad 3.8$$

Figure 3.3(a) defines cylindrical coordinates, a typical relaxation mesh star is shown in Figure 3.3(b) and its residual equation is given by

$$V_1\left(1 + \frac{1}{2\rho}\right) + V_2 + V_3\left(1 - \frac{1}{2\rho}\right) + V_4 - 4*V_0 = \text{Res} \quad 3.9$$

Figure 3.4(a) defines spherical coordinates in which the potential is assumed to be symmetrical in the azimuth direction. Laplace's equation is given by

$$\frac{2}{r} \frac{\partial V}{\partial r} + \frac{\partial^2 V}{\partial r^2} + \frac{\cot \theta}{r^2} \frac{\partial V}{\partial \theta} + \frac{1}{r^2} \frac{\partial^2 V}{\partial \theta^2} = 0 \quad 3.10$$

A typical relaxation mesh star is shown in Figure 3.4(b), the residual equation becomes

$$\text{Res} = V_1(1+1/r) + V_2(1+\cot\theta/2)/r^2 + V_3(1-1/r) + \frac{V_4(1-\cot\theta/2)}{r^2} - 2V_0(1+1/r^2) \quad 3.11$$

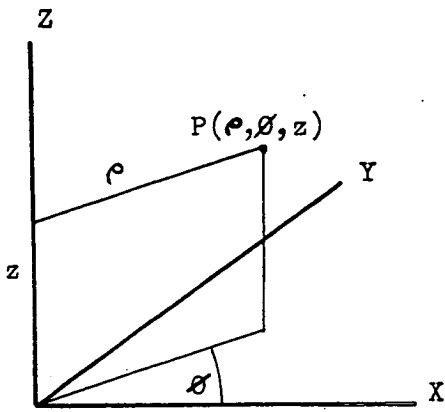
All the above coordinate systems can be extended to describe three dimensional fields, the simplest case being the rectilinear coordinate system in which Laplace's equation becomes

$$\frac{\partial^2 V}{\partial x^2} + \frac{\partial^2 V}{\partial y^2} + \frac{\partial^2 V}{\partial z^2} = 0 \quad 3.12$$

and the mesh-star shown in Figure 3.5 would be used when the residual equation is changed to

$$\text{Res} = V_1 + V_2 + V_3 + V_4 + V_5 + V_6 - 6*V_0 \quad 3.13$$

The residual equation will also be changed at boundaries between two different mediums, this will be described later. All the residual equations described so far were used at some stage in the computer simulation work.



Cylindrical Coordinate System
Figure 3.3(a)

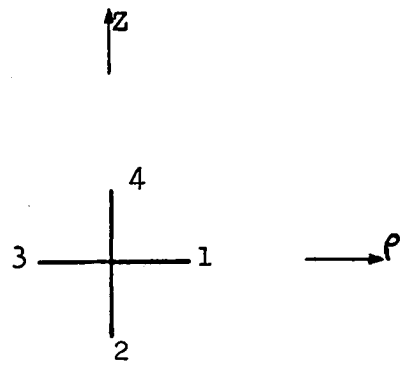
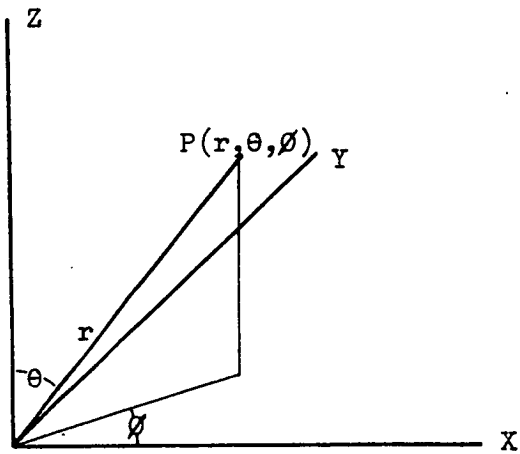


Figure 3.3(b)
Typical Star in Cylindrical Coordinates



Spherical Coordinate System
Figure 3.4(a)

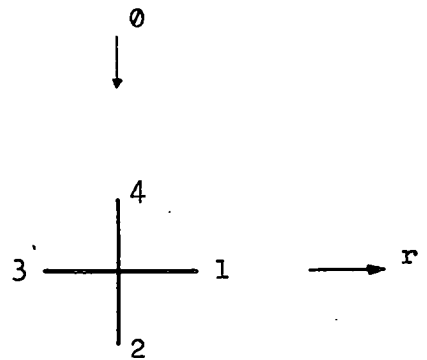
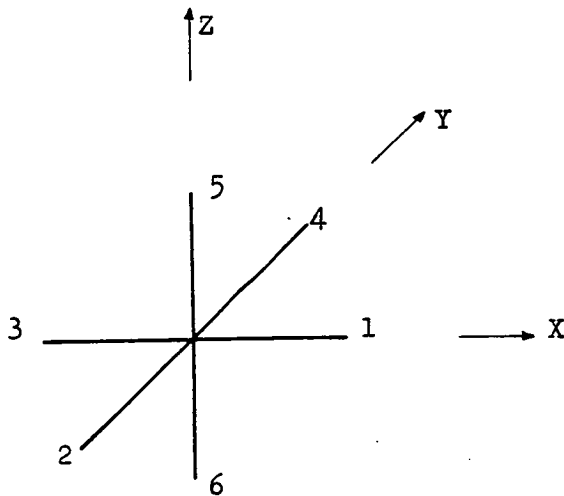


Figure 3.4(b)
Typical Star in Spherical Coordinates



Relaxation Star in Rectilinear Coordinates
Figure 3.5

3.2.2 Electron Trajectory Plots

The equation of motion for electrons passing through an electrostatic field is given by,

$$m\mathbf{r} = eE\mathbf{r} \quad 3.14$$

$$m\dot{x} = eE_x \quad 3.15$$

$$m\dot{y} = eE_y \quad 3.16$$

$$m\dot{z} = eE_z \quad 3.17$$

where e is the electron charge, m is the electron mass, E_r, E_x, E_y and E_z are electric fields in the r, x, y and z directions. In general these equations are coupled since E_x, E_y, E_z are all functions of (x, y, z) . If however a small time interval is considered over which E_x, E_y and E_z can be approximated to be constant, then Equations (3.15-3.17) are decoupled and can be directly resolved into the following form

$$dx = V_x dt + (1/2)(e/m)E_x dt^2 \quad 3.18$$

$$dy = V_y dt + (1/2)(e/m)E_y dt^2 \quad 3.19$$

$$dz = V_z dt + (1/2)(e/m)E_z dt^2 \quad 3.20$$

where V_x, V_y and V_z are velocities in the x, y and z directions respectively and dt is a small time interval. Hence if E_x, E_y and E_z can be calculated at every point in the field then the electron trajectory can be plotted in small steps within which the electric field is assumed to be constant and Equations (3.18-3.3.20) apply. The time interval can also be made variable so as to restrict the spatial step within specified limits and hence make sure each trajectory step is small enough for the linear electric field approximations. Figure 3.6 shows a flow diagram of the trajectory

Plotting an Electron Trajectory

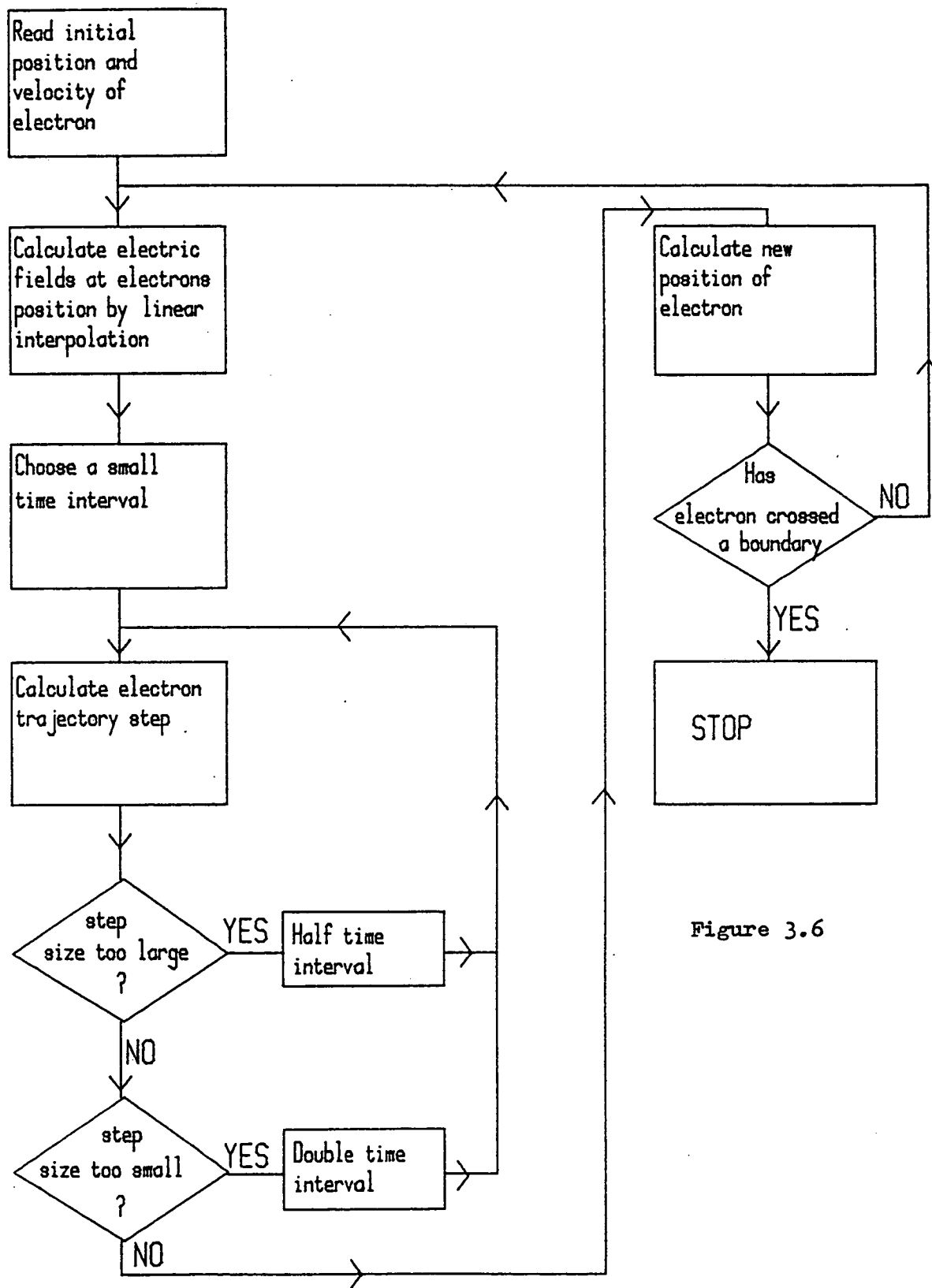


Figure 3.6

plotting principle for a single electron, this approach was used by Hannah(1974).

In general, trajectory plotting in coordinate systems other than rectilinear is much more difficult. Even when electric fields are assumed to be constant over a small time interval the resulting differential equations are still coupled and hence difficult to solve. The standard numerical technique employed to compute electron trajectories in these cases is the Runge-Kutta method. The Runge-Kutta method, however, greatly increases the computational time of the electron trajectory plot. A variable time-step in this case would be much more difficult to achieve and further increases overall computational time. Since a requirement of programs written to analyse voltage contrast detectors is that they should be capable of large-scale simulation of many electron paths, the above problems with the Runge-Kutta method were avoided and in most cases electron paths were calculated in rectilinear coordinates. In cases where the field distribution was solved in coordinate systems other than rectilinear, linear interpolation was used to create a rectilinear potential field.

3.2.3 Calculation of Electric Fields for the Electron Trajectory

Electric fields are required for the computation of every step in the path of an electron trajectory. This in turn necessitates the knowledge of the electric potential at every step in the electron trajectory. The electric field is related to electric potential by

$$\underline{E} = -\nabla V \quad 3.21$$

In general the potential of the field will be known at the nodes of the relaxation mesh. Linear interpolation is used to find the electric field between mesh nodes. This technique is illustrated in Figure 3.7. Small segments parallel to the coordinate axis are projected from the electron's position; these are depicted by XD and YD in Figure 3.7. The length of XD and YD are specified by the programmer as initial conditions. Potentials at P, Q, S are found by linear interpolation from the mesh nodes. Hence approximate values of electric fields can be found from

$$E_x = (V_S - V_P) / 2 \cdot X_D \text{ and } E_y = (V_Q - V_P) / 2 \cdot Y_D \quad 3.22$$

where V_S , V_P and V_Q are voltages at points S, P and Q respectively. The directions in which points Q and S are projected depend upon the sign of the electron's velocity components in the x and y directions.

Calculating Electric Fields

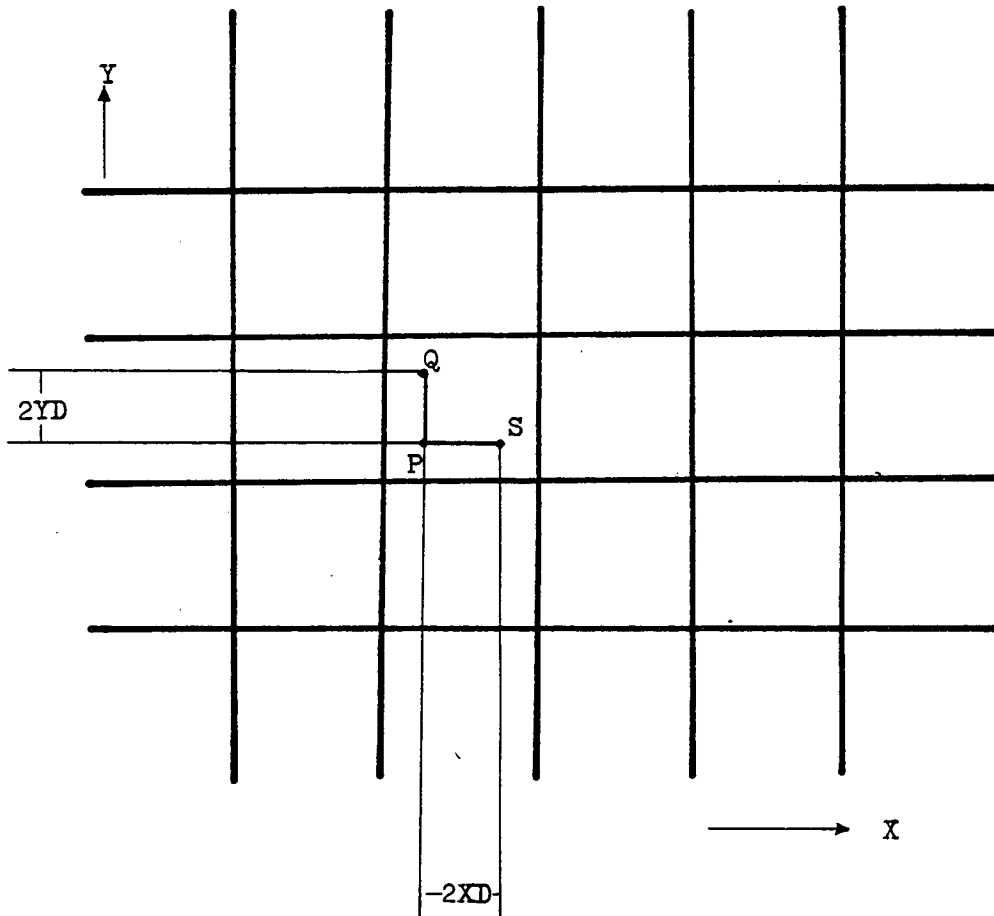


Figure 3.7

3.3 Program Options

All programs can provide the following options :

- 1) A single trajectory plot
- 2) Plots of trajectories at different initial angles
- 3) Calculation of electron transport efficiencies
- 4) Collected current variations from electrode-voltage changes(S-curves)
- 5) Error assessment

Figure 3.8 shows a general flow diagram incorporating the above options. Options (3-5) require large-scale simulation of secondary electrons.

3.3.1 Simulation of Secondary Electrons leaving a Specimen

In order to properly assess a detector's performance, secondary electrons leaving a specimen need to be modelled. Once this has been done various characteristics, like transport efficiency and S-curves, can be found for a detector. As already mentioned, electrons leaving a specimen have both an energy and angular distribution. The energy distribution has been found experimentally (Bruining(1954)) and takes the form shown in Figure 3.9(a). For the purposes of the computer simulation, an analytical expression was developed to model this distribution. It takes the following form,

$$N(E) = E^2 \exp(-E^2/k^2) \quad 3.23$$

General Program Options

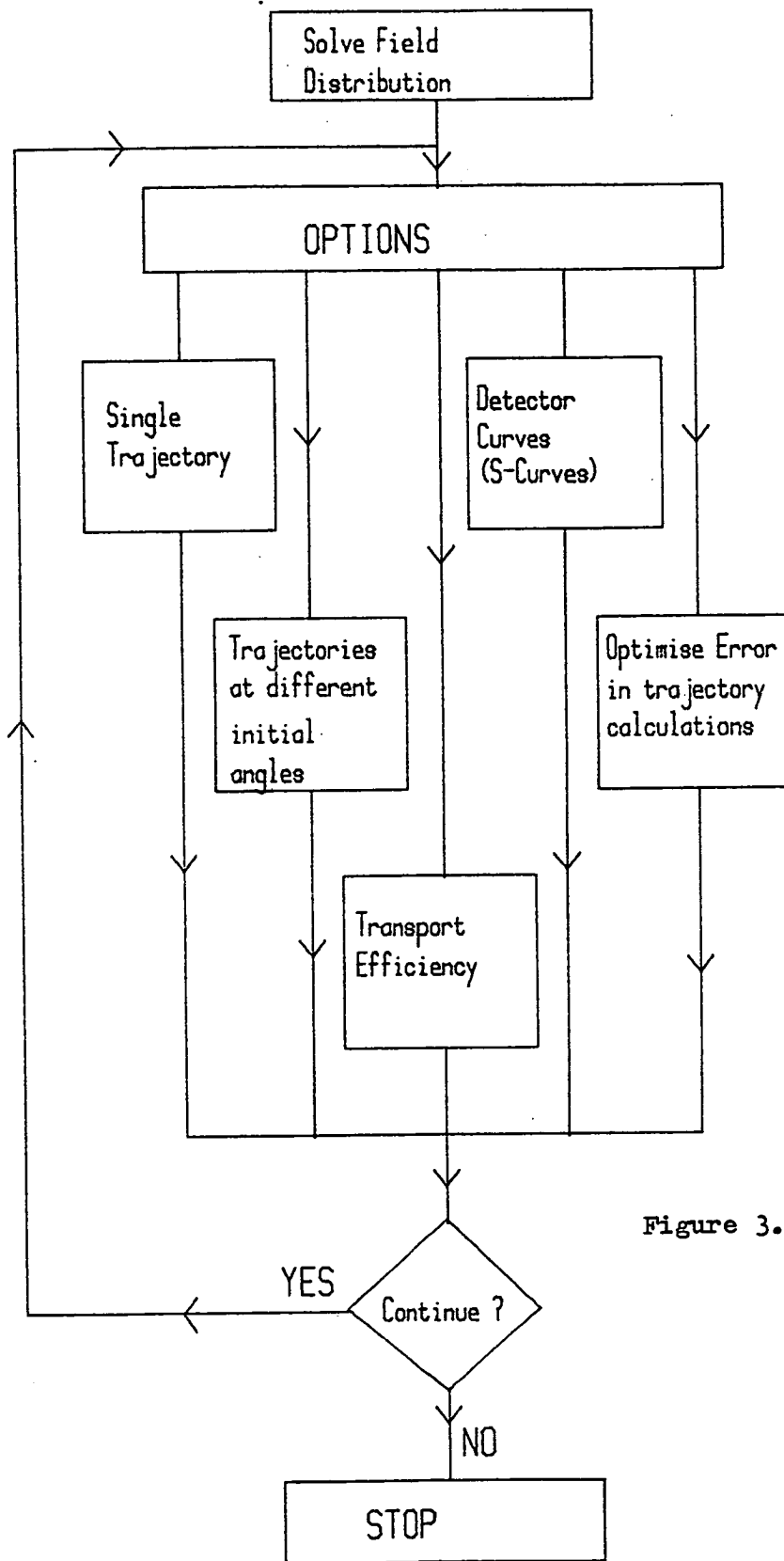
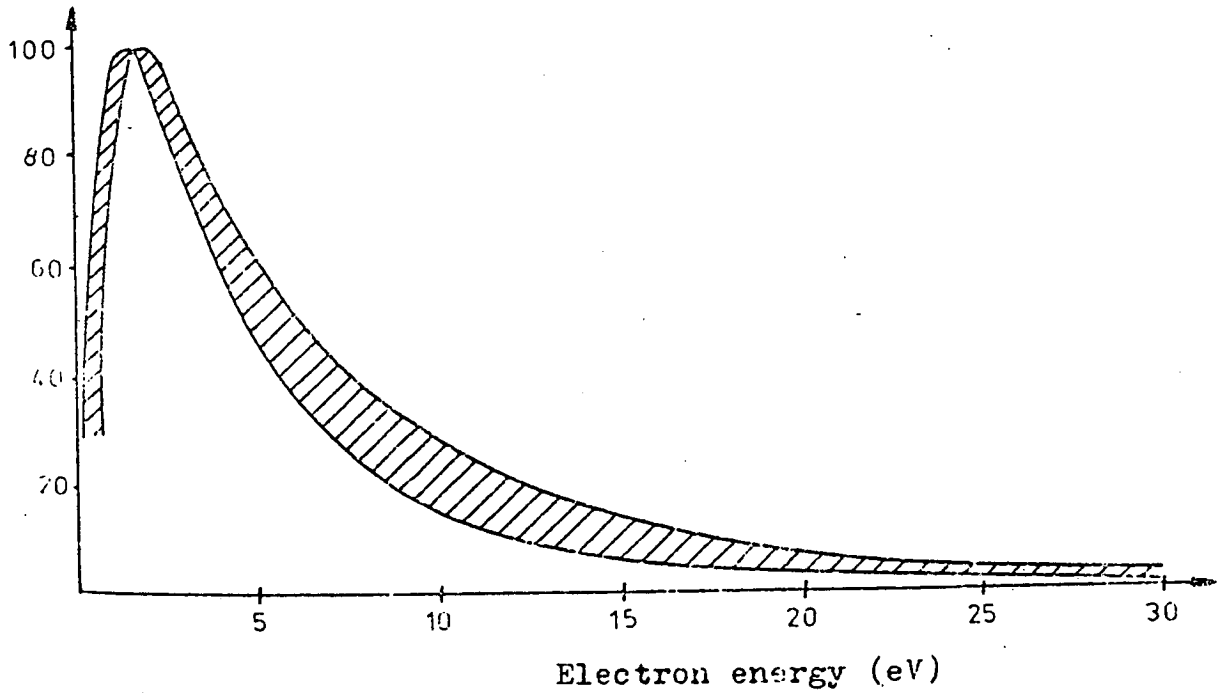


Figure 3.8

Relative number of electrons



Range of energy spectra measured for 10 different metals

Figure 3.9(a)

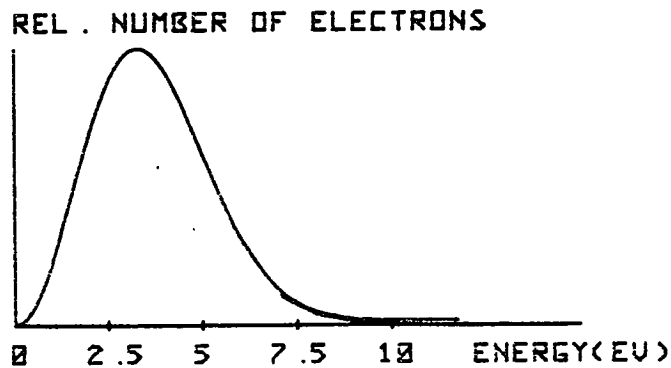


Figure 3.9(b)

Analytical Approximation to Energy Spectra

k represents the energy of the peak value of the spectrum and is chosen to be 3eV and E represents the electron's energy. The approximate analytical curve is drawn in Figure 3.9(b). The secondaries have an angular distribution which takes a cosine form neglecting the effects from any surface fields. Figure 3.9(c) shows that the angular distribution is only present for the off-axis angle and is independent of the azimuth angle. The total number of electrons leaving the surface is given by

$$N_{\text{total}} = \int_{\phi=0}^{2\pi} \int_{\theta=0}^{\pi/2} \int_{E=0}^{\infty} E^2 \cdot \exp(-E^2/k^2) \cdot \cos\theta \cdot dE \cdot d\theta \cdot d\phi \quad 3.24$$

A discrete form of the above expression was taken. The energy range was truncated to 12eV and intervals of typically 1eV were taken. Similarly the angle ranges were approximated by a limited number of angles, typically 4 for θ and 5 for ϕ . Hence secondary electrons were generated over a wide range of initial angles and energies, the distribution was given by

$$N_{\text{total}} = \sum_{\phi=0}^{2\pi} \sum_{\theta=0}^{\pi/2} \sum_{E=0}^{12\text{eV}} E^2 \cdot \exp(-E^2/k^2) \cdot \cos\theta \cdot (\Delta E) \cdot (\Delta\theta) \cdot (\Delta\phi) \quad 3.25$$

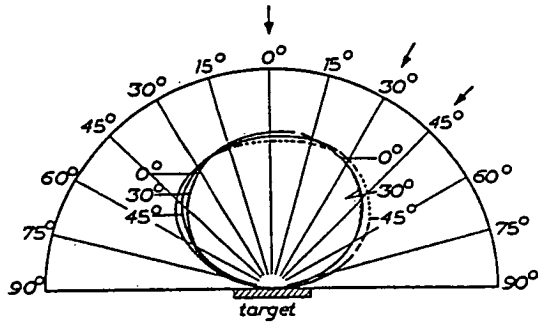
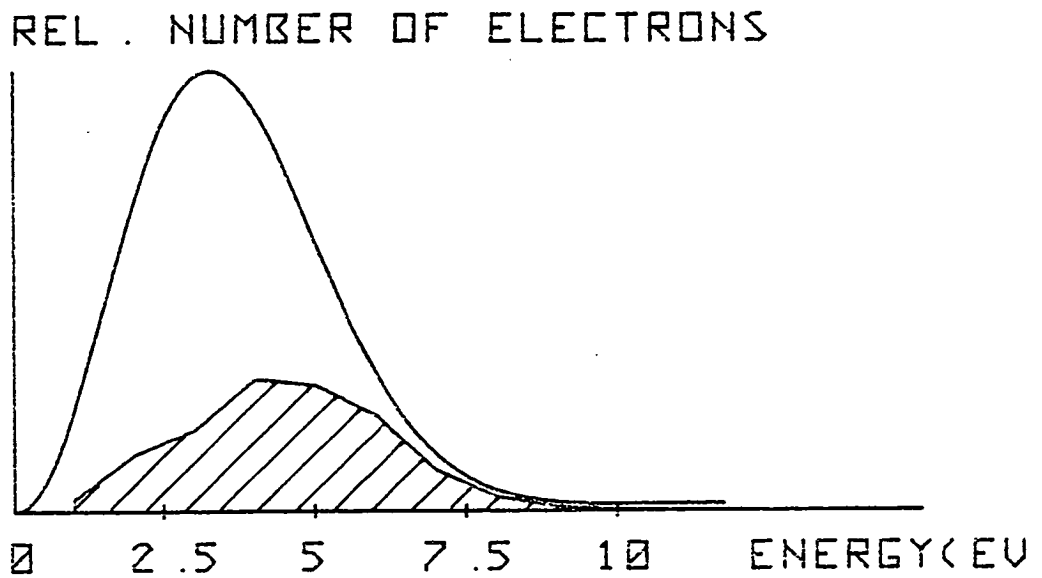


Figure 3.9(c) Angular Distribution of emitted electrons



TRANSPORT EFF. = 0.31

Figure 3.10

Transport Efficiency over the Electron Energy Range

3.3.2 Overall Transport Efficiency

Particular areas in the electrode layout were defined as collection areas. If an electron passed through such an area its trajectory was terminated and its contribution to a 'collected current total' was registered. The collected total can be represented by

$$N_{\text{collected}} = \sum_{\phi} \sum_{\theta} \sum_{E} E^2 \cdot \exp(-E^2/k^2) \cdot \cos\theta \cdot P(E, \theta, \phi) \cdot (\Delta E) \cdot (\Delta\theta) \cdot (\Delta\phi) \quad 3.26$$

where $P(E, \theta, \phi) = 1$ for a collected electron

$= 0$ for an electron not collected

The Transport Efficiency is computed by

$$\text{Transport Efficiency} = N_{\text{collected}} / N_{\text{total}} \quad 3.27$$

This provides an important figure of merit for each detector. The Transport Efficiency can also represent a relative measure of the current collected in the scintillator.

3.3.3 Filter Response

Transport Efficiencies can also be calculated for each energy interval and hence a graph of transport efficiency and electron energy can be drawn. Figure 3.10 shows a typical graph of this type. The shaded area represents collected electrons, the total shaded area would equate to the overall transport efficiency given by

Equation (3.27). Hence the energy-filter action of a detector can be fully investigated and its 'energy-filter' curve displayed.

3.3.4 Collected S-curves

The overall Transport Efficiency figure can represent a relative measure of the current collected by the scintillator in the S.E.M. An option in the computer simulation work was written to model time-varying electrodes on a detector. Such variations will cause characteristic changes in the output current, the most important of these is the time-variations in the retarding electrode voltage which produces S-curves in the output current. This option was by far the most demanding on overall computational time; detector curves were calculated in overnight batch-operations typically 4800 trajectories were required to generate one S-curve. The computer results from this program option were directly compared with experimental results from some real detectors. The experimental results were photographed from an oscilloscope or obtained on a X-Y recorder. The detector curves also gave insight about the theoretical performance and operation of voltage contrast detectors. Shifts in S-curves could also be displayed. Backscattered electrons are not modelled in the calculation of output currents but this does not detract from the simulation work since currents due to backscattered electrons are usually constant whereas only relative changes in current are simulated in this option.

3.3.5 Error Option

There are four main sources of error inherent in a single trajectory path:

- 1) Errors in calculations of potential field distributions
- 2) Errors in using linear interpolation between mesh nodes
- 3) Errors in the linearization of electric fields in a small neighbourhood around the electron
- 4) Errors in the finite trajectory step sizes used in the calculation of an electron's trajectory

The overall error is composed from a complex interaction of the above errors. Analytical expressions for these errors, in this case have little practical value and empirical methods are required. Errors in the calculation of the potential field distribution can further be divided into truncation errors and computational errors. The former arises from neglecting higher order terms in the Taylor's expansion used to approximate Laplace's equation in finite-difference form. The latter results from the existence of a finite residual value in Equation 3.3, obviously an infinite number of iterations are required to put this residual to zero and hence a tolerable value must be reached.

The empirical approach in reducing the overall error was to vary certain free parameters into regions where further variation had negligible effects on the electron's trajectory. Within these regions the error was assumed to change very slowly and hence could

be neglected. Four parameters were optimised, these were:

- 1) The resolution of the relaxation mesh
- 2) The number of iterations in the relaxation process
- 3) The electric field step size
- 4) The electron trajectory step size

The first three parameters could usually be chosen from program experience. Careful attention had to be devoted to the choice of a suitable relaxation mesh size. In general several different mesh resolutions were initially prescribed for each detector and after trial simulations an optimised size was found. The fourth parameter was found to be the most dependent on specific detector designs, and a special program option was written to optimise this parameter. In general, errors due to this parameter are large when electrons cross areas with sharp field changes. Changes in output currents were noted against variations in electron trajectory step size and a graph showing this relationship was drawn initially for each detector. Working values of electron step size were chosen in regions of constant output current. The generation of a single graph in this option required overnight operations and typically took the plotting of 4800 trajectories.

3.4 DETECTOR DESIGN PROGRAMS

The aim of this section was to write general programs to model any electrode geometry and voltage configuration in two-dimensional rectilinear and two-dimensional cylindrical coordinates. Such flexibility is difficult to obtain for detectors in three-dimensional coordinate systems and in these cases separate programs were written. To achieve the aforementioned aim the following techniques had to be developed:

- 1) Versatile methods of prescribing electrode layout
- 2) Versatile methods of solving the resulting field distributions
- 3) Sophisticated interpolation routines for electrons near electrodes
- 4) Special error-reducing routines in the calculation of electron trajectory steps
- 5) Methods to simulate electrons colliding with electrodes and electrons traversing grids

Another important requirement was to make the programs interactive, and hence make them more powerful as a design tool. Figure 3.11 shows how the interactive facility can enhance the design of a detector. A tentative design is initially specified into the program, the field is solved and its performance is simulated. Based upon these results appropriate changes in the detector design can be made. The process is then repeated until a

Interactive Design

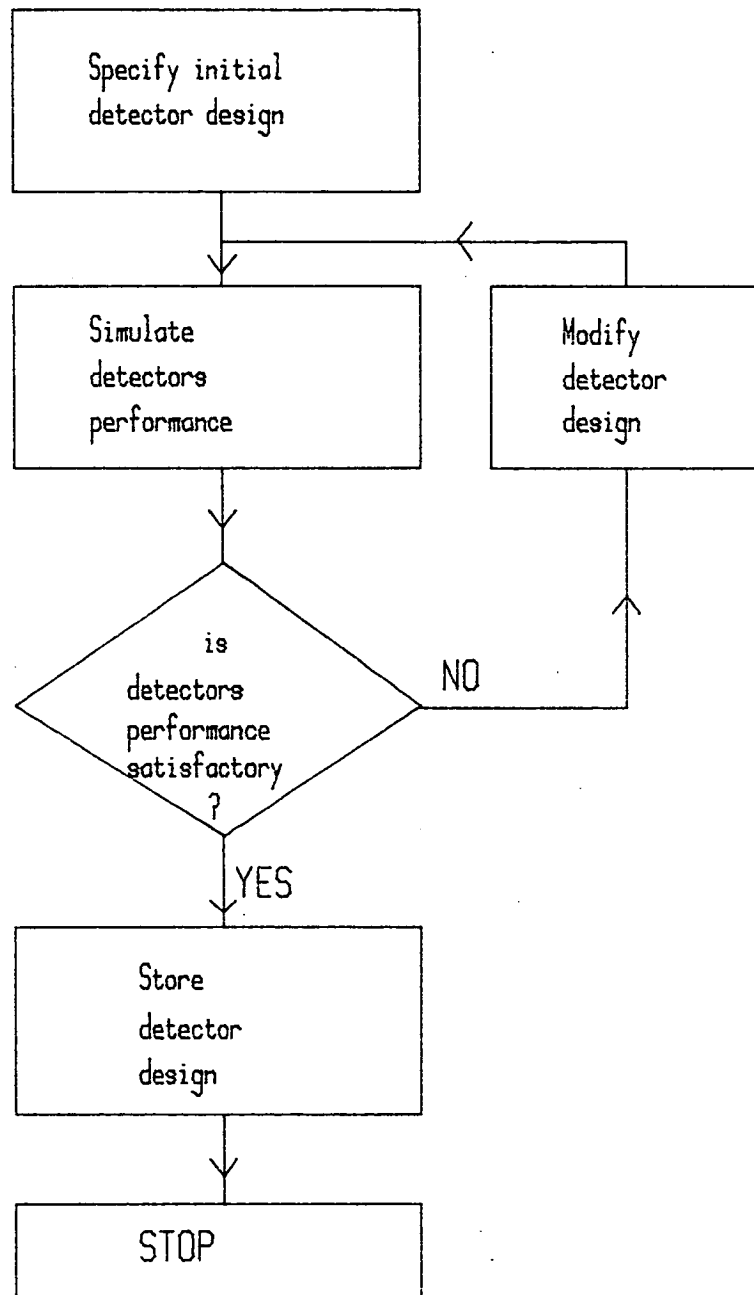


Figure 3.11

high performance detector is found;the detector can then be permanently stored. The facility to read any previous designs into the programs also exists, enabling the simulation of past detectors whose fields can be described in two dimensions.To achieve the interactive facility the programs had to be continually optimised at each stage of their development,in order to reduce program run times. However the conflicting requirement of high accuracy in field and trajectory calculations tended to increase program run-times.In general a compromise had to be reached between making the programs interactive and at the same time obtaining the required accuracy.

3.4.1 Computer Graphics in Specifying Detector Design

Graphics terminals were used in the display of input and output information.The standard cursor facility on these terminals was used to interactively specify a detector's geometrical and voltage configuration.The cursor facility is invoked by a command within the main design program.When this command is called the cursor position coordinates and an instruction character are input by the programmer.The cursor position is defined by a set of perpendicular cross-hairs and its position is entered simultaneously with the instruction character from the terminal keyboard.Figure 3.12 shows the cursor cross-hairs defining electrode segments from which a complete electrode layout can be specified.

3.4.2 Instruction Characters

So far five instruction characters exist, although many more could be added. The existing characters perform the following functions :

M - defines the initial coordinates of a segment

D - draws a line from the last cursor position to the current cursor position and registers this position as the end of a segment.

F - registers another boundary

G - registers a grid boundary

S - terminates the drawing of the electrode arrangement. Figure 3.13 shows the flow diagram for specifying an electrode layout using instruction characters.

There are three boundary or electrode types which are defined; a conductor; a grid; and a collection boundary. All electrode segments are divided into the above categories, and within each category every segment is numbered and stored. Collection boundaries are specified after the other boundaries using the same method. The relaxation field mesh is not affected by collection segments.

3.4.3 The Relaxation Mesh

As each segment of a conductor or grid is drawn by the cursor, it modifies the relaxation mesh by creating asymmetrical stars in the mesh. The coordinates of both the beginning and the end of a segment are transformed from picture space to their corresponding positions

Prescribing an Electrode Layout

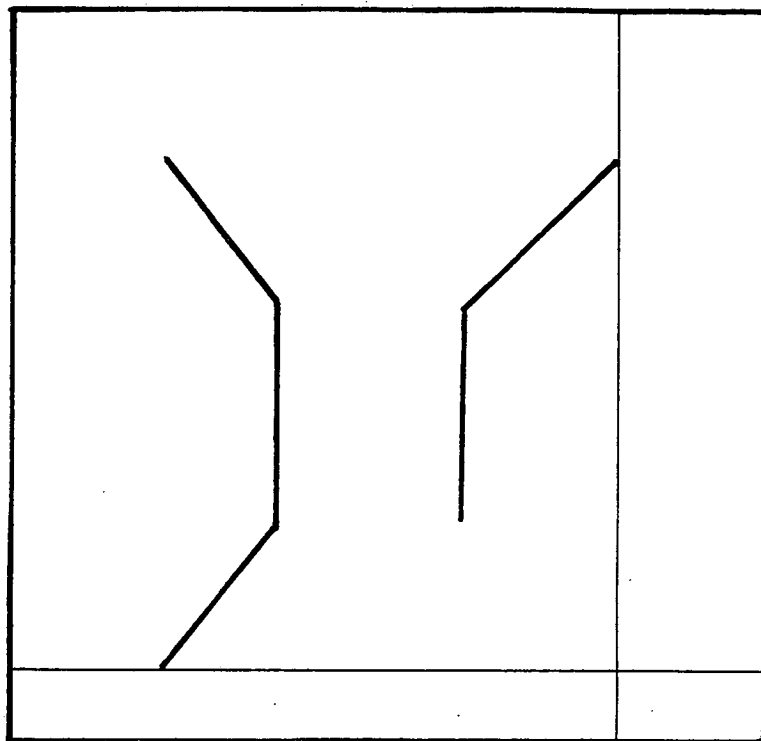


Figure 3.12

Relaxation Mesh on Graphics Screen

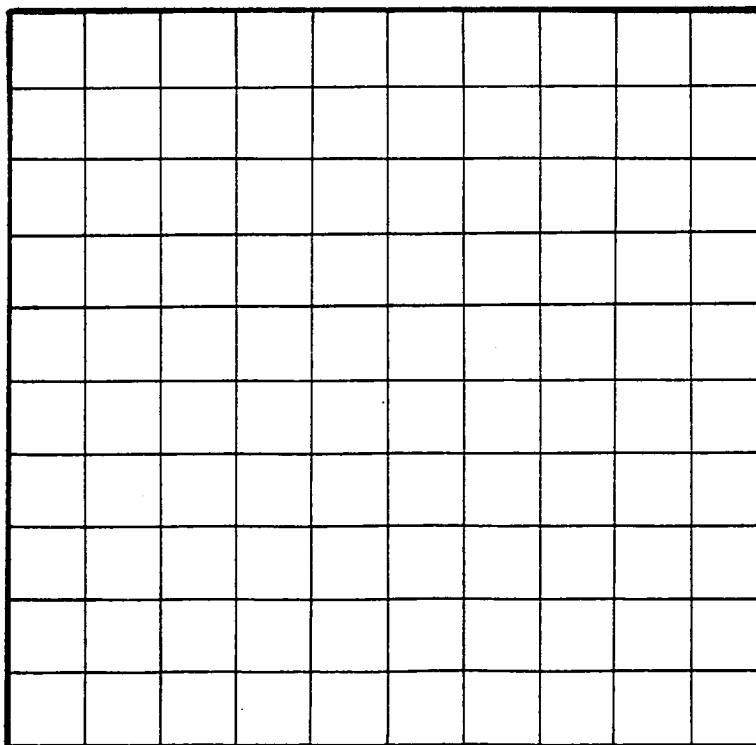


Figure 3.14

Specifying an Electrode Layout

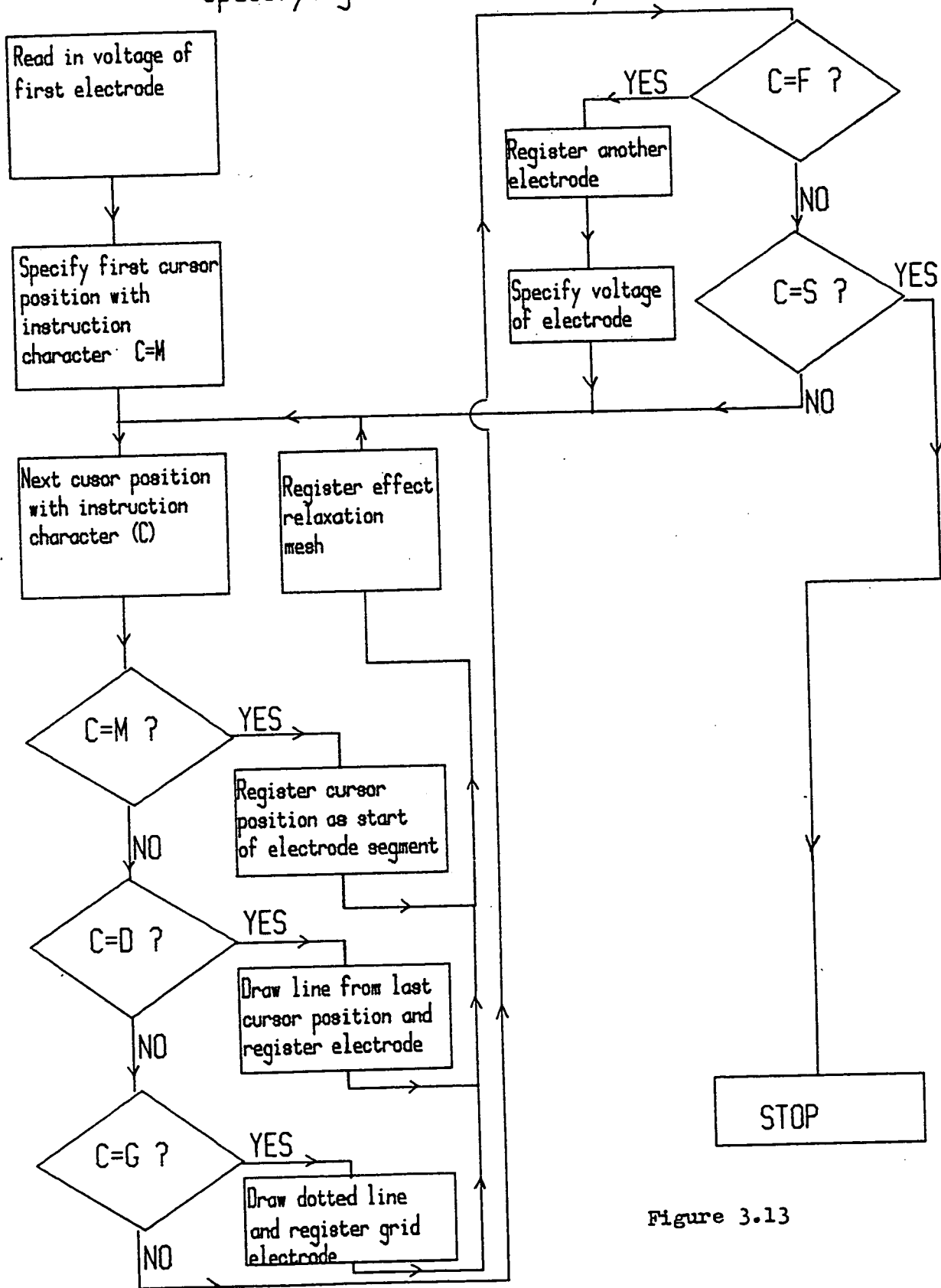


Figure 3.13

on the relaxation mesh. The size and resolution of the mesh is specified by the user and the mesh is automatically drawn on the terminal screen before the electrode layout is drawn. A general window is first drawn which represents the outer edges of the electrostatic field and the relaxation mesh is drawn onto this field. Figure 3.14 shows a 10*10 relaxation mesh before any electrodes are drawn on the graphics screen. The program assumes constant electric field conditions at the outer edges of this field.

Initially the relaxation mesh is made up of the normal symmetrical stars shown in Figure 3.15, the position of any star is given by I and J. Quantities DBX1(I,J), DBX2(I,J), DBY1(I,J) and DBY2(I,J) are all provisionally set to 1.0.

Once the electrode segments are transformed on to the relaxation mesh all points of intersection between a segment and mesh are calculated and stored. Asymmetrical stars are formed and, where appropriate, values of DBX1(I,J), DBX2(I,J), DBY1(I,J) and DBY2(I,J) are modified. Figure 3.16 shows a typical asymmetrical star created in this way. The voltage value of the electrode changes the stars' potentials and a new voltage configuration is stored in arrays VDBX1(I,J), VDBX2(I,J), VDBY1(I,J) and VDBY2(I,J). If two electrode segments cross the same side of a particular star an error message is generated and the user can choose to redraw the electrode structure. The residual equation used for the asymmetrical star shown in Figure 3.16 is :

$$\text{Res} = C1 + C2 + C3 + C4 + C6 - C7 - V0 * (C5 - C8)$$

Symmetrical Stars

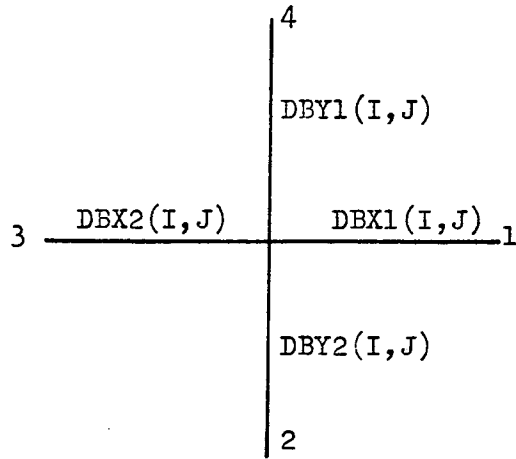


Figure 3.15

Asymmetrical Stars

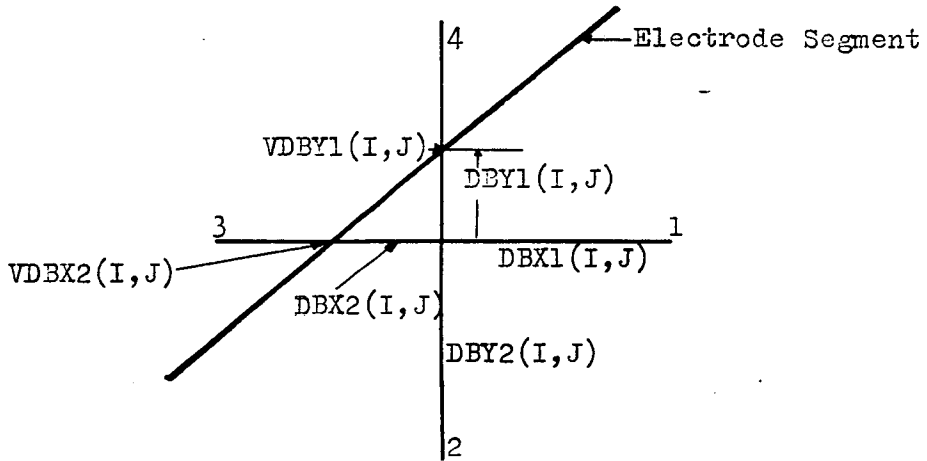


Figure 3.16

where

$$C1=2.0*V1*D3/(D1*D3(D1+D3))$$

$$C2=2.0*V3*D1/(D1*D3(D1+D3))$$

$$C3=2.0*V2*D4/(D2*D4(D2+D4))$$

$$C4=2.0*V4*D2/(D2*D4)/(D2+D4)$$

$$C5=2.0*(1./(D1*D3)+1./(D2*D4))$$

$$C6=(D3*V1)/(R*D3*(D1+D3))$$

$$C7=(D1*V3)/(R*D3*(D1+D3))$$

$$C8=D1/(R*D3(D1+D3)) - D3/(R*D1(D1+D3))$$

R is the radius of the star

This equation applies to the cylindrically symmetric field, in the two-dimensional rectilinear field C6, C7 and C8 are put to zero.

3.5 Trajectory Plotting for Design Programs

3.5.1 Interpolation

Electron trajectory calculations were computed in three-dimensional rectilinear coordinates. Linear interpolation between field mesh nodes was found to be insufficient when electrons were near electrodes. A way of interpolating between mesh nodes and electrodes was required. All mesh squares were put into several categories, covering every possible way electrode segments intersect with them. The category, shown in Figure 3.17(a) is free from any electrode intersections and the normal method of linear interpolation using four mesh nodes is used. Squares whose corners are intersected are shown in Figures 3.17(b-e), and squares with intersections in their opposite sides are shown in Figures 3.17(f) and 3.17(g). Before any trajectory calculations are made all meshes are put into the afore-mentioned categories.

Special interpolation of the squares in the (2-5) category have only to be developed for one orientation, the other configurations have only to be transformed to the chosen orientation, say type 2. Figure 3.18 shows that the electron can be in any one of five areas in this square, a different interpolation routine will be required for each area. Consider the case of an electron in area A; let the position of the electron be (DX, DZ) relative to the bottom left hand corner of the square. This situation is depicted in Figure 3.19.

The mesh corners are at voltages V_1, V_2, V_3 and V_4 ; the intersection point between electrode segment and square is defined to be (DCX, DCZ) . The basic interpolation method consists of linearly interpolating to find voltages $V_{N1}, V_{N2}, V_{N3}, V_{N4}$ and from there interpolating between these voltages to find the voltage at the electron's position. In this case (category (2)) interpolations between mesh corners and electrode have to be made for V_{N1} and V_{N4} . Expressions for $V_{N1}, V_{N2}, V_{N3}, V_{N4}$ are as follows :

$$V_{N1} = V_1 + (DZ / DCZ) * (V - V_1)$$

$$V_{N2} = V_4 + DZ * (V_3 - V_4)$$

$$V_{N3} = V_1 + DX * (V_4 - V_1)$$

$$V_{N4} = V_3 + ((1 - DX) / (1 - DCX)) * (V - V_3)$$

Linearly interpolating between $V_{N1}, V_{N2}, V_{N3}, V_{N4}$ gives two estimates of the voltage at the electron's position V_{P1}, V_{P2} and the average V_P is taken :

$$V_{P1} = V_{N1} + DX * (V_{N2} - V_{N1})$$

$$V_{P2} = V_{N3} + DZ * (V_{N4} - V_{N3})$$

$$\text{so } V_P = 0.5 * (V_{P1} + V_{P2})$$

The same interpolation methods are used to find potentials in areas B, D, C, E shown in Figure 3.18 but these are more complicated than for area A. This is because the perpendicular lines that extend from the electron position can in some cases intersect the electrode segment. Hence any of the voltages V_{N1}, V_{N2}, V_{N3} and V_{N4} may lie on the electrode. Figure 3.20 shows the case of an electron in area E and for this case the quantities DPX and MB are

calculated. The following expressions are used

$$DPX = (DZ - DCZ) / MB \quad \text{where } MB = (1 - DCZ) / DCX$$

$$VN3 = V$$

$$VN2 = V$$

$$VN1 = V2 + ((1 - DZ) / (1 - DCZ)) * (V - V2)$$

$$VN4 = V2 + (V - V2) * DX / DCX$$

and interpolation between VN1 and VN2 gives

$$VP1 = VN1 + (VN2 - VN1) * DX / DPX$$

$$\text{let } DCR = DCZ + DX * MB$$

interpolation between VN4 and VN3 is

$$VP2 = VN4 + (VN3 - VN4) * (1 - DZ) / (1 - DCR)$$

$$\text{and } VP = 0.5 * (VP1 + VP2)$$

Mesh squares which had not been intersected were assigned a length of one unit. Interpolation routines were also written for areas B, D, C. Altogether five routines were written for the five different areas in Figure 3.18. Electron positions in the squares of type (3-5) were transformed into electron positions in the square of type (2). Figure 3.21 shows the transformation between type (3) to type (2); the quantities DX, DZ, V1, V2, V3, V4 are replaced by DX', DZ', V1', V2', V3', V4' respectively after which the same interpolation routines are used. These quantities are now given by

$$DX' = 1.0 - DX$$

$$DZ' = DZ$$

$$V4' = V1$$

$$V1' = V4$$

$$V2' = V3$$

Interpolation Between Mesh Nodes and Boundary

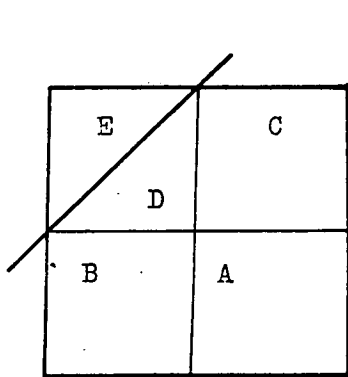
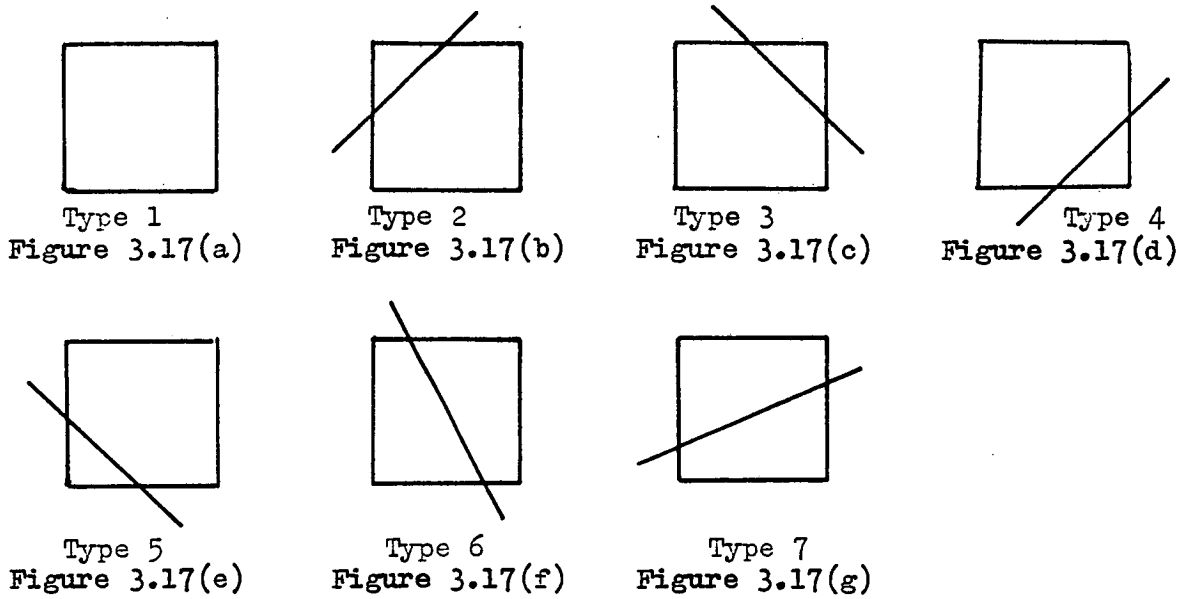
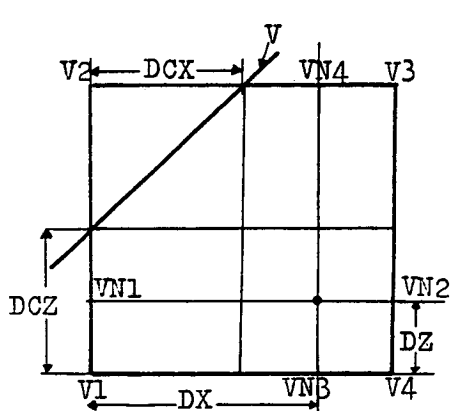
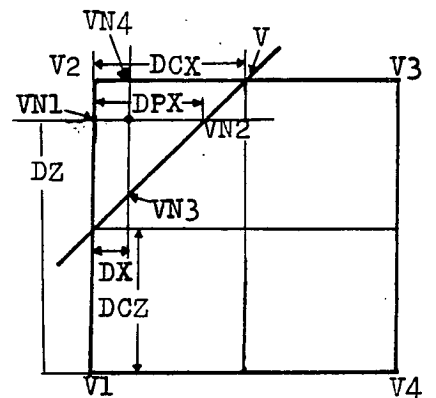


Figure 3.18



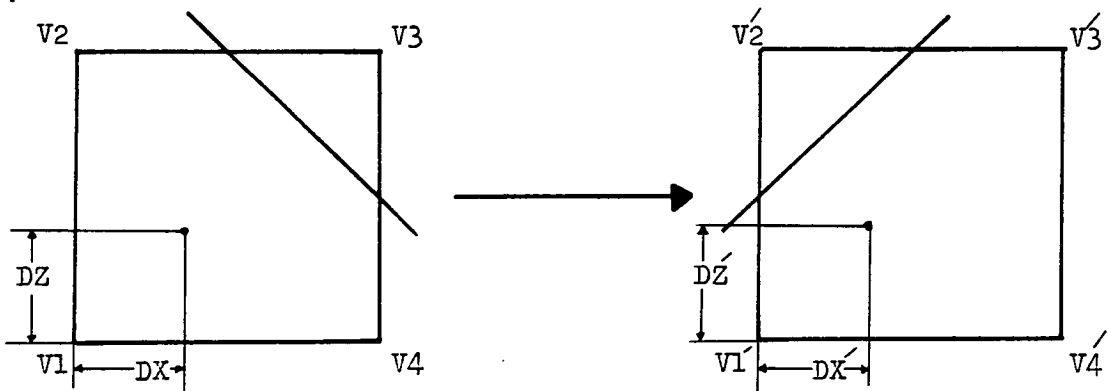
Electron in area A

Figure 3.19



Electron in area E

Figure 3.20



Transformation to a Standard Mesh Type

Figure 3.21

Interpolation Between Mesh Nodes and Boundary

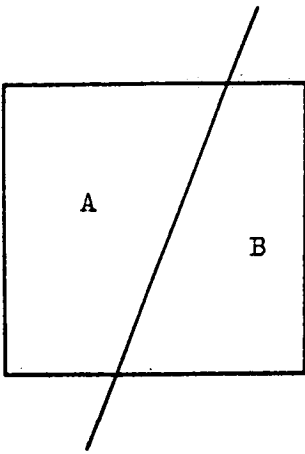


Figure 3.22(a)

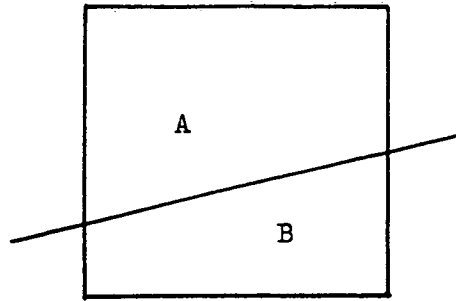


Figure 3.22(b)

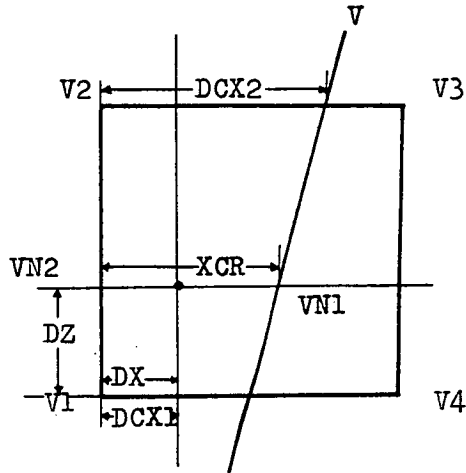


Figure 3.22(c)

$$V3 = V2$$

Similar transformations are made for squares of types 4 and 5. The interpolation routines written for squares of types (6) and (7) were much simpler than those for types (2-5). For the cases of (6) and (7) an electron can only be in two areas shown by A and B in Figures 3.22(a) and 3.22(b). Figure 3.22(c) shows an electron in area A for type (6) square. The quantity XCR is calculated by

$$XCR = DCX1 + DZ / MB$$

$$\text{and } MB = 1. / (DCX2 - DCX1)$$

$$\text{so } VN1 = V \text{ (electrode potential)}$$

$$VN2 = V1 + DZ * (V2 - V1)$$

$$\text{so } VP = VN2 + (VN1 - VN2) * DX / XCR$$

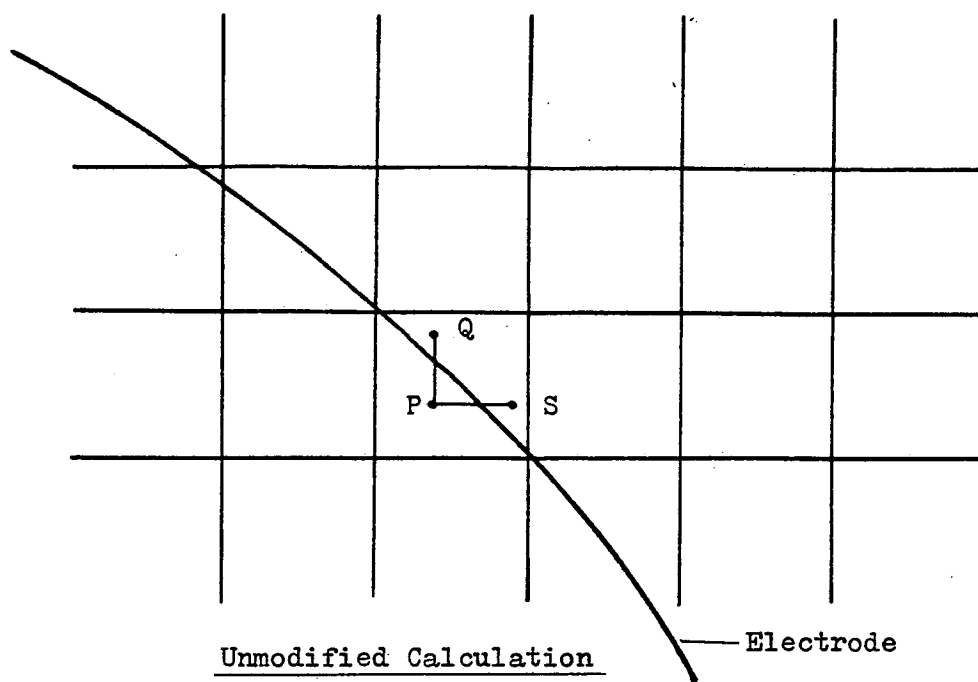
a similar method is used for the square of type (7).

3.5.2 Electron Field Step near Boundary

Special precautions were taken to prevent electric field calculations being made across any boundaries or electrodes. Figure 3.23(a) shows the previous technique of the projection of small steps parallel to the coordinate axis. In this case the segments cross the boundary and hence incorrect electric field values will be found between points P, Q and S. To prevent such an error the points of intersection are found and the modified calculation is based on the diagram shown in Figure 3.23(b). The electric field values are now given by

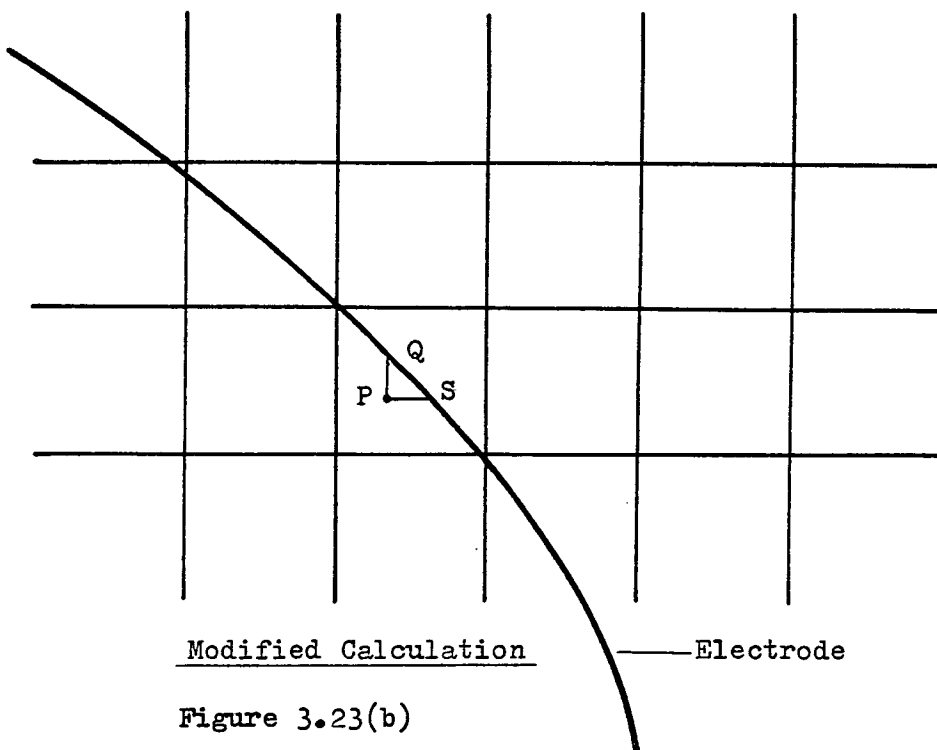
$$EZ = (V_{\text{boundary}} - VP) / (Z2 - Z1)$$

Calculating Electric Fields Near an Electrode



Unmodified Calculation

Figure 3.23(a)



Modified Calculation

Figure 3.23(b)

$$EX = (V_{\text{boundary}} - VP) / (X2 - X1)$$

where $(X1, Z1)$ is the electron's position, VP is the potential at the electrons position, $(X1, Z2)$ and $(X2, Z1)$ are intersection points with the boundary. These intersection points are calculated from finding the gradient of the boundary segment.

3.5.3 Turning Points in the Electron's Trajectory

Points at which the electrons velocity changes sign can introduce large errors in the trajectory calculation if not guarded against. An electron when close to a boundary may cross and recross the same boundary in a single step and as a result not appear to have crossed the boundary at all, Figure 3.24(a) illustrates this effect. A special subroutine was written to reduce the electron step so that the electron step finished precisely on the turning point. A test was then made to find whether the electron had really crossed the boundary. If the turning point is only considered in one coordinate direction then the modification involves the solution of a quadratic equation whose variable is the time interval of the trajectory step. This direction was chosen to be the Z-direction since most electrons are extracted vertically and retarded vertically in most detectors. Let the initial and final velocities of an electron step be V_{zi} and V_{zf} respectively and the electric field be E_z , then since V_{zf} is to be zero the quadratic equation is

$$V_{zi} * dt + (1/2) * (e/m) * E_z * dt^2 = 0$$

Where e is the electron charge, m the electron mass and dt the time interval.

Uncorrected Boundary Crossings

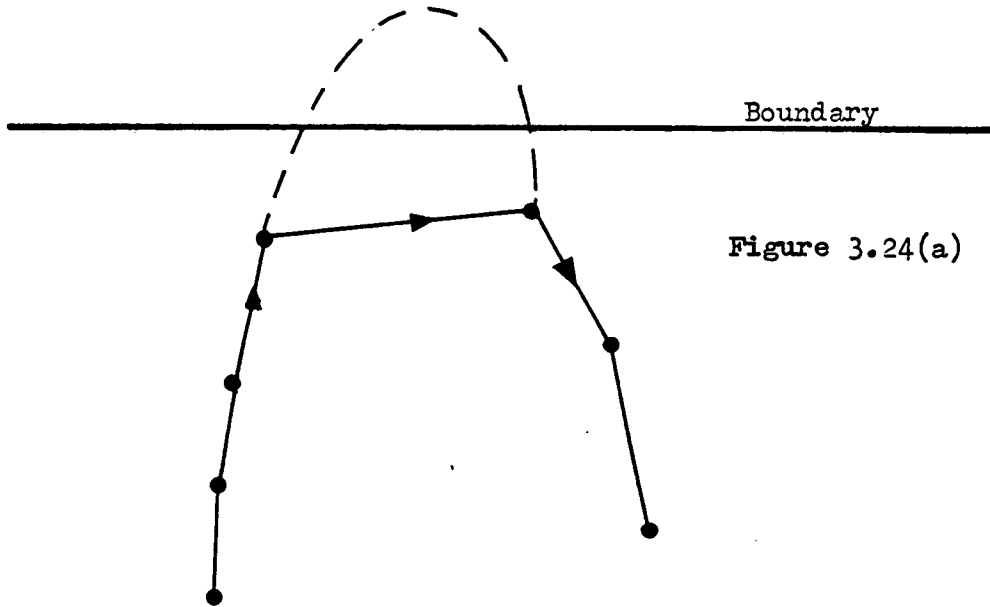


Figure 3.24(a)

Corrected Boundary Crossing

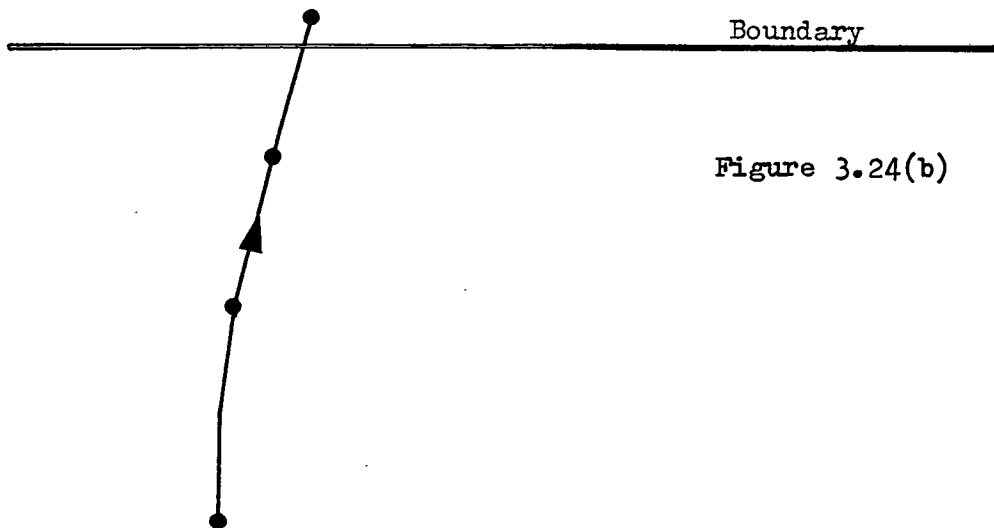


Figure 3.24(b)

Once the correct time-step is found it is put back into the normal trajectory Equations (3.15-3.17) and a revised electron step is computed. Figure 3.24(b) shows one possible effect of this modification in the electron trajectory; in this case the electron is absorbed into the boundary whereas an uncorrected trajectory would escape the boundary.

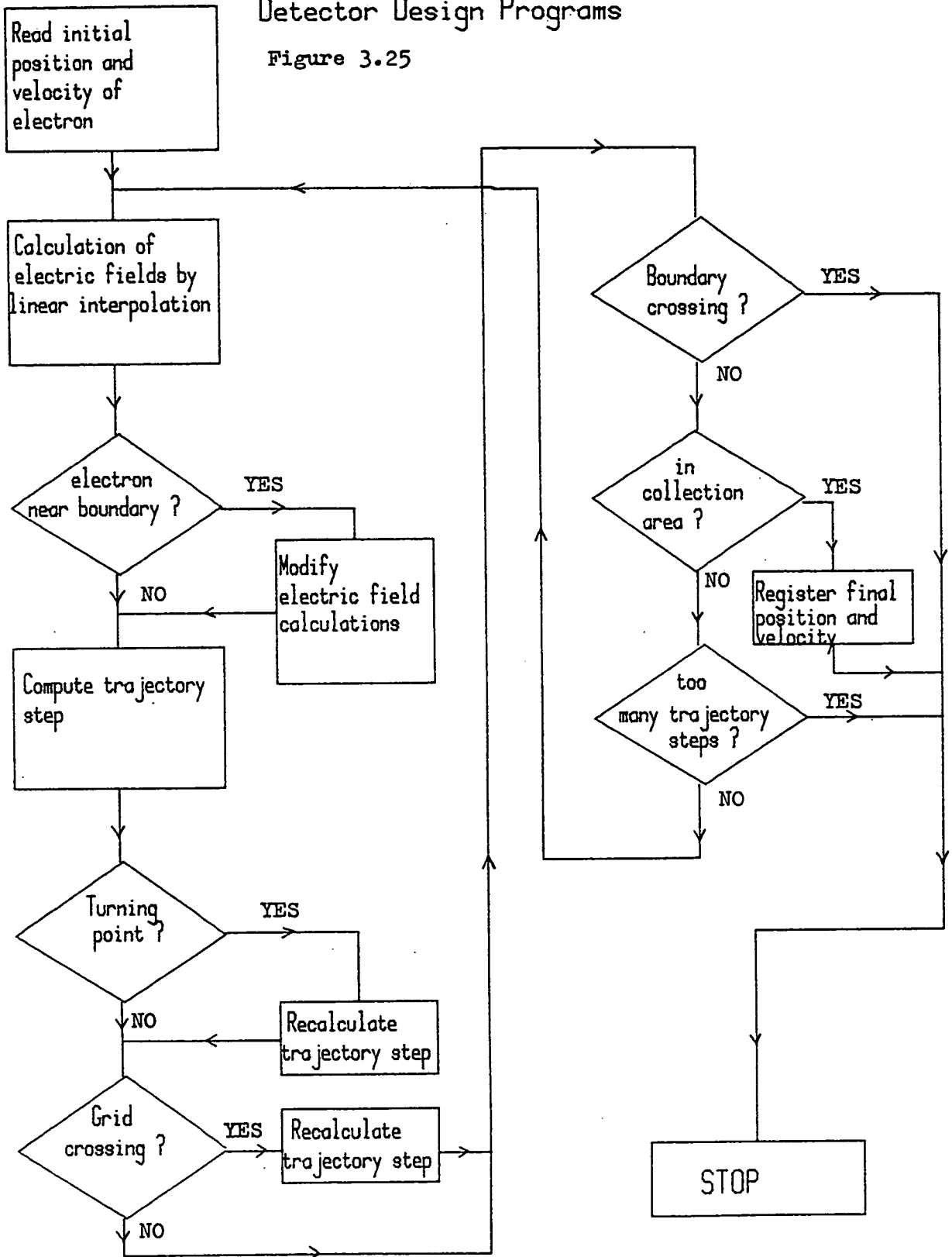
3.5.4 Grids

Electrons are prevented from 'stepping' across grids. Generally electric fields vary extremely sharply across grids but the program assumes constant electric fields in a single step and hence introduces a large error into the trajectory calculations. The size of an electron step which crosses a grid is adjusted to bring the electron directly onto the grid. A similar method to that used in correcting the error in turning points is used. A quadratic equation in the trajectory time-step is solved, high accuracy in this technique is essential since grids play an important role in many detectors as a way of reconstructing the electron secondary distribution.

The flow diagram depicted in Figure 3.25 serves to illustrate how the error-reducing routines described in sections 3.5.2 to 3.5.4 were incorporated into the calculation of an electron trajectory.

Trajectory Plotting in Detector Design Programs

Figure 3.25



3.6 APPLICATIONS OF 2-D DESIGN PROGRAMS

3.6.1 Different Detector Designs

Several types of deflection fields were specified above linear retarding and extraction fields and the two-dimensional rectilinear program was used for this purpose. The simulation of each detector was not rigorous, but allowed the author to become familiar with electron behaviour through deflection fields in a general sense. The analysis used the interactive capability of the programs written to provide a 'sketch pad design' facility through which different ideas were developed.

Electron trajectories with initial energies of 3eV, 6eV and 10eV are plotted through each detector design and are shown in Figures 3.26-3.29. A 25 by 25 mesh size was used for each detector design and heights of 20mm were specified in each case. In Figure 3.26 electrons pass through two pointed electrodes at voltages 100 volts and -10 volts. Most electrons are deflected to one side but leave the field diverging, whereas electrons in the two circular grid case shown in Figure 3.27 are only deflected by an angle of 40 degrees from the vertical but appear to be converging as they leave the field. The best performance of all detectors for voltage contrast purposes is given by the two curved-grid detector shown in Figure 3.29. Electrons are deflected over 90 degrees from the vertical axis; this is a desirable feature since, for most S.E.Ms, the scintillator is normally placed below or on the specimen plane. This detector can also be effective in filtering out backscattered

electrons which can pass through its upper deflection grid.

Electron Detector with Pointed-Electrode Arrangement

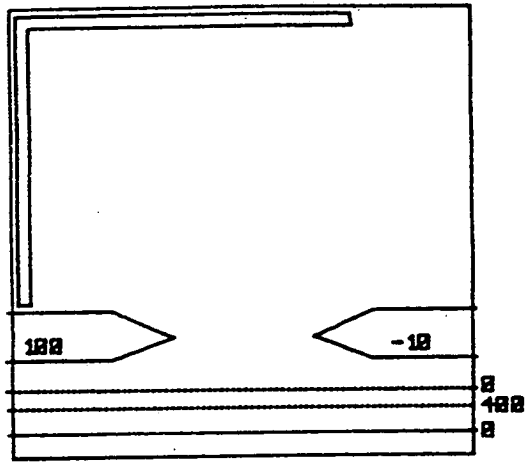
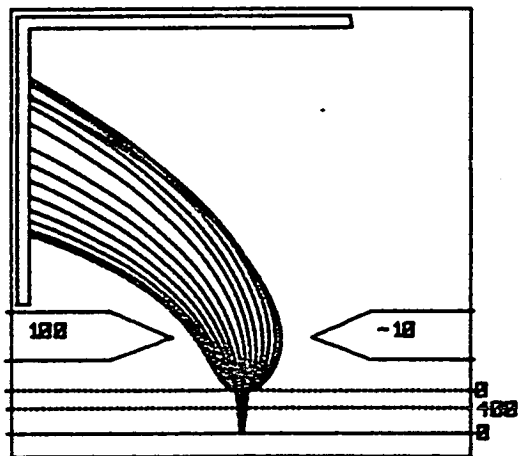
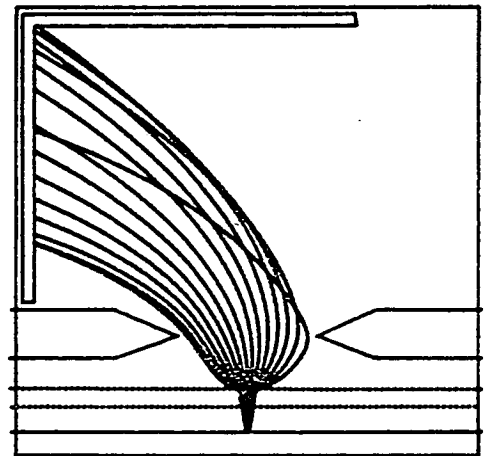


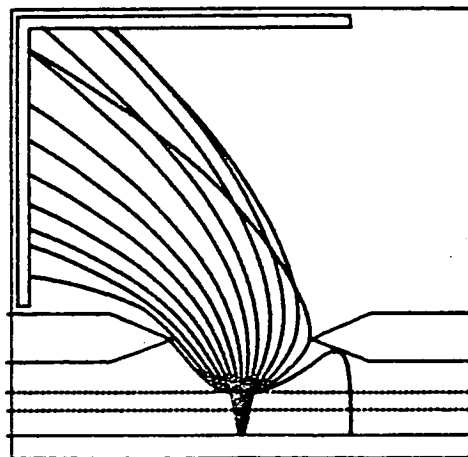
Figure 3.26



(a) 3eV



(b) 6eV



(c) 10eV

Trajectories for Electrons emitted with energies of :

- (a) 3eV
- (b) 6eV
- (c) 10eV

Electron Detector with Semi-Circular Grid
Arrangement

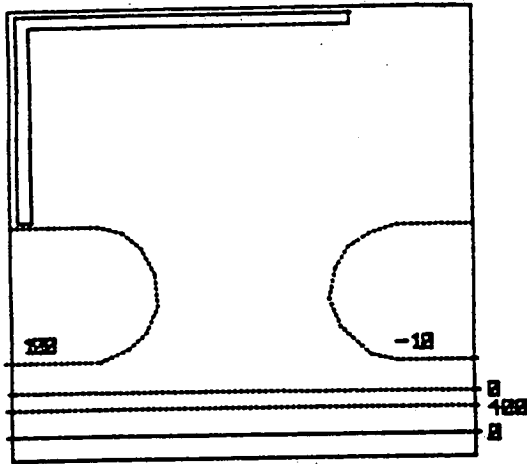
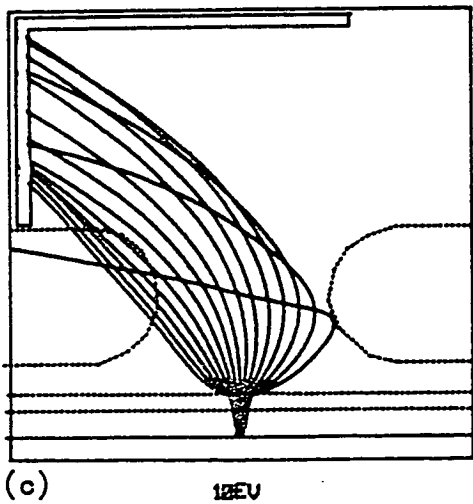
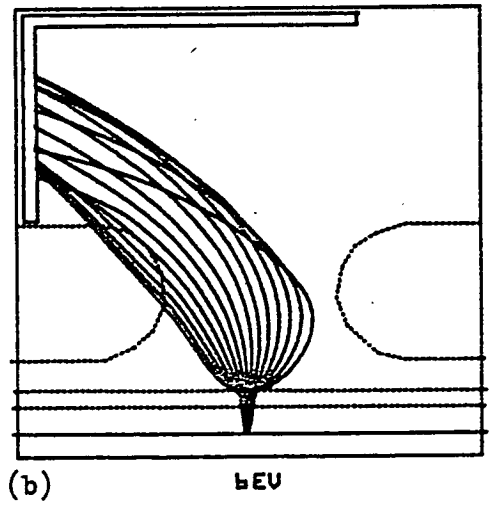
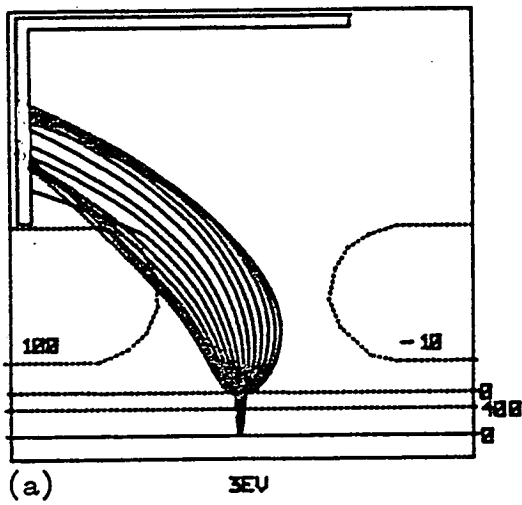
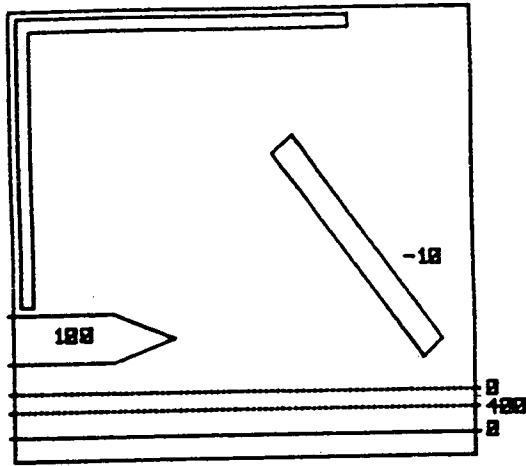


Figure 3.27



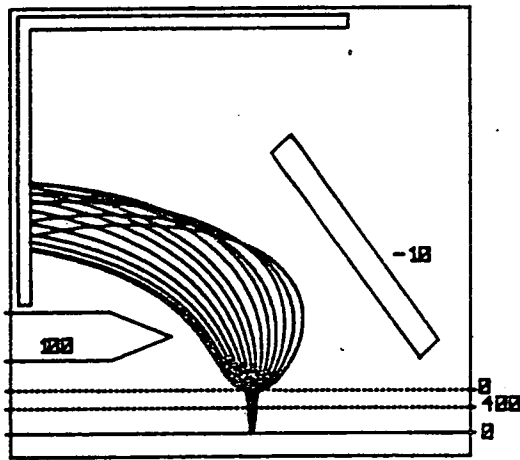
Trajectories for electrons
emitted with energies of:

- (a) 3eV
- (b) 6eV
- (c) 10eV

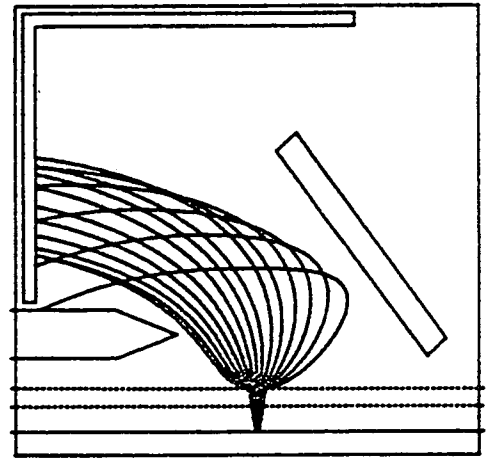


Electron Detector with Plate-Deflection Arrangement

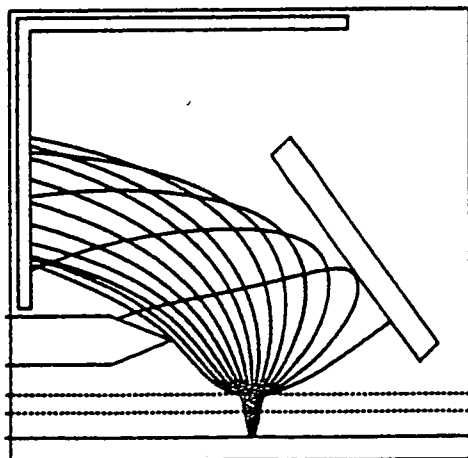
Figure 3.28



(a) 3eV



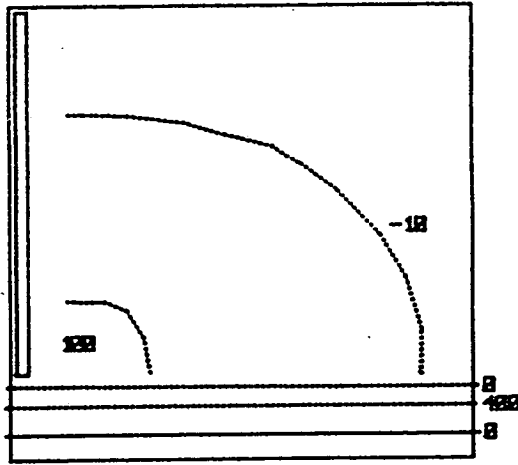
(b) 6eV



(c) 10eV

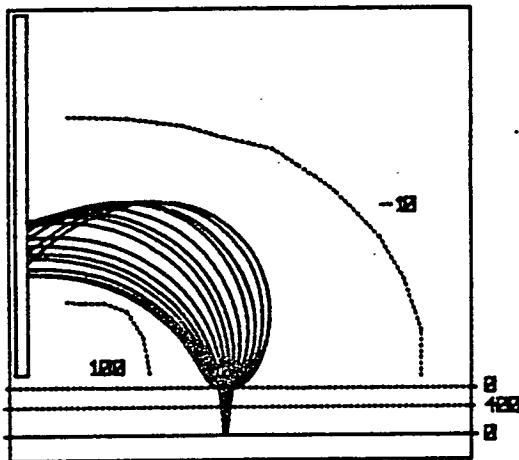
Trajectories for electrons emitted with energies of:

- (a) 3eV
- (b) 6eV
- (c) 10eV



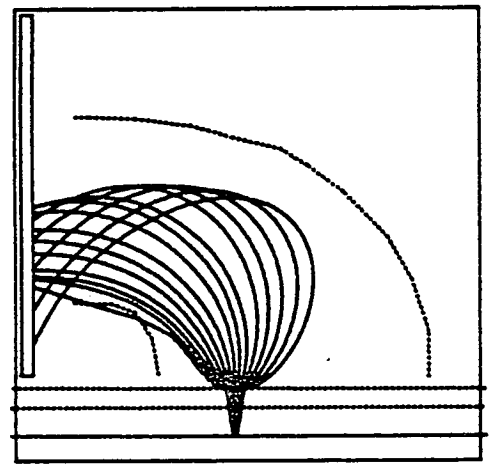
Electron Detector with Curved Grid Arrangement

Figure 3.29



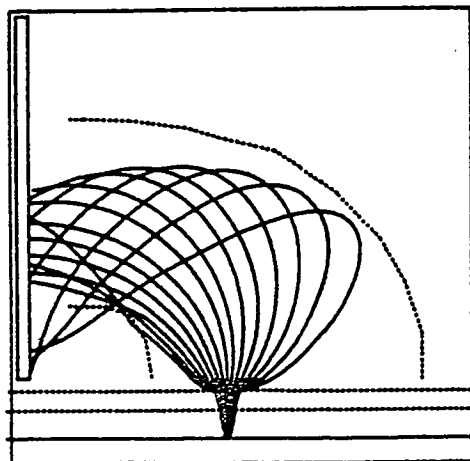
(a)

3eV



(b)

6eV



(c)

10eV

Trajectories for electrons emitted with energies of:

- (a) 3eV
- (b) 6eV
- (c) 10eV

3.6.2 Dinnis Detector

The two-dimensional rectilinear design program was used to simulate the performance of the detector made by Dinnis et al (1981). The detector is essentially a retarding field detector and has planar extracting and retarding fields (Figure 3.30). Two angled plates deflect electrons to a normal scintillator/photomultiplier collection system. The two-dimensional field approximation for this detector is valid for most secondary electrons below 12eV. A small number of electrons above 8eV and at emission angles close to the horizontal will experience some fringe effects at the edges of the detector's deflection plates. This is due to the finite width of 30mm of the deflection plates and an average 10^{-8} seconds time of flight for most electrons which was found from trial program simulations. The number of electrons experiencing fringe effects however is found to be very small compared to the total number of emitted electrons. From the energy and angular distributions of emitted secondaries, most electrons lie within an energy of 6eV and have angles above 10 degrees from the horizontal. Hence the fringe effects from the detector's finite width were neglected. All electron trajectory paths were calculated in the Z-X plane.

A 25 by 25 mesh was initially used to solve field distributions in the Dinnis detector. Figure 3.31 shows that an electron trajectory step size of less than 0.16 (SLT>61) was required to give a constant output current and hence give sufficient accuracy. Figure

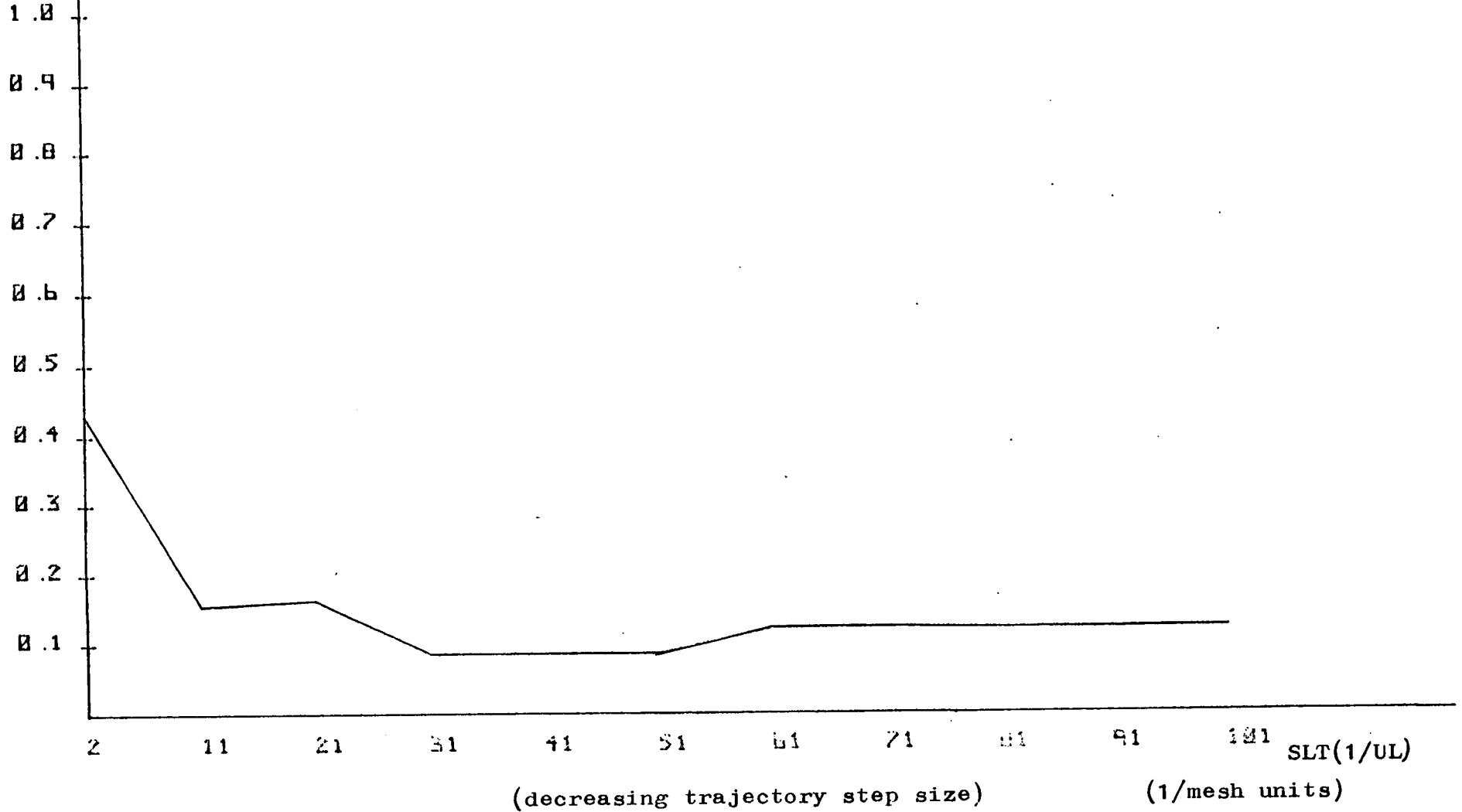
3.31 was produced from the error option described earlier. Better accuracy was achieved when a 40 by 40 mesh was used and its effect on the required trajectory step is shown in Figure 3.32.

The solution to the detector's field distribution was interactive to the programmer and took less than 2 minutes real time. An equipotential line representation of the field is shown in Figure 3.33. As expected, the equipotentials are straight and parallel between specimen, extraction grid and retarding grid. A degree of uniformity also exists between deflection plates. Non-linear areas are significant at the entrance and exit of these plates, particularly around their entrance.

Electron trajectory paths are traced in Figures 3.34(a-d) with initial energies of 3eV, 6eV, 10eV and 50eV respectively, each set of trajectories have been calculated for a wide range of initial angles (0 to π in steps of 0.3 radians). All Figures 3.34(a-d) show that electrons with shallow angles (close to the horizontal) are absorbed into the base of the deflection plates, a greater number of higher energy electrons are absorbed this way. A large number of electrons which traverse the deflection field entrance are attracted to either deflection plate and subsequently lost. This seems to happen independently of electron energy below 50eV. Only a small number of electrons are seen to pass through the detector's exit. This proportion is approximately the same for all electrons with energies below 10eV, and is confirmed by Figure 3.35 implying a 'flat filter response' for the detector in this energy region. The detector

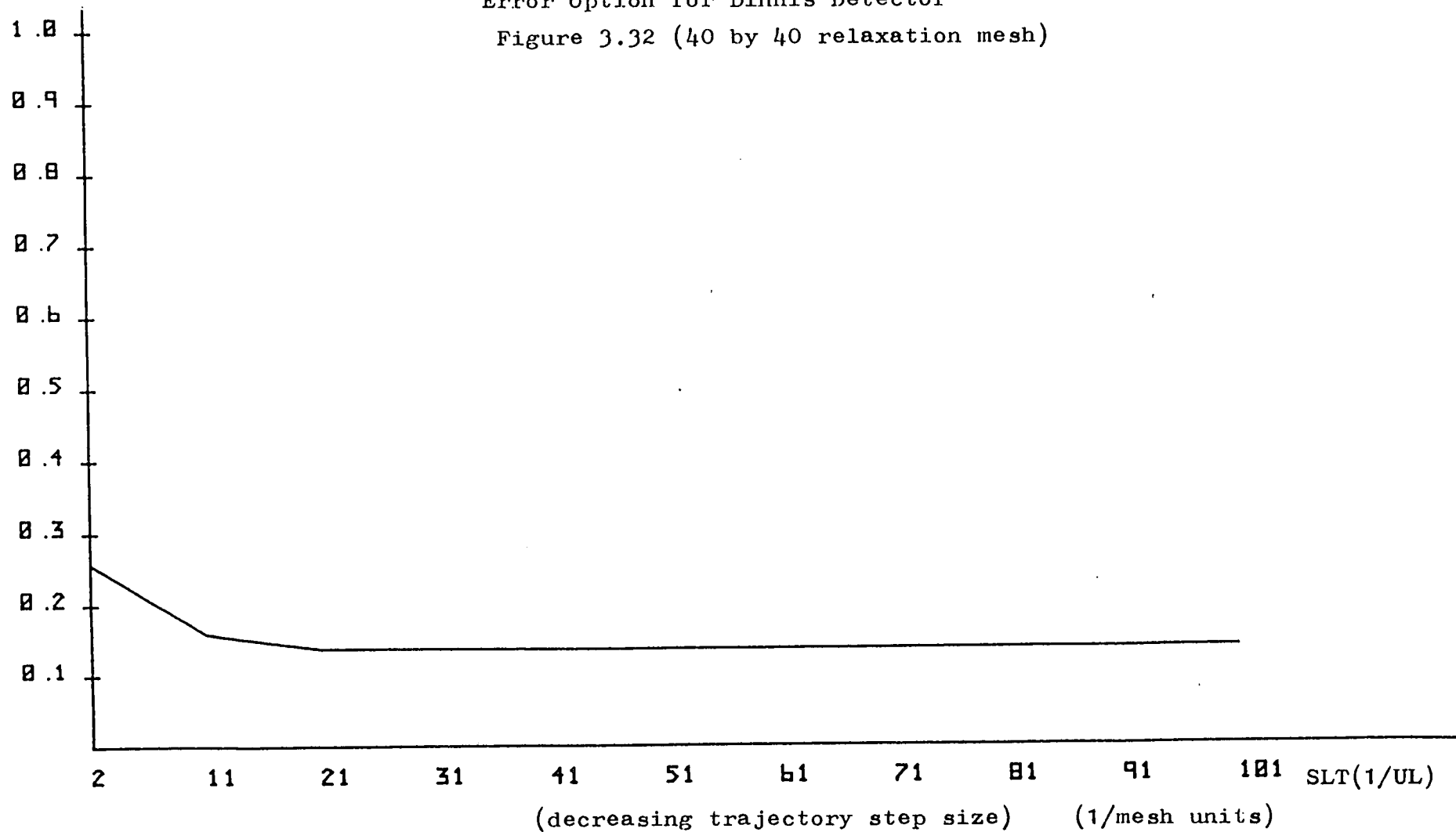
Transport
Efficiency

Error Option for Dinnis Detector
. Figure 3.31 (25 by 25 relaxation mesh)



Transport
Efficiency

Error Option for Dinnis Detector
Figure 3.32 (40 by 40 relaxation mesh)



Equipotentials for Dinnis
Detector

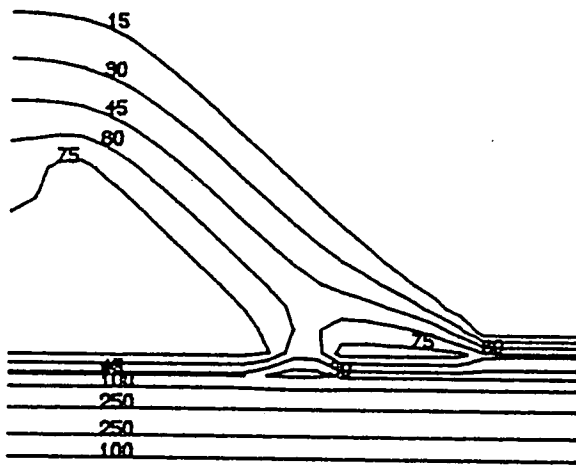
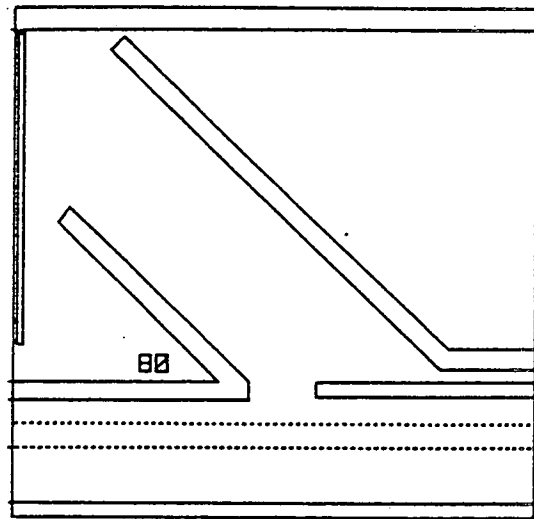


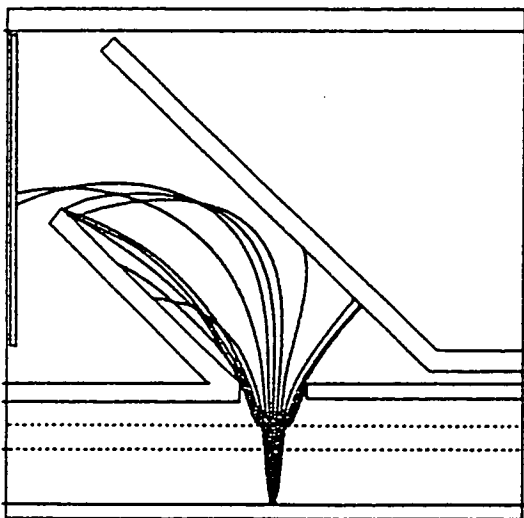
Figure 3.33

Schematic diagram of Dinnis
Detector



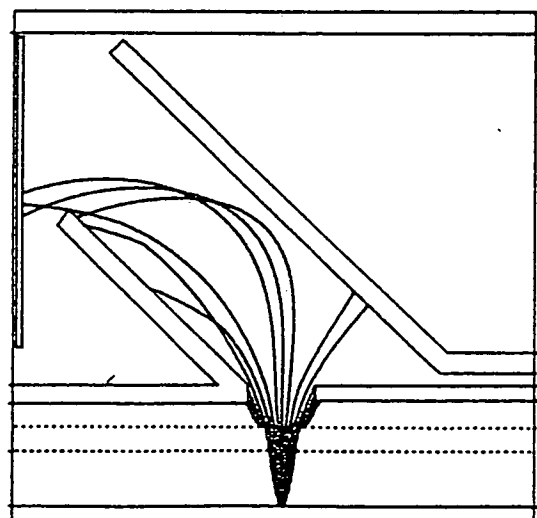
25 * 25 MESH

Figure 3.30



3eV

Figure 3.34(a)



6eV

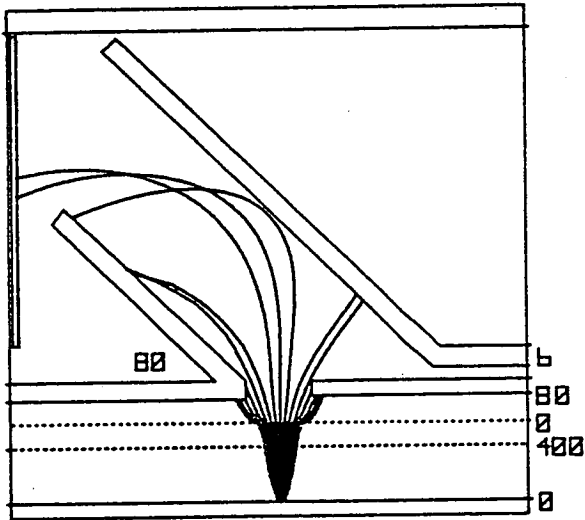
Figure 3.34(b)

Trajectories for Dinnis Detector for electrons emitted with energies
(a) 3eV , (b) 6eV

Trajectories for Dinnis Detector for electrons emitted
with energies

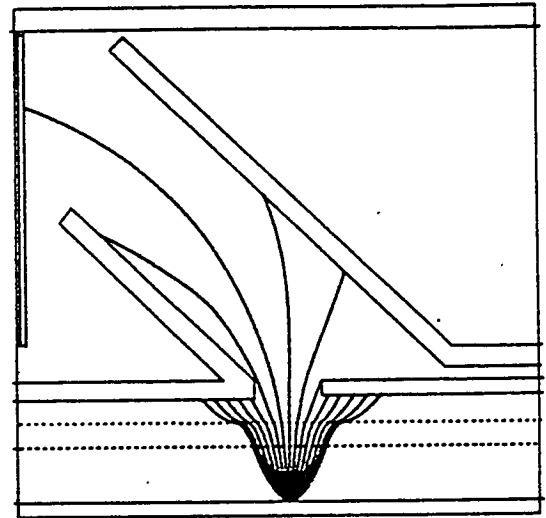
(c) 10eV

(d) 50eV



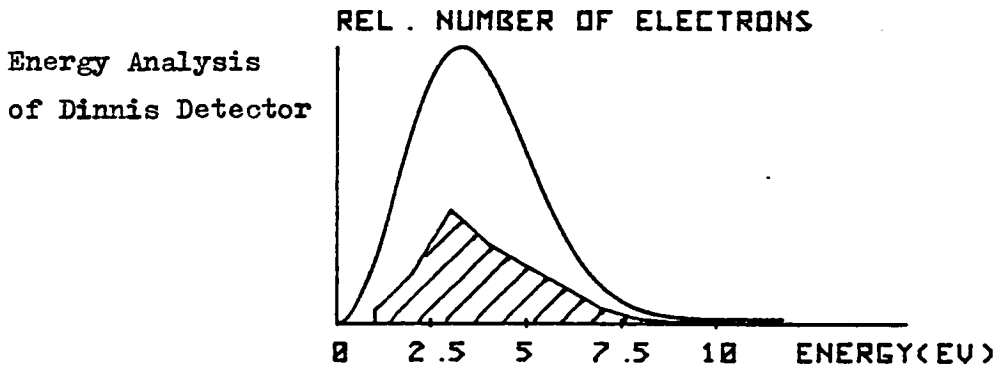
10 EU

Figure 3.34(c)



50 EU (BACKSCATTERED)

Figure 3.34(d)



Transport Efficiency = 0.327

Figure 3.35

performs well in filtering backscattered electrons, one out of every fifteen 50ev electrons are collected, as shown by Figure 3.34(d).

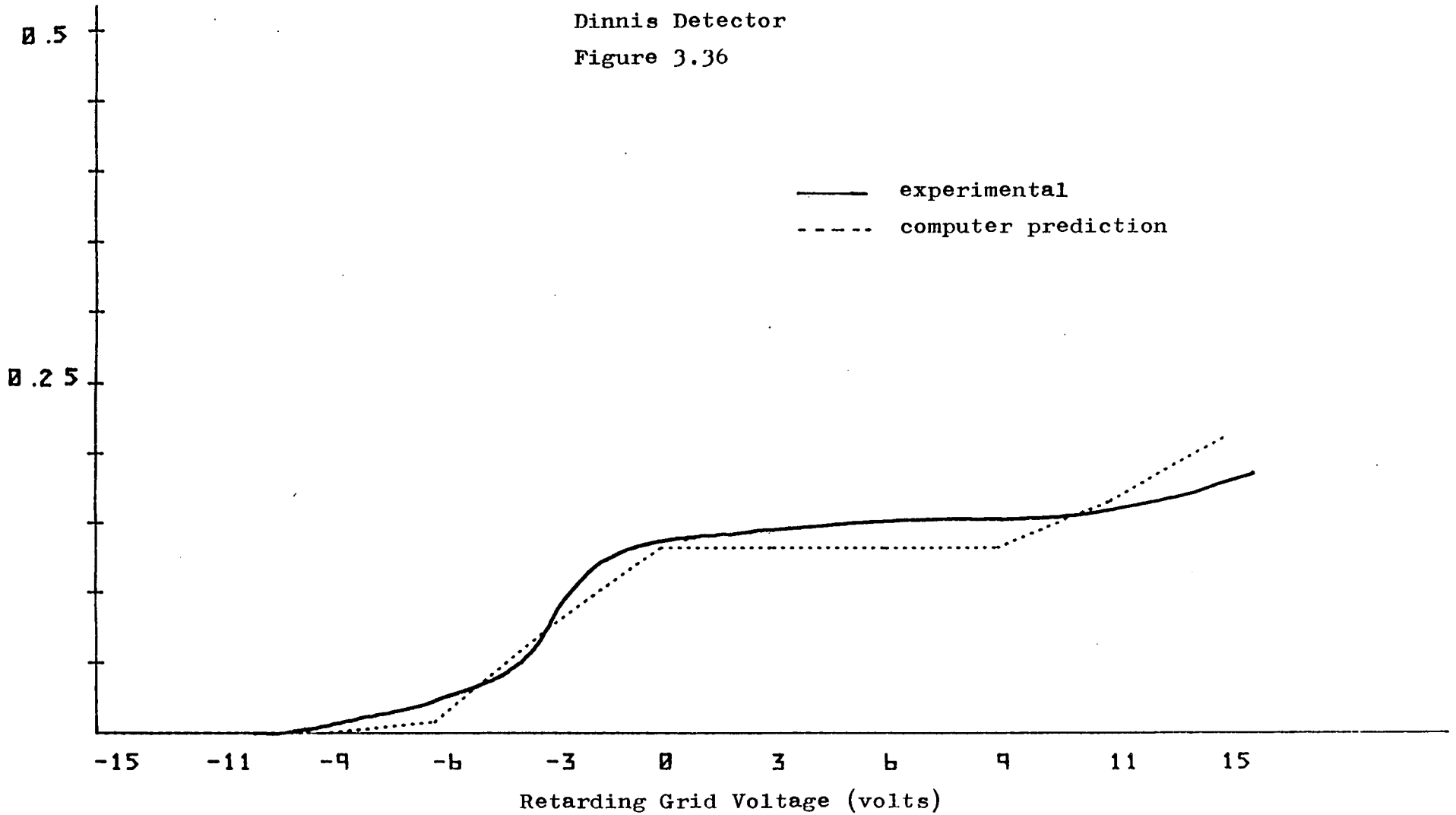
3.6.3 Detector Curves

The overall transport efficiency of the Dinnis detector was found to be low. For the voltage configuration depicted in Figure 3.30 a transport efficiency of 12% was obtained. This value was found from the error option and also from the plotting of the detector's S-curve. The S-curve is found to have a normal 'S' shape except for a slight rise for higher retarding grid voltages (>9 volts), the detector's S-curve is shown in Figure 3.36. Figure 3.37 shows that varying the extraction grid voltage above 50 volts does not produce a significant change in output current., while the same is true for voltages on the lower deflection plate in the range between 10 and a 100 volts (a 9% maximum deviation) as shown in Figure 3.38. Variation in the upper deflection plate voltage causes a rise in collected current as shown in Figure 3.39, the overall transport efficiency goes up to 38% for voltage values of greater than 9 volts on this plate.

Experimental results were found to agree reasonably well with the computer predictions shown in Figures 3.36-3.39. These experimental results were obtained on a S2 Cambridge Instruments Microscope. Large aluminium pads were probed with large conductor areas being used to minimise surface field effects. The experimental curves were taken on a graph plotter and subsequently rescaled to obtain a best fit to the theoretical curves. Significant changes in output current occur

Transport
Efficiency

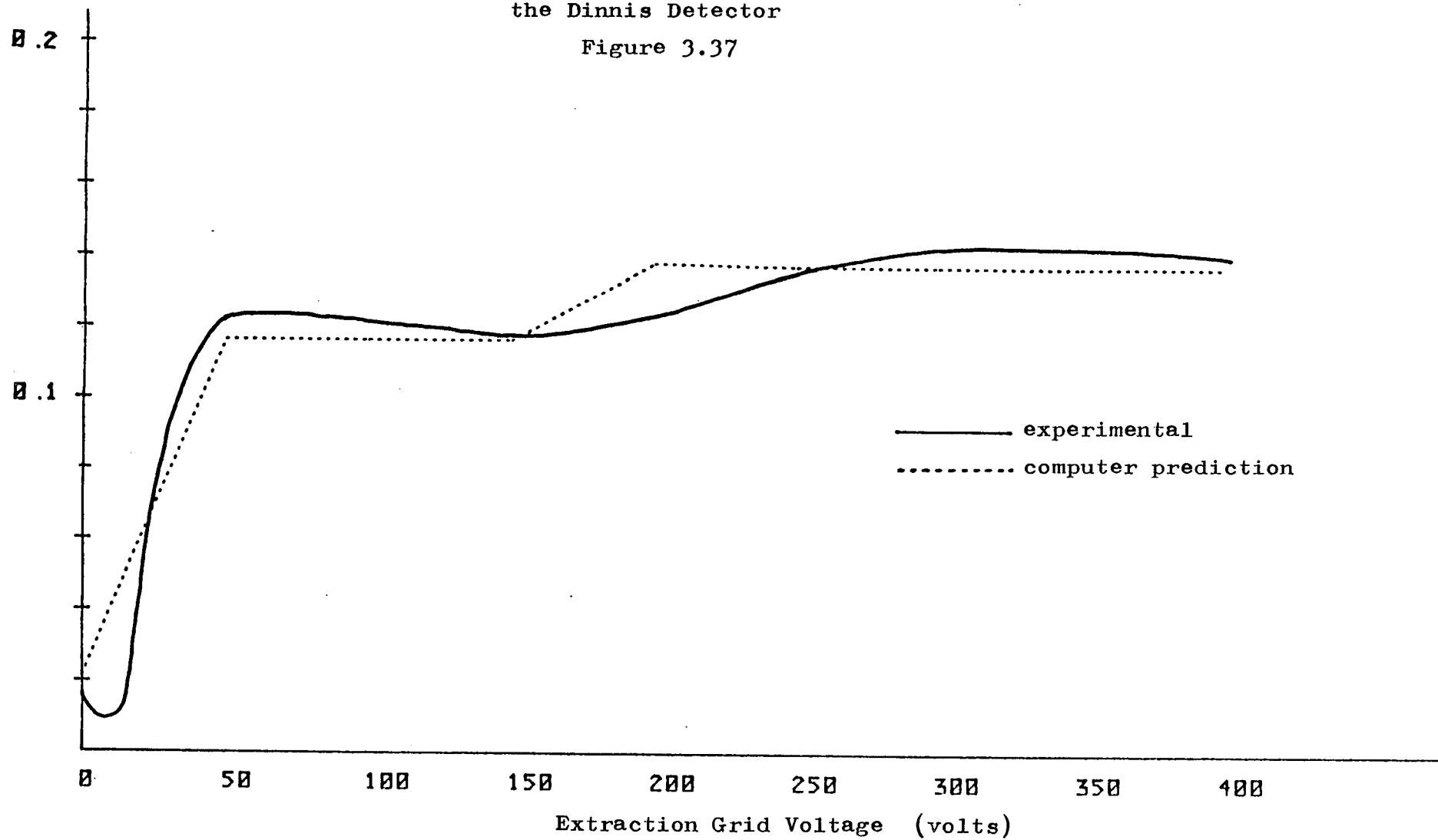
Variation in the Retarding Grid Voltage for the
Dinnis Detector
Figure 3.36



Transport
Efficiency

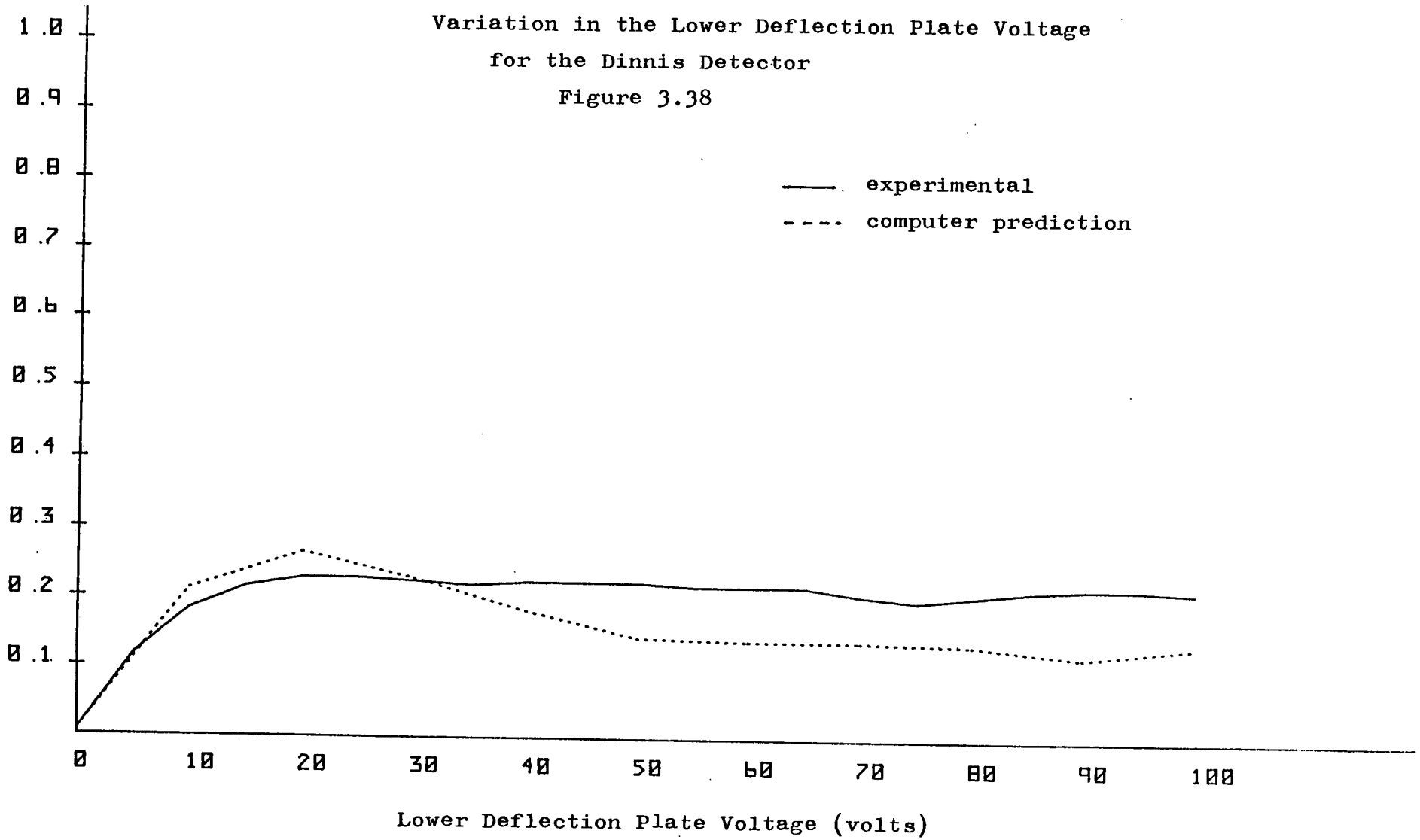
Variation in the Extraction Grid Voltage for
the Dinnis Detector

Figure 3.37



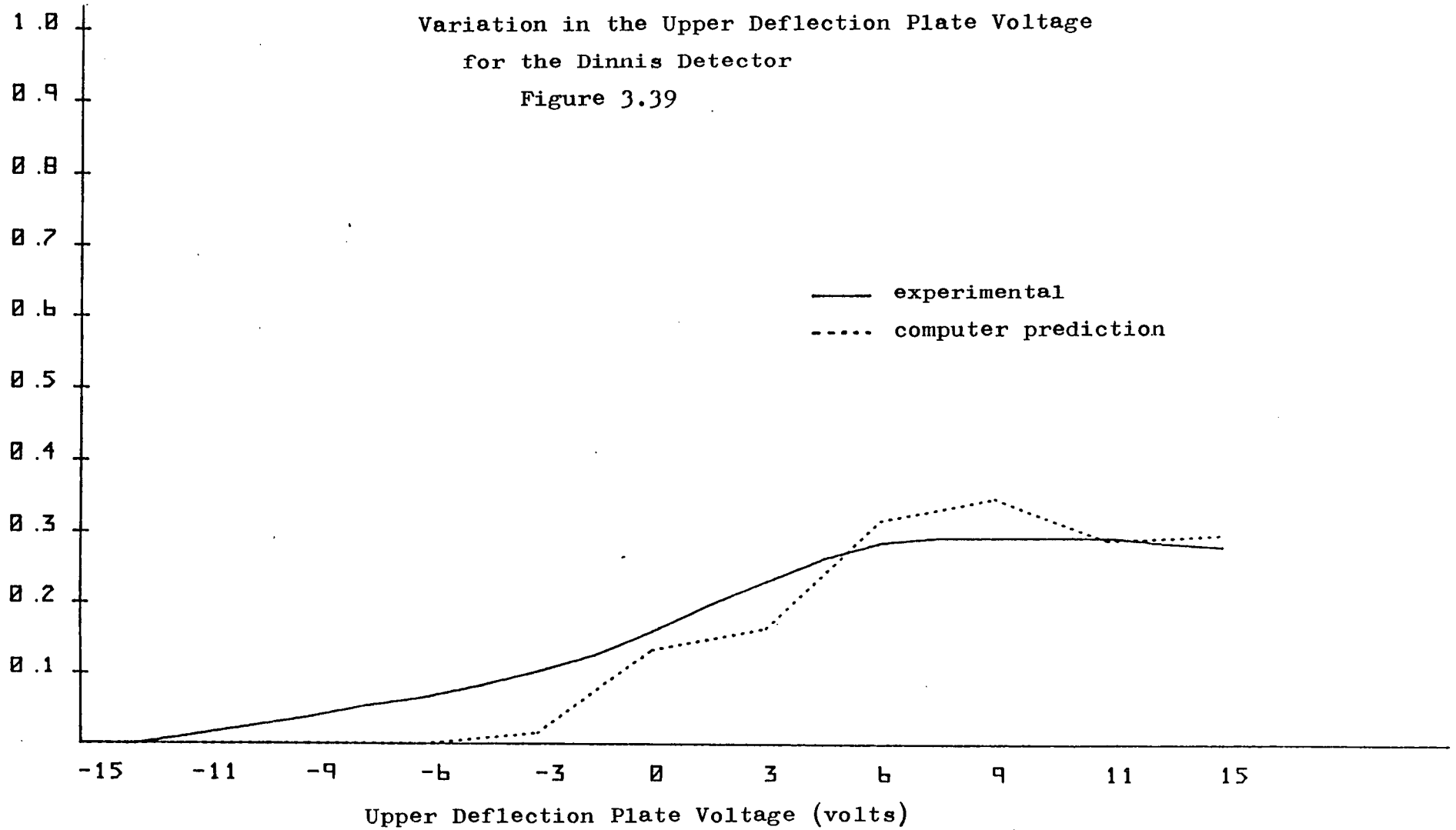
Transport
Efficiency

Variation in the Lower Deflection Plate Voltage
for the Dinnis Detector
Figure 3.38



Transport
Efficiency

Variation in the Upper Deflection Plate Voltage
for the Dinnis Detector
Figure 3.39



at the same plate voltages for both theoretical and experimental curves. The output currents in the S-curves shown by Figure 3.36 reach a plateau in both experimental and theoretical curves at a retarding voltage of 0 volts, and both curves subsequently rise for voltages greater than 9 volts. Figure 3.37 shows that both experimental and theoretical curves reach a local peak at 50 volts for variations in extraction grid voltage, while both curves peak around 20 volts for variations in the lower deflection plate voltage shown in Figure 3.38. A similar rise occurs for voltages greater than 6 volts on the upper deflection plate as shown in Figure 3.39.

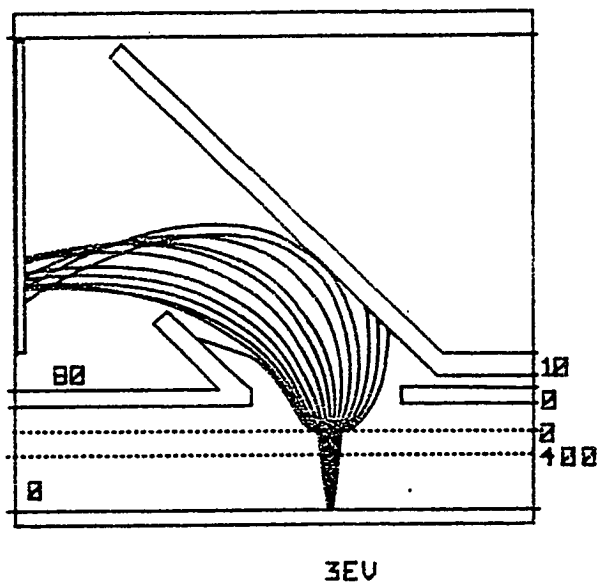
From the computer simulation of the Dinnis detector the following recommendations can be made:

- 1) That the deflection aperture size be significantly increased at least doubled
- 2) That the upper deflection plate be biased with voltages greater than 9 volts
- 3) That the right-hand deflection plate be biased to 0 volts.
- 4) That the left hand deflection plate be shortened

Figure 3.40 shows the predicted performance of the detector if the above recommendations are incorporated.

Redesign of Dinnis Detector

Figure 3.40

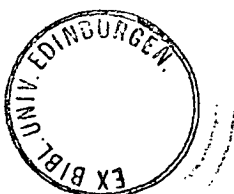


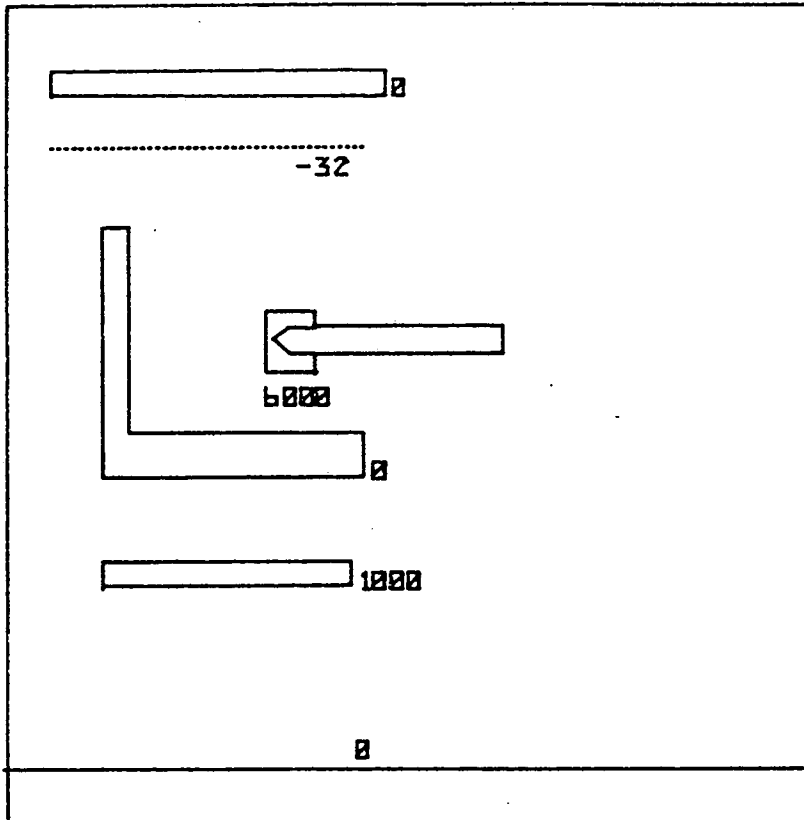
3.6.4 Lintech Detector

This was the first detector commercially produced by Lintech Ltd.(Plows (1981)), the detector has a radially symmetric geometry and one of the design programs was used to simulate its performance. Figure 3.41 shows a cross-section of the detector's geometry and voltage configuration. Electrons are attracted from the specimen by a flat extraction plate which has a 7.6mm hole at its centre. The electrons then pass through a retarding field which is caused by a ferrule shaped plate, a suppressor grid at -32 volts further retards their motion until they are deflected and collected on a 6KV annular scintillator. The computer model shown in Figure 3.41 was used to simulate the detector's performance in the R-Z plane.

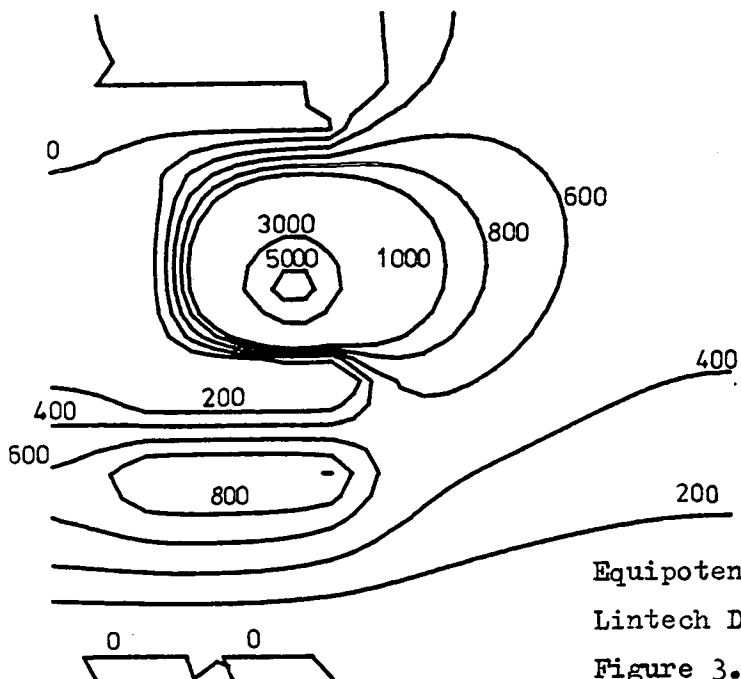
After using many different mesh resolutions a 25 by 25 mesh was found to give an adequate description of the detector's potential distribution. The maximum residual at any node was brought down to less than 0.01. Figure 3.42 shows the equipotential lines that describe the detector's field distribution. The optimum value for the trajectory step was found to be 0.01, as illustrated from Figure 3.43 which shows constancy in output current for $SLT > 91$.

Figure 3.44 shows electron trajectories at different initial angles and all at an initial energy of 3eV, most electrons reach the scintillator. Some electrons with 'shallower' initial angles strike the retardation plate and are not collected; this happens for angles





25*25 MESH Lintech Detector Figure 3.41

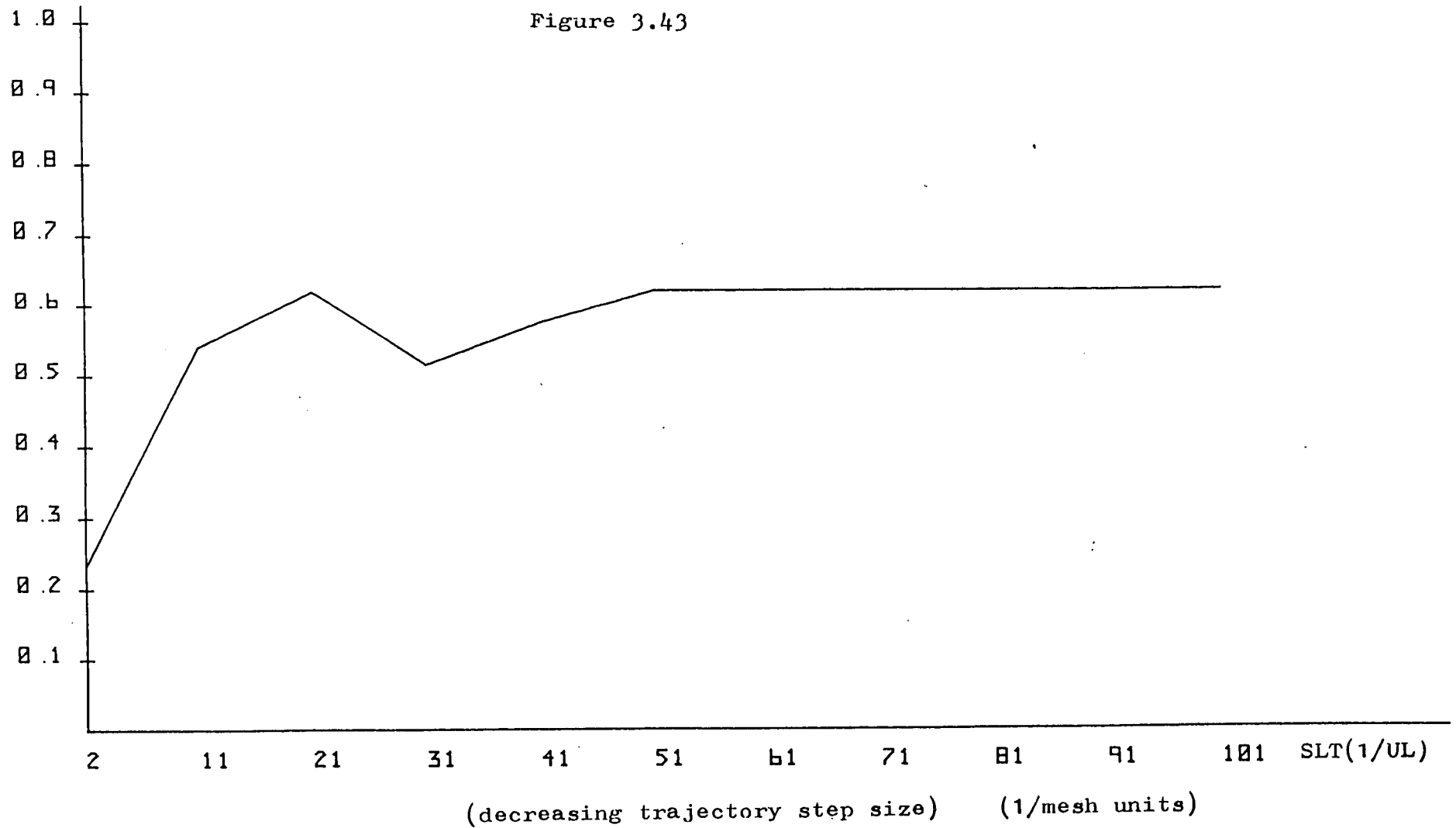


Equipotentials of Lintech Detector Figure 3.42

Transport
Efficiency

Error Option for the Lintech Detector

Figure 3.43



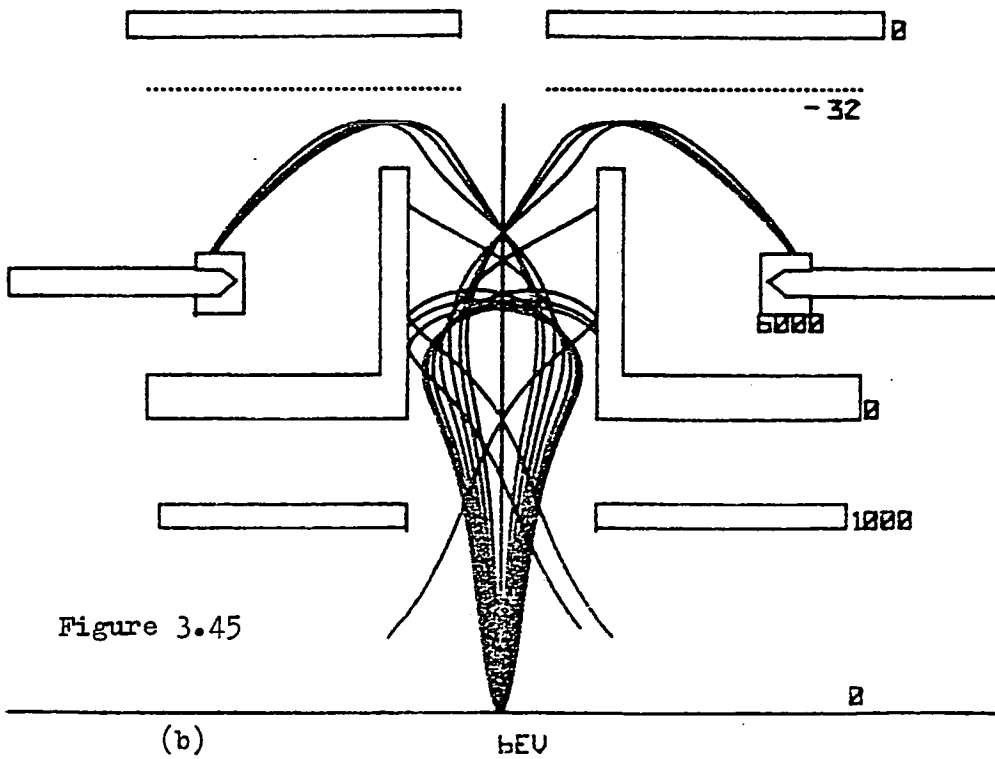
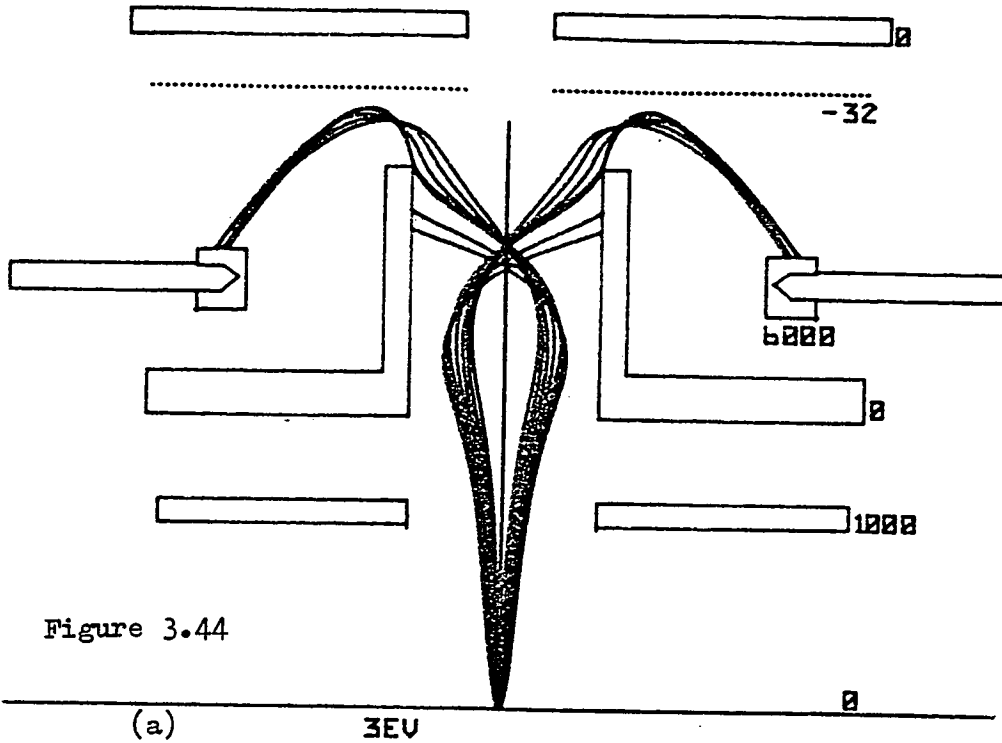
of 1.2 and 1.5 radians. Figures 3.45 and 3.46 show that a greater percentage of higher energy electrons do not reach the scintillator. Electrons at 10eV require to have initial angles in the range between 0 and 0.9 radians to be collected. All electrons very close to the central axis are not deflected on to the scintillator, this is explained from the equipotential lines in Figure 3.42 which show that the penetration field of the scintillator does not reach the central axis of the detector.

Figure 3.48 shows the energy transport efficiency of the detector and shows the detector is effective in filtering backscattered electrons. Figure 3.47 illustrates how backscattered electrons are rejected, 50% of these electrons collide with the bottom and inner side of the retarding plate while the other 50% penetrate the suppressor field and are lost in the aperture of the top plate. From Figures 3.44-3.46 the operation of the detector's extraction and retarding fields can be modelled to have a convergent lens effect on the emitted secondaries. The focal length and spot or cross-over region is dependent on the initial energies of the secondaries. Electrons at 3eV are spread over 1mm on the central axis in the cross-over region, while electrons at 6eV and 10eV are spread over 2.8mm and 4.0mm respectively.

3.6.5 Transport Efficiency

Figure 3.49 shows the relationship between the output current and the retardation plate voltage for an extraction voltage of 1kV. The graph shows considerable deviance from the normal expected S-curve

Trajectories for Lintech Detector for electrons emitted
 with energies of (a) 3eV
 (b) 6eV



Trajectories for Lintech Detector for electrons
emitted with energies of (c) 10eV

(d) 50eV

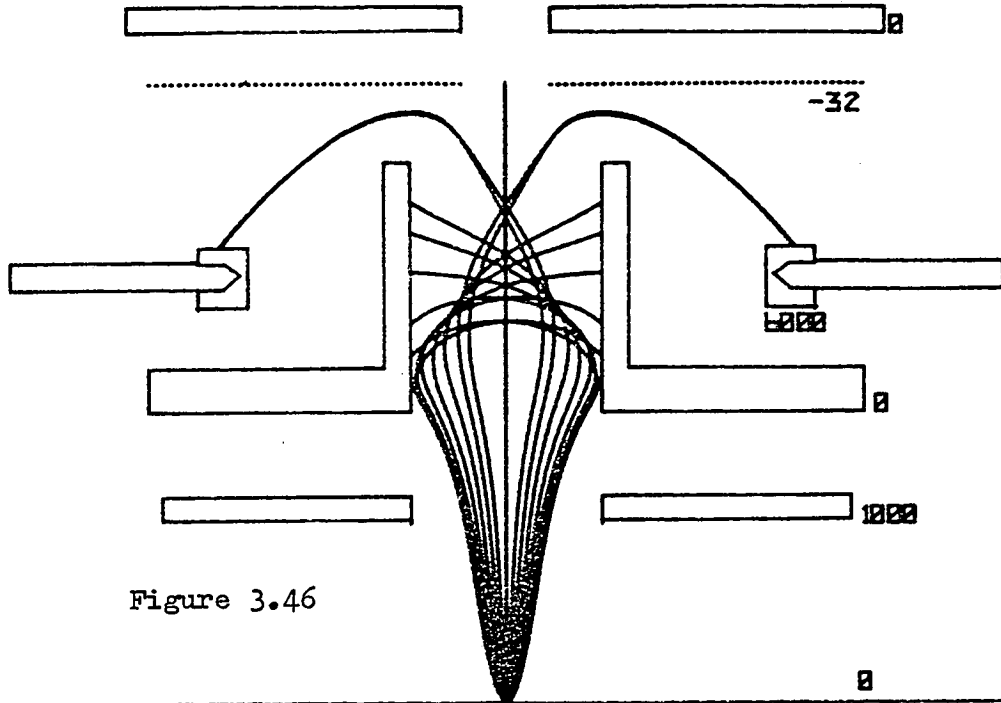


Figure 3.46

(c) 10eV

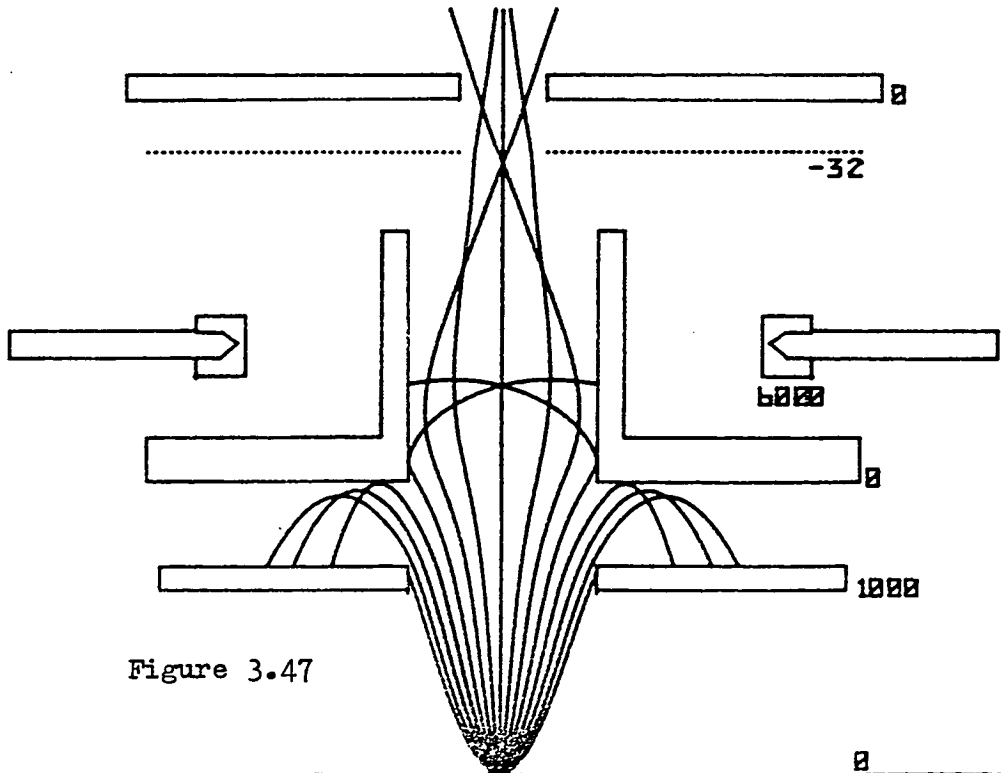
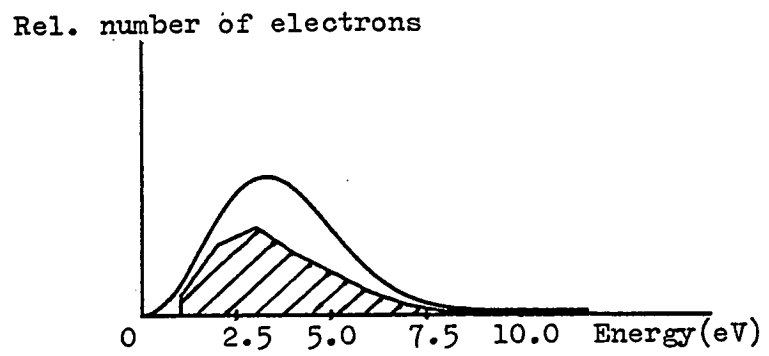


Figure 3.47

(d) 50eV (BACKSCATTERED)

Energy Analysis of Lintech Detector
Figure 3.48

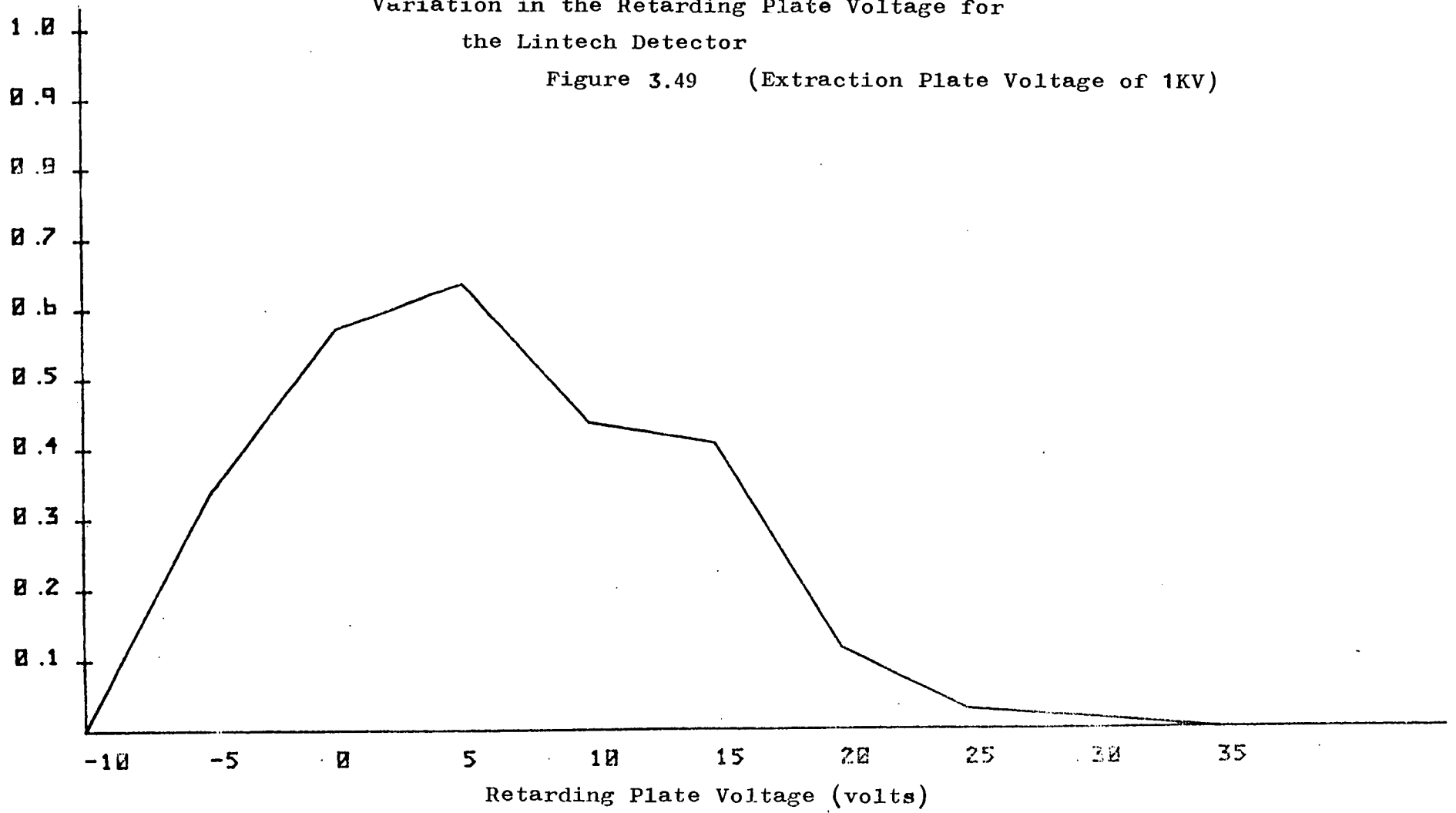


Transport Efficiency = 0.566

Transport
Efficiency

Variation in the Retarding Plate Voltage for
the Lintech Detector

Figure 3.49 (Extraction Plate Voltage of 1KV)



and illustrates an inherent non-linearity in the Lintech detector. The maximum value in the output current is approximately 0.62 or 62% transport efficiency and is found at 5 volts on the retardation plate. Hence making voltage measurements under these conditions is not practically viable due to the detector's non-linearity.

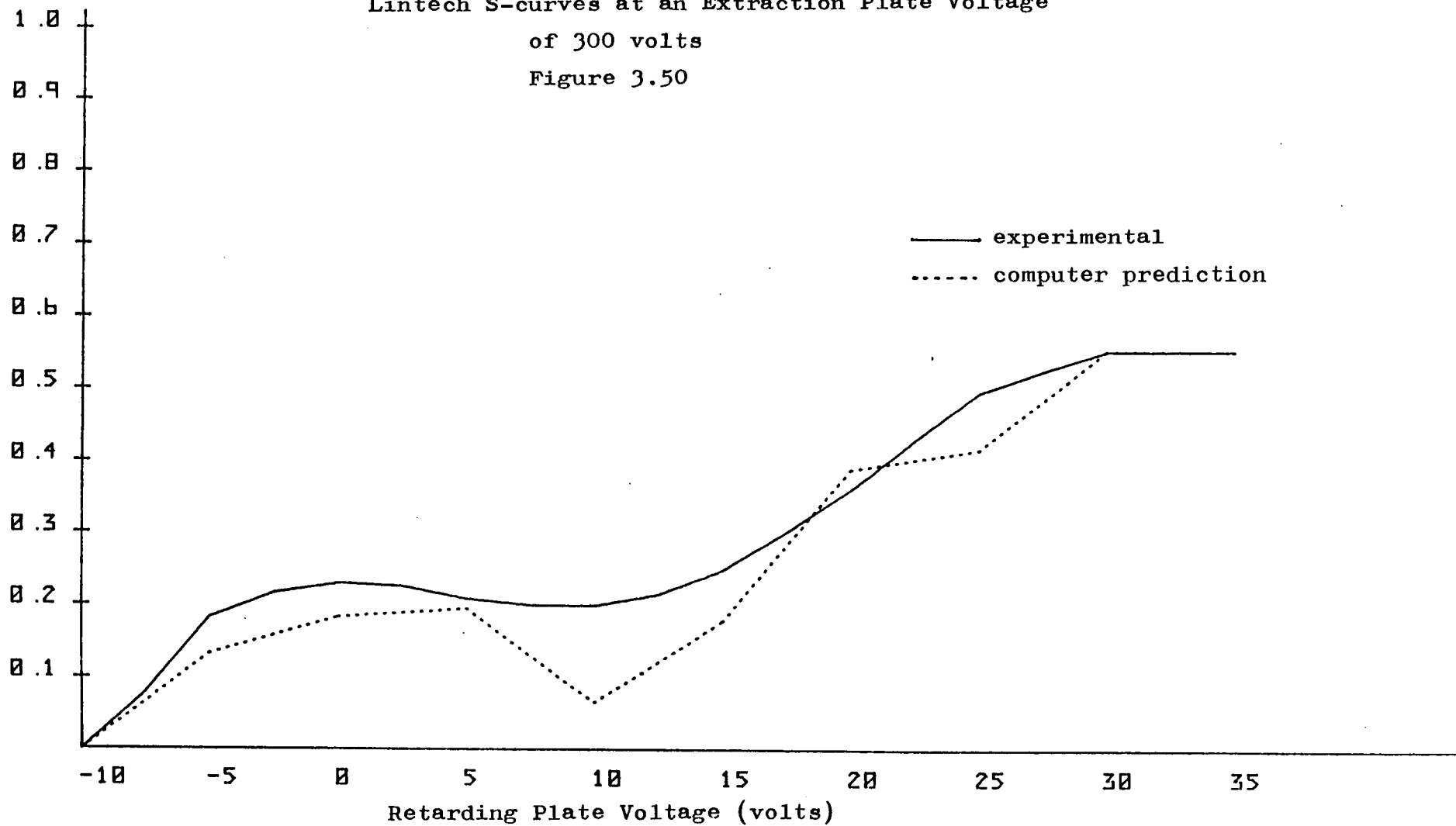
The greatest resemblance of an S-curve from the detector was found at extraction voltages at or near 300 volts; Figure 3.50 shows such a curve. The overall transport efficiency for 0 volts on the retardation plate is seen to be significantly reduced to 19% compared to 58% in the 1KV extraction case. Figure 3.52 shows how electrons at 3eV are rejected at an extraction voltage of 330 volts and retarding plate voltage of 0 volts. The focussing effect of the previous extraction and retarding fields is no longer exhibited and electrons are generally more dispersed and as a result of this fewer electrons reach the scintillator.

3.6.6 Comparison of computing results with practical results

Comparison of some computer predictions on the Lintech detector were made with experimental results provided by British Telecom made on their Cambridge Instruments S 150 S.E.M at Martlesham Research laboratories. Results were made from using a Lintech detector on a copper stub specimen. Figures 3.50 and 3.51 show a comparison of experimental and computer predicted detector curves at extraction voltages 300 and 330 volts respectively. The experimental curves were fitted arbitrarily to the theoretical curves by rescaling and shifting the graph axis. This was necessary since the precise black

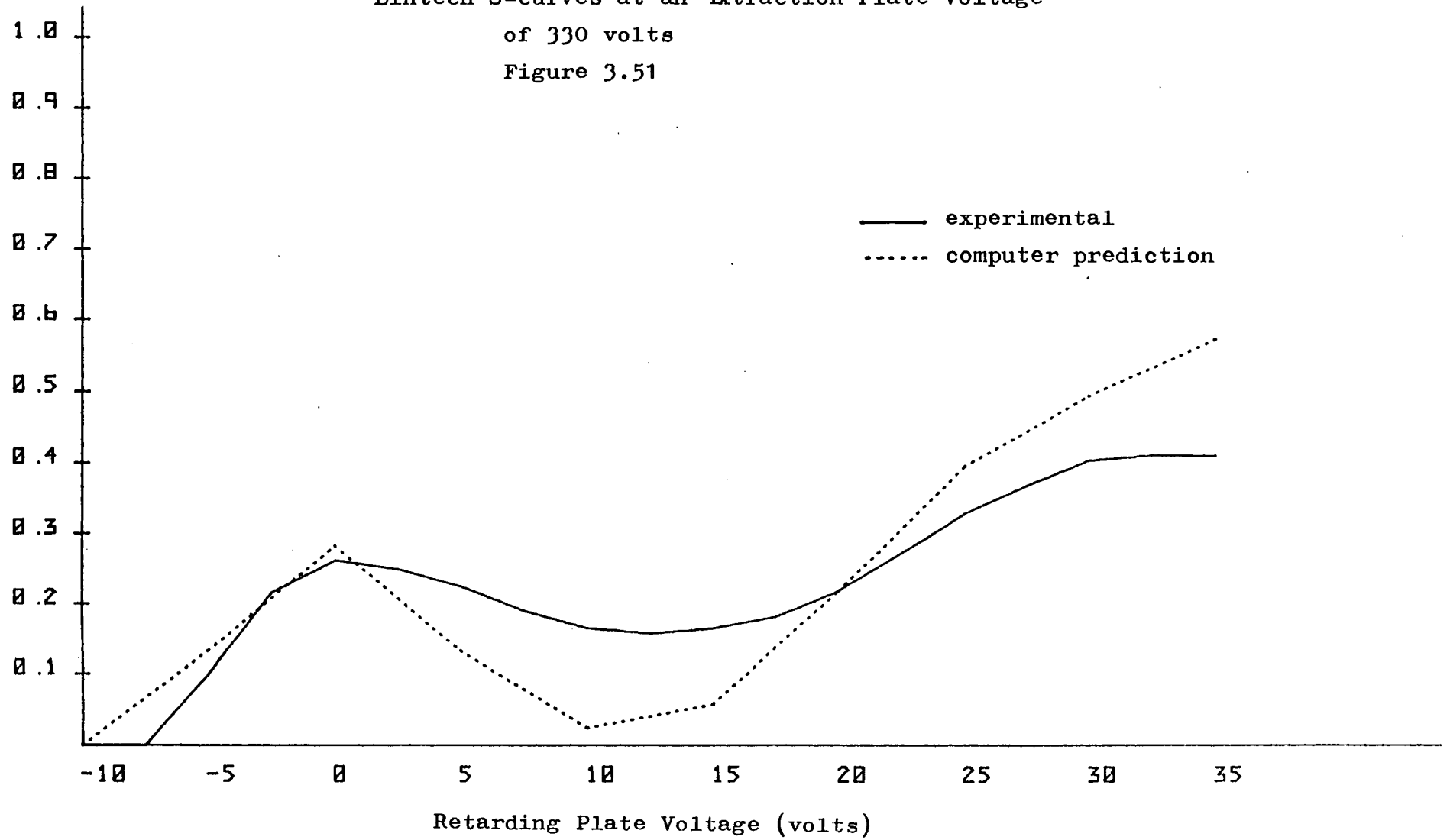
Transport
Efficiency

Lintech S-curves at an Extraction Plate Voltage
of 300 volts
Figure 3.50



Transport
Efficiency

Lintech S-curves at an Extraction Plate Voltage
of 330 volts
Figure 3.51



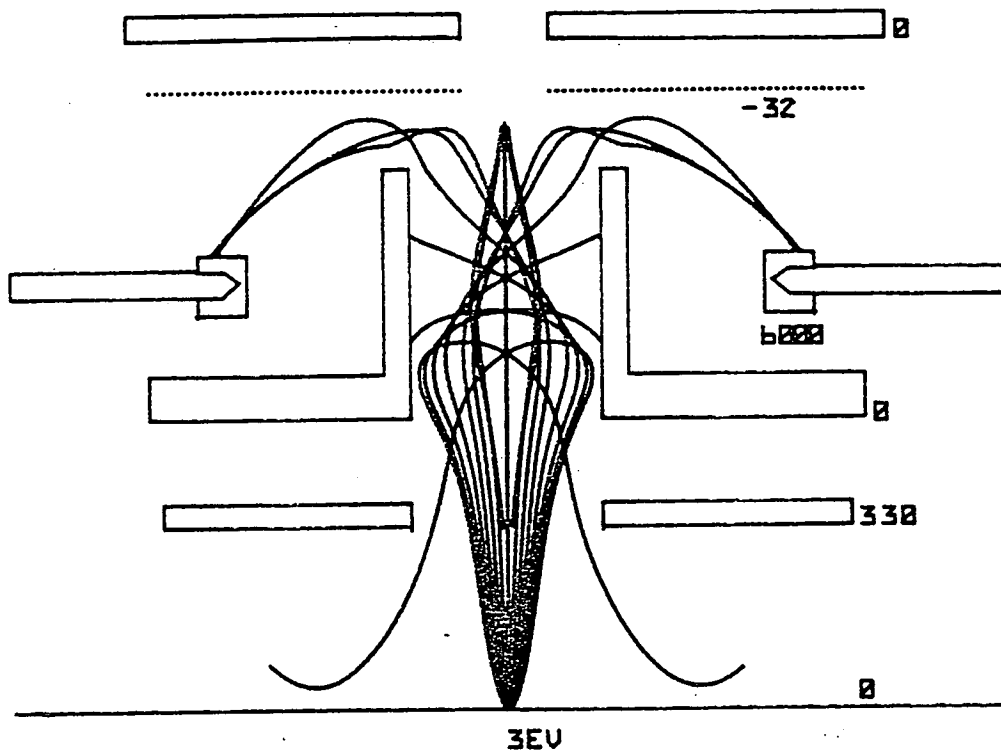


Figure 3.52

Trajectories for Lintech Detector for electrons emitted with an energy of 3eV and with 330 volts on the extraction electrode

level and photomultiplier amplification in the S.E.M during the time when measurements were made had not been recorded. The curves in Figures 3.50 and 3.51 however show a general correspondence between theory and experiment. In each case turning points in the theoretical and experimental curves occur at the same retarding grid voltages, 0 volts and 10 volts in Figures 3.50 and 3.51 respectively. An exact correspondence is not expected since many second order effects are present in the practical measurement which are not taken into account in the computer model. These include backscattered electrons, charging of dielectrics, contamination from an impure vacuum and many others.

Summary

Computing techniques have been developed to provide detector designs in 2-D rectilinear and 2-D cylindrically symmetric coordinates. Special error-reducing routines were found to be necessary and computer graphics facilities enhanced the prescription of different electrode layouts. The programs were used to simulate two specific detectors and gave the performance of each detector.

CHAPTER 4SIMULATION OF PARTICULAR DETECTORS4.1 Introduction

From Chapter 2 it was shown that past voltage contrast detectors have had little theoretical foundation in their design and that theoretical analysis for each detector is important in assessing its performance. Such a study also provides general criteria on which a new detector can be designed. All programs written in this section simulate the performance of detectors in three-dimensional coordinates. The detectors chosen fall into two categories; hemispherical detectors and cylindrically asymmetric detectors.

Within the class of hemispherical symmetry, detectors by Fentem(1974) and Tee(1976) are modelled and simulated. Figures 4.1(a-c) show the approximate models used, various practical features of each detector were approximated to help simplify the simulation. The boundary values at the base of Tee's detector are found by interpolating between grids. This approximation is valid since in practice this detector was mounted on long cylindrical pillars which kept the field uniform. In contrast Fentem's detector has an earth-plate at its base and has a non-uniform field between grids. The small apertures in the apex of each grid on Fentem's detector were neglected. Inclusion of such apertures would require a much more detailed description of the detector's potential field distribution and greatly increase overall run times of the computer programs. The outer mesh in Tee's detector is also neglected since

Figure 4.1(a)

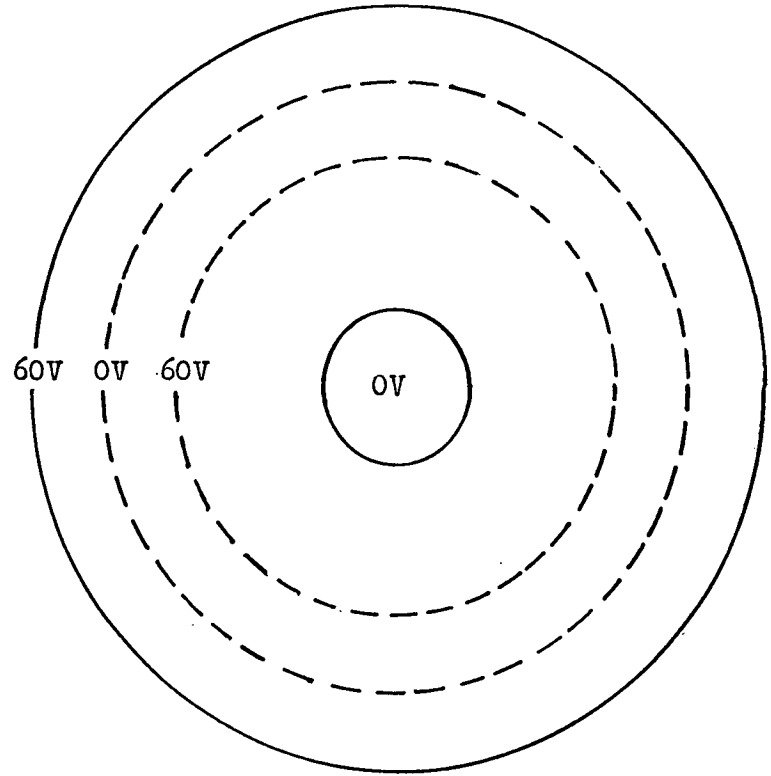
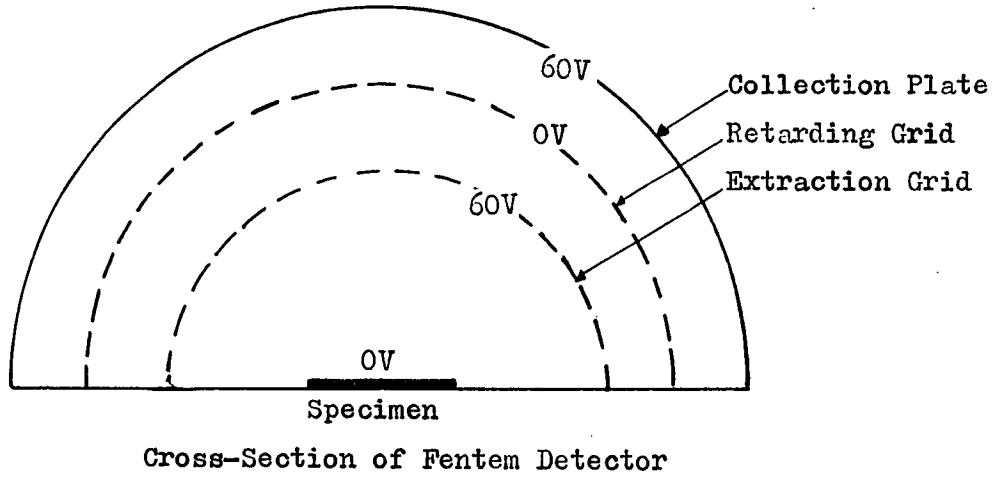


Figure 4.1(c)

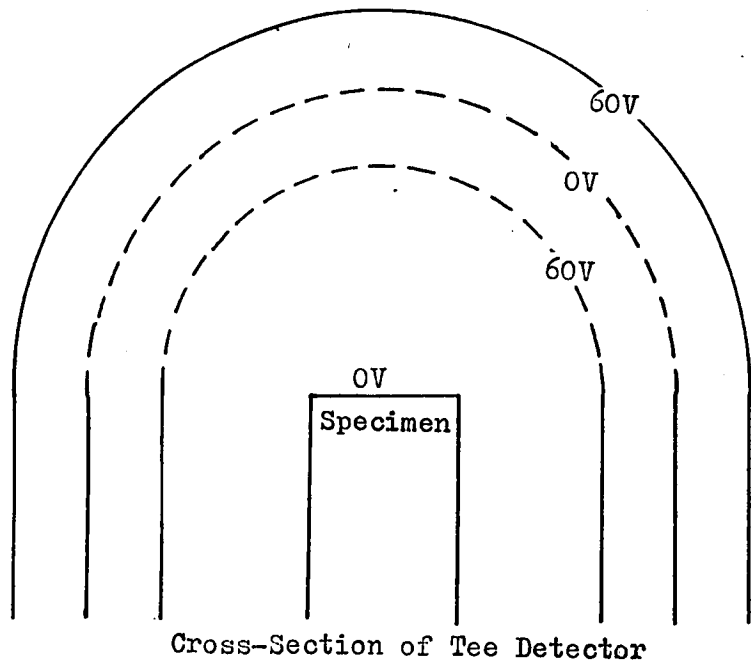
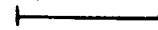


Figure 4.1(b)

Scale: 5.0m.m



this does not affect electrons within the detector. In practice the collection plate in Figure 4.1(b) should be a grid but for the programs, backscattered electrons were neglected and only relative changes in current were noted on the collection plate. Hence in this case little difference exists between modelling a solid plate or grid as the collection medium for electrons. The main difference between the detectors remains the uniform field for part of Tee's detector and the non-uniform field for Fentem's detector. The dimensions of both detectors were taken to be identical.

4.2 Potential Field Distributions for Hemispherical Detectors

The potential field distributions for both hemispherical detectors were found analytically and numerically. The only uniform field was found to exist for Tee's detector and in this case linear interpolation was used; however the field between the specimen and extraction grid was non-linear. The field for both detectors is radially symmetric and constant for the azimuth angle.

4.2.1 The Analytical approach to Fentem's Detector

Analytical methods were only used to solve the field distribution for Fentem's detector. This work was done in two sections, firstly the field between grids was solved and secondly the field between the extraction grid and specimen was found.

4.2.2 The Hemispherical Shell

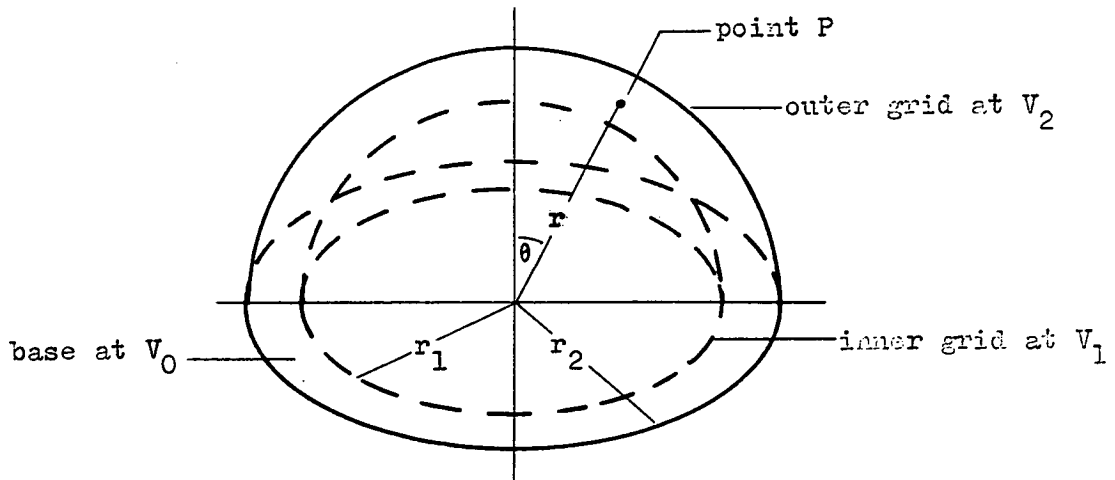
Finding the potential field between the grids in Fentem's detector is done by finding the field for the closed hemispherical shell shown in Figure 4.2. Laplace's equation in symmetrical spherical coordinates as already mentioned in Chapter 3 is given by

$$\frac{1}{r^2} \frac{\partial}{\partial r} \left(r^2 \frac{\partial V}{\partial r} \right) + \frac{1}{r^2 \sin \theta} \frac{\partial}{\partial \theta} \left(\sin \theta \frac{\partial V}{\partial \theta} \right) = 0 \quad 4.1$$

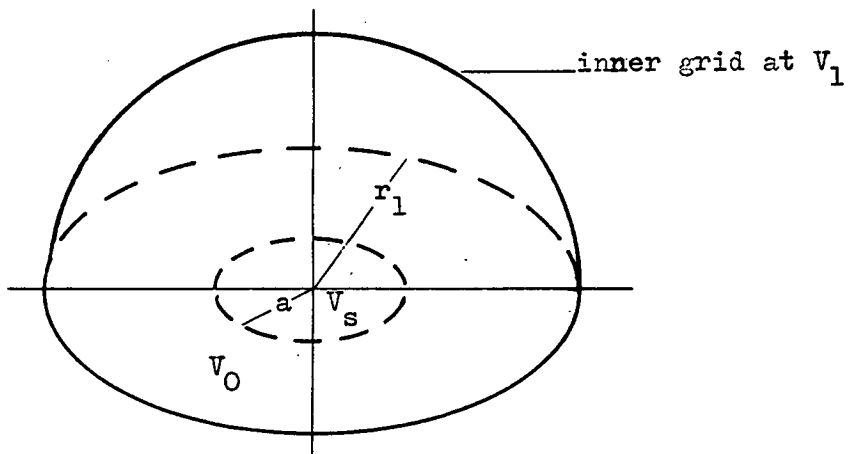
by the normal method of separating variables let

$$V(r, \theta) = R(r) \cdot H(\theta)$$

Hemispherical Shell Figure 4.2



Inner Hemisphere Figure 4.3



Problem A Figure 4.4(a)

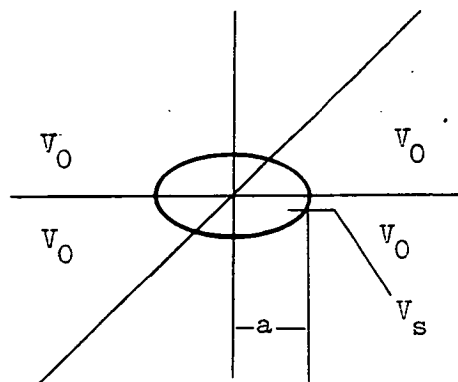
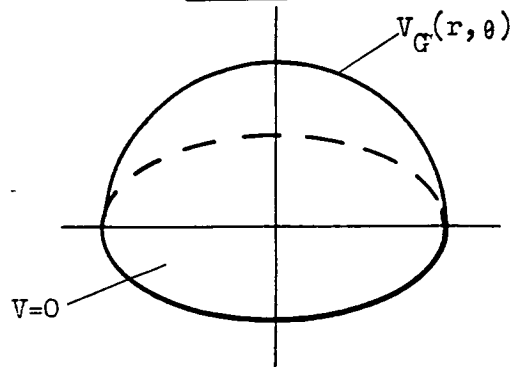


Figure 4.4(b)
Problem B



it can be shown that the general solution is given by

$$V(r, \theta) = \sum_{n=0}^{\infty} (a_n r^n + b_n / r^{n+1}) \cdot P_n(\cos \theta) \quad 4.2$$

where a_n and b_n are constants that depend on the precise boundary conditions considered and $P_n \cos(\theta)$ represents an n th degree Legendre polynomial. For the boundary conditions of the hemispherical shell, the solution is given by

$$V(r, \theta) = V_0 + \sum_{\substack{m=1 \\ \text{ODD}}}^{\infty} \frac{(2m+1)P_{m-1}(0)P_m(\cos \theta)}{(m+1)(1-(r_1/r_2)^{2m+1})} \times \\ \left\{ (V_2 - V_0) \left[(r/r_2)^m - (r_1/r_2)^m (r_1/r)^{m+1} \right] \right. \\ \left. - (V_1 - V_0) \left[(r_1/r_2)^{m+1} (r/r_2)^m - (r_1/r)^{m+1} \right] \right\} \quad 4.3$$

The proof of this is given in Appendix(1). From the above expression it is possible to calculate the field between the retarding grid and the extraction grid and also the field between the collection plate and retarding grid. The appropriate grid potentials are substituted for V_1 and V_2 and the dimensions r_1 and r_2 are also specified.

4.2.3 Inner Hemisphere

The potential in the inner hemisphere is much more difficult to solve than that for the hemispherical shell. Figure 4.3 depicts the problem. The field distribution is solved by considering two separate problems. The first problem is shown in Figure 4.4(a) and consists of

a flat circular disc lying in an infinite plane, the disc represents a specimen in the detector and is at a voltage V_s . The rest of the plane is at voltage V_0 . The second problem consists of a hemispherical top placed on a 0 volt base and is shown in Figure 4.4(b). The potential distribution on the hemispherical top ($V_G(\theta)$) is constructed from the potential distribution at r_1 in problem A by,

$$V_G(\theta) = V_1 - V_A(r_1, \theta) \quad 4.4$$

This is done to provide the boundary condition of voltage V_1 at a radius r_1 in the final hemisphere by adding the potential distributions of problems A and B. Hence at radius r_1 ,

$$\begin{aligned} V(r_1, \theta) &= V_A(r_1, \theta) + V_B(r_1, \theta) \\ &= V_A(r_1, \theta) + V_G(\theta) \\ &= V_A(r_1, \theta) + V_1 - V_A(r_1, \theta) \\ &= V_1 \end{aligned}$$

Once the potential distribution of problem B is found ($V_B(r, \theta)$) the final potential distribution of the inner hemisphere is given by,

$$\begin{aligned} V(r, \theta) &= V_A(r, \theta) + V_B(r, \theta) \quad 4.5 \\ \text{for } 0 &\leq r \leq r_1 \\ 0 &\leq \theta \leq \pi/2 \end{aligned}$$

4.2.4 Solving Field A

The potential for the circular disc in an infinite plane is solved by considering the solution of Laplace's equation in cylindrical polar coordinates. For an axially symmetric field the general solution is

$$V(\rho, z) = \int_0^{\infty} A(\xi) \cdot e^{-\xi z} J_0(\xi \rho) \xi + B \quad 4.6$$

where ξ is a dummy variable in the integration and $A(\xi), B$ are quantities that depend on the boundary conditions, $J_0(\xi\rho)$ is the zeroth order Bessel function. Appendix (2) solves $A(\xi)$ and B for the boundary conditions shown in Figure 4.4(a) and finds the field distribution in field A to be given by

$$V_A(r, \theta) = V_0 + (V_s - V_0)(a^2 - r^2 \sin^2 \theta)^{1/2} \int_0^\infty \sin(a\xi) e^{-\xi r \cos \theta} J_0(\xi r \sin \theta) d\xi \quad 4.7$$

The distribution at r_1 is then given by

$$V_A(r_1, \theta) = V_0 + (V_s - V_0)(a^2 - r_1^2 \sin^2 \theta)^{1/2} \int_0^\infty \sin(a\xi) e^{-\xi r_1 \cos \theta} J_0(\xi r_1 \sin \theta) d\xi \quad 4.8$$

4.2.5 Solving Field B

The solution to field B involves the use of spherical polar coordinates and a general solution of Laplace's equation in these coordinates,

$$V(r, \theta) = \sum_{m=0}^{\infty} (a_m r^m + b_m / r^{m+1}) P_m(\cos \theta)$$

Appendix (3) applies the boundary conditions shown in Figure 4.4(b) for field B and finds the following solution,

$$V_B(r, \theta) = (V_1 - V_0) \sum_{\substack{m=1 \\ \text{ODD}}}^{\infty} \frac{\alpha_m}{\beta_m} (r/r_1)^m \cdot P_m(\cos \theta) \\ - (V_s - V_0) \sum_{\substack{m=1 \\ \text{ODD}}}^{\infty} \frac{1}{\beta_m} (r/r_1)^m \left[\int_0^{\pi/2} P_m(\cos \theta') \cdot \sin \theta' \cdot (a^2 - r_1^2 \sin^2 \theta')^{1/2} d\theta' \right. \\ \left. \int_0^\infty \sin(a\xi) \cdot e^{-\xi r_1 \cos \theta'} \cdot J_0(\xi r_1 \sin \theta') d\xi \right]$$

where

$$\alpha_m = \int_0^1 P_m(x) dx$$

$$\beta_m = \int_0^1 [P_m(x)]^2 dx$$

Hence the complete solution to the inner hemisphere is given by

$$\begin{aligned} V(r, \theta) &= V_A(r, \theta) + V_B(r, \theta) \\ &= V_0 + (V_s - V_0) (a^2 - r^2 \sin^2 \theta)^{1/2} \int_0^\infty \sin(a\xi) e^{-\xi r \cos \theta} J_0(\xi r \sin \theta) d\xi \\ &+ (V_1 - V_0) \sum_{\substack{m=1 \\ \text{ODD}}}^{\infty} \frac{\alpha_m}{\beta_m} (r/r_1)^m \cdot P_m(\cos \theta) \\ &- (V_s - V_0) \sum_{\substack{m=1 \\ \text{ODD}}}^{\infty} \frac{1}{\beta_m} (r/r_1)^m \left[\int_0^{\pi/2} P_m(\cos \theta') \cdot \sin \theta' \cdot (a^2 - r_1^2 \sin^2 \theta')^{1/2} d\theta' \right. \\ &\quad \left. \int_0^\infty \sin(a\xi) \cdot e^{-\xi r_1 \cos \theta'} \cdot J_0(\xi r_1 \sin \theta') d\xi \right] \end{aligned}$$

4.3 Numerical Methods for Solving Fields in a Hemispherical Detector

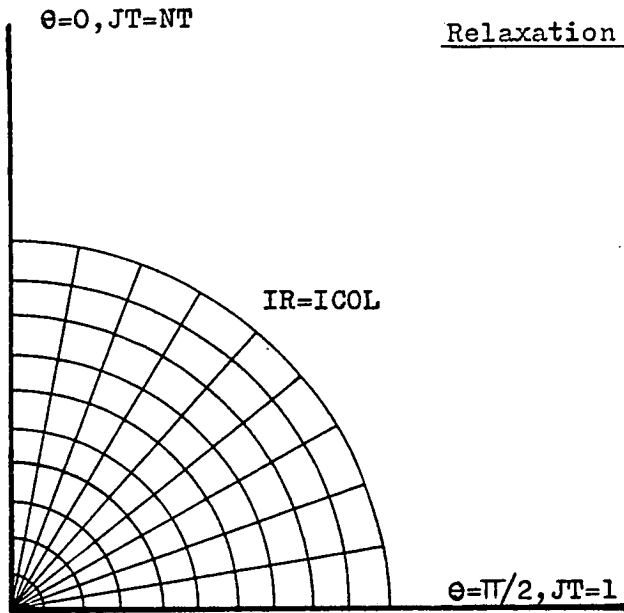
The normal relaxation method in spherical coordinates was used to find potential distributions inside the hemispherical detectors. Since the field was axially symmetric a two dimensional mesh was used, Figure 4.5(a) shows such a mesh. The total number of mesh lines in the theta direction is given by NT and in the radial direction by ICOL, these numbers could be set interactively by the user. A typical finite-difference star is shown in Figure 4.5(b), the residual equation for this star is given by

$$\begin{aligned} \text{Res} = & V_4(1/HR^2 + 1/(rHR)) + V_2(1/HR^2 - 1/(rHR)) + V_1(\cot\theta/2H\theta + 1/H\theta^2)/r^2 \\ & + \frac{V_3}{r^2}(1/H\theta^2 - \cot\theta/2H\theta) - V_0(2/HR^2 + 2/(r^2H\theta^2)) \end{aligned} \quad 4.11$$

where HR and Hθ are the lengths of the star in the radial and theta directions respectively. If HR=1 then

$$\begin{aligned} \text{Res} = & V_4(1+1/r) + V_2(1-1/r) + V_1(\cot\theta/2H\theta + 1/H\theta^2)/r^2 \\ & + V_3(1/H\theta^2 - \cot\theta/2H\theta)/r^2 - V_0(2 + 2/(r^2H\theta^2)) \end{aligned} \quad 4.12$$

In the radial direction each mesh line was designated by IR where $1 \leq IR \leq ICOL$ and in the theta direction each mesh line was designated by JT for $1 \leq JT \leq NT$



IR=1
 Figure 4.5(a)
 Mesh in hemisphere

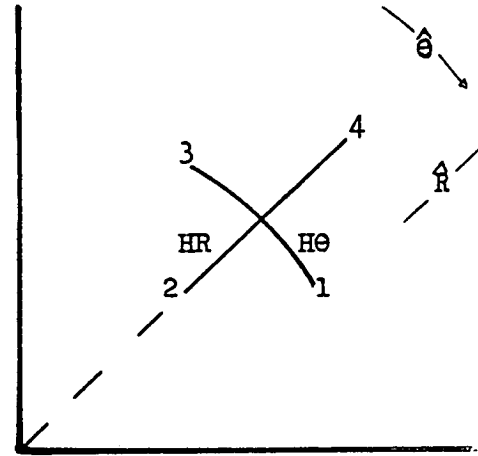


Figure 4.5(b)
 Typical star in hemisphere

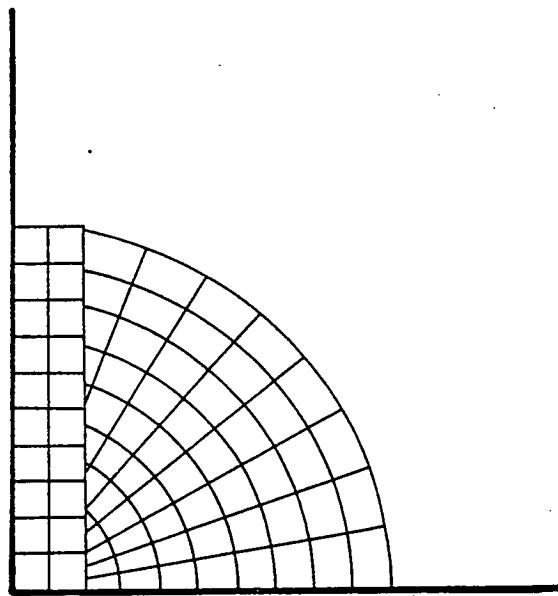
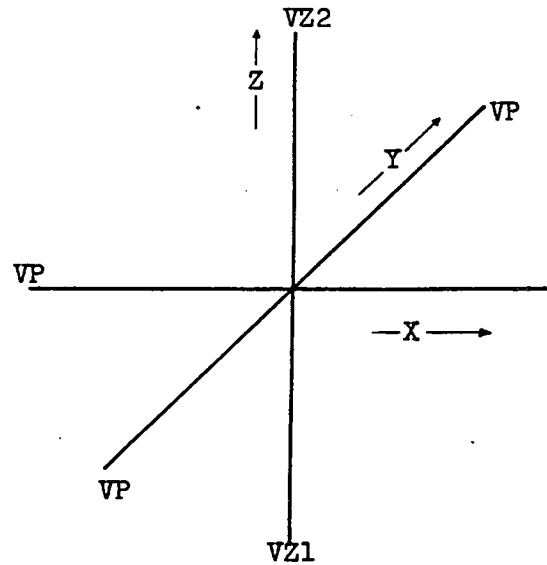


Figure 4.6(a)
 Revised mesh to avoid singularities
 on the central axis



Typical Star on Central Axis
 Figure 4.6(b)

The conversion to real space was

$$\begin{aligned} r &= IR - 1.0 \\ \theta &= \pi/2 - (JT-1.0)H\theta \end{aligned}$$

so limits on r and θ were

$$\begin{aligned} 0 &\leq r \leq ICOL \\ 0 &\leq \theta \leq \pi/2 \end{aligned}$$

and

$$H\theta = (\pi/2)/(NT-1)$$

For each node successive over-relaxation was applied in the following form

$$V_0 = V_0 + \frac{\text{Res} * \alpha}{2(1+1/(r^2 H\theta^2))} \quad 4.13$$

To avoid a singularity at $r=0$ a rectilinear mesh was used at the centre of the hemisphere. A cross-section of the rectangular cuboid is shown in Figure 4.6(a), the voltages at the sides of this three-dimensional mesh are interpolated from the larger two-dimensional spherical mesh. Figure 4.6(b) shows a typical star on the central axis of the hemisphere. The voltage V_P remains constant in both the X-Y directions so that the residual equation in the rectilinear mesh is given by

$$\text{Res} = VZ1 + VZ2 + 4*VP - 6*VP$$

Each node on the central axis is relaxed by this equation.

4.4 Trajectory Plotting

4.4.1 Interpolation

Trajectory calculations were done in three-dimensional coordinates. Electric field values E_x, E_y, E_z in the X, Y, Z directions respectively, were computed by transforming from rectilinear coordinates into polar coordinates and using linear interpolation. Hence to find the potential at (X, Y, Z) interpolation between mesh lines JT, IR and $JT+1, IR+1$ was carried out where JT and IR were given by

$$JT = 1.0 + (\pi/2 - \theta)/H\theta$$

$$IR = r + 1.0$$

θ and r were given by

$$r = (x^2 + y^2 + z^2)^{1/2}$$

$$\theta = \cos^{-1}(z/r)$$

4.4.2 Preventing the Electron from Stepping across a Grid

Previously this problem was solved in one dimension, the Z -direction, where a suitable time step (dt) was found to increment the electron to bring it exactly on the grid. The time step (dt)

was easily solved from the following trajectory equation

$$dz = V_z * dt + (1/2) * (e/m) * E_z * (dt)^2 \quad 4.15$$

where V_z is the electron velocity in the Z-direction, E_z is the electric field in the Z-direction and dz is the required increment to bring the electron on the grid.

In the hemispherical situation, however, the geometry of the grid is much more complicated and a time step (dt) must be found to step the electron a distance (dR), which brings the electron exactly on the spherical grid. Although dR may be known there is no simple equation which relates it to increments dx, dy, dz . These are all related to dt by

$$dx = V_x * dt + (1/2) * (e/m) * E_x * dt^2 \quad 4.16$$

$$dy = V_y * dt + (1/2) * (e/m) * E_y * dt^2 \quad 4.17$$

$$dz = V_z * dt + (1/2) * (e/m) * E_z * dt^2 \quad 4.18$$

$$dR = (dx^2 + dy^2 + dz^2)^{1/2} \quad 4.19$$

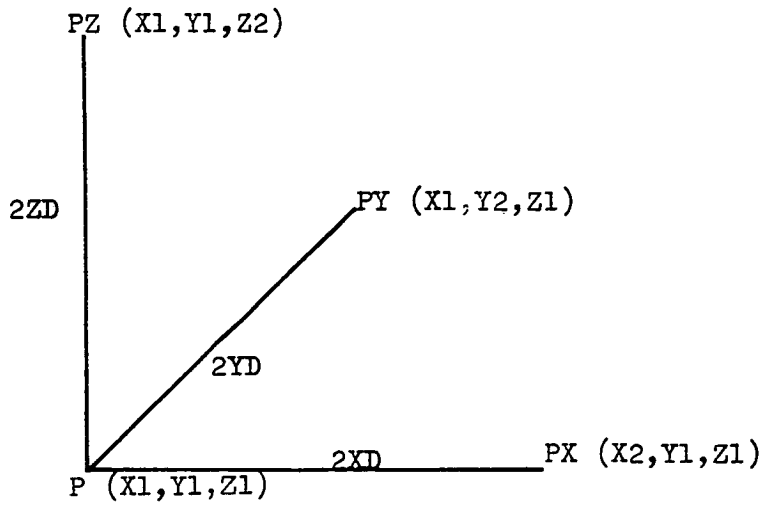
substituting in Equation(4.19) the following fourth degree polynomial in dt is obtained

$$dt^4 C_1 + dt^3 C_2 + dt^2 C_3 - dR^2 = 0 \quad 4.20$$

C_1, C_2, C_3 are constants dependent on $E_x, E_y, E_z, V_x, V_y, V_z$ and em .

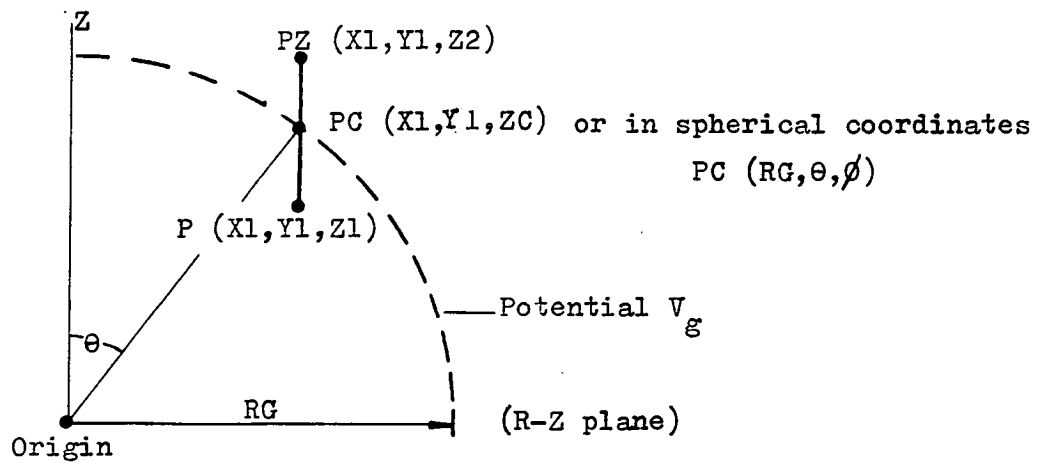
Equation(4.20) is solved by the method of repeated Linear Interpolation (Buckingham(1957)). This method starts with an initial value for dt and uses a convergent algorithm to find an accurate value. Let

$$F(dt) = dt^4 C_1 + dt^3 C_2 + dt^2 C_3 - dR^2 \quad 4.21$$



Calculating Electric Fields in 3D

Figure 4.7(a) (2XD, 2YD and 2ZD are electric field segment lengths)



Modifying Electric Field in the Z-Direction

Figure 4.7(b)

the standard algorithm used is

$$dt_{n+1} = dt_n - F(dt_n)/M_n \quad 4.22$$

where

$$M_n = \left[F(dt_n) - F(dt_{n-1}) \right] / (dt_n - dt_{n-1})$$

M_n denotes the gradient of the function $F(dt_n)$ at the n th computation.

dt is the n th approximation of the time step while dt is the $n+1$ approximation.

At most n reaches 10 before dt is accurate to six decimal places and $F(dt)$ falls below 10^{-15}

4.4.3 Calculating Electric Fields near Grids

Another problem arising from the complex geometry of hemispherical grids is that electric field values need to be modified when electrons are close to grids. Figure 4.7(a) illustrates the normal way of calculating electric fields in three-dimensional coordinates Ex, Ey, Ez . Three points PX, PY and PZ are projected from the electron's position P ; the coordinates defining the electron's position are $(X1, Y1, Z1)$ giving radius RP . The coordinates of PX, PY, PZ are $(X2, Y1, Z1), (X1, Y2, Z1)$ and $(X1, Y1, Z2)$ respectively where

$$X2 = X1 + 2XD$$

$$Y2 = Y1 + 2YD$$

$$Z2 = Z1 + 2ZD$$

Radii at PX, PY, PZ are calculated from

$$RPX = (X2^2 + Y1^2 + Z1^2)^{\frac{1}{2}}$$

$$RPY = (X1^2 + Y2^2 + Z1^2)^{\frac{1}{2}}$$

$$RPZ = (X1^2 + Y1^2 + Z2^2)^{\frac{1}{2}}$$

Inaccuracies in the electric field calculations emerge when $\overline{RPX} - \overline{RP}$ or $\overline{RPY} - \overline{RP}$ or $\overline{RPZ} - \overline{RP}$ cross a grid, in such cases their intersections with the grid are found and the appropriate electric fields modified.

4.4.4 Modifying Electric Fields

Electric fields were modified; if necessary all three electric fields E_x, E_y and E_z could be changed. Figure 4.7(b) shows $\overline{RPZ} - \overline{RP}$ crossing a grid of radius R_G and the electron's position before crossing as (X_1, Y_1, Z_1) . The point of intersection is shown by PC and its coordinates being (X_1, Y_1, Z_C) . X_1, Y_1 are known but Z_C is unknown. Z_C is calculated from finding the off-axis angle θ for the point PC. The relationship between spherical coordinates (Figure 3.4(a)) and rectilinear coordinates is given by

$$x = r \sin\theta \cos\phi$$

$$y = r \sin\theta \sin\phi$$

$$z = r \cos\theta$$

at the point PC

$$X1 = RG \sin\theta \cos\phi$$

$$Y1 = RG \sin\theta \sin\phi$$

$$ZC = RG \cos\theta$$

θ is found by eliminating ϕ

$$X1^2 + Y1^2 = RG^2 \sin^2\theta$$

$$\therefore \theta = \sin^{-1}((X1^2 + Y1^2)/RG^2)^{\frac{1}{2}}$$

If the potential at the electron's position is V_p and the potential on the grid is V_g the electric field in the Z-direction is modified to

$$E_z = (V_g - V_p)/(ZC - Z1)$$

Like the modified field in the Z-direction E_x requires the calculation of θ and ϕ at the intersection point ($X_C, Y1, Z1$) in the X-direction so

$$X_C = RG \sin\theta \cos\phi,$$

$$\theta = \cos^{-1}(Z1/RG)$$

$$Y1 = RG \sin\theta \sin\phi,$$

$$\phi = \sin^{-1}(Y1/RG \sin\theta)$$

$$Z1 = RG \cos\theta,$$

$$E_x = (V_g - V_p)/(X_C - X1)$$

Lastly the modified electric field in the y-direction is calculated by finding θ and ϕ for the intersection point (XC, YC, Z1),

$$X1 = RG \sin\theta \cos\phi ,$$

$$YC = RG \sin\theta \sin\phi ,$$

$$Z1 = RG \cos\theta ,$$

$$\theta = \cos^{-1}(Z1/RG)$$

$$\phi = \cos^{-1}(X1/RG\sin\theta)$$

$$E_y = (V_g - V_p)/(YC - Y1)$$

Once E_x, E_y, E_z are calculated the normal trajectory step was computed.

4.5 The Feuerbaum Detector

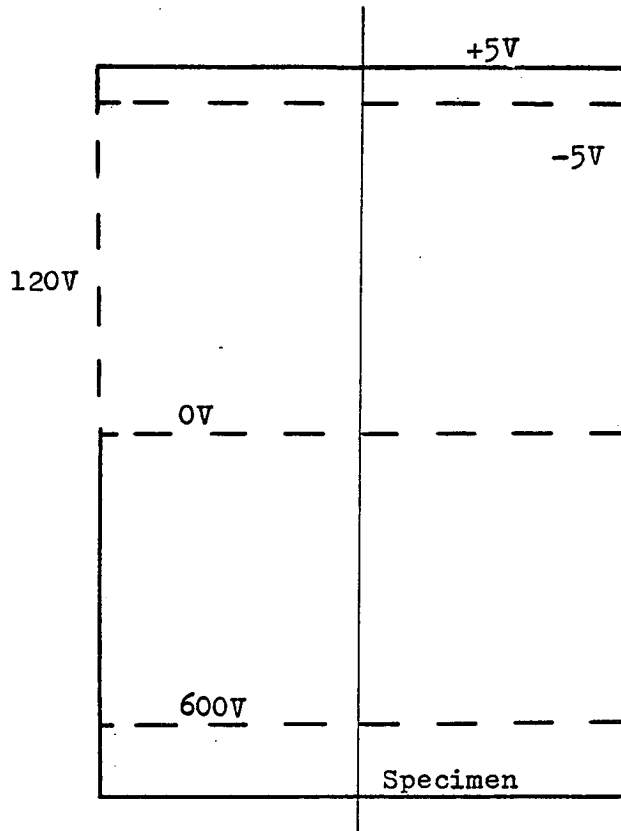
4.5.1 Introduction

The computer model to simulate the performance of this detector is shown in Figure 4.8. Electrons are attracted away from the specimen by an extraction field V_e and retarded by a grid at voltage V_r ; these grids are planar in the horizontal cross-section. A linear retarding and extracting field is assumed, although in practice the dielectric walls between the grids will tend to charge up and cause slight non-linear field variations. After traversing the retarding field, electrons are deflected by a semi-circular gauze so that this deflection field is similar to the Banbury and Nixon detector (1970). The electrons are collected by the normal scintillator and photomultiplier arrangement placed near the deflecting gauze. The computer simulation of this detector was much simpler than that for the hemispherical detectors.

4.5.2 Field Distributions for the Feuerbaum Detector

The potential distribution can be calculated analytically or numerically. The analytical solution to the deflection field is given in Appendix (4). The Fourier-Bessel series used to describe this field is identical to the form used by Munro (1971) for the field inside the Banbury and Nixon detector, because the two detectors have similar electrode geometries. Although the potential distribution can be found analytically, the numerical method of relaxation was

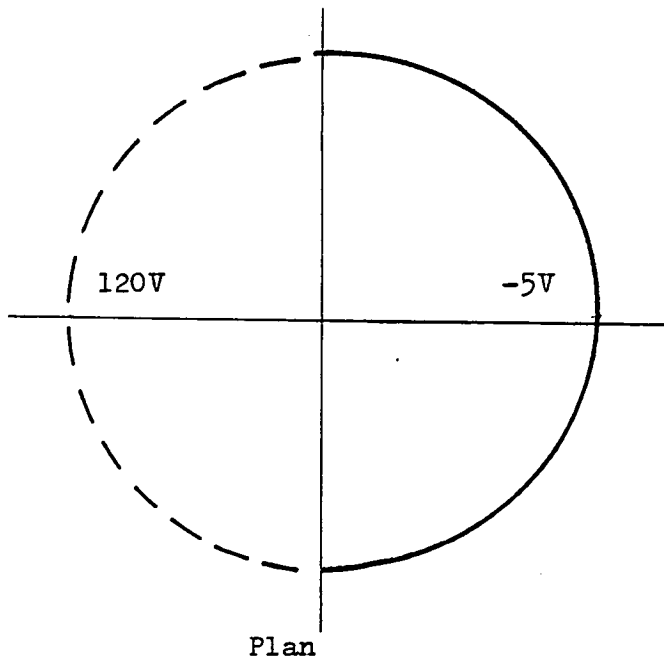
Feuerbaum Detector



Vertical Cross-Section

Scale: 1m.m
|-----|

Figure 4.8



Plan

used. This is because the analytical method would still require numerical computations and a program written for this purpose would take much longer to write than one based on the relaxation method. Since relaxation techniques have been used in other programs, quick modifications of existing routines were made. Another reason for not using the analytical method was the extra interpolation required to transform the analytical solution from cylindrical coordinates into rectilinear coordinates for electron trajectory calculations.

4.5.3 Deflection Field Distribution solved by the Relaxation Method

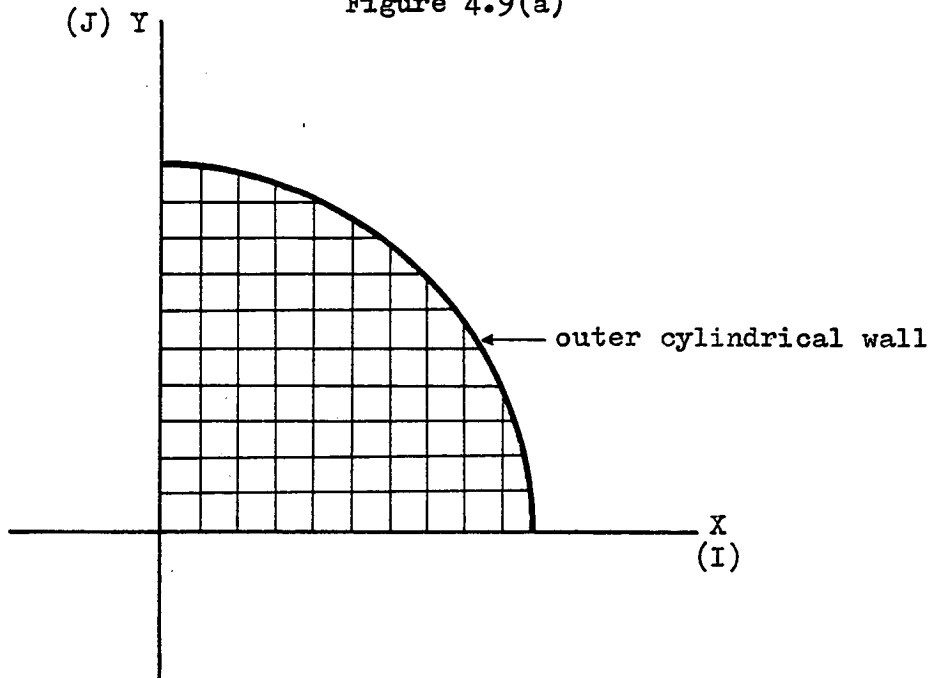
A three-dimensional rectilinear mesh was used, since planar boundary conditions existed in the Z-direction, asymmetrical stars were only required in the X-Y plane. Figure 4.9(a) shows a typical cross-section of the relaxation mesh in this plane where only the first quadrant is shown. The cylindrical wall boundary was taken into account by constructing asymmetrical stars whose lengths were represented by DBX(J) and DBY(I) near the outer boundary, Figure 4.9(b) depicts such a star. The relaxation-residual equation was modified for these stars and symmetry was used for computing the field in other quadrants. The dimensions of the detector and mesh resolutions were specified interactively by the program user.

4.5.4 Trajectory Calculations

Trajectory calculations were made in three-dimensional rectilinear coordinates. Error precautions against electrons crossing grids and turning points were taken and are similar to that of the error-reducing routines described in Chapter 3. Electron trajectories were displayed in two views, a side view and a plan view.

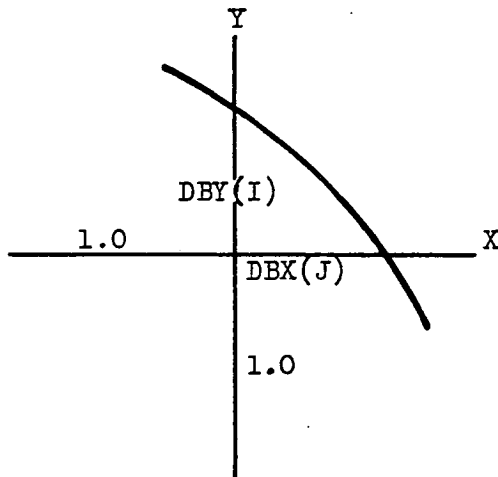
Relaxation Mesh for Feuerbaum Detector

Figure 4.9(a)



Asymmetrical Star Near Outer Wall Boundary

Figure 4.9(b)



4.6 RESULTS ON THE HEMISPHERICAL DETECTORS

4.6.1 Electrons Leaving Specimen Centre

A 10 by 26 relaxation mesh size was used for both the Fentem and Tee detectors. An error test for the optimum electron trajectory step size was made. Figure 4.10 shows that the output current stays relatively constant for electron step sizes of $UL < 0.03$ or $SLT > 31$. Figure 4.10 was calculated for a retarding grid voltage of -4 volts.

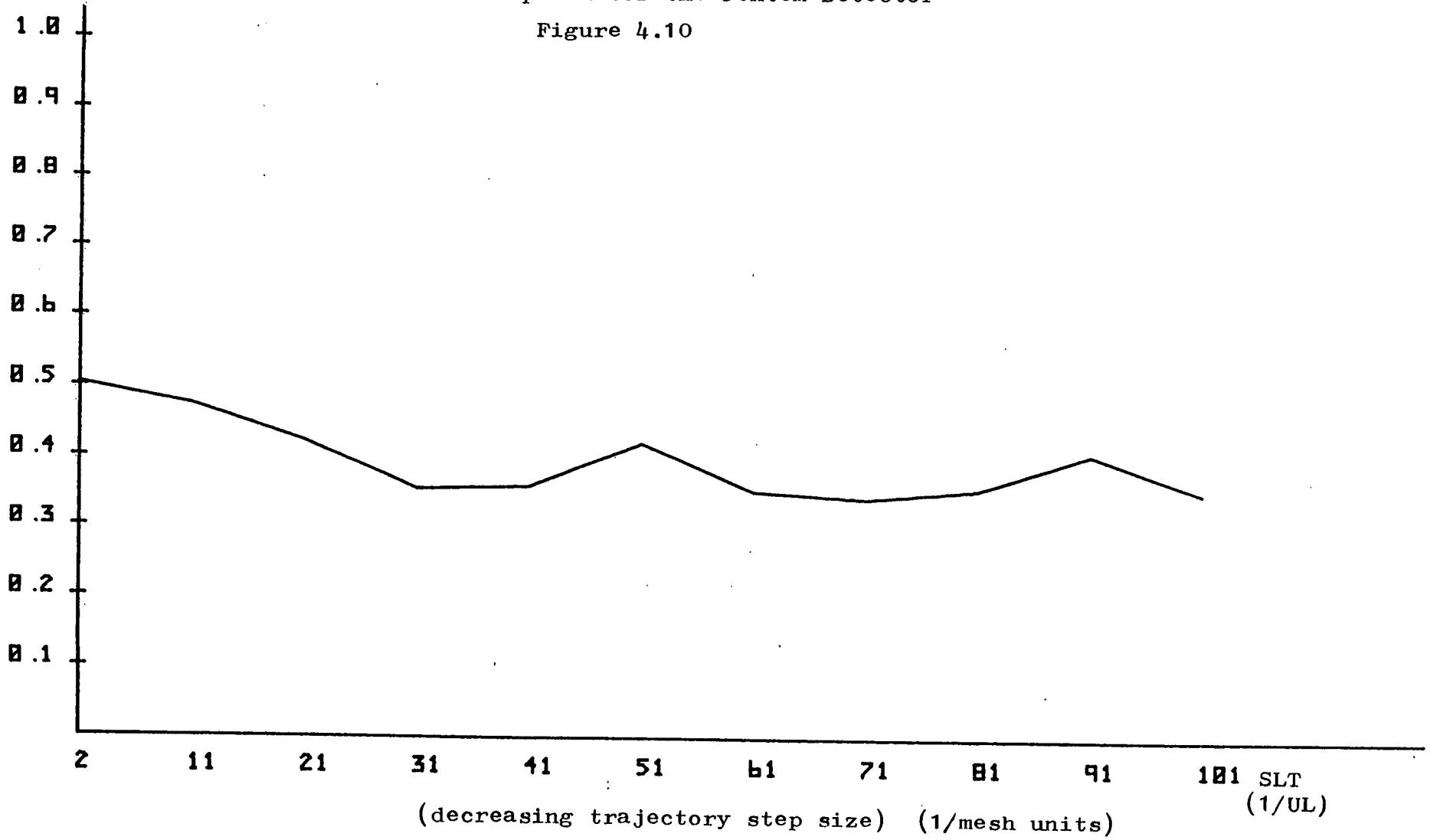
Figures 4.11 and 4.12 show equipotential lines for the Fentem and Tee detectors respectively. The field for Fentem's detector exhibits greater non-linearity at the edge of the specimen-earth plate than for the field in Tee's detector around the same region. Above the centre of the specimen, potential values are approximately the same for both detectors. The potential at the first node along the central axis was found to be 4.9 volts for Fentem's detector and 7.0 volts for Tee's detector. Equipotential lines near the central axis are uniform for both detectors, from this it can be deduced that both detectors will not differ greatly in performance.

Figures 4.13 and 4.14 show electron trajectories at an initial energy of 3eV for Fentem and Tee detectors. Electron trajectories appear to be identical in each case and all trajectories reach the collection electrode. Figure 4.15 show S-curves for each detector. Both S-curves are almost identical except for a 0.3 volt shift of the S-curve from Tee's detector behind that from Fentem's

Transport
Efficiency

Error Option for the Fentem Detector

Figure 4.10



Equipotentials of the Pentem Detector

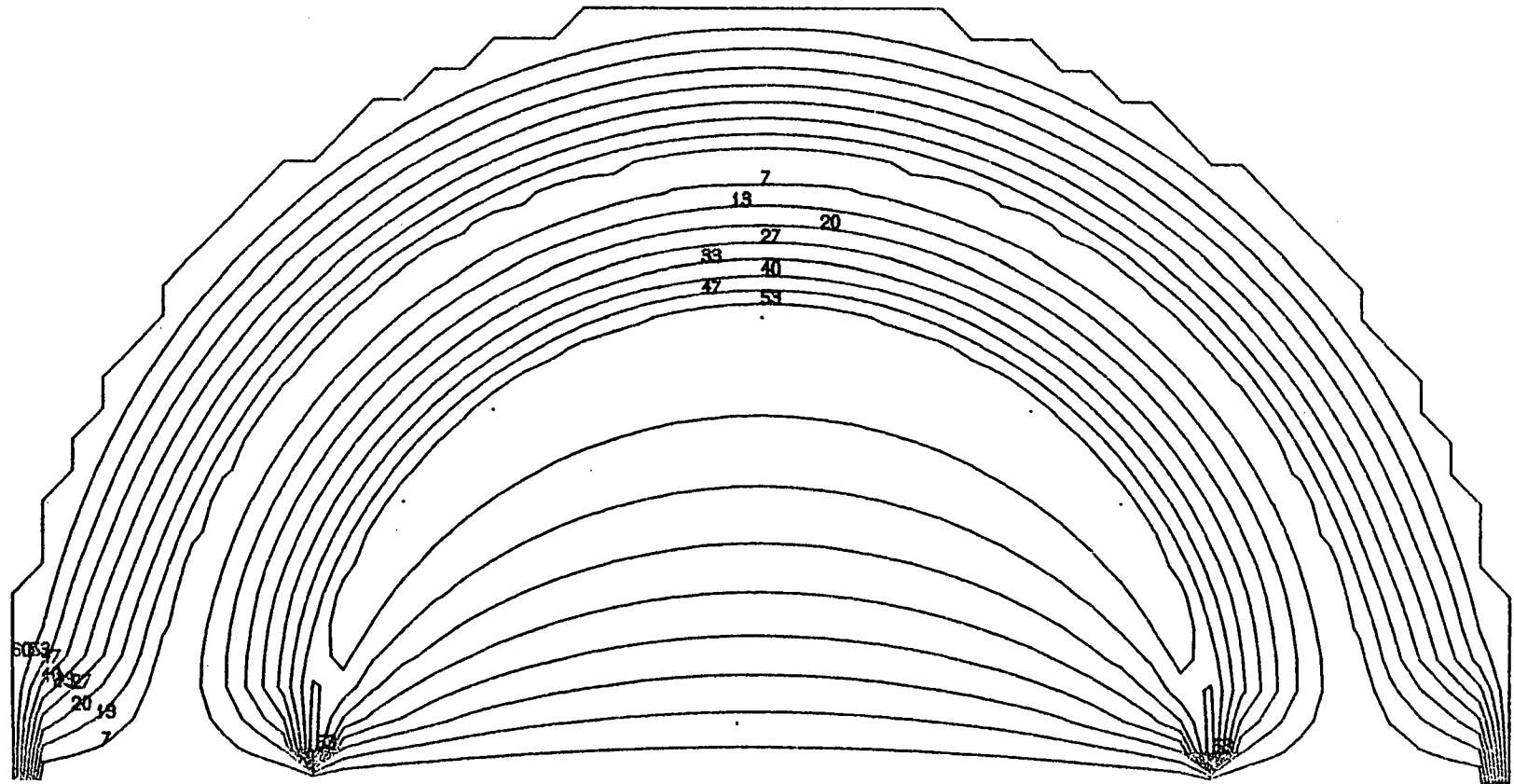


Figure 4.11

Equipotentials of the Tee Detector

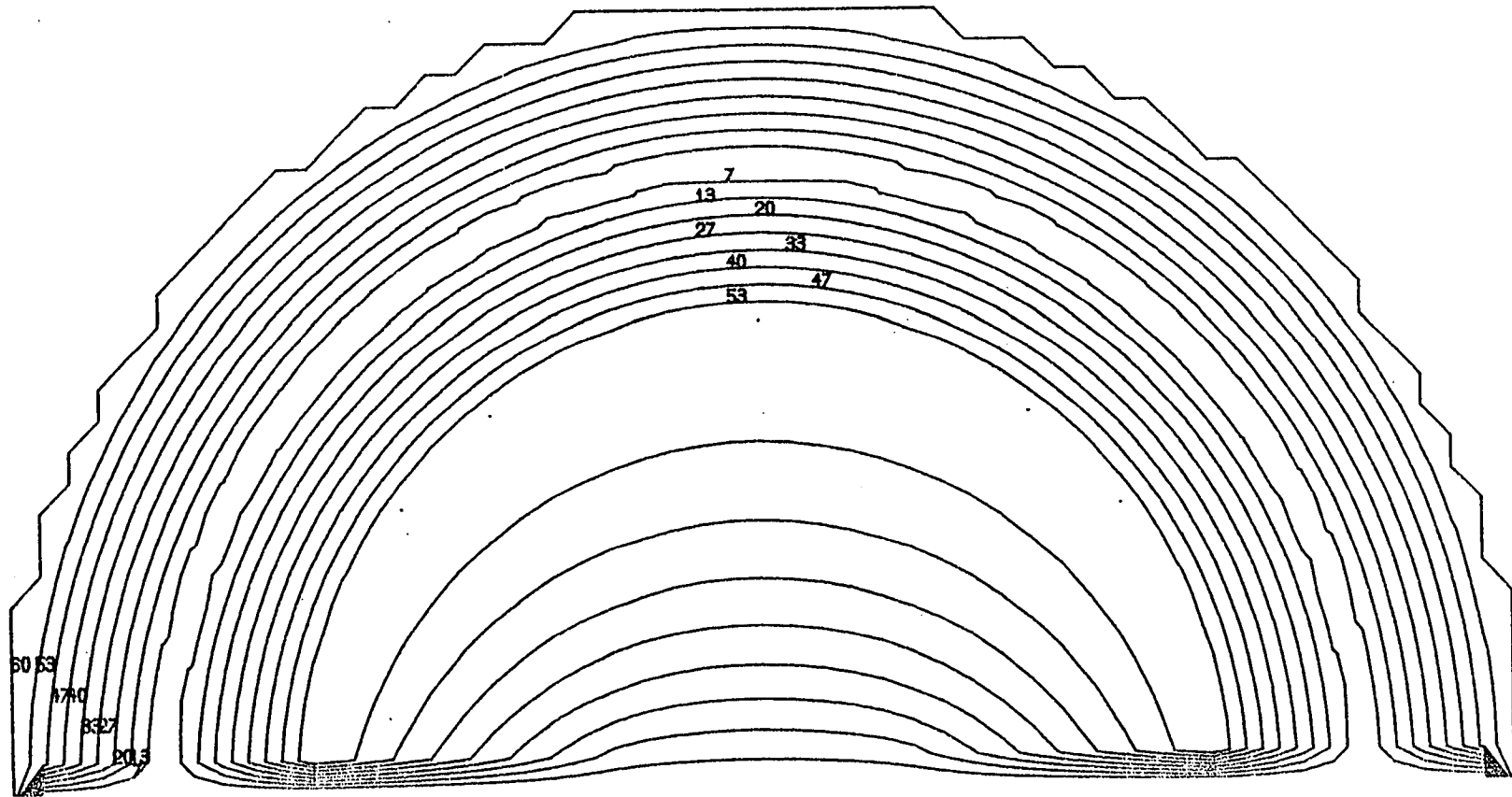
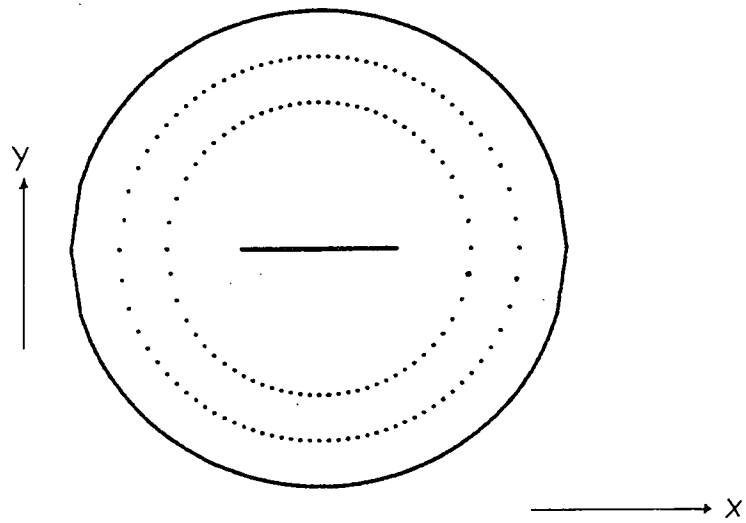
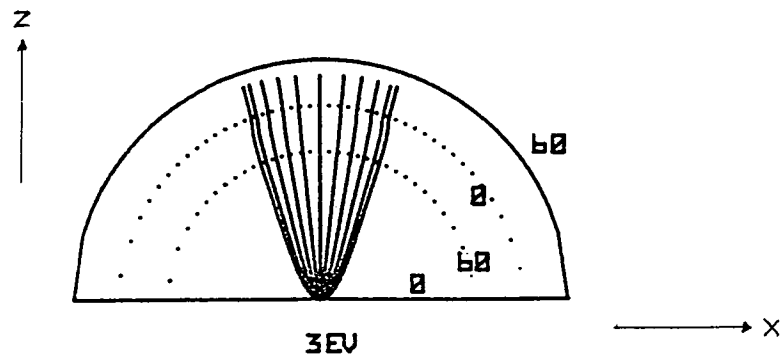


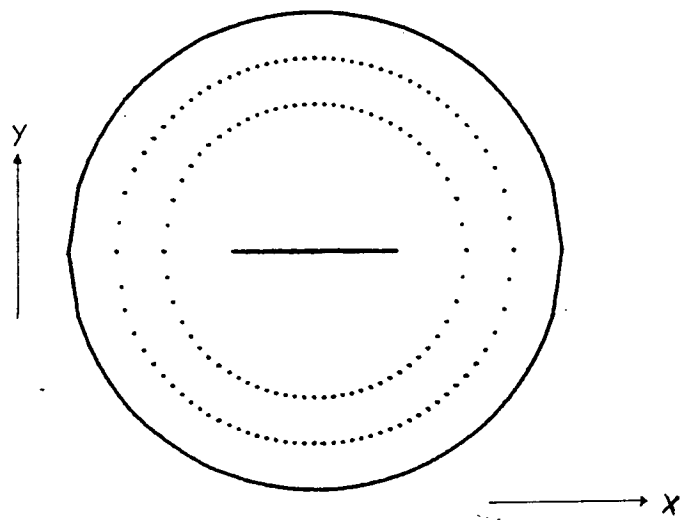
Figure 4.12



Trajectories Through Fentem Detector

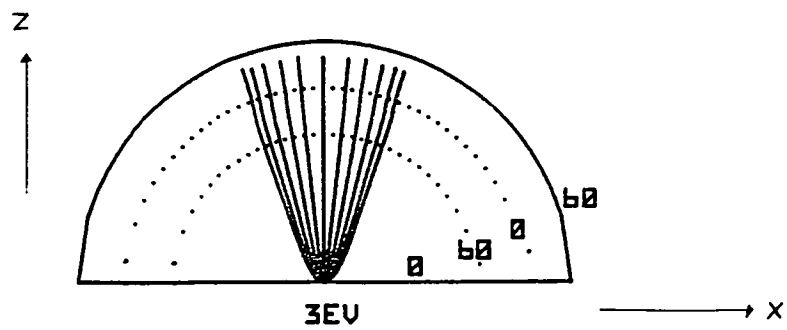
Figure 4.13





Trajectories Through Tee Detector

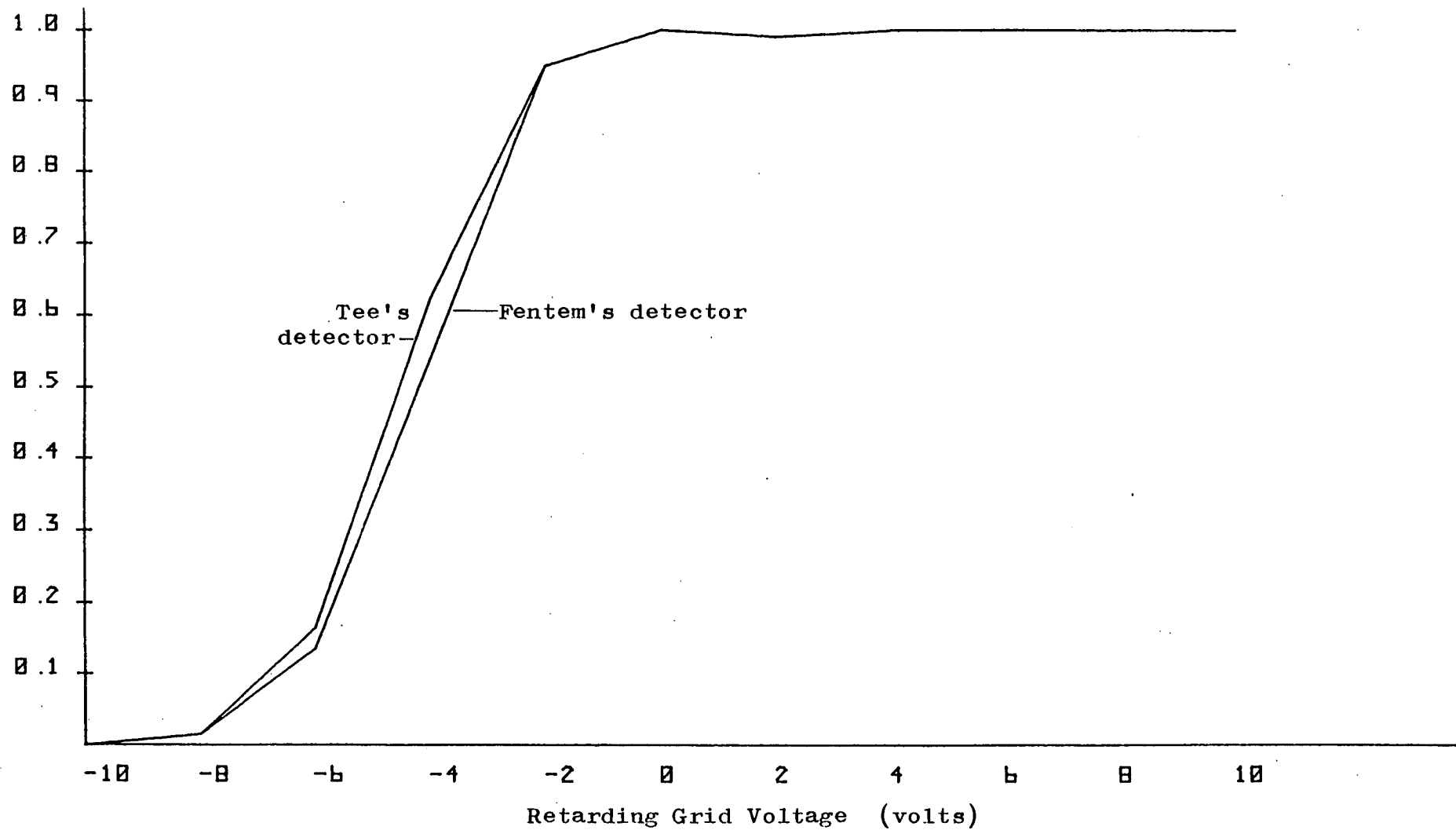
Figure 4.14



Transport
Efficiency

Comparison of S-curves for the Fentem and Tee Detectors

Figure 4.15



detector. As expected Figure 4.15 shows that both detectors have high transport efficiencies; 100% for electrons with energies below 12eV. Their output currents however in practice are very small (1-10nA). This is due to their method of collecting electrons on a conducting electrode as opposed to using the normal scintillator/photomultiplier arrangement. Hence in this case ideal or theoretical efficiency does not yield important information on the normal operation of both hemispherical detectors.

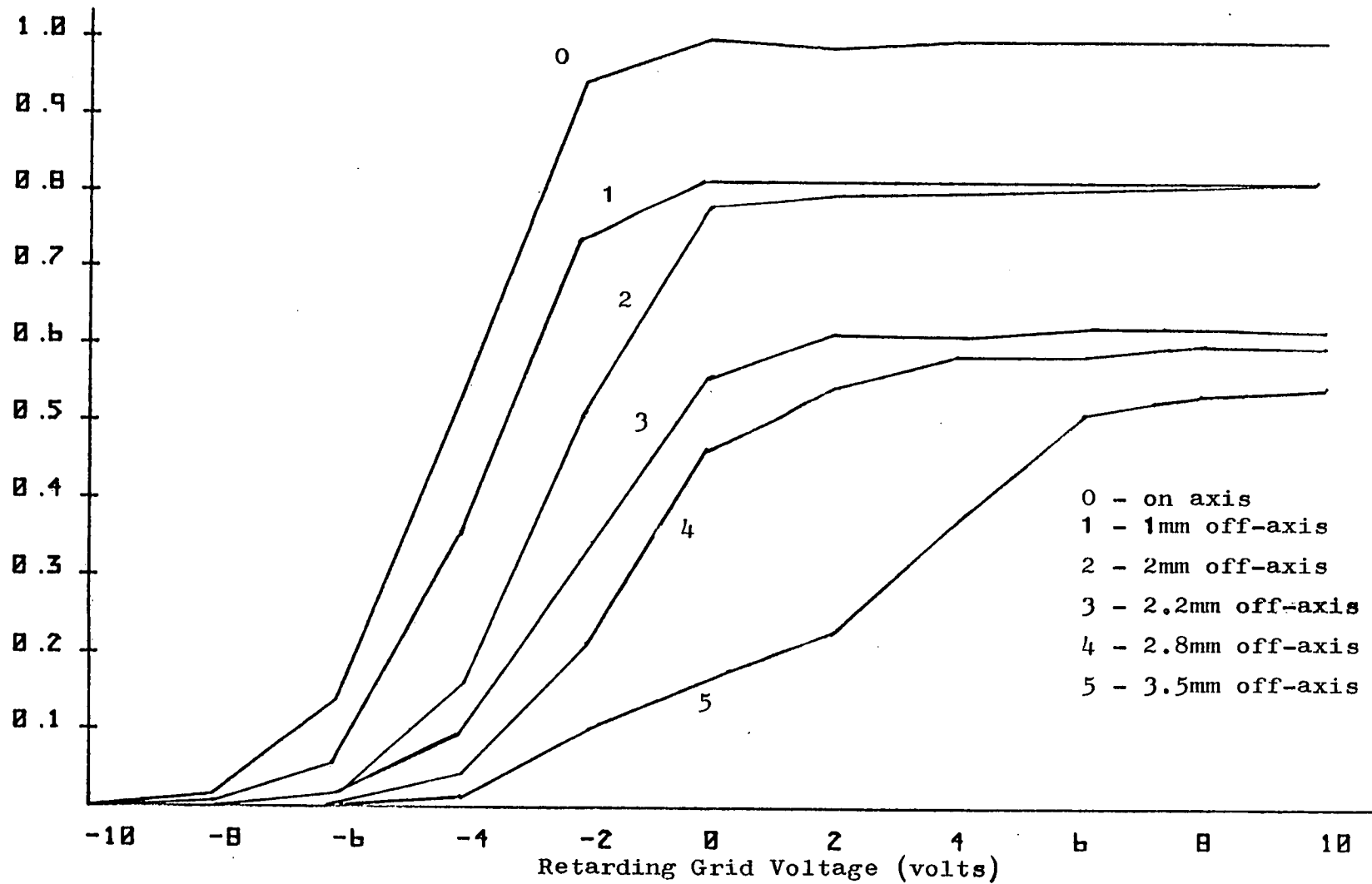
4.6.2 Off-axis electrons

Different S-curves were calculated for different radial positions on the specimen of Fentem's detector. Figure 4.16 shows S-curves plotted for off-centre distances of 0, 1, 2, 2.2, 2.8 and 3.5mm. As the radial distance of the emission point increases its S-curve drops in height and shifts to the right. At a distance 3.5mm from the specimen centre the S-curve is reduced to approximately 50% of its original height and has shifted more than 4 volts at its base and greater than 7 volts at its top. Figures 4.17(a-c) show electron trajectories at 2mm, 2.8mm and 3.5mm respectively from the specimen centre. These Figures show that off-axis electrons experience forces which attract them towards the central axis and hence prevent them from traversing the retarding grid; all electrons in Figures 4.17(a-c) start with an energy of 3eV. The above results show that S-curves from different specimen positions cannot be directly compared to yield accurate voltage contrast information. It is suggested that the primary beam remain on the detector's central axis and the specimen be moved if an off-axis measurement is required.

S-curves for Off-axis Positions in the Fentem Detector

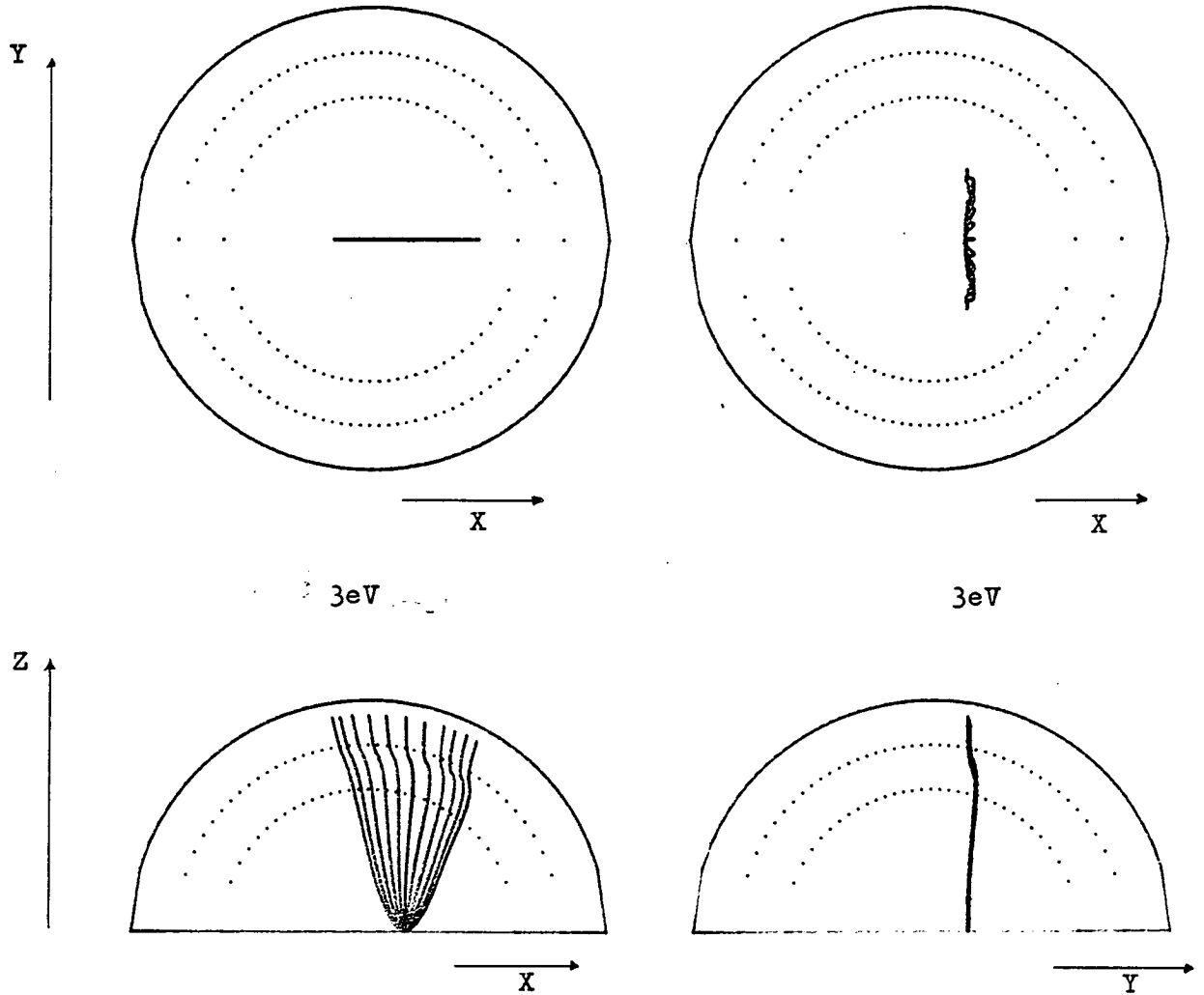
Figure 4.16

Transport
Efficiency



Electron trajectories for a 2mm off-axis position
in the Fentem Detector with an emitted energy of 3eV

Figure 4.17(a)



3eV

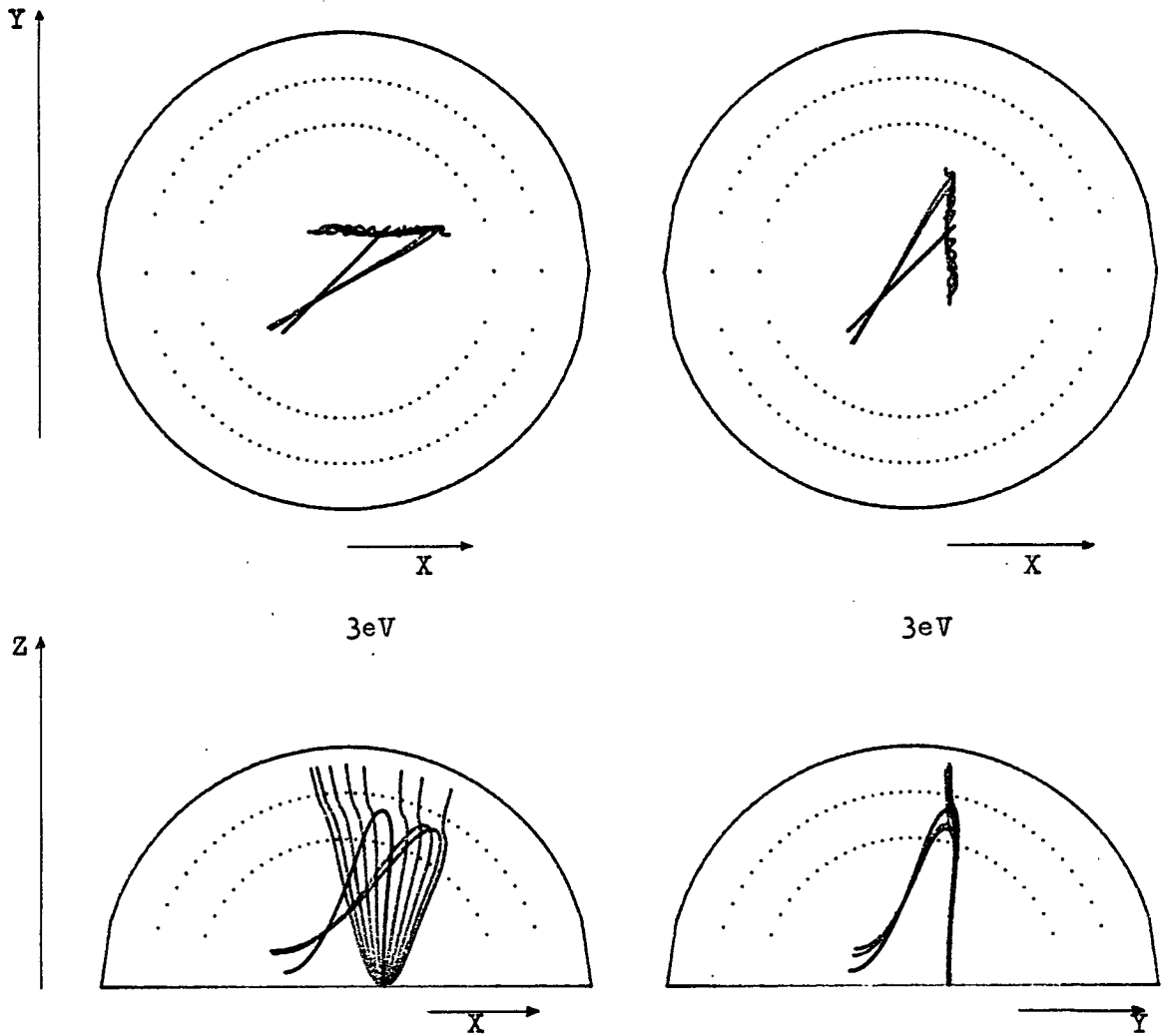
3eV

Emission in the Z-X Plane

Emission in the Z-Y Plane

Electron trajectories for a 2.8mm off-axis position in the Femtem Detector with an emitted energy of 3eV

Figure 4.17(b)

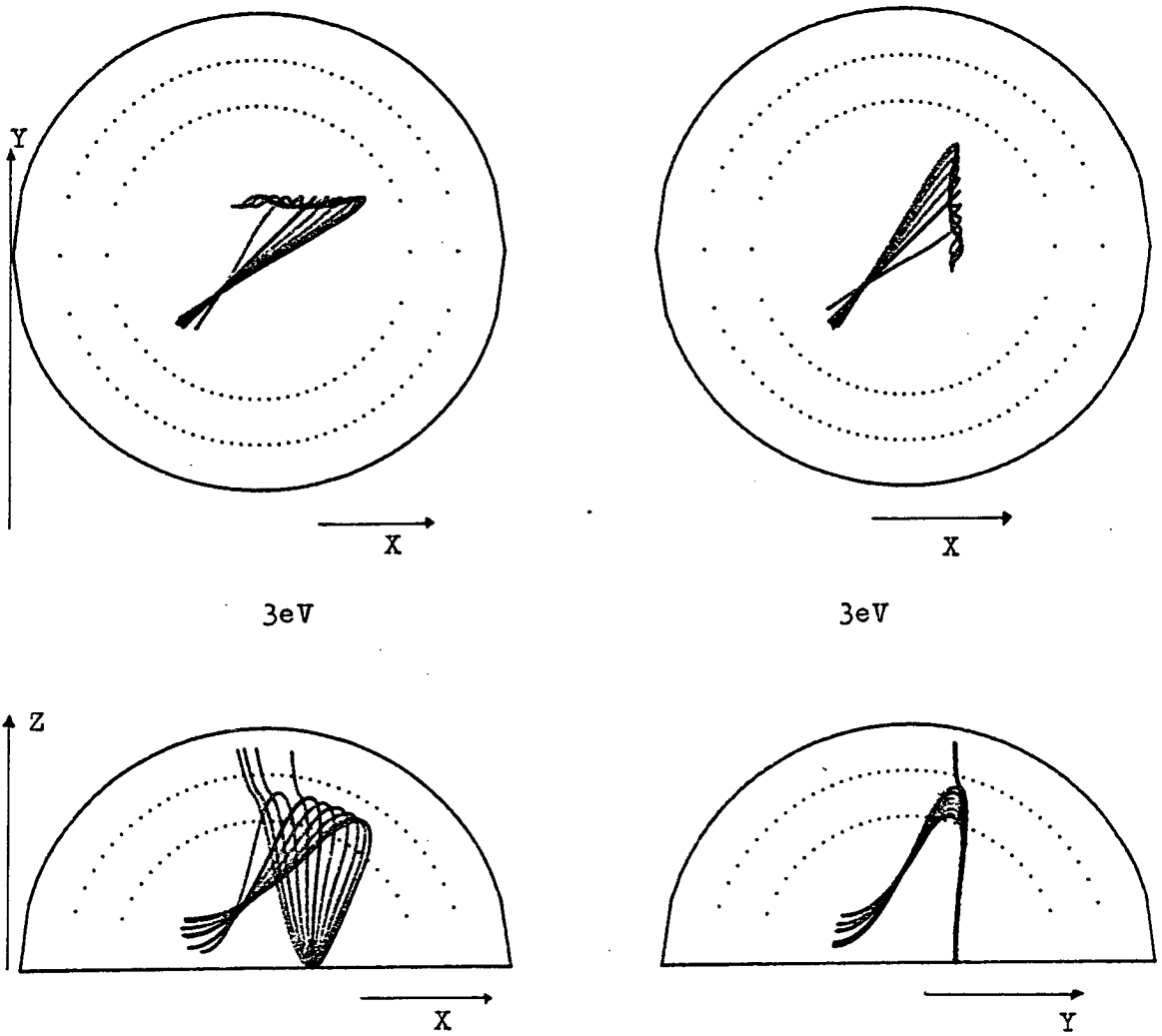


Emission in the Z-X Plane

Emission in the Z-Y Plane

Electron Trajectories for a 3.5mm off-axis position in
the Fentem Detector with an emitted energy of 3eV

Figure 4.17(c)



Emission in the Z-X Plane

Emission in the Z-Y Plane

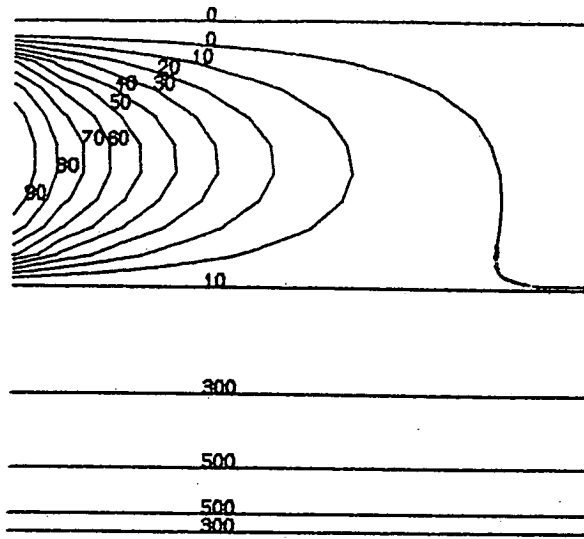
4.7 Results on the Feuerbaum Detector

4.7.1 Electrons Leaving Specimen Centre

A 14 by 14 by 21 relaxation mesh was used to find the potential distribution in the Feuerbaum Detector. Figure 4.18 shows equipotential lines for a central vertical cross-section through the detector, this cross-section was made in the Z-X plane. As expected Figure 4.18 depicts uniform retarding and extracting fields and shows the penetration of the deflection field reaching the outer walls of the detector.

The electron trajectory step size was optimised for values below 0.5(SLT>2) and is shown in Figure 4.19.

Figure 4.20(a) shows electron trajectories plotted through the detector with an initial energy of 3eV. For simplicity electron emission was divided into two cases; emission in the Z-X plane and emission in the Z-Y plane. Figure 4.20(a) shows that all 3eV electrons reach the deflecting gauze. Figures 4.20(b) and 4.20(c) similarly depict electrons with initial energies of 6eV and 10eV respectively. Approximately 10% of electrons at 6eV are absorbed into the wall opposite the deflecting gauze while 20% of 10eV electrons are lost this way and all electrons below 12eV in the Z-Y plane reach the deflecting gauze. Figures 4.20(a-c) show this detector has a high transport efficiency for electrons below 12eV. Figure 4.20(d) shows the energy transport efficiency curve for the detector and gives an overall transport efficiency of 96%. This



Equipotentials for the Feuerbaum Detector

Figure 4.18

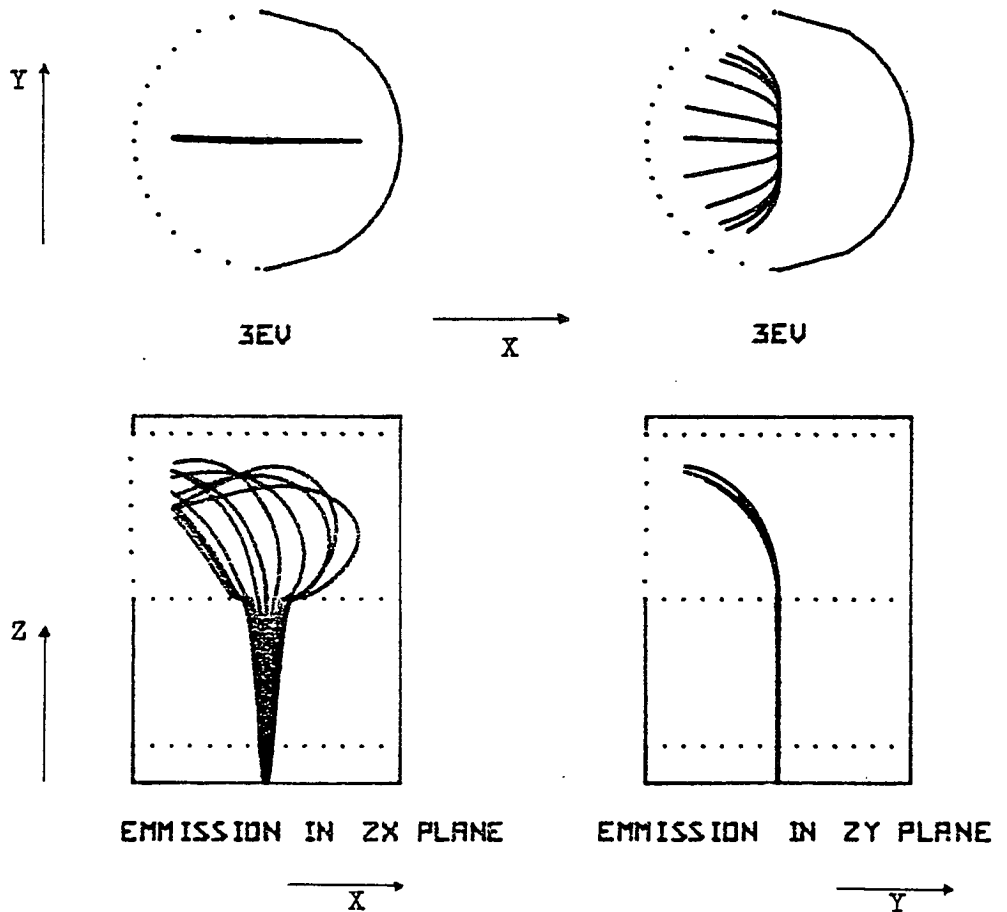


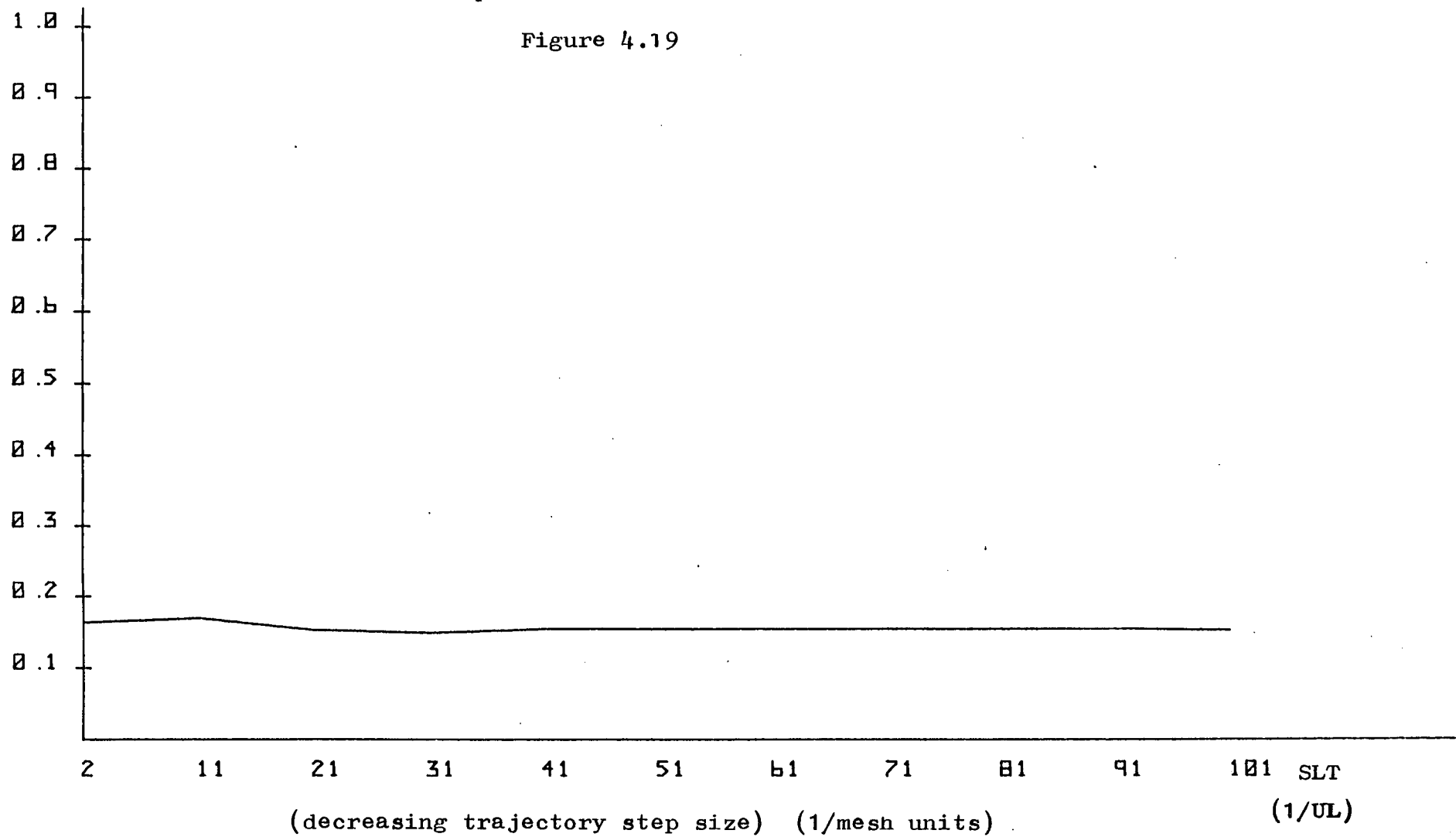
Figure 4.20(a)

Trajectories for the Feuerbaum Detector for electrons with emitted energy of 3eV

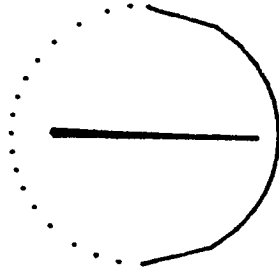
Transport
Efficiency

Error Option for the Feuerbaum Detector

Figure 4.19

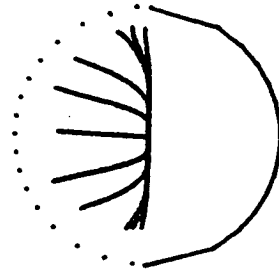


Trajectories for the Feuerbaum Detector for electrons with
emitted energies of (b) 6eV
(c) 10eV

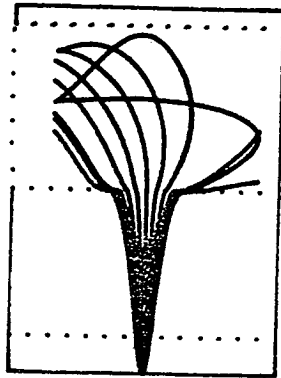


6eV

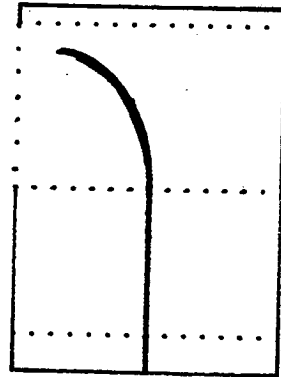
Figure 4.20(b)



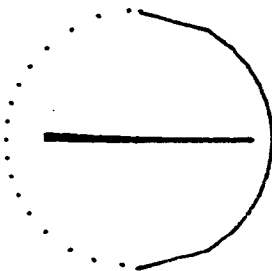
6eV



ZX PLANE

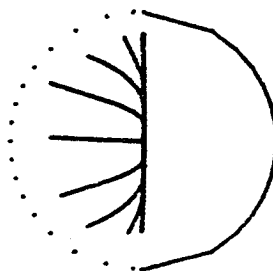


ZY PLANE

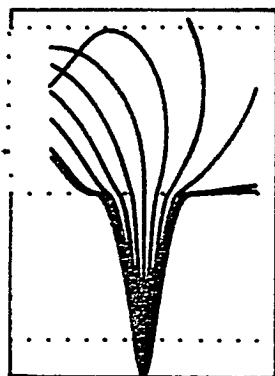


10eV

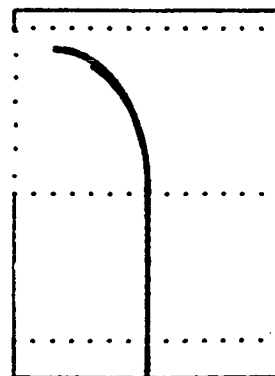
Figure 4.20(c)



10eV



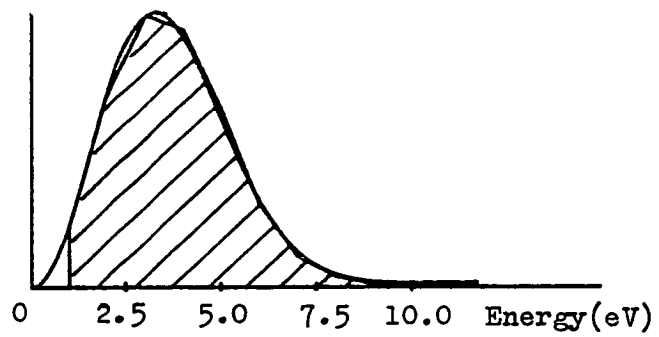
ZX PLANE



ZY PLANE

Energy Analysis of the Feuerbaum Detector
Figure 4.20(d)

Relative number of electrons



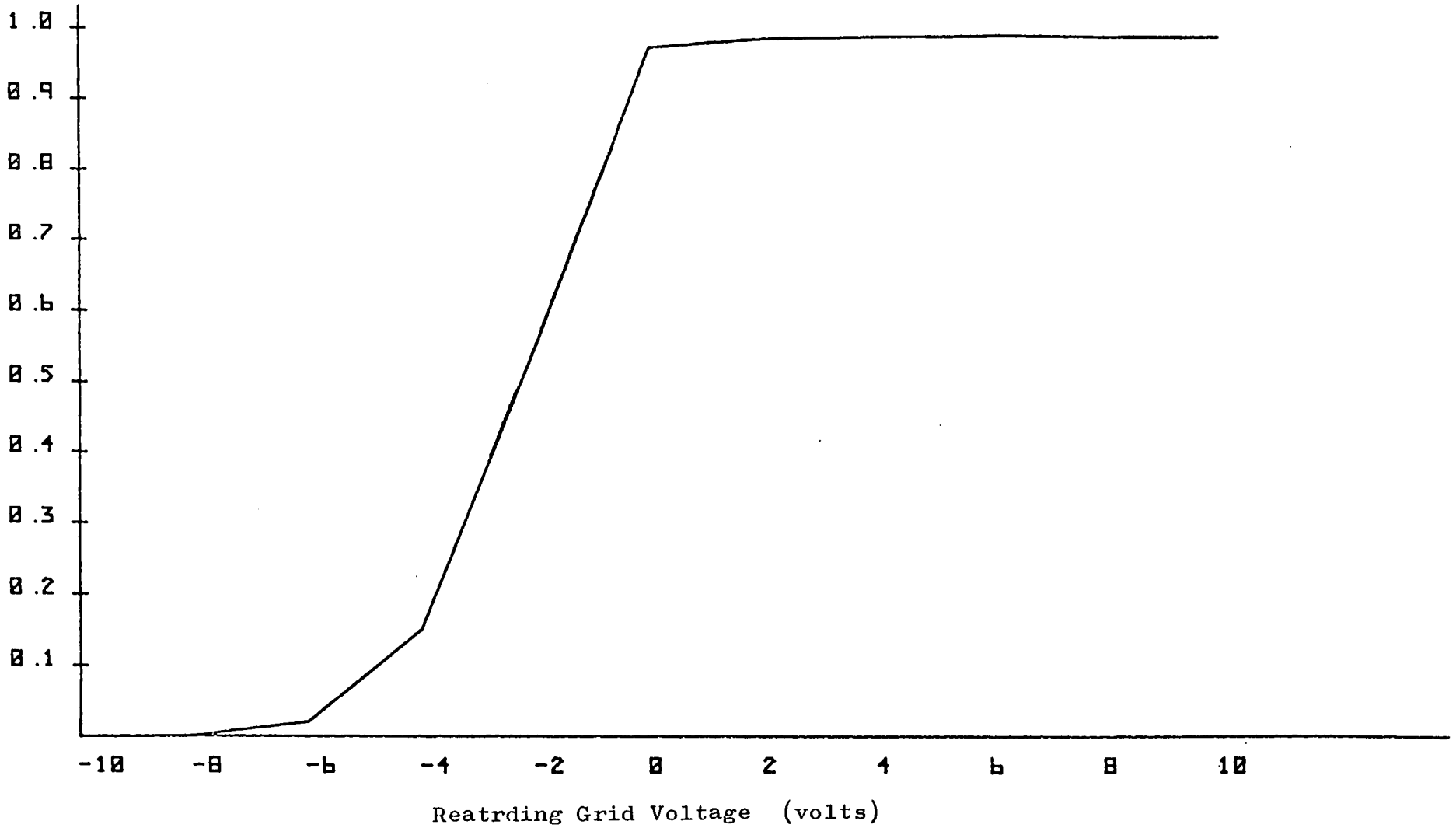
Transport Efficiency = 0.975

is also confirmed by the S-curve shown in Figure 4.21, Figure 4.21 shows the S-curve is close to the ideal 'S'-shape. Hence the Feuerbaum detector is seen to have a high ideal transport efficiency and a linear S-curve response. It must be remembered that the complete collection system was not simulated and that many electrons which reach the deflection gauze may not reach the scintillator. This is particularly true for electrons in the Z-Y plane which reach the deflection gauze with a large velocity in the Y-direction, these electrons are often close to the outer walls and may be absorbed into these walls. An estimated reduction of at least 5% in transport efficiency may result if the scintillator was incorporated into the simulation work.

Transport
Efficiency

S-curve for the Feuerbaum Detector

Figure 4.21



4.7.2 Off-axis electrons

Figure 4.22 shows different emission positions from the base of the Feuerbaum detector, S-curves were generated for each position. It was found that S-curves for positions 1-9 were identical to the S-curve obtained from the central axis position, labelled 15 in Figure 4.22. Figure 4.23 shows that as the emission position moves to the right (positions 10,11,12) its corresponding S-curve drops in height and becomes non-linear. For position 12, 1.5mm off-centre on the X-axis, the S-curve drops 8 to 25% in height. Figure 4.24 shows S-curves for positions 15,13,14. Both positions 13 and 14 are an equal distance off-centre yet the S-curve for position 14 has been reduced by 10 to 30% in height and the S-curve for position 13 is almost identical to that from position 15 (central axis). The results in Figures 4.23 and 4.24 show that the field of view is only restricted significantly in the positive X-direction. Off-axis distances of up to 1.5mm can be examined on the other axis without significant alteration in the S-curve. However, a position 0.5mm off-centre on the positive X-axis causes an 8% reduction in the output current at 0 volts on the retarding grid.

Summary

Both analytical and numerical solutions to the potential distribution inside the Fentem and Feuerbaum detectors were given. Both detectors are seen to yield higher transport efficiencies and give greater linearity in their S-curves than those obtained from the Dinnis or Lintech detectors simulated in Chapter 3.

Specimen Plane for the Feuerbaum Detector

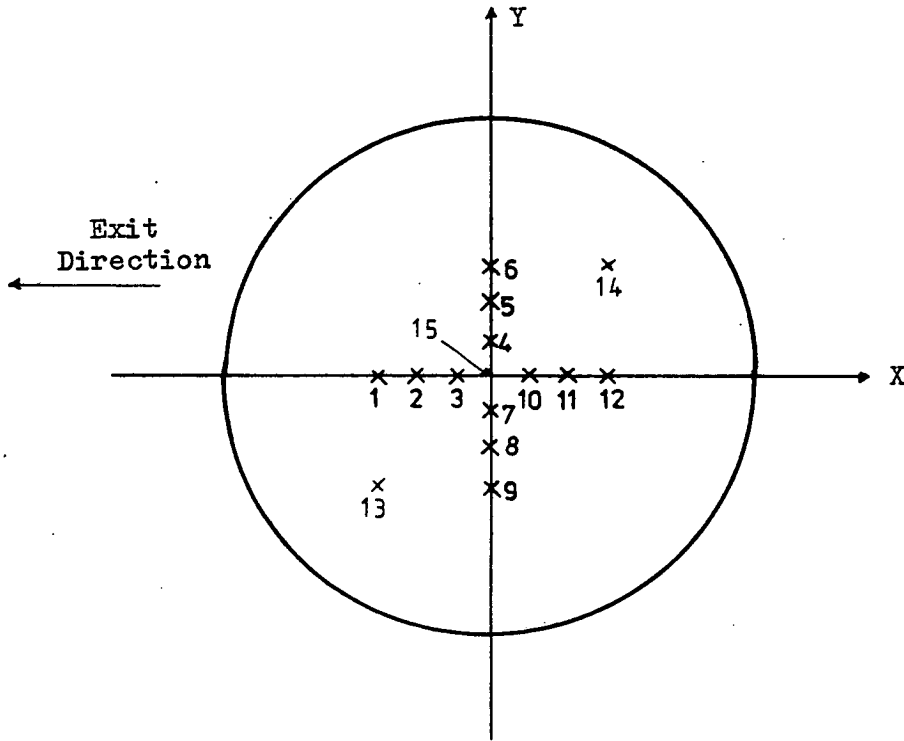
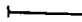
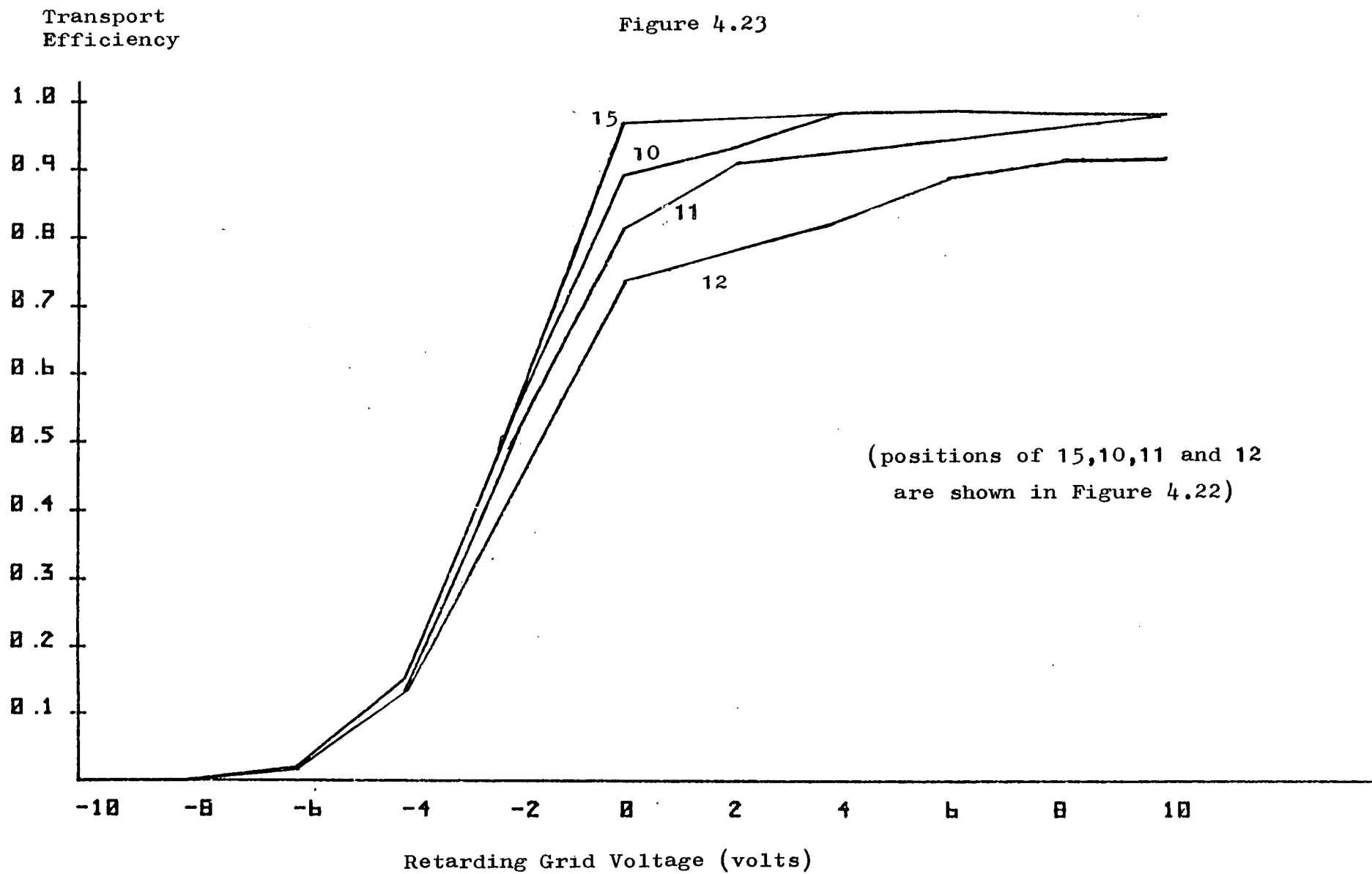


Figure 4.22

Scale: 
1mm

S-curves for Off-axis Positions in the Feuerbaum Detector

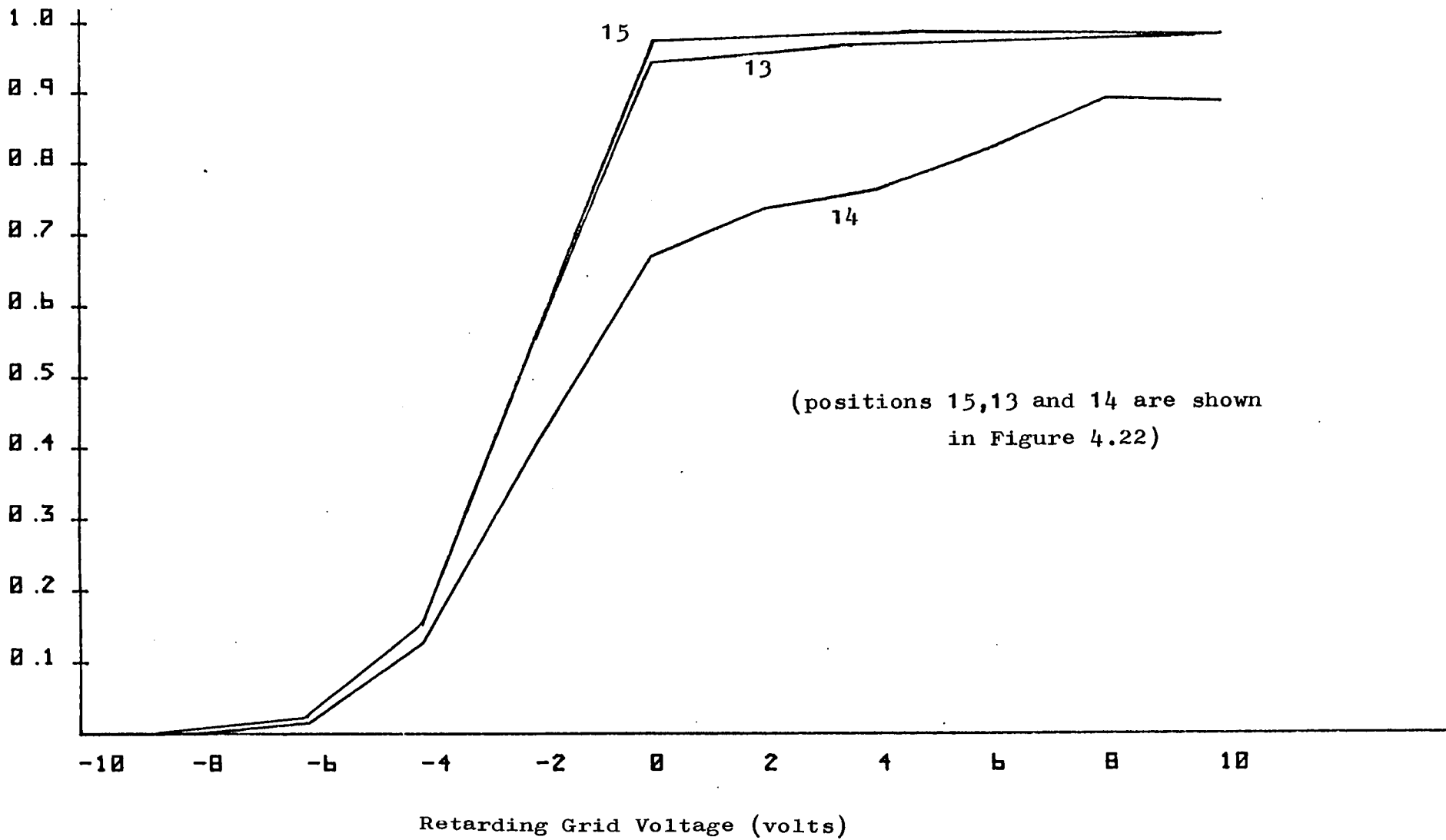
Figure 4.23



Transport
Efficiency

S-curves for Off-axis Positions in the Feuerbaum Detector

Figure 4.24



CHAPTER 5SURFACE FIELDS5.1 Introduction

To make a more realistic study of electron detectors it was decided to analyse the effect of surface fields. This effect imposes significant limitations on the performance of any detector (Fujioka et al(1981)). Separate studies on the nature of surface fields were also carried out. Other second order effects such as charging of dielectrics and tertiary electrons also affect a real measurement from a voltage detector; these effects, however, are more difficult to model and are outwith the scope of the present programs.

The surface field problem was briefly discussed in Chapter 2. The effect of surface fields on the practical results of a detector has been acknowledged by many (Fujioka et al(1981), Feuerbaum(1979), Tee(1975) and Hannah(1974)), yet their theoretical study has been made by only a few, (Menzel(1982) and Fujioka et al(1981)). The aim of this work was to investigate surface fields on MOS devices and study their effect on some detectors. Like previous programs, results were based on the plotting of electron trajectories. To do this the electrostatic potential distribution near the specimen had to be solved.

5.2 Field Distributions Near a Specimen

5.2.1 Introduction

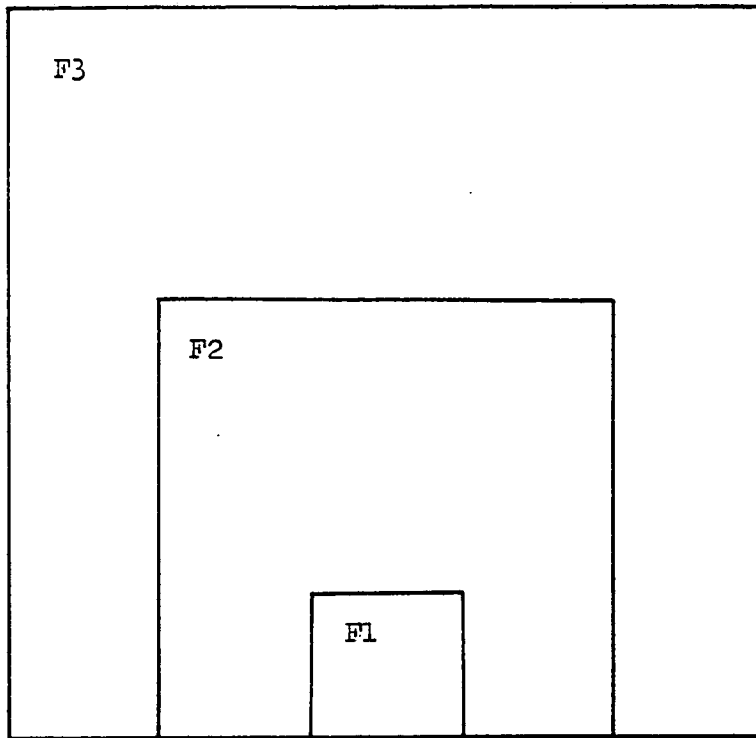
There are many ways to approach the problem of finding potential distributions near a specimen. For specimens with relatively simple surface layouts, analytical methods can be used, an example of this is the expression found by Wells (reviewing Macdonald(1970)) for a P-N junction. However, the surface fields created by MOS devices are too complex for current analytical methods and hence numerical methods were used. Special techniques even in the category of numerical methods are required, since the potential problem of surface fields is more difficult than previously described field problems. This is due to the fact that surface conductors can be very close together (eg, a few microns) whereas the distance to a detector's nearest electrode is typically a thousand times greater (a few millimeters). Hence while the numerical technique used must resolve field changes between the specimen and detector it must also resolve very sharp field changes at the specimen's surface. The finite-element method can deal with such large variations of field strengths in a single potential problem, whereas cumbersome modifications in the finite-difference method are required to achieve the same result. However, it was decided to use the finite-difference method since the time required to develop the appropriate finite-element program would exceed the time required to modify and develop existing finite-difference programs.

5.2.2 Techniques of Graded Meshes in the Finite-Difference Method

Two approaches in solving surface field distributions using the finite-difference method were considered. The first approach was used by Hannah(1974) and consists of using a method of mesh expansions. Figure 5.1 shows the use of three different meshes, each mesh has the same resolution but represents a different area in the surface field problem. The different field meshes are relaxed successively, the boundary conditions for an inner field mesh are found by using values from its surrounding outer mesh. The potential values in a mesh are only accurate in the area covered by its inner mesh; this complicates the plotting of electron trajectories. This method of successive mesh expansions was seen as unnecessarily complicated and hence the other approach of graded meshes was used.

The method of graded meshes consists of using adjoining field areas with different mesh resolutions, in this case three different meshes were used. Figure 5.2 shows the mesh-layout used to model surface fields in a retarding field detector. The shaded areas represent areas for which the electric fields are assumed to be constant. The three surface meshes only extend to the extraction grid and the electric field between the extraction grid and retarding grid is assumed to be constant. The resolution and size of each mesh are specified interactively by the user.

Method of Expanded Meshes

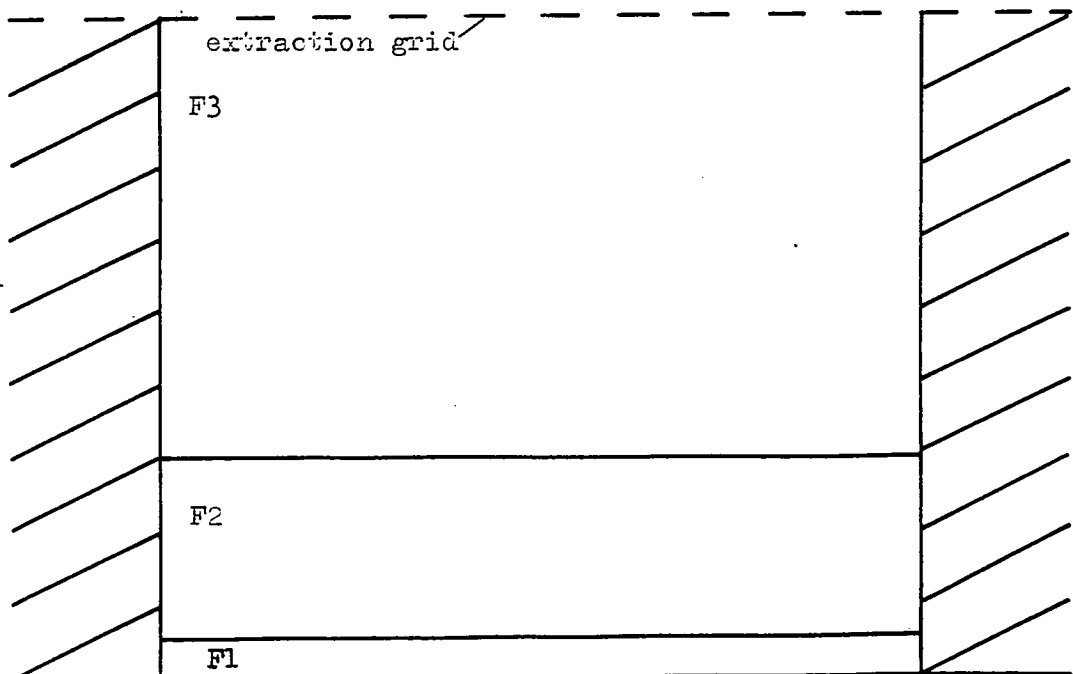


Specimen

Figure 5.1

(not to scale)

Graded Meshes



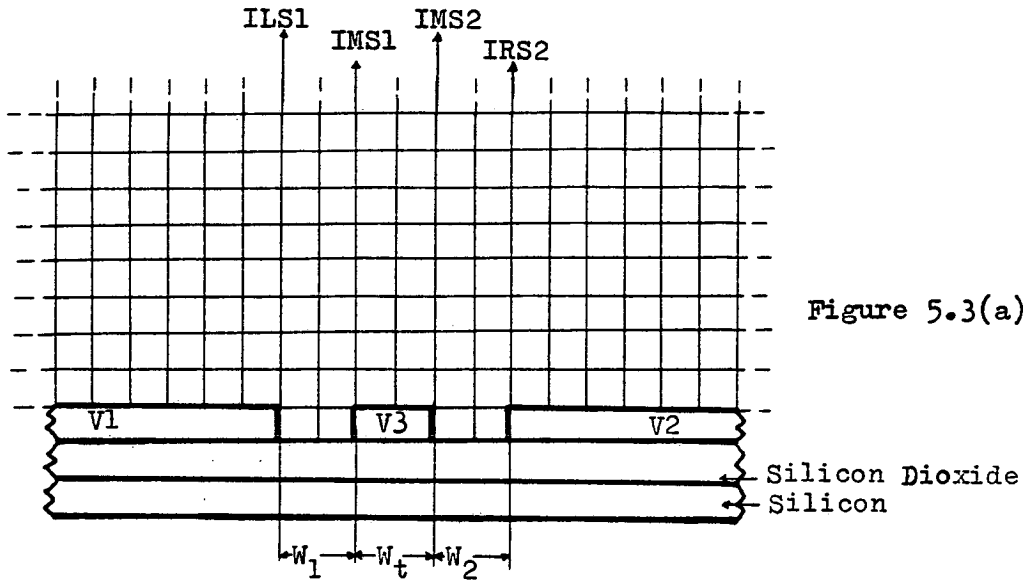
Specimen

Figure 5.2

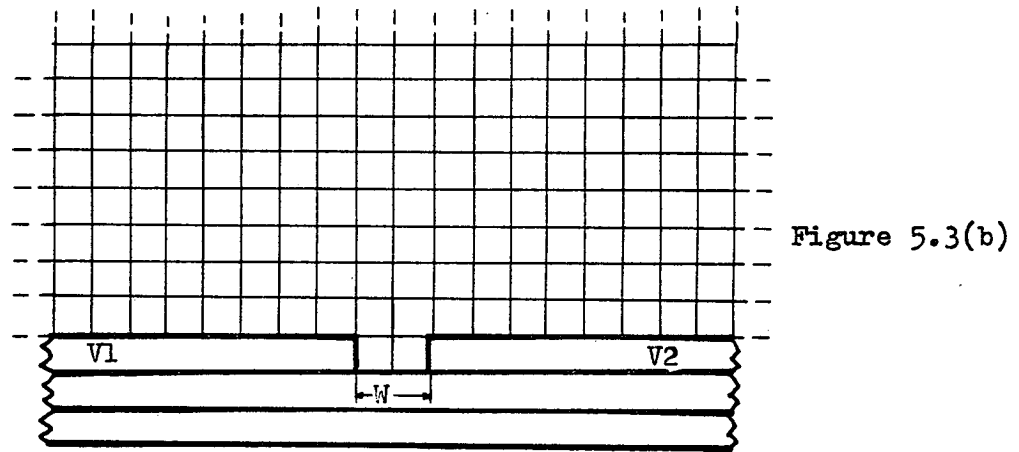
5.2.3 Surface Mesh

Different MOS layouts are prescribed by the programmer and act as boundary conditions on the surface mesh F1. The specimens that are modelled consist of three layers, aluminium on silicon dioxide on a grounded silicon substrate with both the aluminium and silicon dioxide layers one micron thick. Figures 5.3(a) and 5.3(b) show two standard specimen configurations which commonly occur in MOS devices. These were specified on the mesh F1. Figure 5.3(a) shows the cross-section of a track between two large conductors. The sizes of gaps between conductors and track-widths are determined by ILS1, IMS1, IMS2, IRS2 which are specified by the programmer. Their voltages V1, V2, V3 are also input by the programmer. Figure 5.3(b) shows the cross-section of a single gap between two large conductors, in this case IMS1=IMS2. The resolution of mesh F1 is given by NX1, NZ1 and a typical relaxation star inside this mesh is shown in Figure 5.3(d). HZ1 is the size of the arm in the Z-direction and is fixed to be one micron. HX1 is chosen to be commensurate with the dimensions of the surface layout. The finite-difference star existing at the silicon dioxide/air interface is shown in Figure 5.3(c) and a modified residual equation for such stars is given in Appendix(5). The boundary conditions at the sides of F1 are interpolated from the two top corner potentials down to the conductors V1 and V2. The conductors V1 and V2 are assumed to be infinitely wide, hence keeping the condition of constant electric fields at either side of mesh F1.

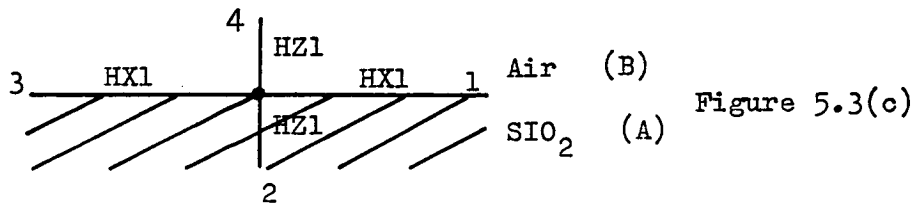
Two-Gap Layout



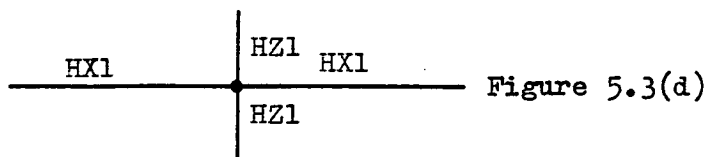
Single-Gap Layout



Star at Silicon/Dioxide Interface



Normal Star in F1



The quantities ILS1, IMS1, IMS2 and IRS2 must be carefully varied to cover many types of surface layouts. In general four different surface layouts can occur on an MOS device, the first of these has already been mentioned and is the single gap between two infinite conductors shown in Figure 5.3(b). The gap width W can vary from a few microns to hundreds of microns and this case can easily be modelled on F1 by choosing a suitable $HX1$. Obviously the more mesh squares in the gap the more accurate the field description. However, $NX1$ cannot be made too large if the programs are to remain interactive, hence a compromise between accuracy and program run-time has to be found. The second mesh layout shown in Figure 5.3(a) is a track between two infinite conductors. In this case the track width Wt is comparable in size to the gaps $W1$ and $W2$ between the track and its neighbouring conductors. This situation can again be easily modelled by choosing an appropriate $HX1$. If $HX1$ is chosen to model gaps $W1$ and $W2$ accurately it will also automatically model the field above the track accurately since $Wt=W1=W2$. The next surface layout has the track width Wt , much greater than the gaps $W1$ and $W2$. In these cases the mesh size in the X-direction would need to exceed one hundred, clearly an impractical number, and hence this layout cannot be modelled by the graded mesh technique described.

In the last configuration Wt is much greater than $W1$ and $W2$. To describe the sharp field changes around the track while at the same time covering changes in the gaps $W1$ and $W2$ would again require $NX1$ to be impractically large. A typical example of this would be a three micron track whose nearest conductors are a distance of 100

microns away. For the last two surface layouts a more comprehensive relaxation technique is required. The two latter cases are also examples where the finite-element method has advantages over finite-difference methods. The finite-element method can model sharp field changes around a small track while also modelling the influence of conductors from large distances.

5.2.4 Fields F2 and F3

Figures 5.4(a) and 5.4(b) show typical relaxation stars found in fields F2 and F3 respectively. HZ2 and HZ3 are specified by the programmer typically, $HZ2=5*HZ1$ and $HZ3=10*HZ2$, HX2 and HX3 are fixed to $HX2=2*HX1$ and $HX3=2*HX2$. Hence field meshes rapidly become coarser as they approach the extraction grid. The number of mesh lines in the horizontal direction is halved at each boundary, $NX2=(NX1-1)/2.+1.$ and $NX3=(NX2-1)/2.+1.$ Typical sizes of fields F1, F2, F3 may be (25,20), (13,5), (7,10) respectively.

5.2.5 Relaxation at Field Boundaries

At field boundaries three different types of mesh-stars are relaxed. Figure 5.5(a) shows the boundary between the fields F1 and F2. Diagonals in the coarser field, F2 are drawn in meshes nearest to the boundary and define points like C. Since Laplace's equation is invariant to rotational operations, then points like C can be relaxed and provide boundary conditions for nodes like A on the fine

Mesh Star in F2

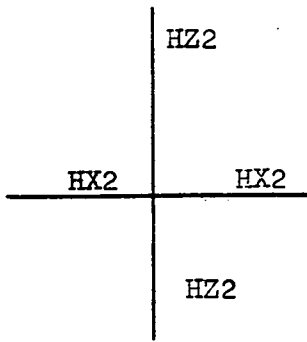


Figure 5.4(a)

Mesh Star in F3

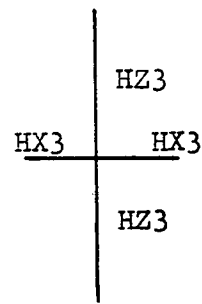


Figure 5.4(b)

Boundaries Between Fields

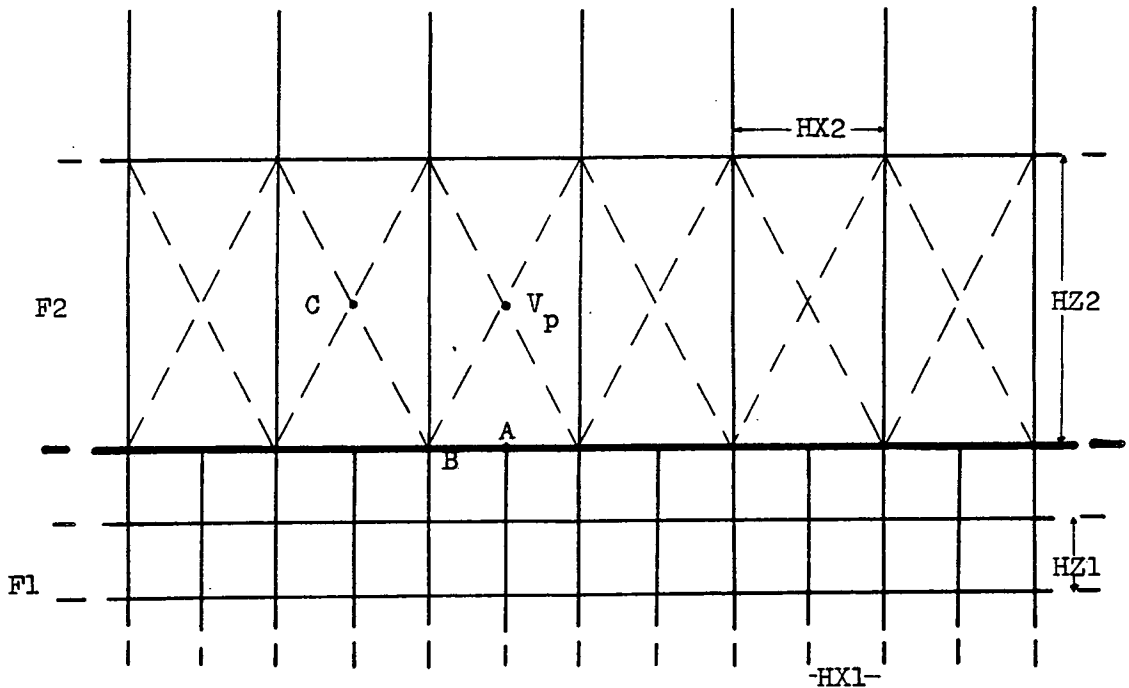


Figure 5.5(a)

Star at B

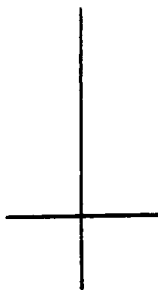


Figure 5.5(c)

Star at A

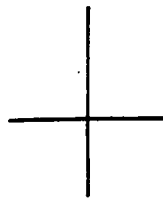


Figure 5.5(b)

Star at C

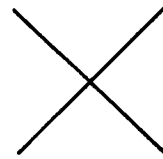


Figure 5.5(d)

mesh. The nodes like A and B are then both relaxed on the fine mesh. The mesh stars for nodes A, B and C are given in Figures 5.5(b-d). Relaxation at A and B both consist of computing residual equations of irregular stars. This is done by the normal method as described in Chapter 3; the boundary between F2 and F3 is treated in a similar way. The flow diagram in Figure 5.6 illustrates the overall technique.

5.3 Trajectory Plotting in Surface Fields

Special electric field routines for each mesh were written. At each trajectory step the electron position was noted and the appropriate electric field routine was called. The potential distribution for each field was stored in separate arrays. Once an electron's position was transformed on a particular mesh an appropriate interpolation routine within this mesh was called and then the electric field calculations were made. The flow diagram in Figure 5.7 illustrates this process, INTA1, INTA2, INTA3 are interpolation routines in meshes F1, F2, F3 respectively. The normal error-reducing techniques as previously described in Chapter 3 were used in the calculation of electric fields.

Relaxation procedure for Surface Fields

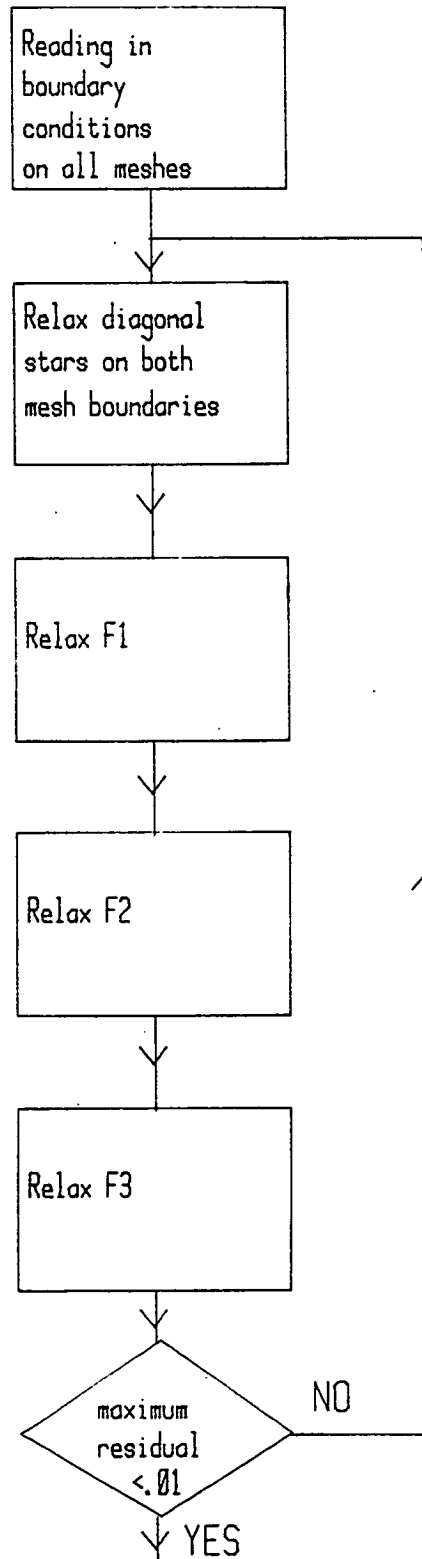
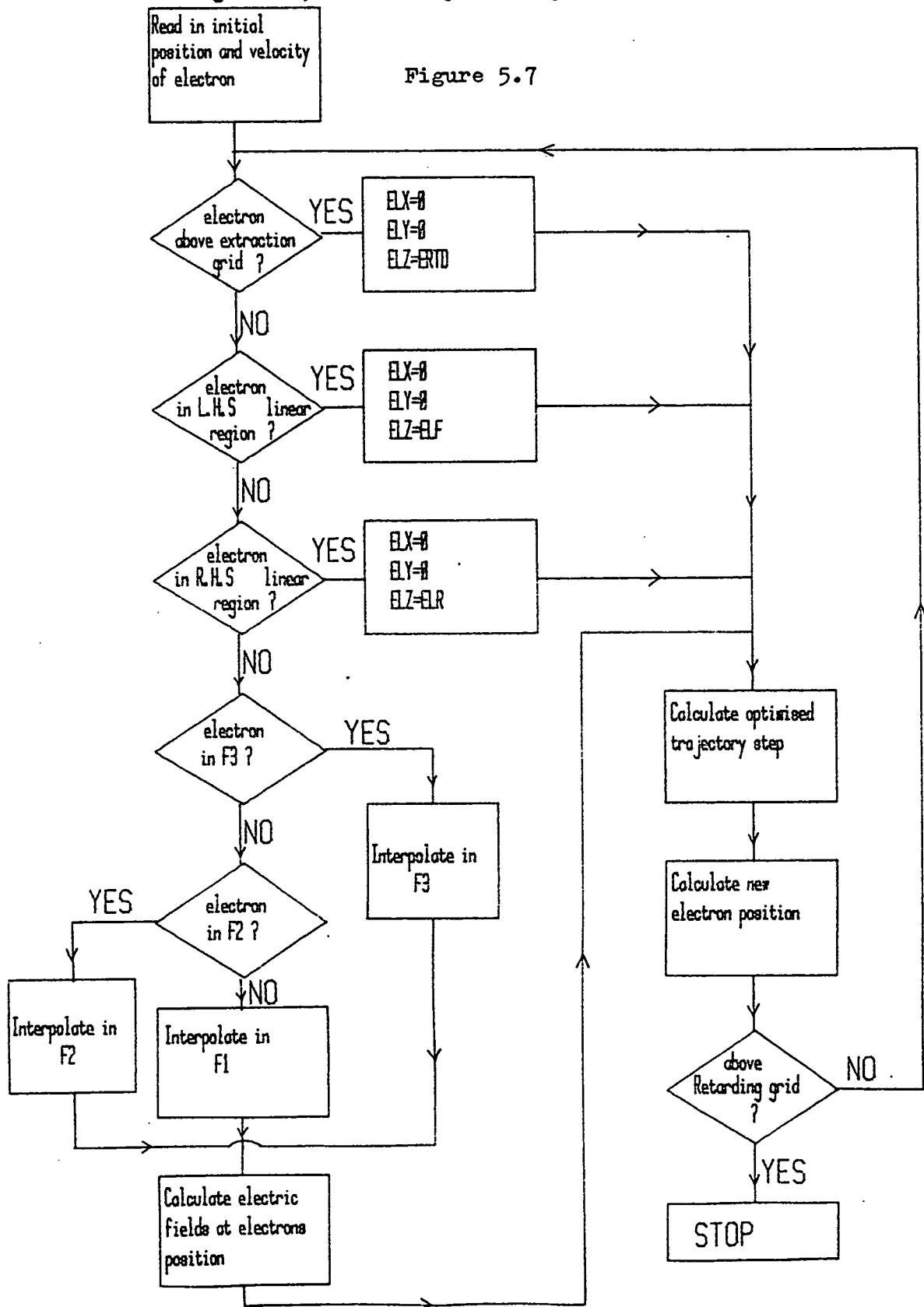


Figure 5.6

Trajectory Plotting through Surface Fields

Figure 5.7



ERTD - electric field between extraction grid and retarding grid
 ELF - electric field in the L.H.S linear region
 ELR - electric field in the R.H.S linear region

5.4 RESULTS ON SURFACE FIELDS

5.4.1 Two Electrode Structure with a 3 micron Gap

The first surface layout considered, consists of two infinitely wide conductors separated by a gap of 3 microns. The relaxation mesh sizes used for all surface layouts were 33 by 25 for F1, 13 by 5 for F2 and 7 by 10 for F3. The graph in Figure 5.8 shows that the output current stays constant for trajectory step of between 0.5 to 0.01. Hence large trajectory steps were used giving low computer run times.

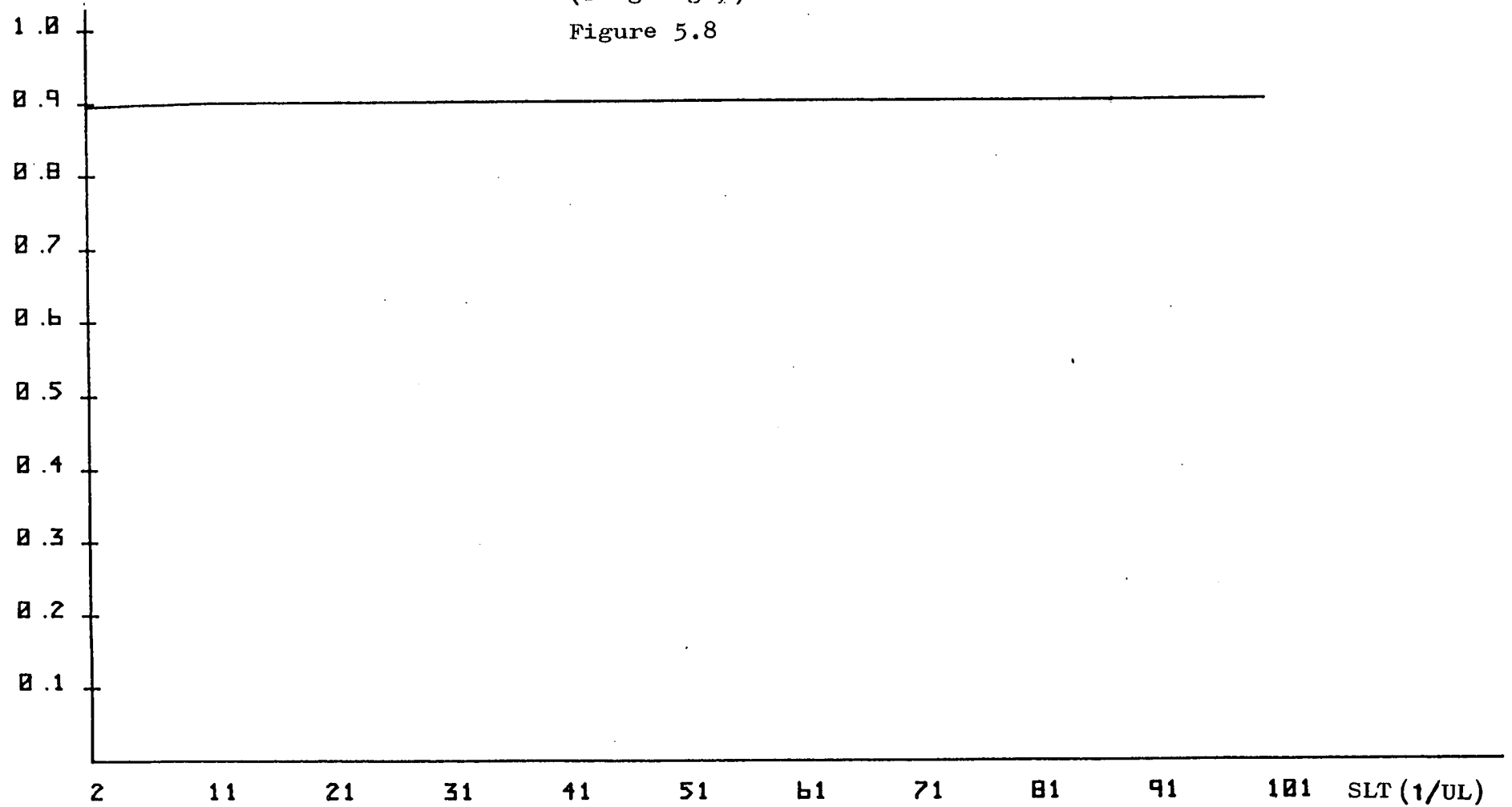
5.4.2 Positive Neighbouring Conductor

Figure 5.9(a) shows the equipotential lines for the 3 micron single gap layout with 0 volts on the left-hand side electrode and 5 volts on the right-hand side electrode.

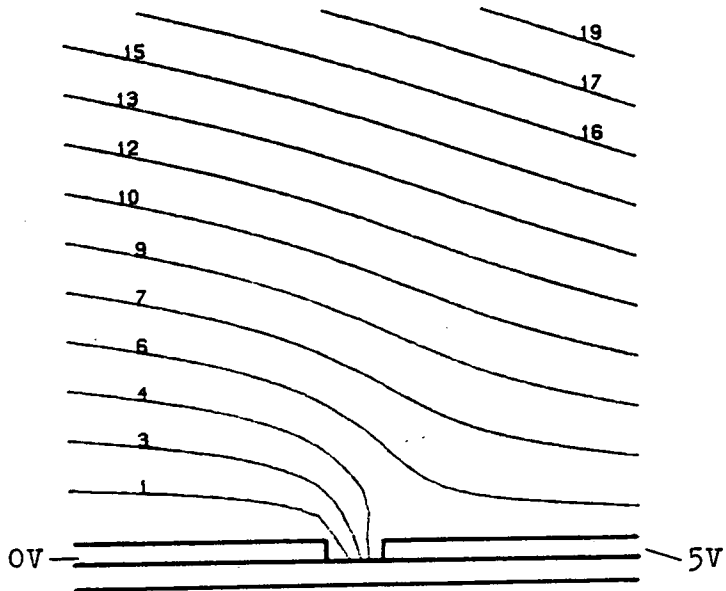
Electron trajectories with initial energies of 3eV, 6eV and 10eV are plotted in Figures 5.9(b-d) respectively, electron trajectories are first displayed in the surface mesh F1 and then displayed in the complete field. Electron trajectories leave the 0 volt conductor on its gap edge. Figure 5.9(b) shows that 3eV electrons are initially deflected from their normal trajectory paths towards the 5 volt conductor and hence are rejected by the retarding electrode; 80% of 3eV electrons are lost this way. This effect occurs for 6eV electrons but to a lesser extent; 70% of 6eV electrons are lost while 60% of 10eV electrons are lost. Figure 5.9(e) shows the energy transport efficiency of electrons traversing the retarding field. The

Transport
Efficiency

Error Option for a Two Conductor Surface Layout
(Single gap)
Figure 5.8



(decreasing trajectory step size) (1/mesh units)

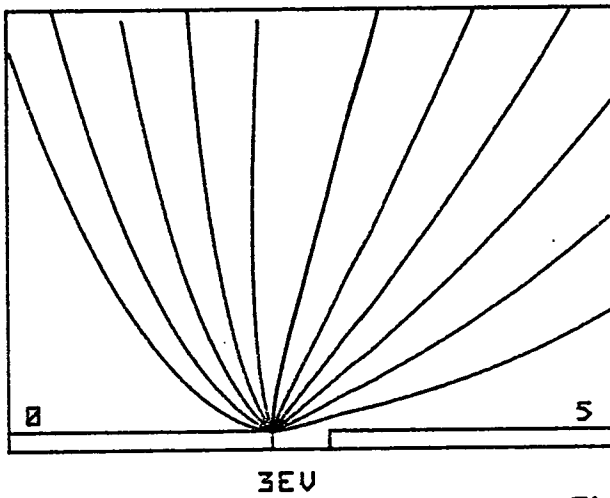


Equipotentials for a
Single 3 micron Gap
Layout

Figure 5.9(a)

(600 volts on extraction
grid)

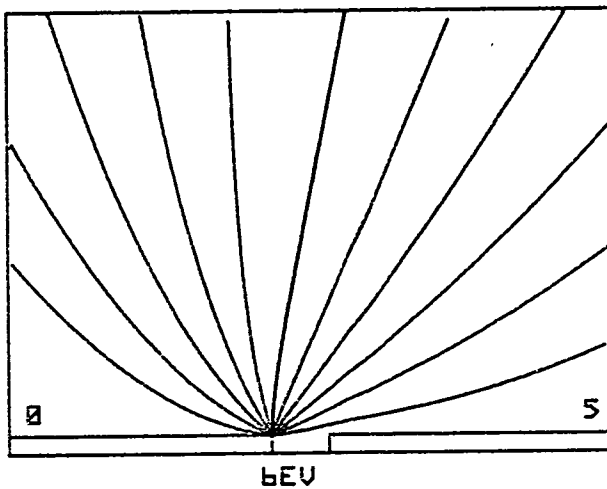
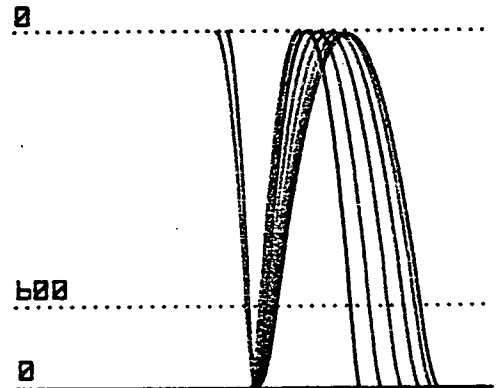
Trajectories for a Single 3 micron gap layout for electrons with
emitted energies of (b) 3eV, (c) 6eV



3eV

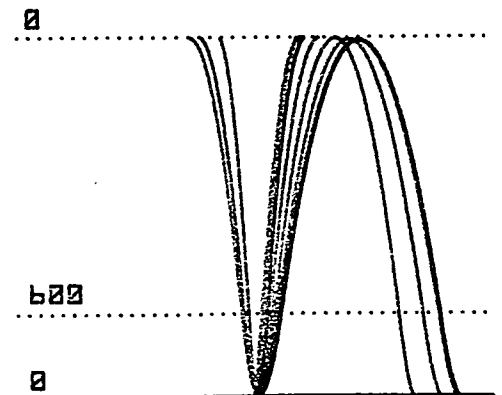
Figure 5.9(b)

(3 micron Gap)



6eV

Figure 5.9(c)



Trajectories for a Single 3 micron layout for electrons emitted
with an energy of 10eV

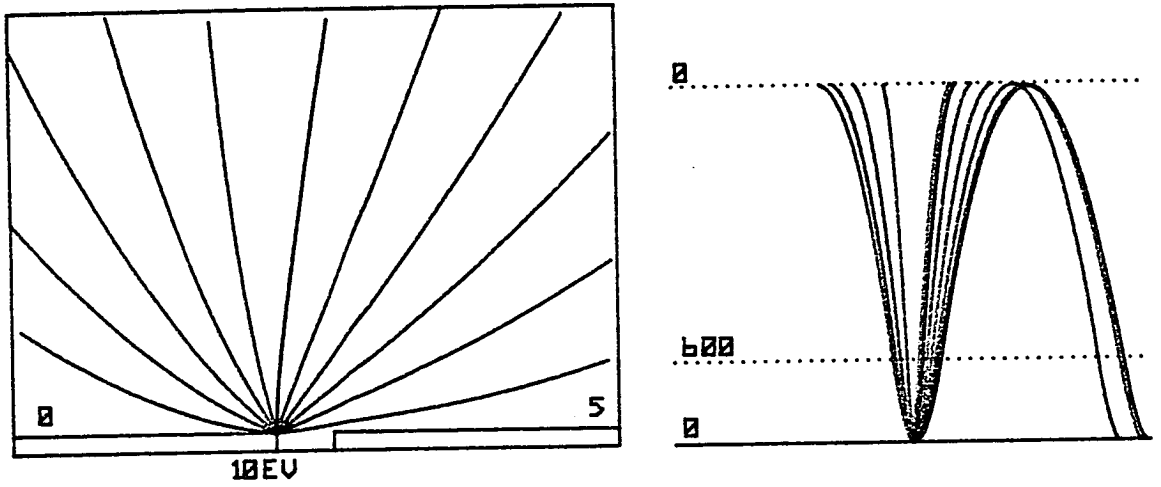


Figure 5.9(d)

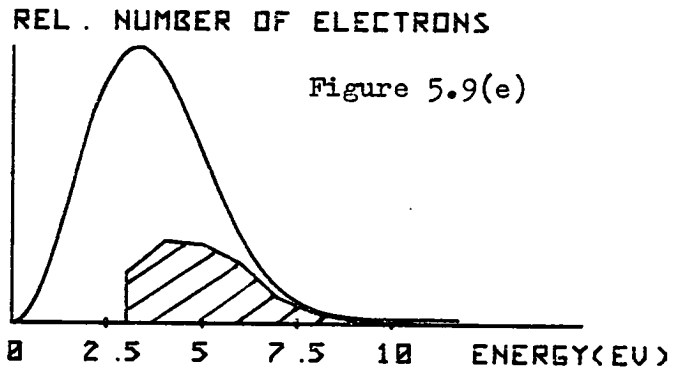


Figure 5.9(e)

Transport Efficiency = 0.27

Energy Analysis for the Single 3 micron Gap Layout

effect of the surface fields is to impose a lower cut-off energy of 3eV and generally reduce the overall transport efficiency to 27%.

5.4.3 Varying the extraction field for the 3 micron single gap layout

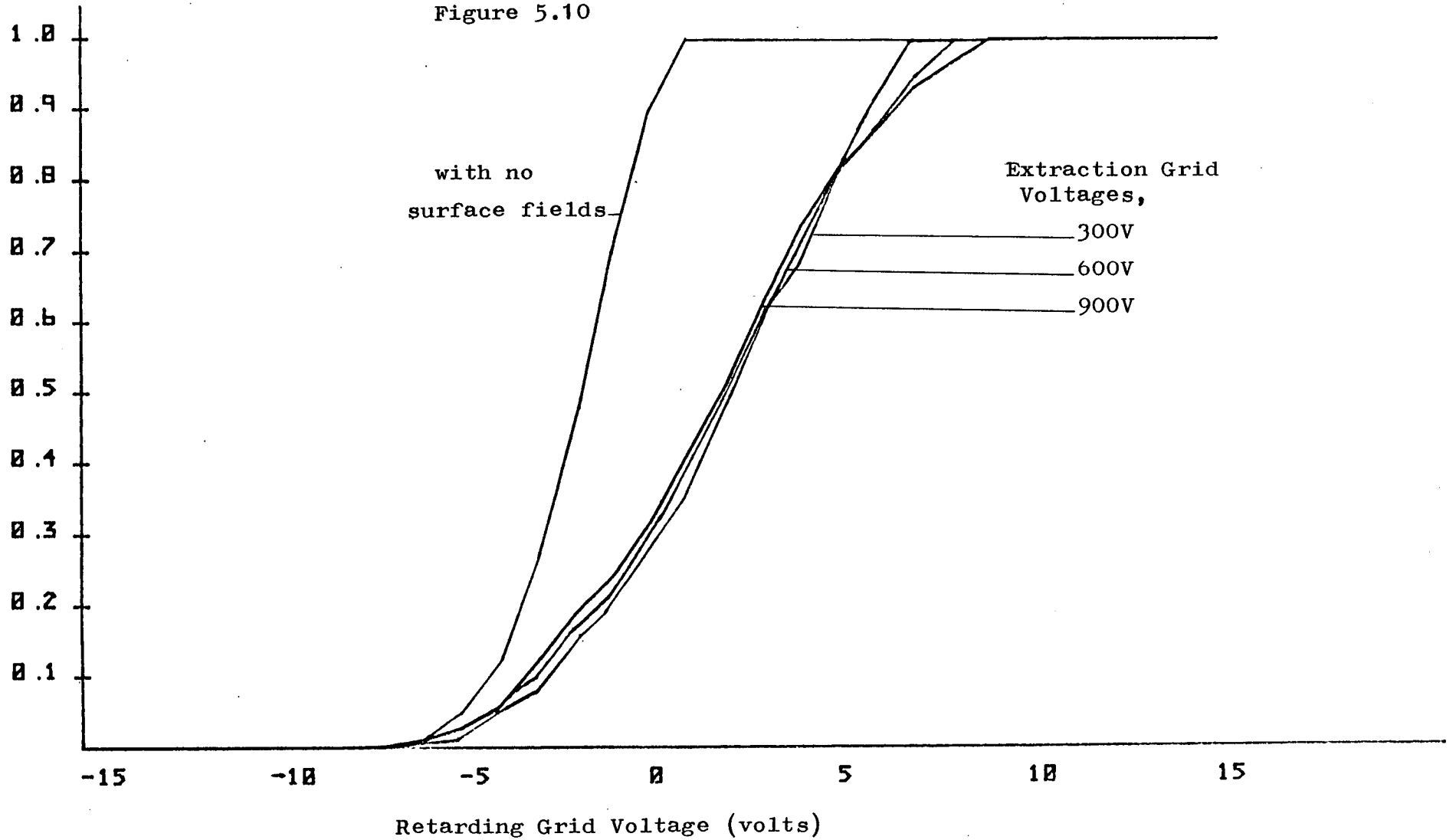
The voltage on the extraction grid was varied for the single 3 micron gap layout. S-curves were plotted for electrons leaving the left-hand gap edge position on the 0 volt conductor. Figure 5.10 shows S-curves calculated at extraction grid voltages of 300, 600 and 900 volts. An S-curve which is unaffected by any surface fields is also plotted for comparison, this S-curve was calculated for both conductors at 0 volts. Figure 5.10 shows that variation in the extraction field does not significantly help in reducing the surface field effects present for the surface layout considered. Changing the extraction grid voltage from 300 to 900 volts only causes a maximum shift of 0.75 volts in the resulting S-curve towards the 'normal' S-curve. The surface field affected S-curves are seen to deviate greatly from the 'normal' S-curve, a shift of 0 volts at their base is seen to linearly increase to 6 volts at their top. At 0 volts on the retarding field an approximate shift of 3eV is observed; this clearly fictitious shift can cause great errors in voltage contrast measurements.

The above results show important limitations to the practical measurements of voltages on conductors separated by 3 micron gaps. If a large conductor is probed at its edge and its neighbouring conductor is 3 microns away then when the neighbouring conductor switches state, say 0 volts to 5 volts then a 0 to 6 volt error will

Transport Efficiency

S-curves for Different Extraction Grid Voltages above a
3 micron Gap Layout

Figure 5.10

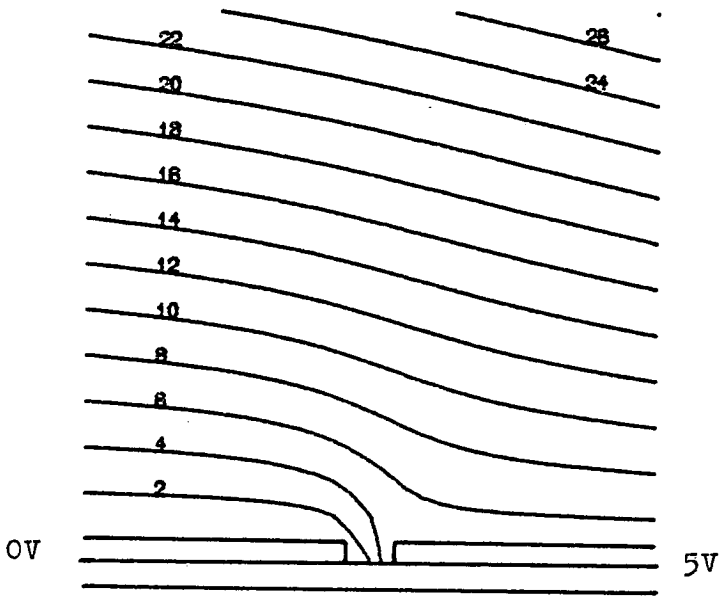


be imposed on the voltage measurement. A realistic measurement is usually made in the linear region of the S-curve and hence the error will range from 1.5 to 6 volts depending on the precise position on the S-curve where the measurement was made. S-curves were calculated more accurately by using a finer relaxation mesh, the error range was changed to 1.5 volts to 5 volts.

Figures 5.11(a-c) show equipotential lines and 3eV electron trajectories through the field for an extraction voltage of 900 volts. It shows how these electron trajectories are similar to those plotted through an extraction voltage of 600 volts. Figures 5.12(a-c) show this is also true for trajectories at an extraction voltage of 300 volts. The shape of the energy transport efficiency curve is similar in each case and the overall transport efficiency remains the same at 27%. Figures 5.13(a) and 5.13(b) shows electron trajectories through a 0 volt extraction grid, although these trajectories differ in shape to those in higher extraction voltages, their percentage collection is the same.

5.4.4 Measurements Near the 3 micron Gap Edge

An S-curve was calculated for a position of 4 microns from the gap edge on the 0 volt conductor (Figure(5.14)). This S-curve was generated at a greater accuracy than for the S-curve in Figure 5.10. The S-curve away from the gap edge is more regular than the S-curve for the gap edge and gives a consistent fictitious shift of 3 volts for most points on the S-curve. The extraction grid for this case was set to 600 volts. Figures 5.15(a-c) show electron trajectories



Equipotentials for a Single
3 micron Gap Layout with
900 volts on Extraction Grid

Figure 5.11(a)

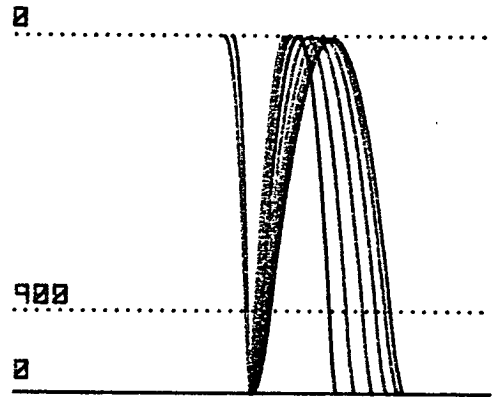
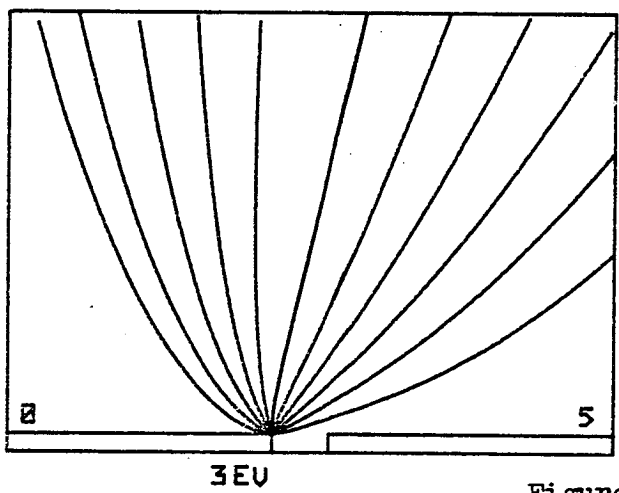


Figure 5.11(b)

Trajectories for a Single 3 micron Gap layout with 900V on Extraction
grid
(electrons emitted at 3eV)

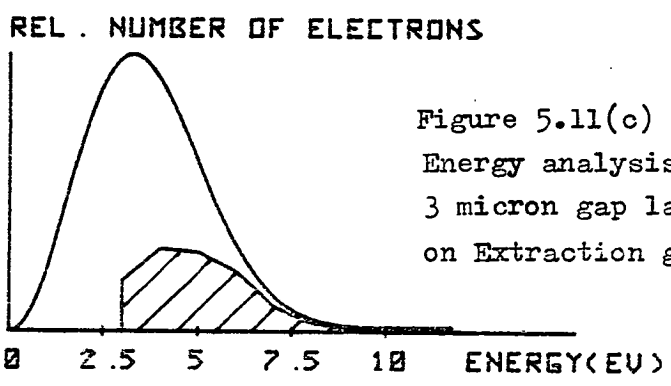
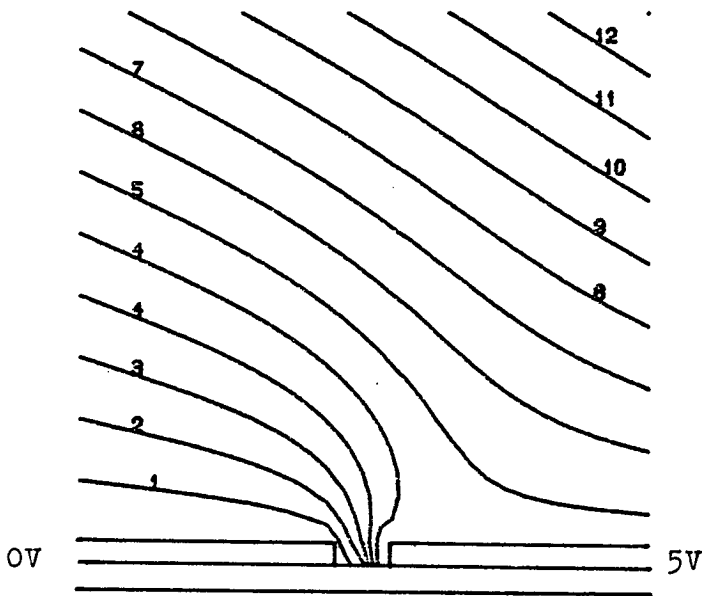


Figure 5.11(c)
Energy analysis for a Single
3 micron gap layout with 900V
on Extraction grid

Transport Efficiency = 0.27



Equipotentials for a Single
3 micron Gap Layout with
300 volts on Extraction
Grid
Figure 5.12(a)

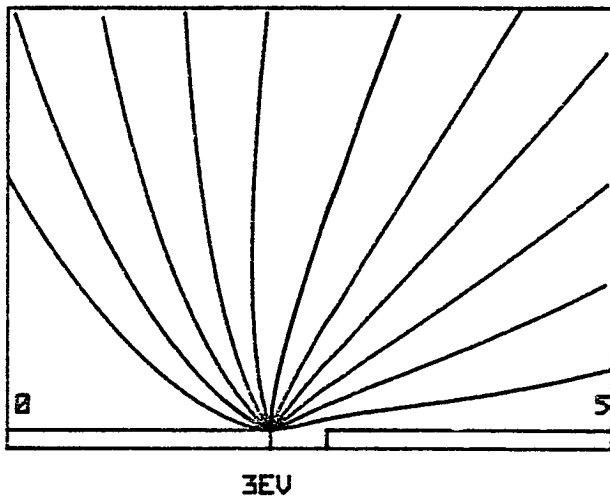
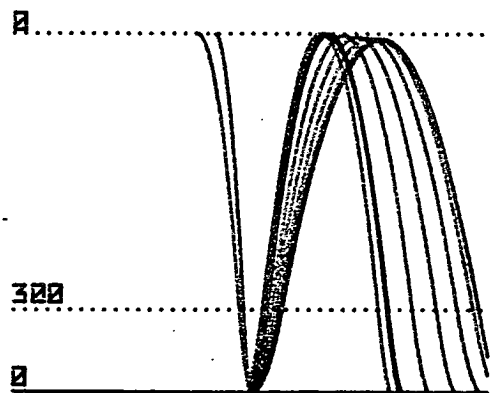


Figure 5.12(b)



Trajectories for a Single 3
micron gap layout with 300V
on extraction grid
(electrons emitted at
3eV)

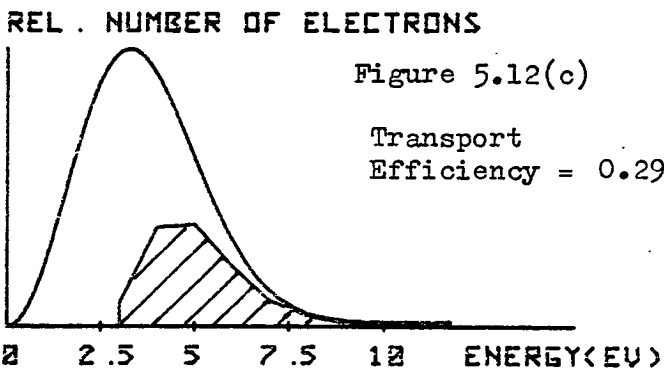


Figure 5.12(c)

Transport
Efficiency = 0.29

Energy analysis for a 3
micron gap layout with 300
on extraction grid

Trajectories for a Single 3 micron gap layout with 0V on the extraction grid and emitted energies of (a) 3eV
(b) 6eV

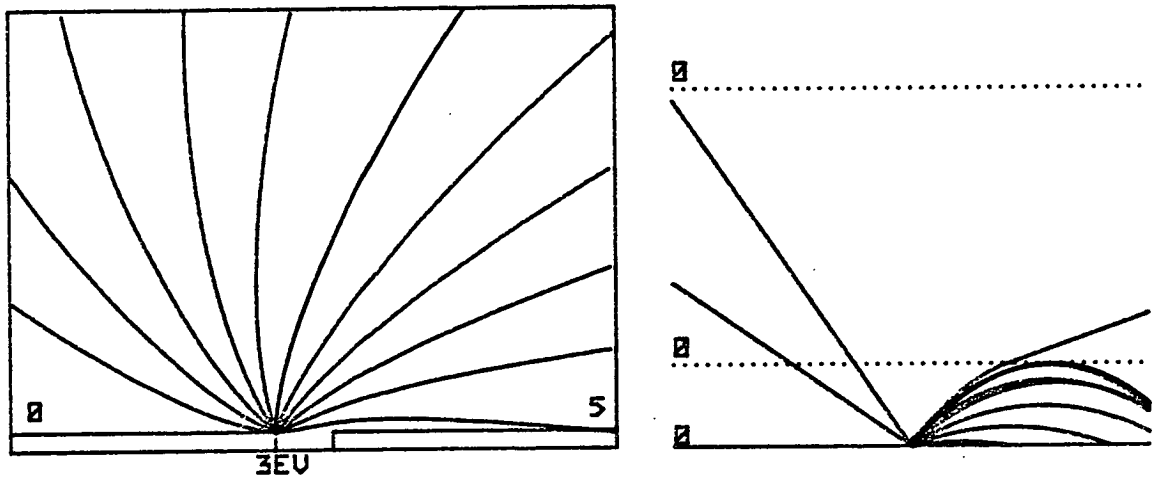


Figure 5.13(a)

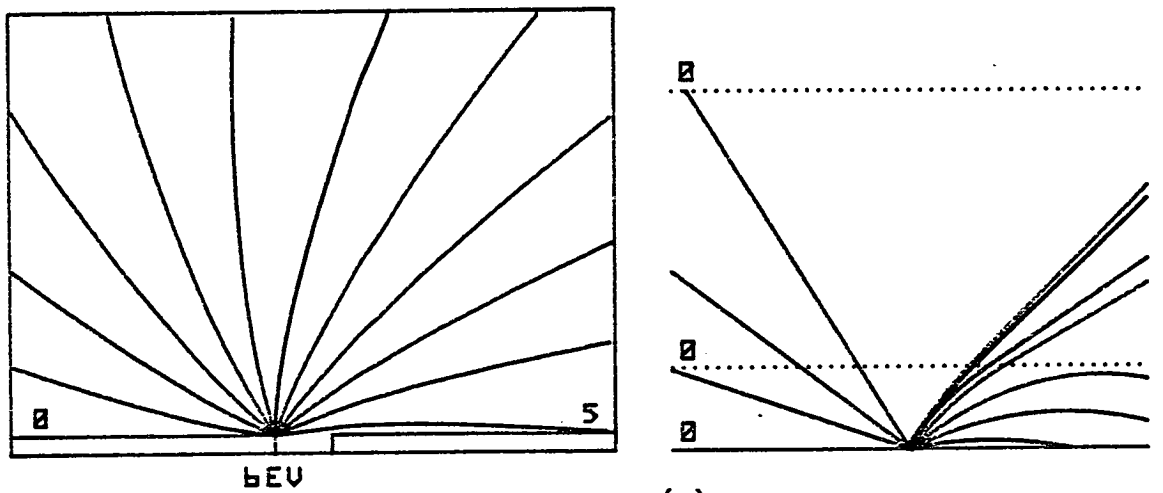
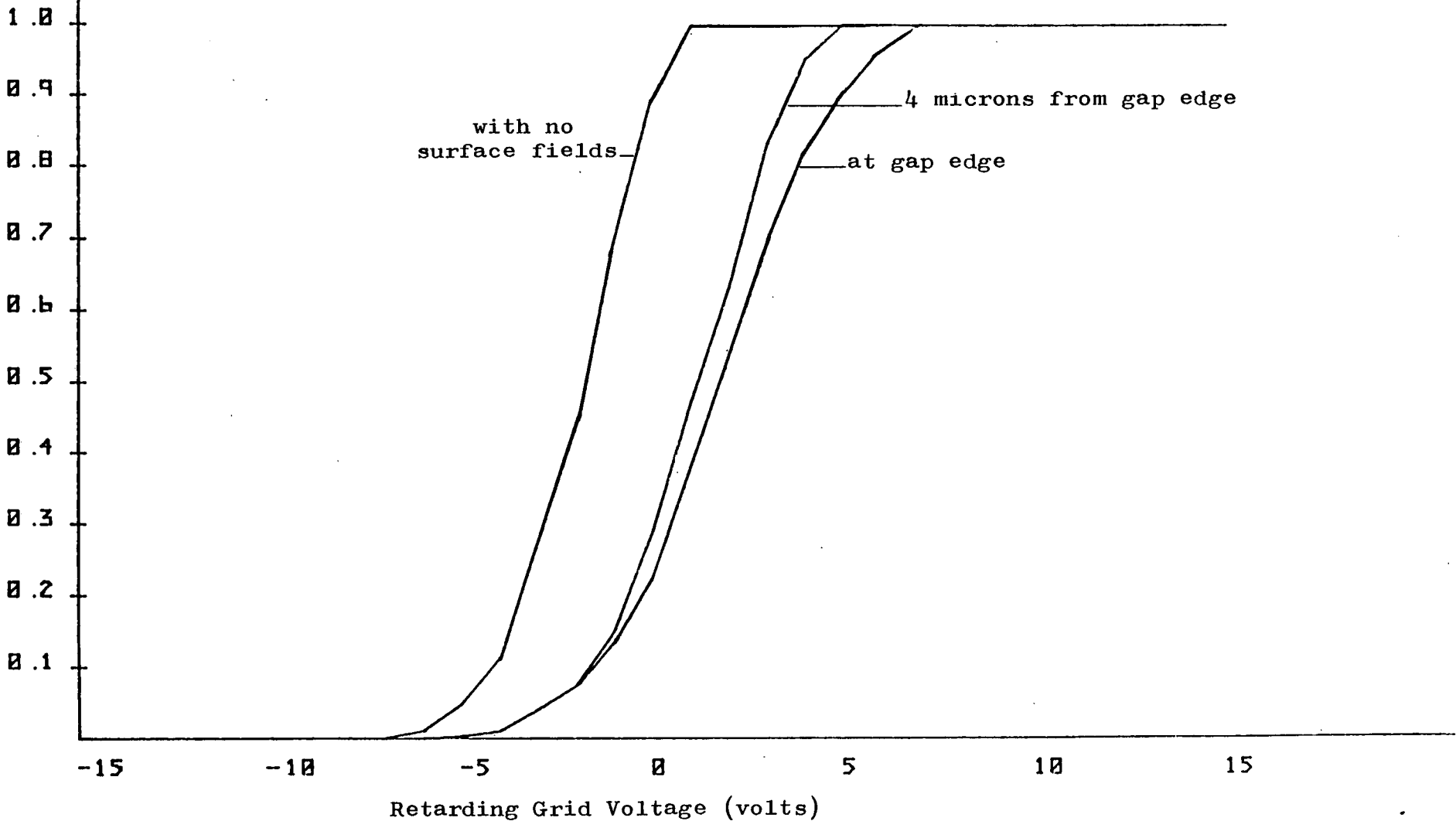


Figure 5.13(b)

S-curves for Different Positions Near a 3 micron Gap Layout

Figure 5.14

Transport Efficiency



Electrons Leaving a Position of 4 microns from Gap Edge
with emitted energies of (a) 3eV, (b) 6eV, (c) 10eV

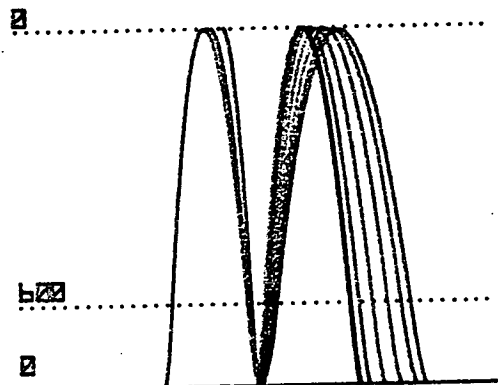
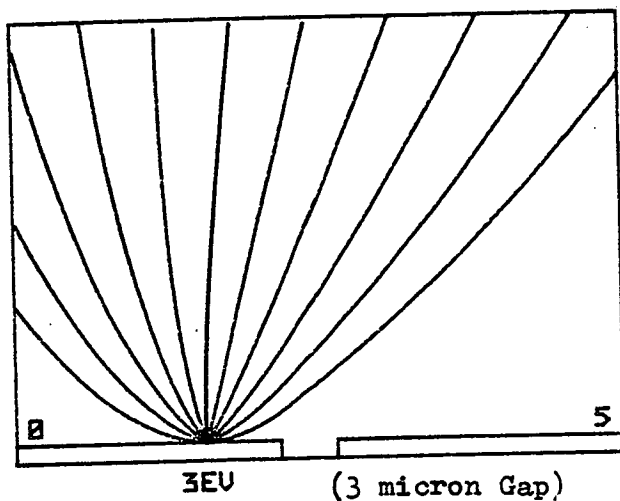


Figure 5.15(a)

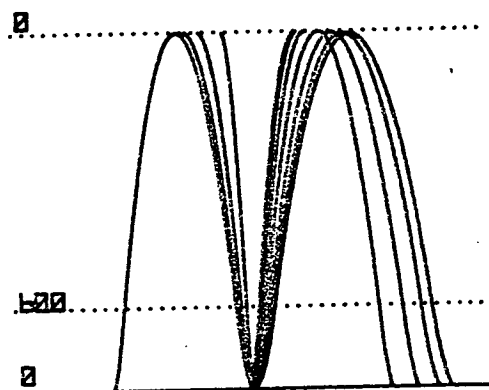
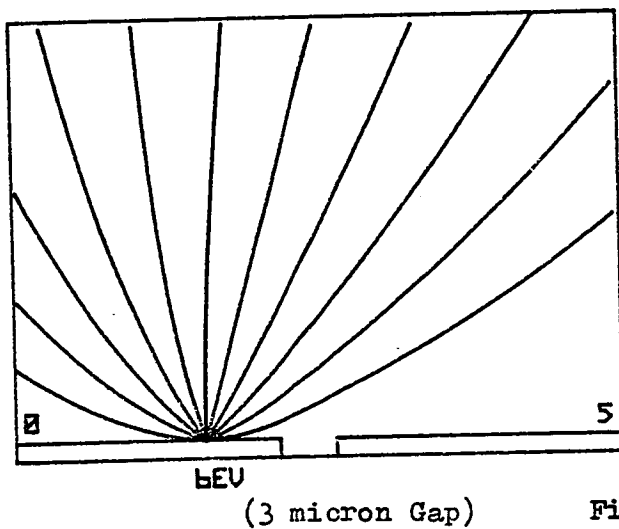


Figure 5.15(b)

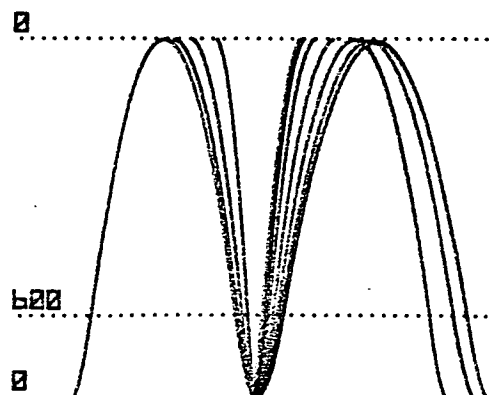
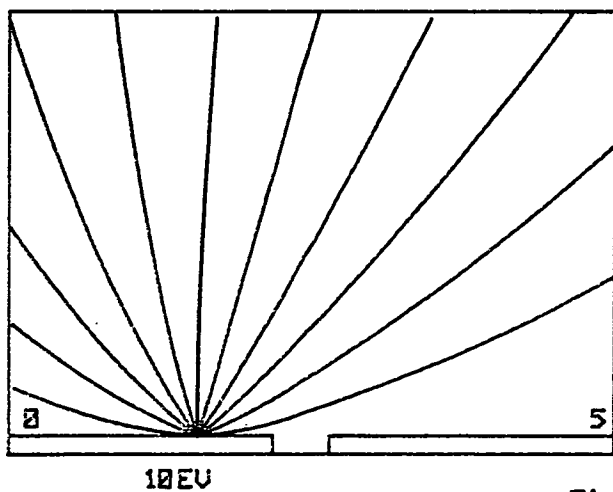


Figure 5.15(c)

(3 micron Gap)

at 3eV, 6eV and 10eV through the field. Slightly more electrons are collected than for the position at the gap edge. Figures 5.15(a-c) also show single electron trajectories being rejected in each case at the left-hand side of the gap. This was due to some computational errors in the electric field values, an inevitable consequence of using a finite mesh size.

5.4.5 A 9 micron Single Gap Layout

A 9 micron gap between two infinitely wide conductors was simulated, their voltage configuration was similar to the last layout, 0 volts for the conductor on the left-hand side of the gap and 5 volts for the conductor on the right-side of the gap. Figure 5.16(a) shows the equipotential lines obtained for this case, the field disturbance near the gap is clearly not as great for the 9 micron gap.

Figures 5.16(b) and 5.16(c) show electron trajectories through this field with initial energies of 3eV and 6eV respectively. These diagrams show a marked improvement in the number of electrons that traverse the retarding grid to that in the 3 micron case. 50% of 3eV electrons are collected compared with 20% in the 3 micron case. Similarly Figure 5.16(d) shows a larger collection area in the energy transport efficiency graph, giving an overall efficiency of 47% compared with 27% for the 3 micron gap.

Equipotentials for a 9 micron Gap Layout with 600 volts on the
Extraction Grid

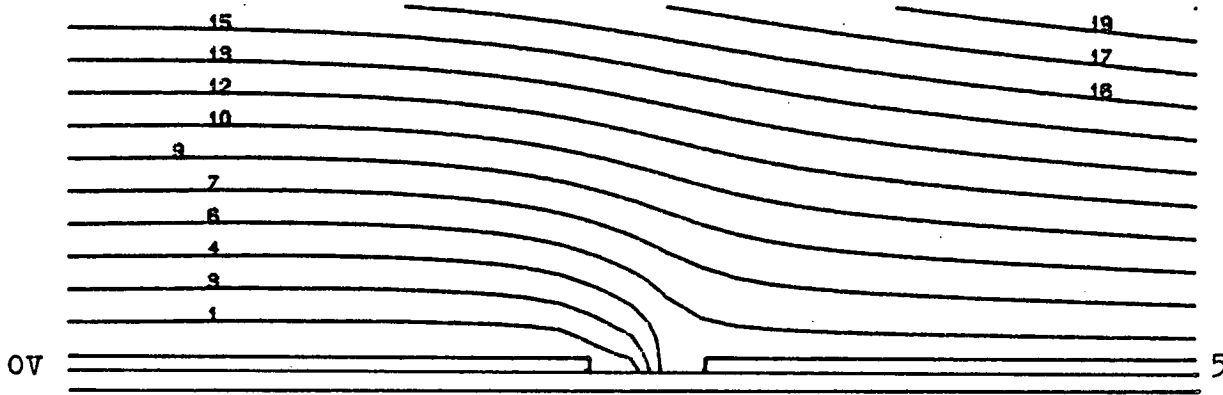


Figure 5.16(a)

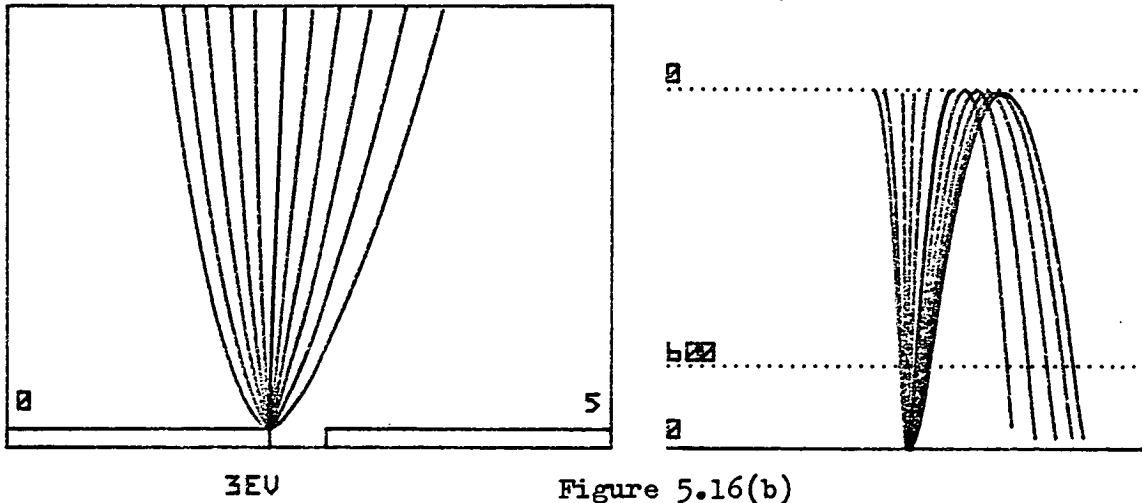
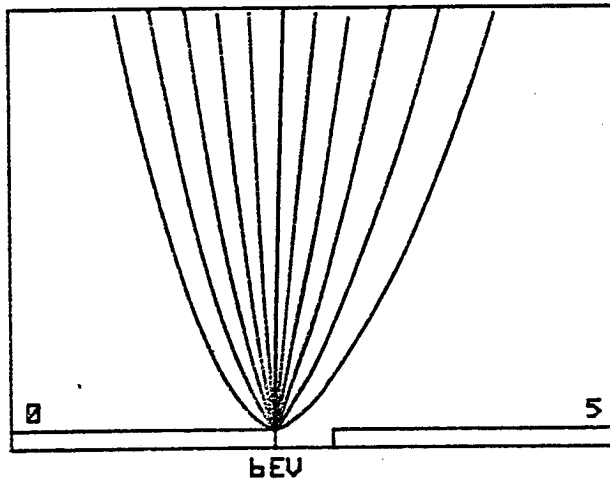


Figure 5.16(b)

(9 micron gap)

Trajectories for a 9 micron gap layout with an emitted
energy of 3eV

Trajectories for 9 micron gap layout with an emitted energy of 6eV



(9 micron gap)

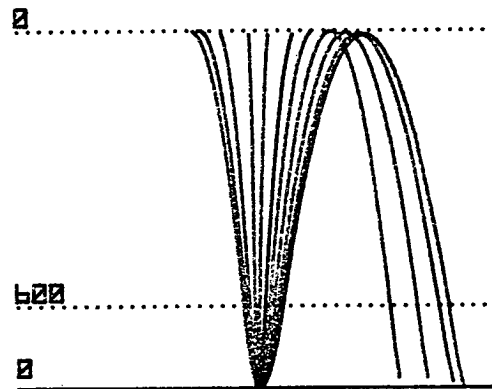


Figure 5.16(c)

REL. NUMBER OF ELECTRONS

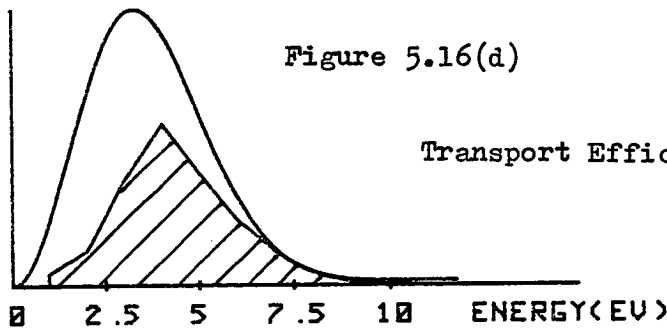


Figure 5.16(d)

Transport Efficiency = 0.47

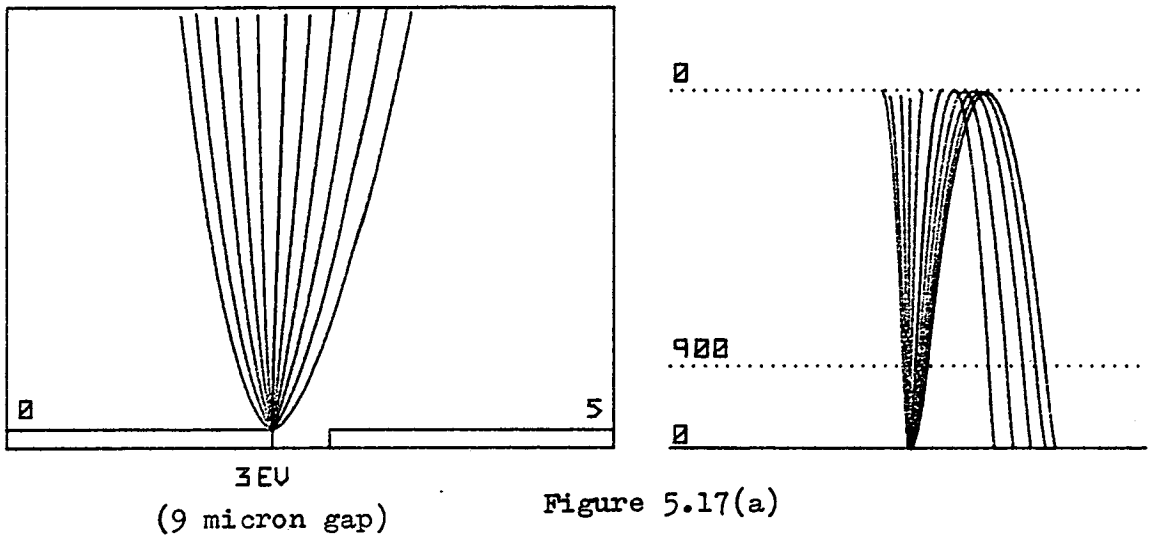
Energy analysis for a 9 micron gap layout

5.4.6 Different Extraction fields for a 9 micron single gap layout

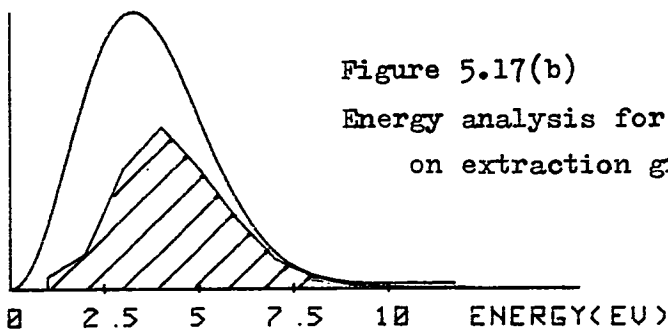
Figure 5.17(a) show electron trajectories with initial energies of 3eV, in this case the extraction grid is set to 900 volts. More electrons are collected than for the 3 micron case under the same conditions. Figure 5.17(b) shows the energy transport efficiency curve giving an overall transport efficiency of 49% compared to the 27% for the 3 micron case. Figure 5.18(a) shows electron trajectories at 3eV with an extraction voltage of 300 volts. Figure 5.18(b) shows that varying the extraction grid voltage has more effect for the 9 micron gap than for the 3 micron gap. The overall transport efficiency is reduced to 43% for an extraction grid voltage of 300 volts. From the energy transport efficiency curve it can be seen that lower energy electrons are collected and the lower cut-off energy has been reduced from 3eV in the 3 micron case to less than 1eV for the 9 micron case. Figures 5.19(a) and 5.19(b) show electron trajectories at 3eV and 6eV for 0 volts on the extraction grid.

Figure 5.20 shows a marked improvement in the calculated S-curves for extraction voltages of 300, 600 and 900 volts for the 9 micron gap. The fictitious shift in voltage measurements is reduced to between 0.75 to 3.7 volts in the linear portion of the S-curve for 900 volts on the extraction grid. This compared with an error range of 1.5 to 5 volts for the 3 micron gap.

Trajectories for a 9 micron layout with an emitted energy of 3eV
and 900V extraction grid



REL. NUMBER OF ELECTRONS



Energy analysis for a 9 micron layout with 900V
on extraction grid

Energy analysis for a 9 micron layout with 900V
on extraction grid

Transport Efficiency = 0.49

Trajectories for a 9 micron layout with an emitted energy of 3eV
and 300V on extraction grid

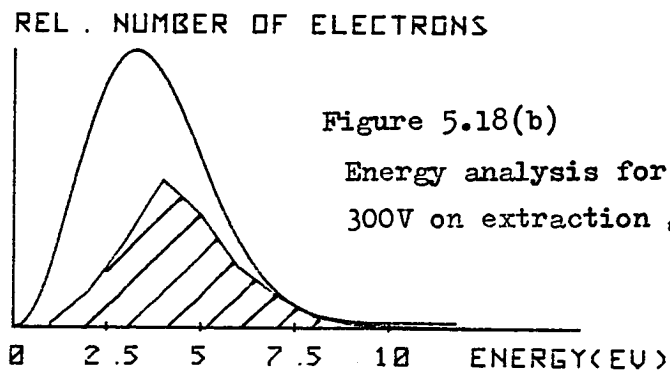
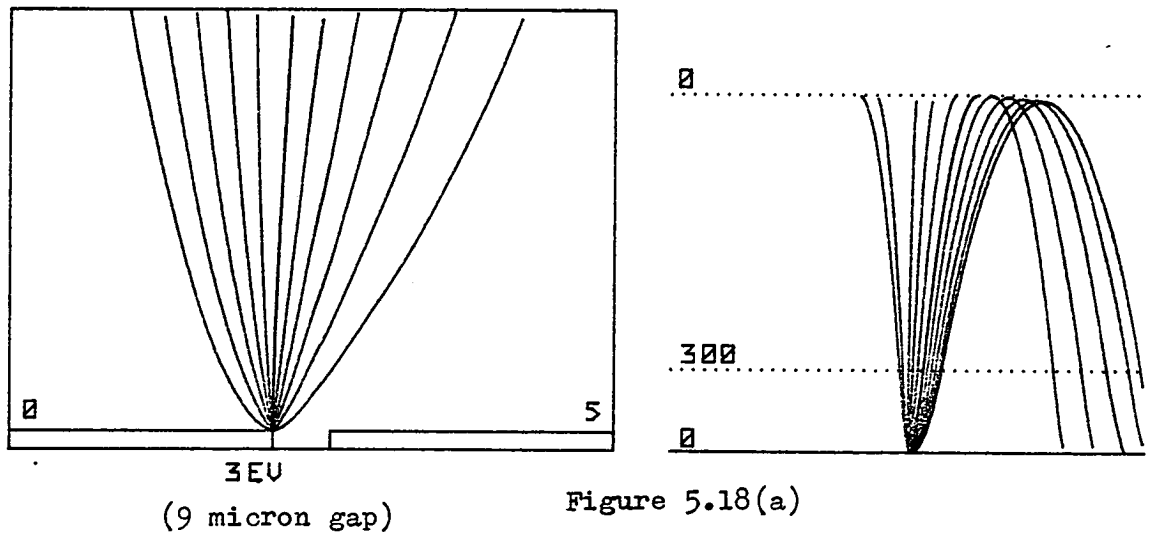
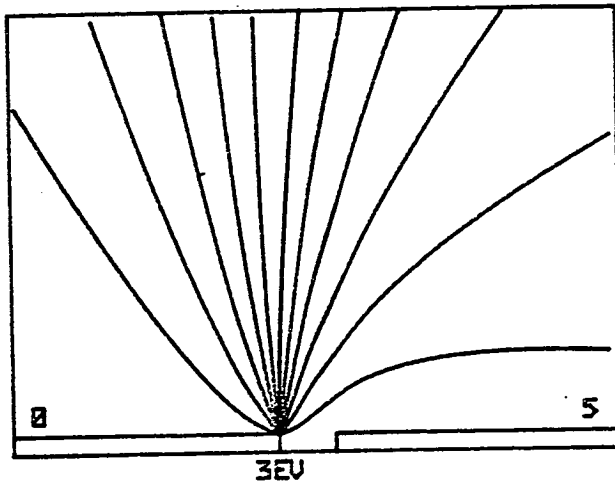


Figure 5.18(b)

Energy analysis for a 9 micron layout with
300V on extraction grid

Transport Efficiency = 0.43

Trajectories for a 9 micron layout with 0V on extraction grid
 and emitted energies of (a) 3eV
 (b) 6eV



(9 micron gap)

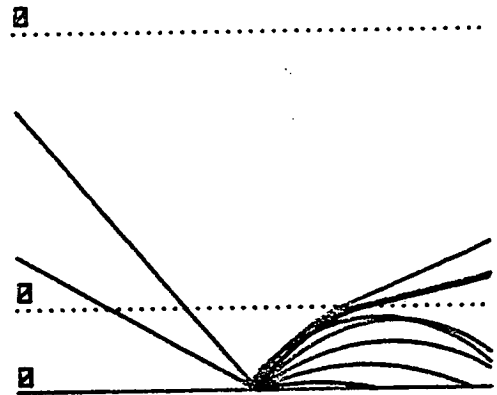
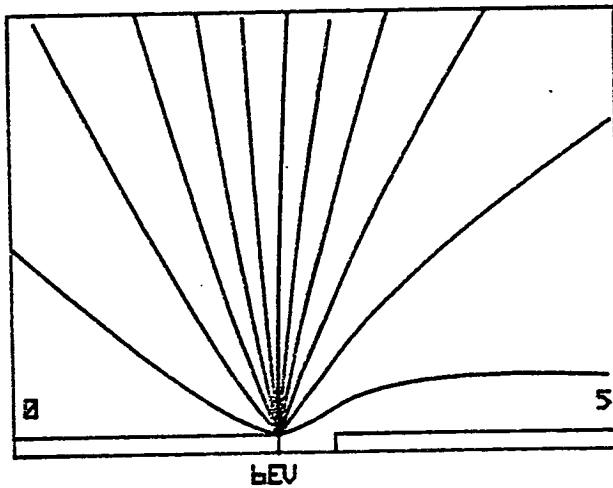


Figure 5.19(a)



(9 micron gap)

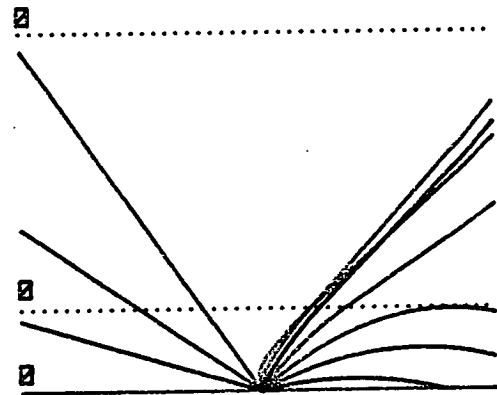
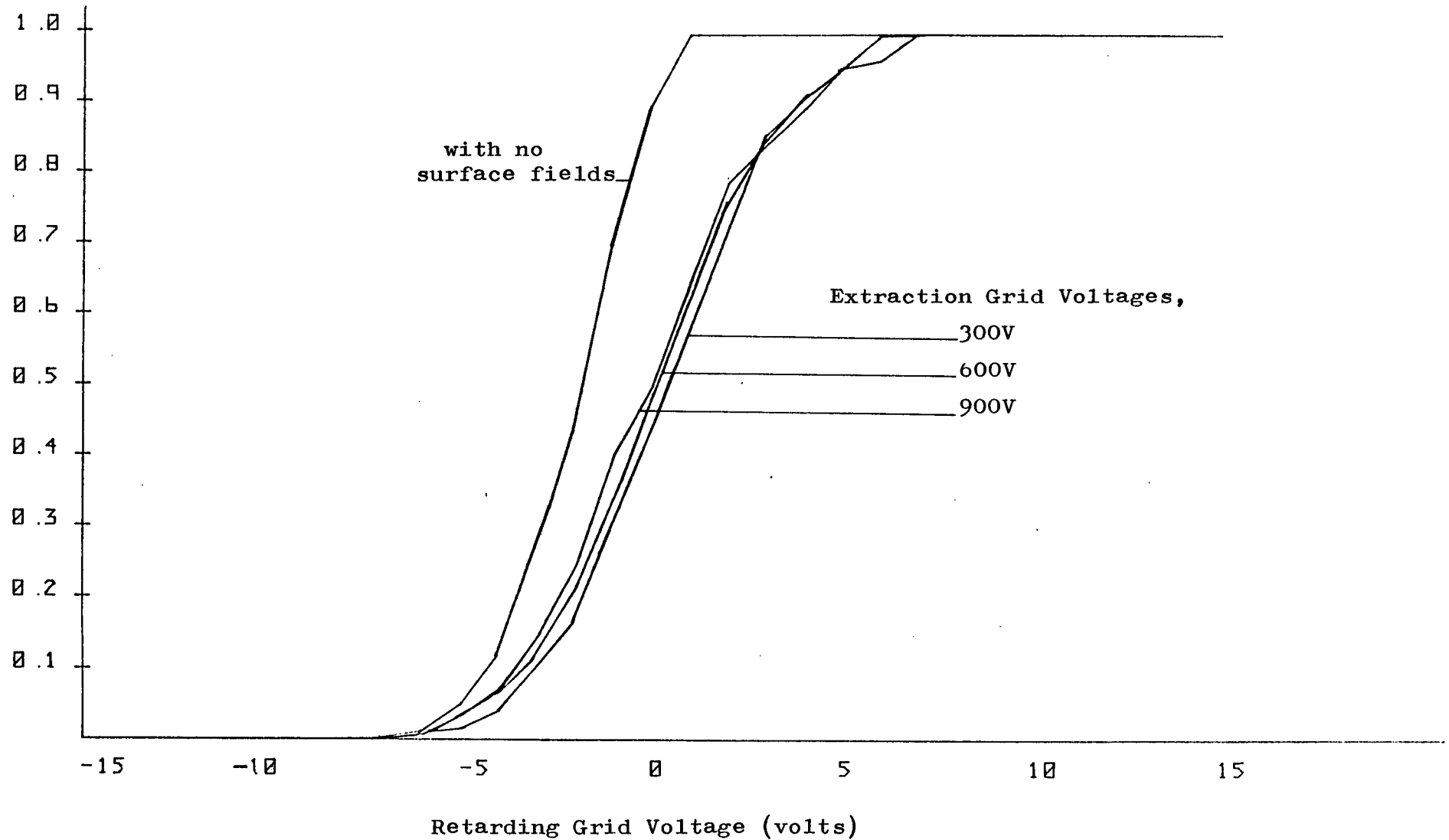


Figure 5.19(b)

Transport
Efficiency

S-curves for Different Extraction Grid Voltages above a
9 micron Gap Layout
Figure 5.20



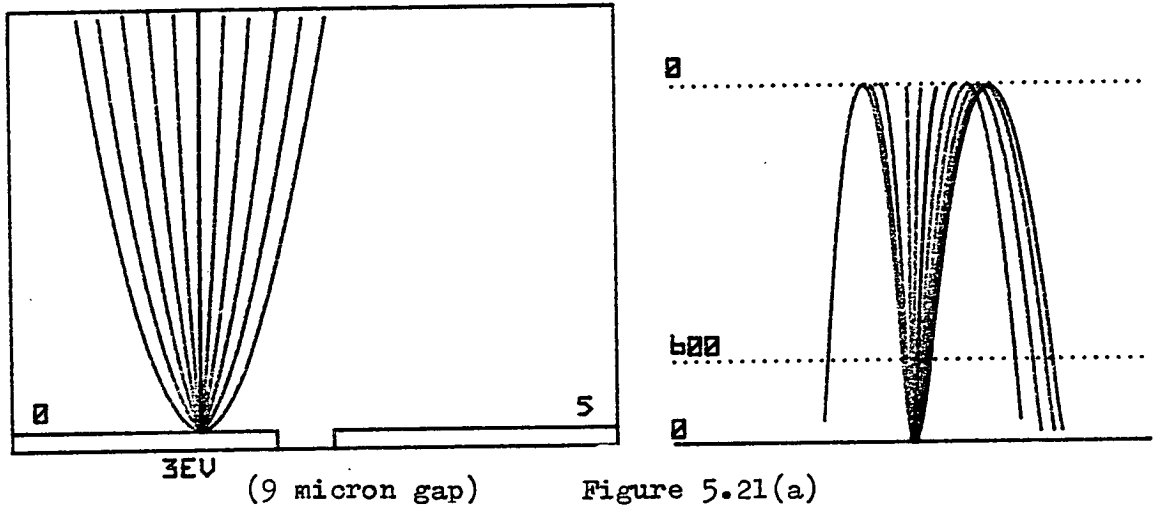
5.4.7 Measurements Near a 9 Micron Gap Edge

Figure 5.21(a) shows electron trajectories at 3eV leaving the 0 volt conductor 12 microns from the gap edge. Figure 5.21(b) shows that a higher percentage are collected at this position than for the gap edge, 67% compared to 43%. These results again indicate a marked improvement over the 3 micron case. Figure 5.22 shows the S-curve generated for 12 microns from the gap edge and compares it with the normal S-curve and the S-curve generated from the gap edge. The S-curve away from the gap edge exhibits greater regularity and has a fictitious voltage shift between 0.6 to 2.2 volts in its linear range.

5.4.8 21 Micron Single Gap Layout

Equipotential lines for a 21 micron gap between an earthed conductor and a 5 volt conductor are given by Figure 5.23(a). The equipotential lines are seen to be more uniform around the gap edges than for both the previous cases of 9 micron and 3 micron gaps. Figures 5.23(b) and 5.23(c) show electron trajectories from the gap edge for initial energies of 3eV and 6eV respectively. More electrons reach the retarding grid than for any of the previous gap sizes. This is confirmed by Figure 5.23(d) which shows the energy transport efficiency curve for the 21 micron gap. An overall transport efficiency of 77% is calculated from this curve, comparing favourably with 47% for the 9 micron gap.

Electrons Leaving a Position of 12 microns from the Gap Edge
of a 9 micron layout



REL. NUMBER OF ELECTRONS

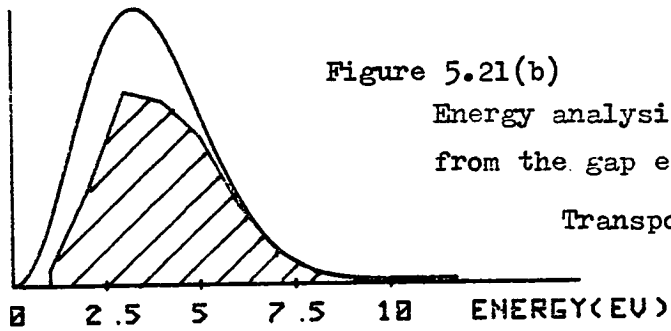


Figure 5.21(b)

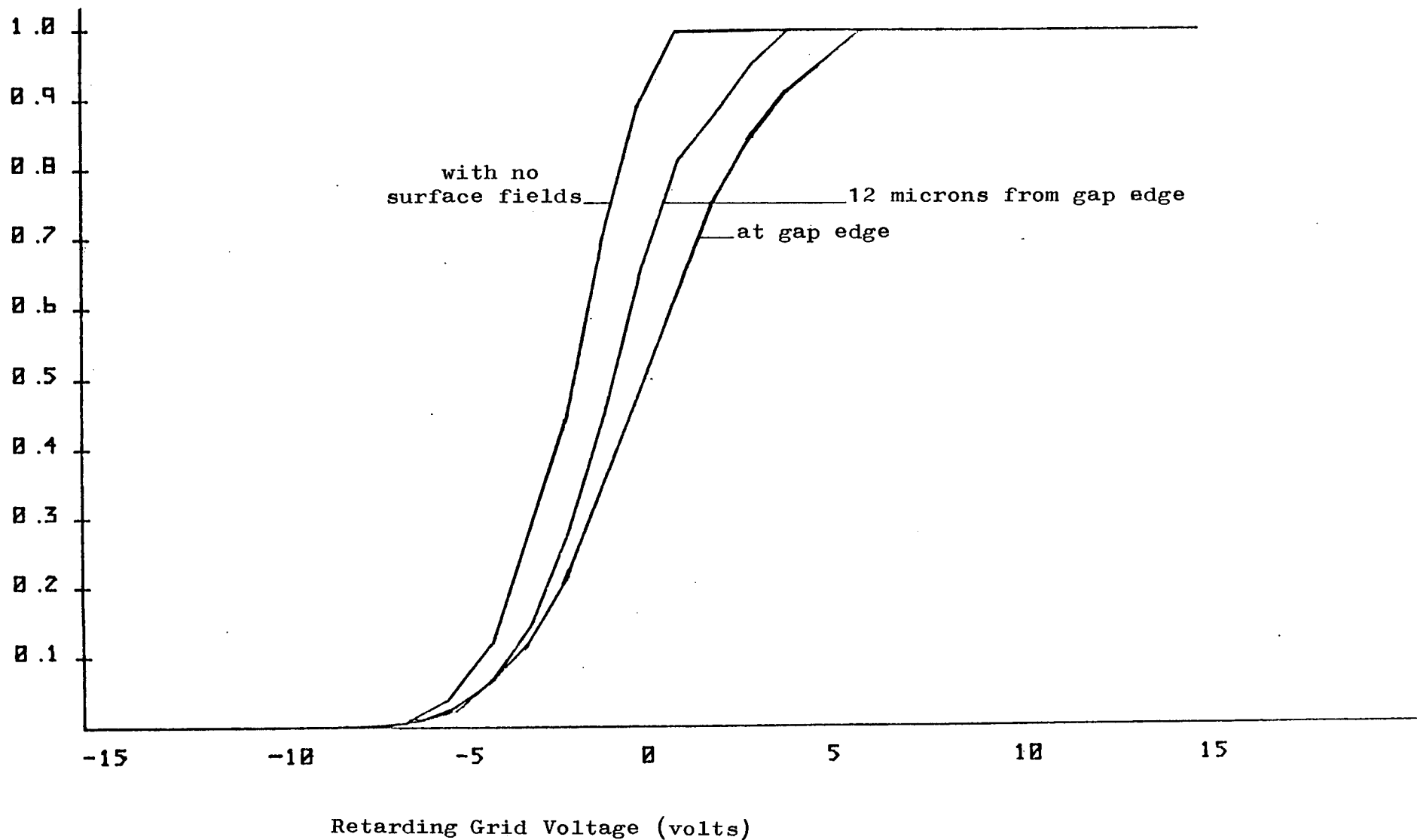
Energy analysis of a position 12 microns
from the gap edge of a 9 micron layout

Transport Efficiency = 0.67

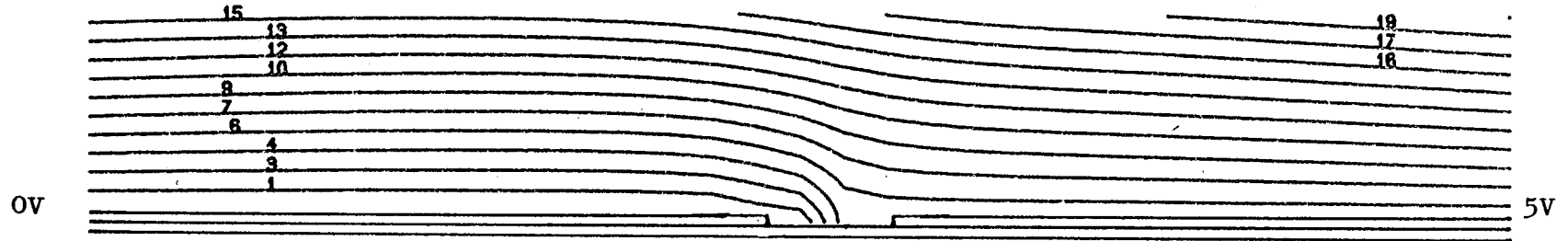
Transport
Efficiency

S-curves for Different Positions Near a 9 micron Gap Layout

Figure 5.22



Equipotentials for a Single 21 micron Gap Layout with 600 volts
on the Extraction Grid



(21 micron gap)

Figure 5.23(a)

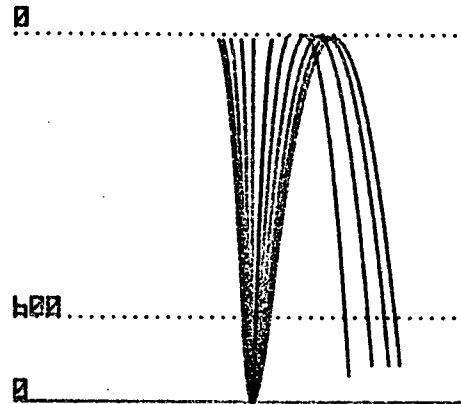
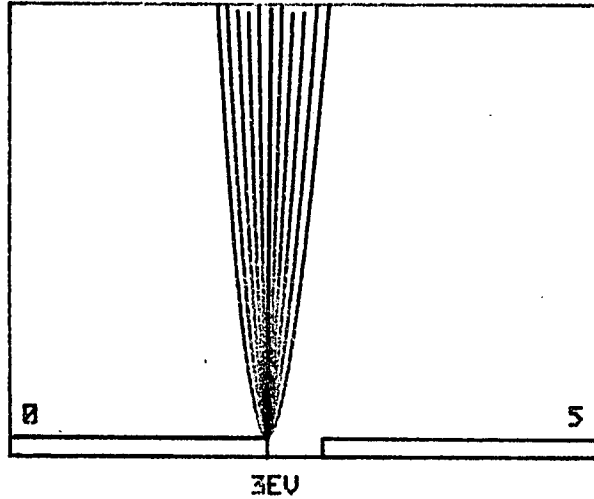
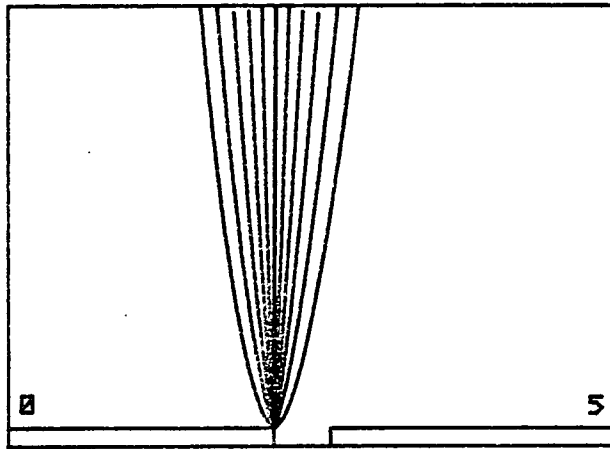


Figure 5.23(b)

Trajectories for a Single 21 micron layout with an emitted
energy of 3eV

Trajectories for a 21 micron layout with an emitted energy of 6eV



6eV
(21 micron gap)

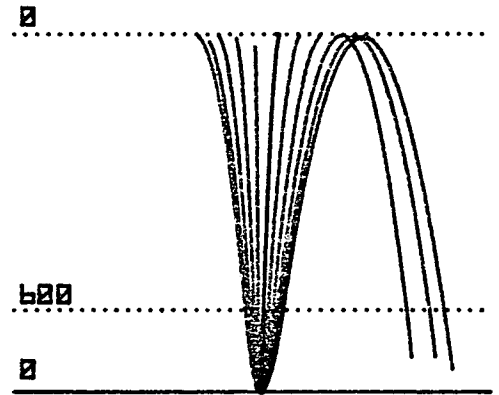


Figure 5.23(c)

REL. NUMBER OF ELECTRONS

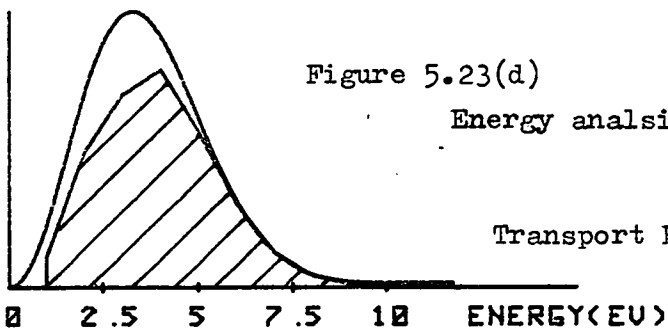


Figure 5.23(d)

Energy analysis for a 21 micron layout

Transport Efficiency = 0.77

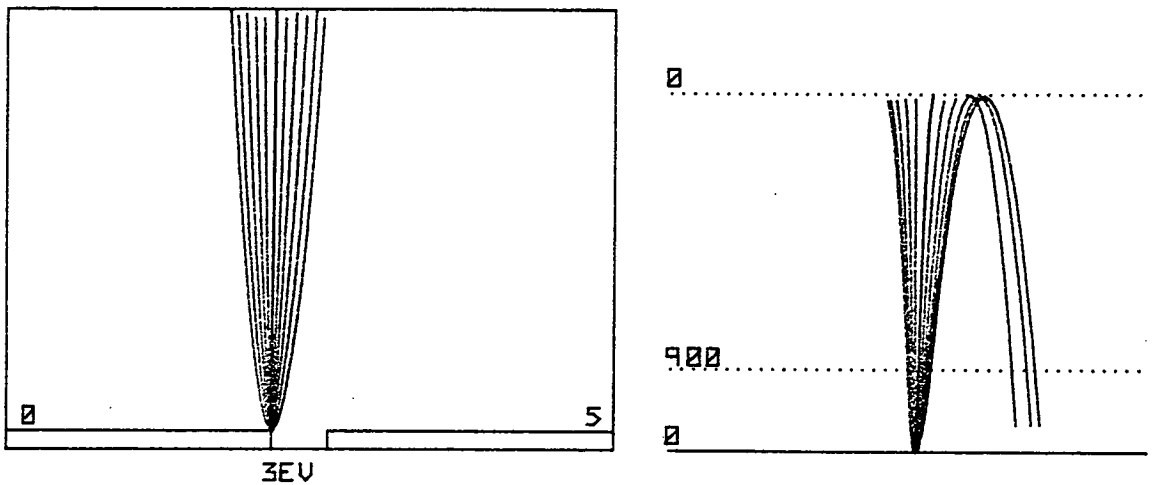
5.4.9 Different Extraction Fields for a 21 micron Gap

Figure 5.24(a) shows electron trajectories with initial energies of 3eV for an extraction grid voltage of 900 volts, while Figure 5.24(b) shows its corresponding energy transport efficiency curve; an overall transport efficiency of 77% is found from this curve. These characteristics are clearly identical to those in Figures 5.11(b) and 5.11(c) for an extraction voltage of 600 volts. Figures 5.25(a) and 5.25(b) however, show a higher rejection of electrons for an extraction voltage of 300 volts; an overall transport efficiency of 67% is given in Figure 5.25(b). These observations are also supported by the S-curves shown in Figure 5.26. S-curves for extraction voltages of 600 and 900 volts are almost identical, while that for 300 volts differs significantly. These S-curves are also much closer to the normal S-curve; they have only fictitious shifts of 0 to 1 volt for the 900 and 600 volt extraction grid voltages and 0 to 2.2 volts for the 300 volt extraction voltage. Figures 5.27(a) and 5.27(b) show that even at a 21 micron gap, surface fields still deflect many electrons from their normal trajectory paths for a 0 volt extraction voltage.

5.4.10 Near a 21 micron Gap

Figures 5.28(a) and 5.28(b) show that most electrons are collected 28 microns away from the gap edge, an overall transport efficiency of 91% found from this position. The S-curves in Figure 5.29 indicate that the S-curve generated for a 28 micron distance from the gap edge is almost identical to the normal S-curve, only

Trajectories for a 21 micron layout with 900V on extraction grid and an emitted energy of 3eV



(21 micron gap)

Figure 5.24(a)

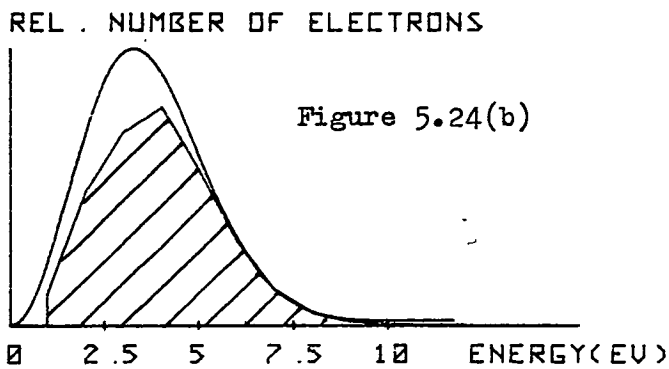
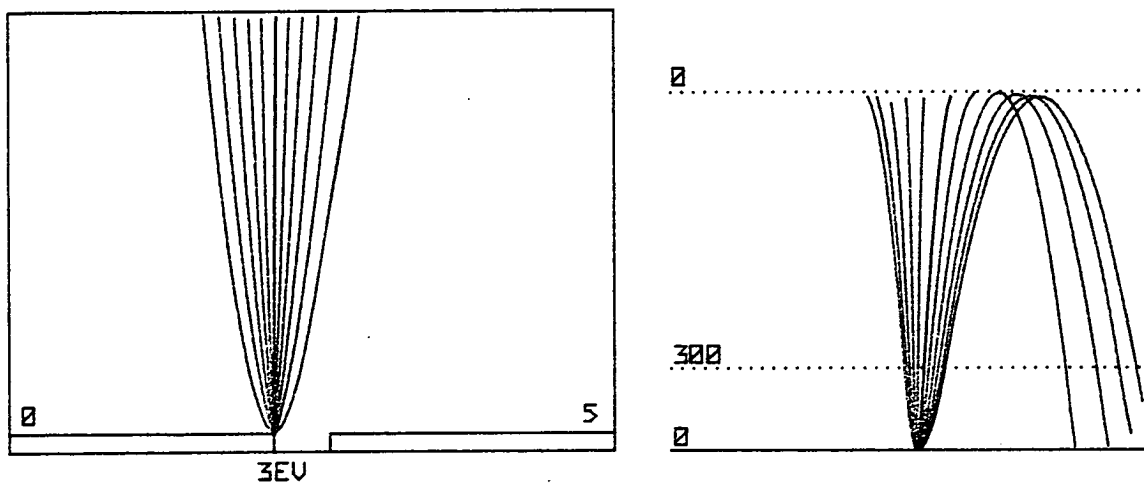


Figure 5.24(b)

Transport Efficiency = 0.77

Energy analysis for a 21 micron layout with 900V on extraction grid

Trajectories for a 21 micron layout with 300V on extraction grid and an emitted energy of 3eV



(21 micron gap)

Figure 5.25(a)

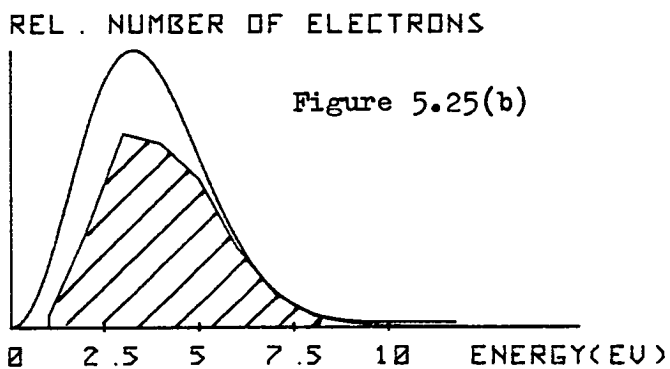


Figure 5.25(b)

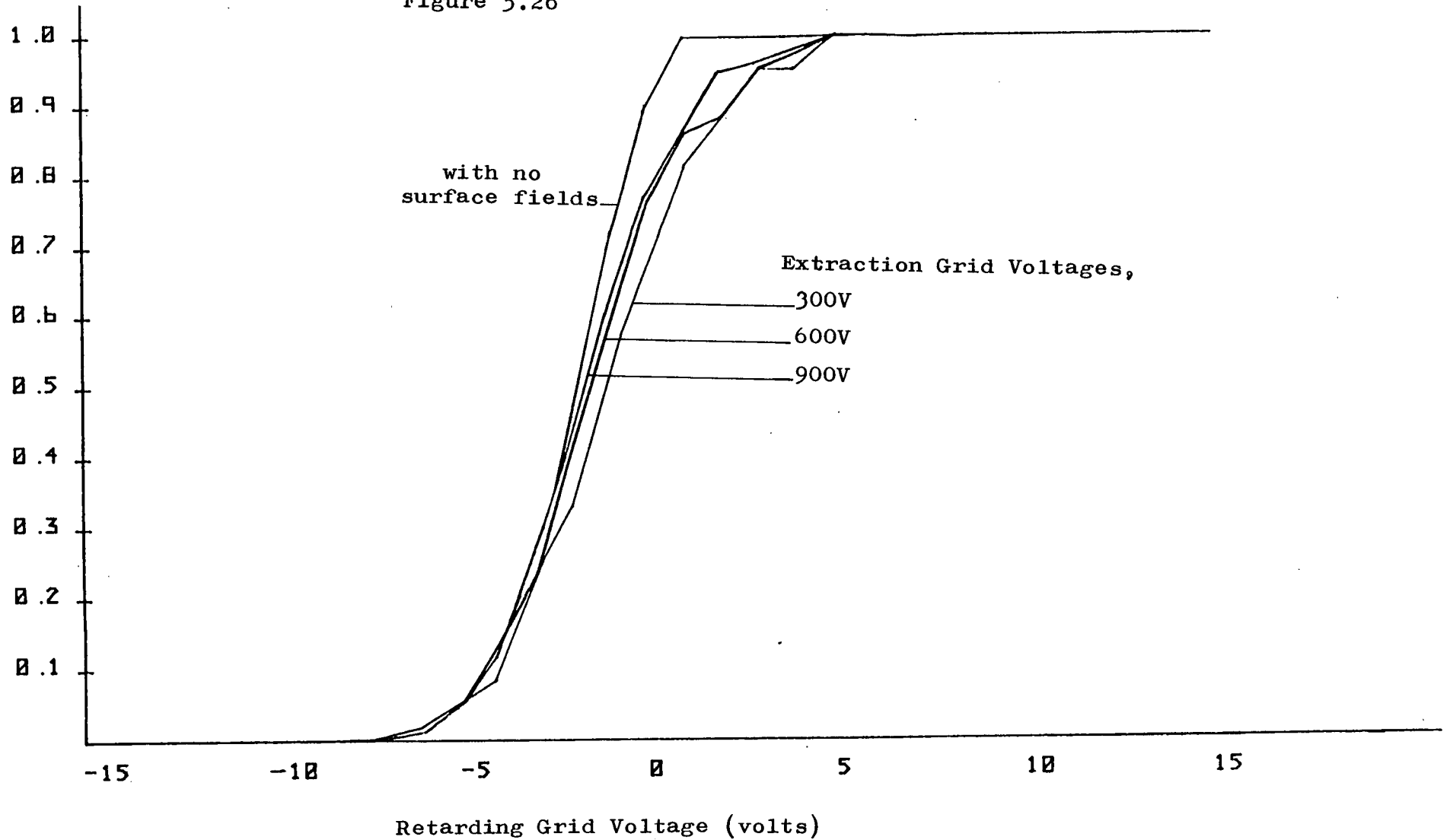
Transport Efficiency = 0.67

Energy analysis for a 21 micron layout
with 300V on extraction grid

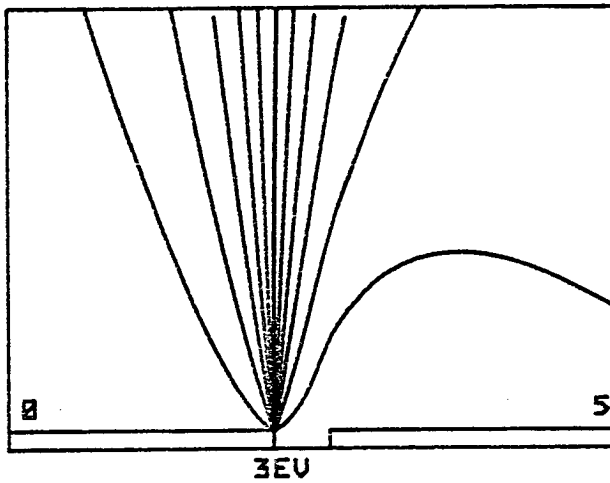
S-curves for Different Extraction Grid Voltages above a
21 micron Gap Layout

Figure 5.26

Transport
Efficiency



Trajectories for a 21 micron layout with 0V on extraction grid
and emitted energies of (a) 3eV
(b) 6eV



(21 micron layout)

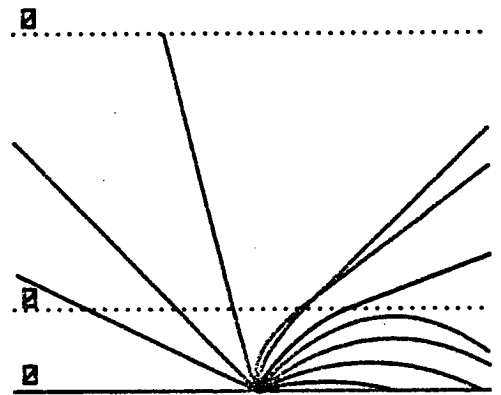
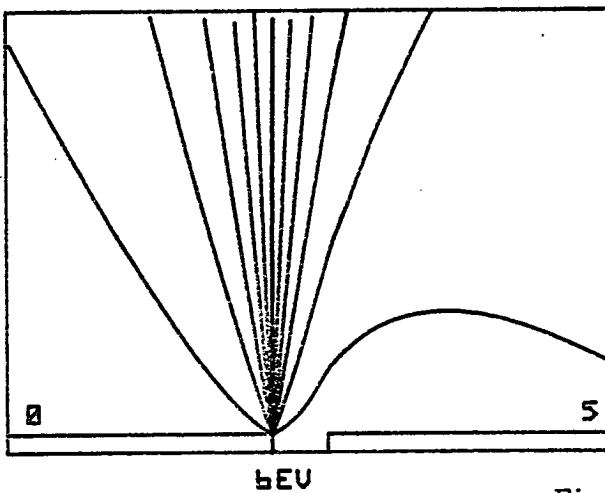


Figure 5.27(a)



(21 micron layout)

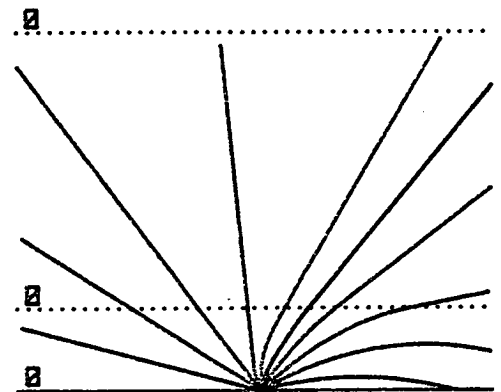
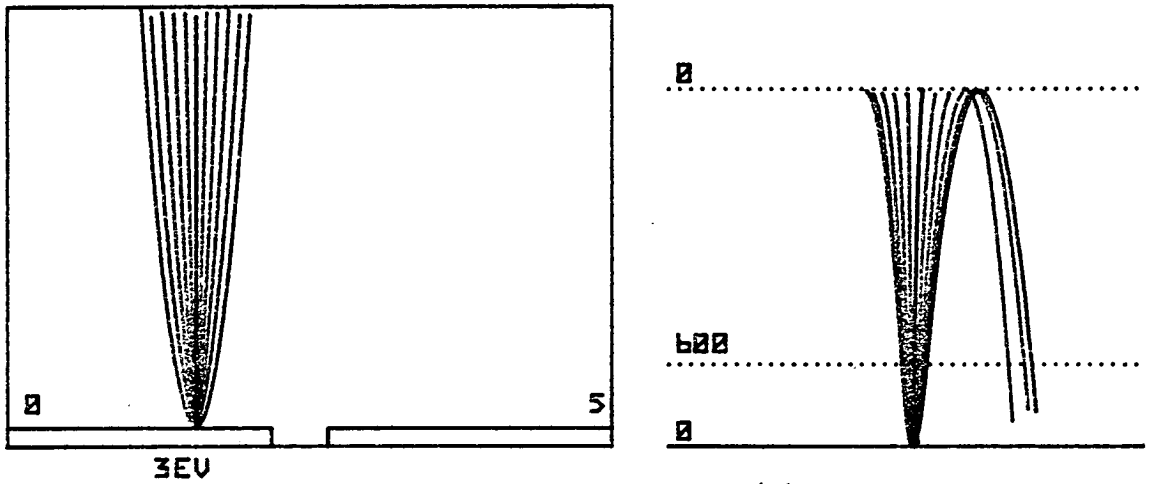


Figure 5.27(b)

Electrons Near a 21 micron Gap
with an emitted energy of 3eV

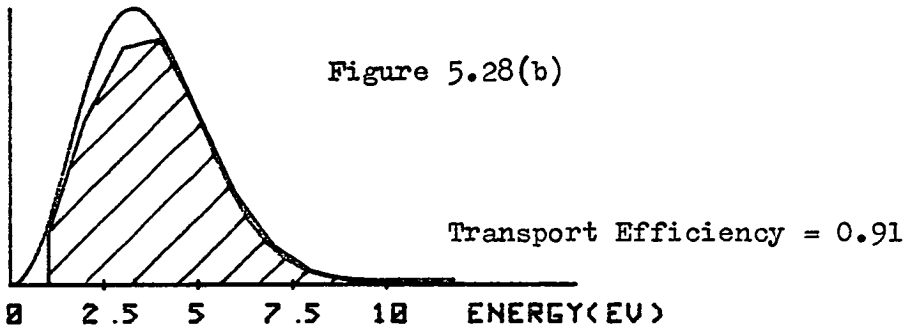


(21 micron gap)

Figure 5.28(a)

REL. NUMBER OF ELECTRONS

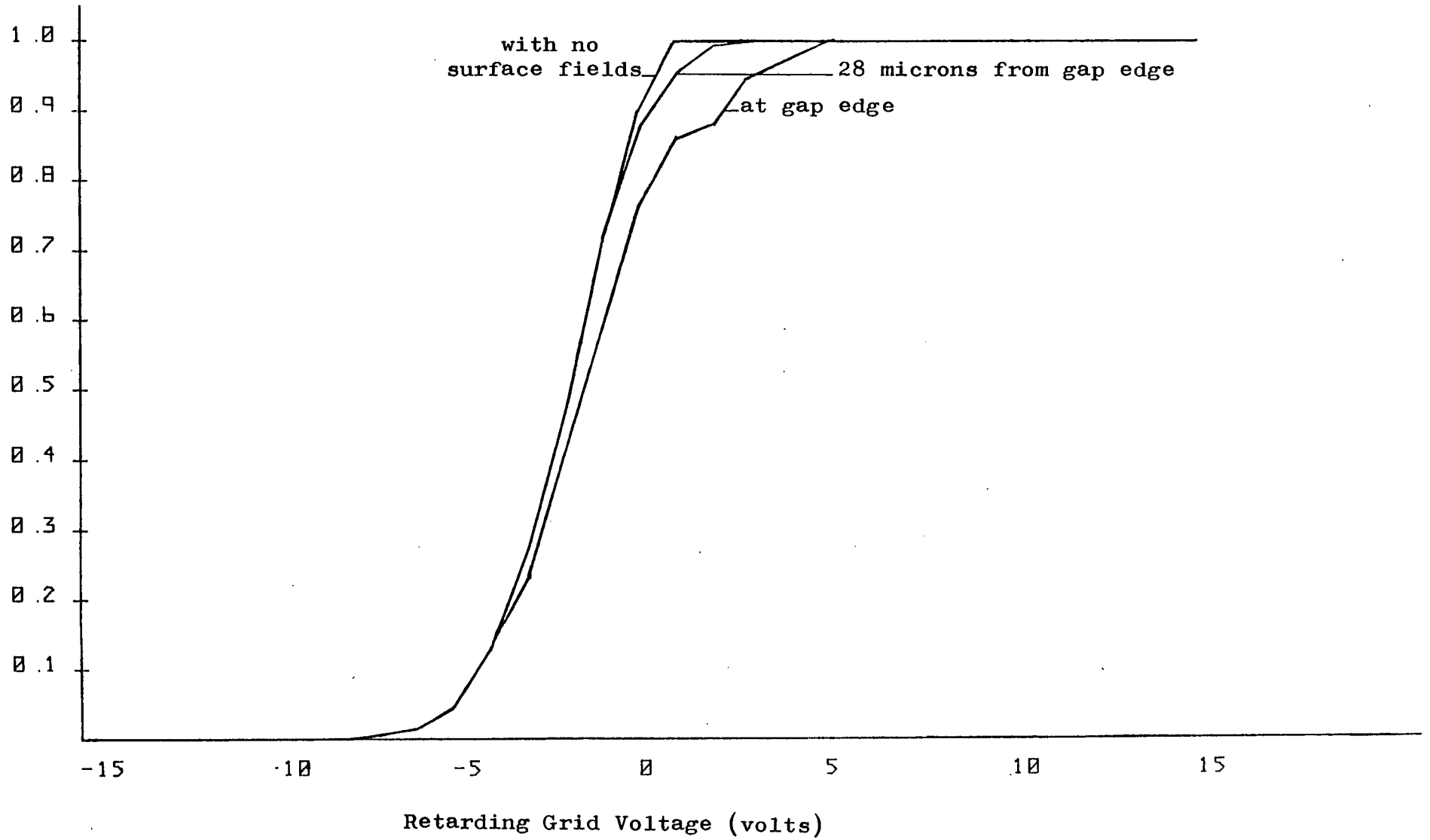
Figure 5.28(b)



Energy analysis of electrons near a 21 micron gap

S-curves for Different Positions Near a 21 micron Gap Layout

Figure 5.29



differing by a few percent over a small region in the retardation grid voltages of 0 to 2 volts.

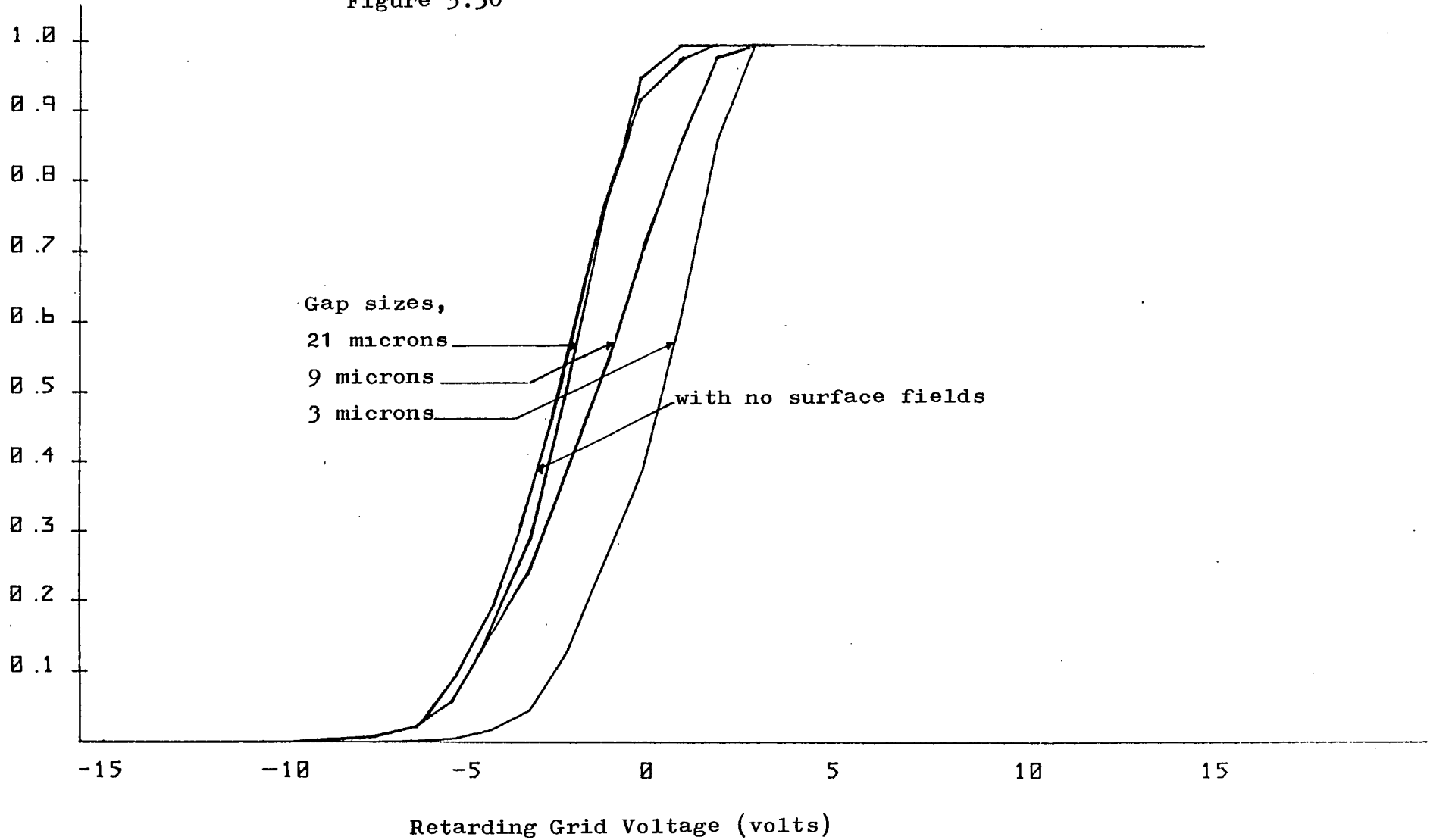
5.4.11 Single Gap Layout with a Negative Neighbouring Conductor

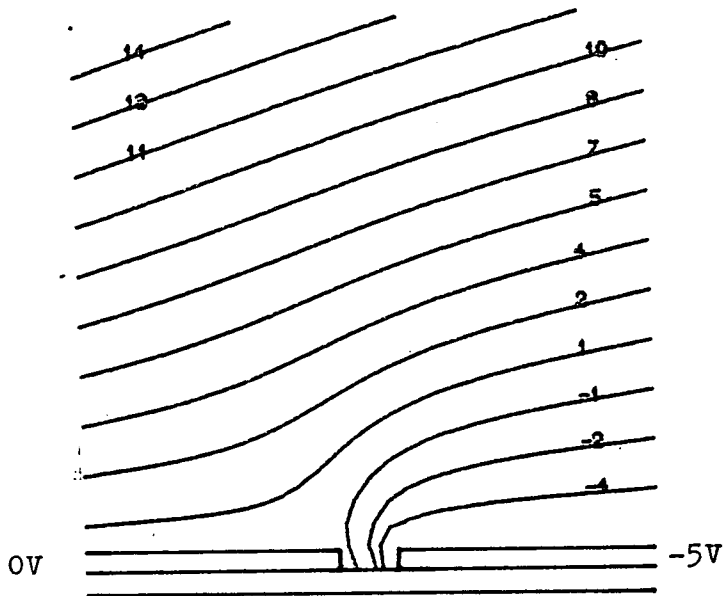
Figure 5.30 shows S-curves generated from a position on the edge of a 0 volt conductor with a neighbouring conductor at -5 volts. Different S-curves are plotted for the different gap sizes of 3, 9 and 21 microns and the normal S-curve is also plotted for comparison. Figure 5.30 indicates that a positive fictitious shift is caused by the influence of the neighbouring conductor and that this shift varies inversely with gap size. For the 3 micron gap the fictitious shift is as much as 2.5 volts. Figures 5.31(a) and 5.31(b) explain how a negative neighbouring conductor causes positive shifts in the measured S-curves. Figure 5.31(a) depicts the equipotential lines for a 3 micron gap, electron trajectories with initial energies of 3eV are traced through this field and shown in Figure 5.31(b). Clearly electrons suffer large deflections from their normal paths in the opposite direction from the neighbouring conductor; as a result no 3eV electrons traverse the retarding grid. Figures 5.32(a), 5.32(b), 5.33(a) and 5.33(b) show that the same is true for 9 and 21 micron gaps, only the neighbouring conductor does not have as much influence in these cases as in the 3 micron case.

Transport Efficiency

S-curves for Different Gap Sizes in a Single Gap Layout with a Negative Neighbouring Conductor

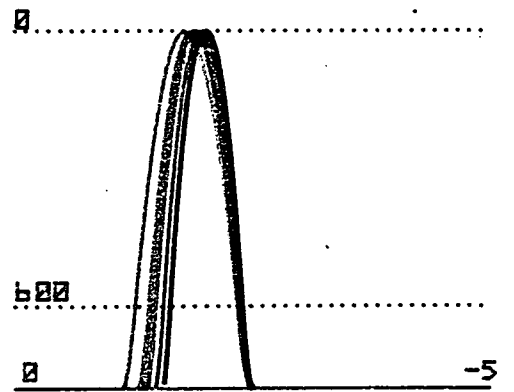
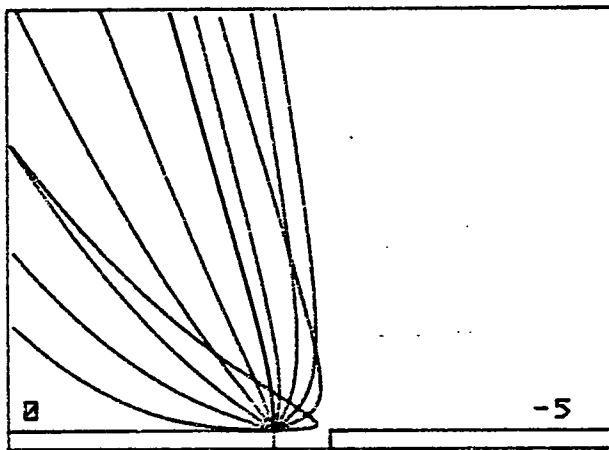
Figure 5.30





Equipotentials for a Single
3 micron Gap with a
Negative Neighbouring
Conductor

Figure 5.31(a)



3eV

Figure 5.31(b)

(3 micron gap)

Trajectories for a Single 3 micron gap with a Negative Neighbouring
and an emitted energy of 3eV

Equipotentials for a 9 micron gap with a Negative Neighbouring Conductor

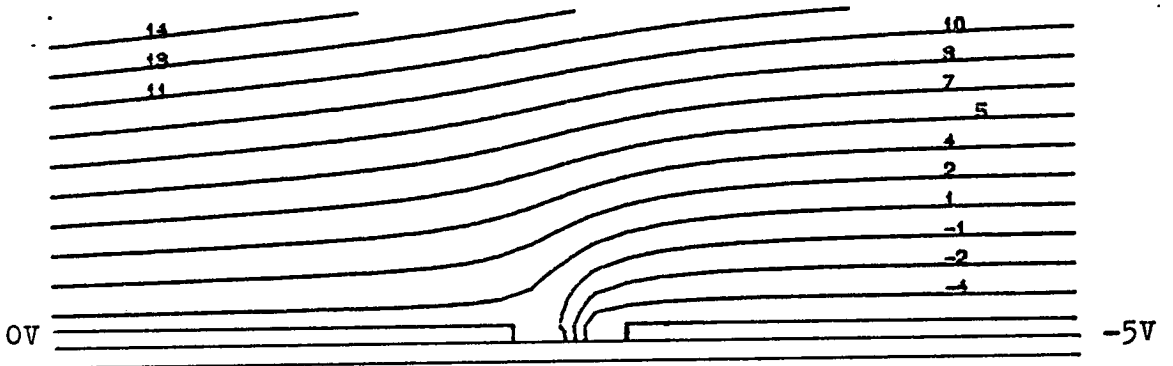


Figure 5.32(a)

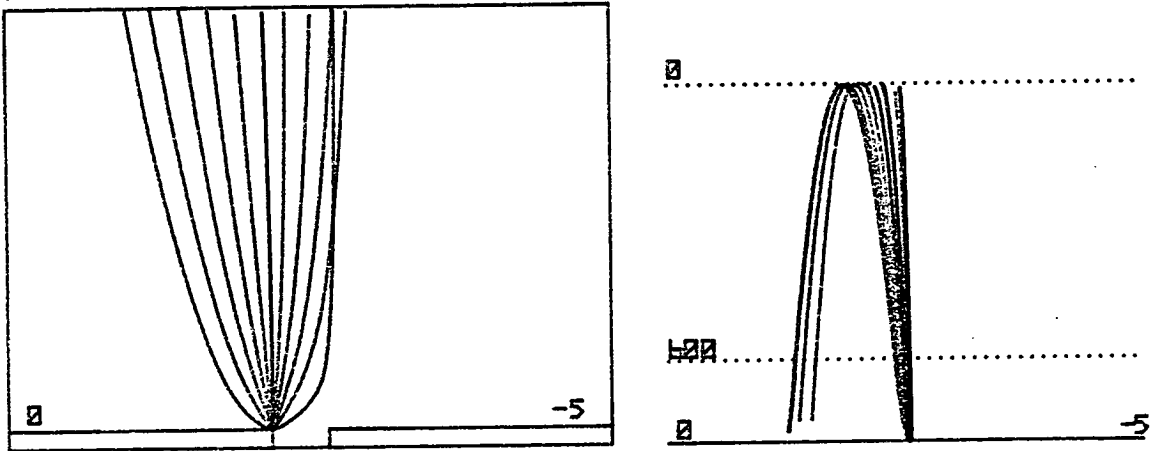


Figure 5.32(b)

(9 micron gap)

Trajectories for a 9 micron gap with a Negative Neighbouring conductor and an emitted energy of 3eV

Equipotentials for a Single 21 micron Gap Layout with a Negative Neighbouring Conductor

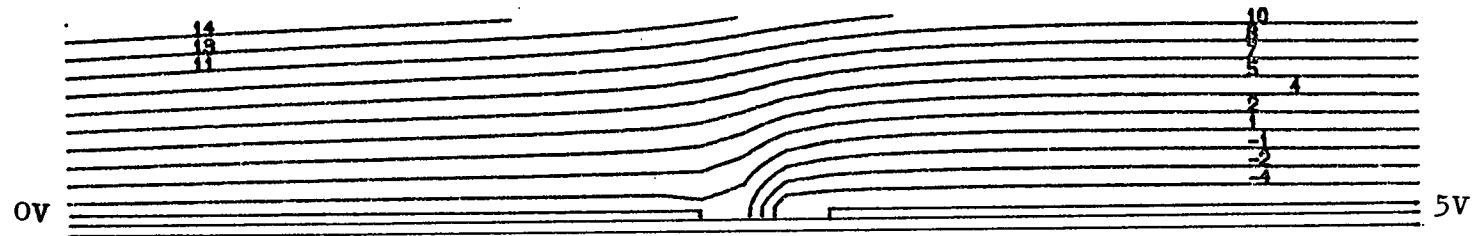


Figure 5.33(a)

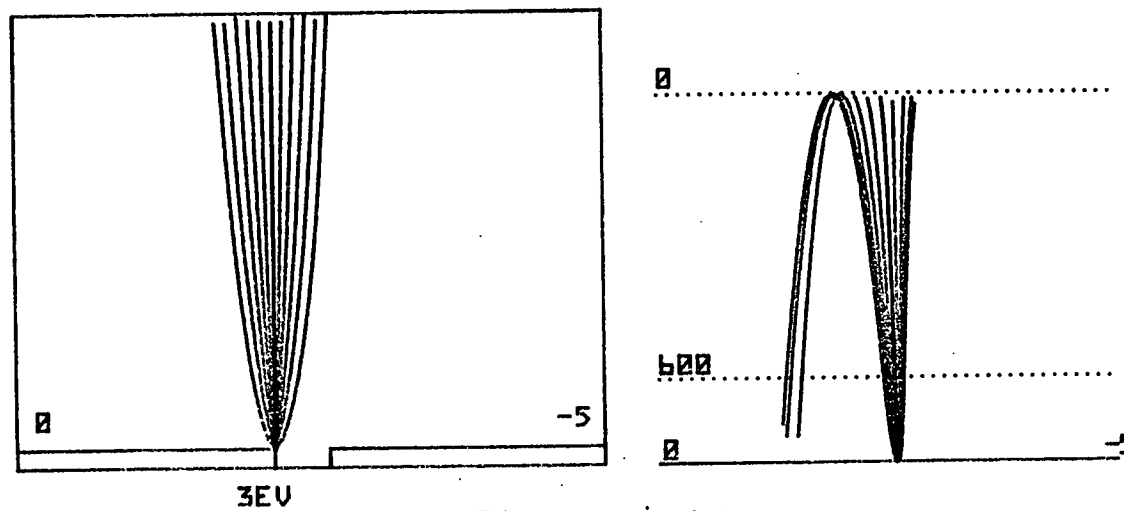


Figure 5.33(b)

(21 micron gap)

Trajectories for 21 micron gap layout with a negative neighbouring conductor and an emitted energy of 3eV

THREE CONDUCTOR LAYOUTS5.4.12 A Positive central track between two earthed conductors

Figures 5.34(a-c) show electron trajectories leaving the centre of a 5 volt, 3 micron track. The electrons leave the surface with initial energies of 3eV, 6eV and 10eV. These diagrams indicate that electrons undergo acute deflections as they leave the surface; however all electrons with the afore-mentioned energies reach the retarding grid. This is confirmed by Figure 5.34(d) which shows a large collection over the secondary electron range and gives an overall transport efficiency of 91%. In this respect the surface layout considered here is very different to the 3 micron single gap layout previously considered which with the same extraction voltage gave an overall transport efficiency of 27%.

Figures 5.35(a) and 5.35(b) show that almost the same number of electrons are collected (88%) if electrons leave at the edge of the central track.

Different S-curves for different extraction voltages are shown in Figure 5.36, in this case electrons leave the centre of the 5 volt track. The horizontal shifts of all the S-curves are close to the expected 5 volts, all lie between 4 to 4.5 volts in their linear regions. The height of each S-curve, however, varies sharply with extraction voltage. The overall transport efficiency varies from 91% at 600 volts to 11% at 0 volts, hence the surface fields arising from this three conductor layout can largely be overcome by increasing

A Positive Track Between Two Earthed Conductors

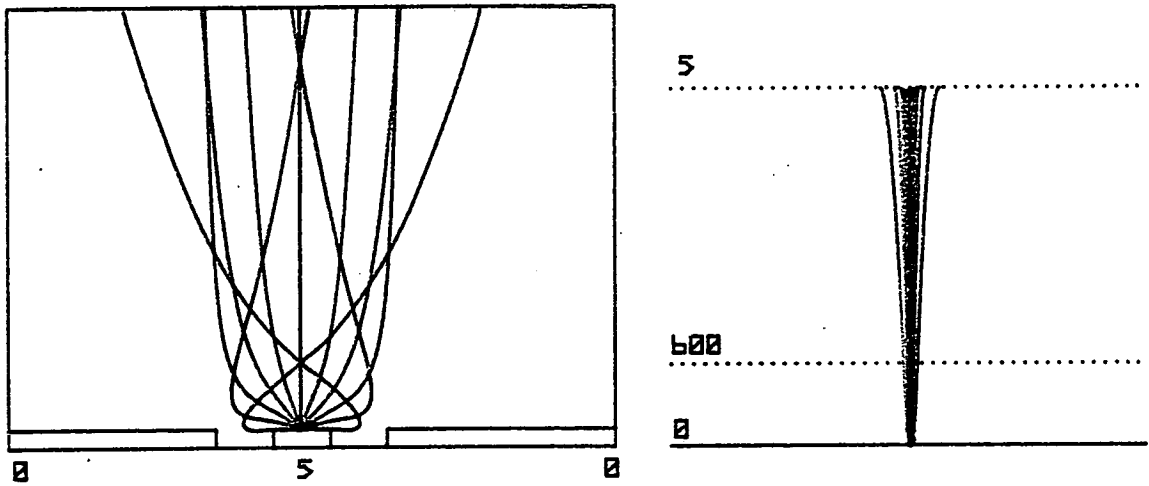


Figure 5.34(a)

3eV (3 micron gaps)

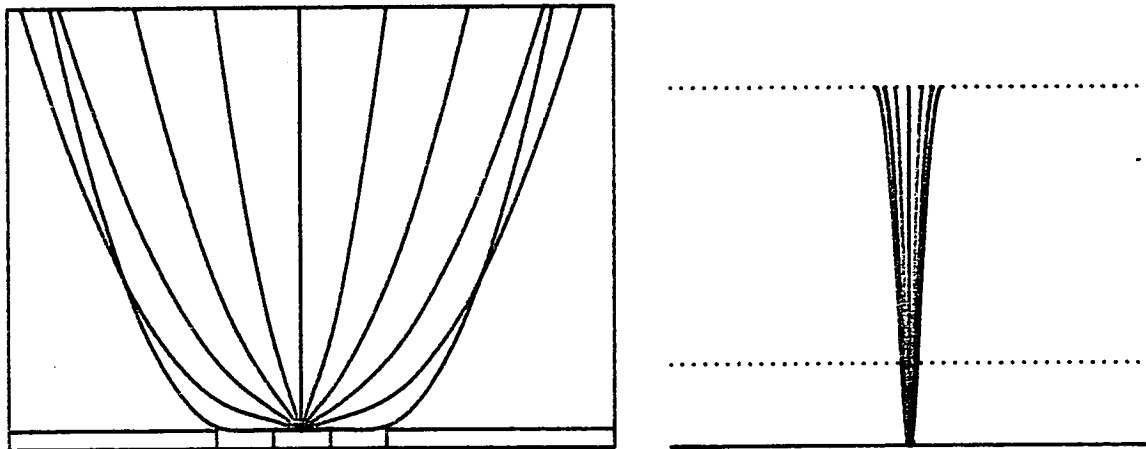
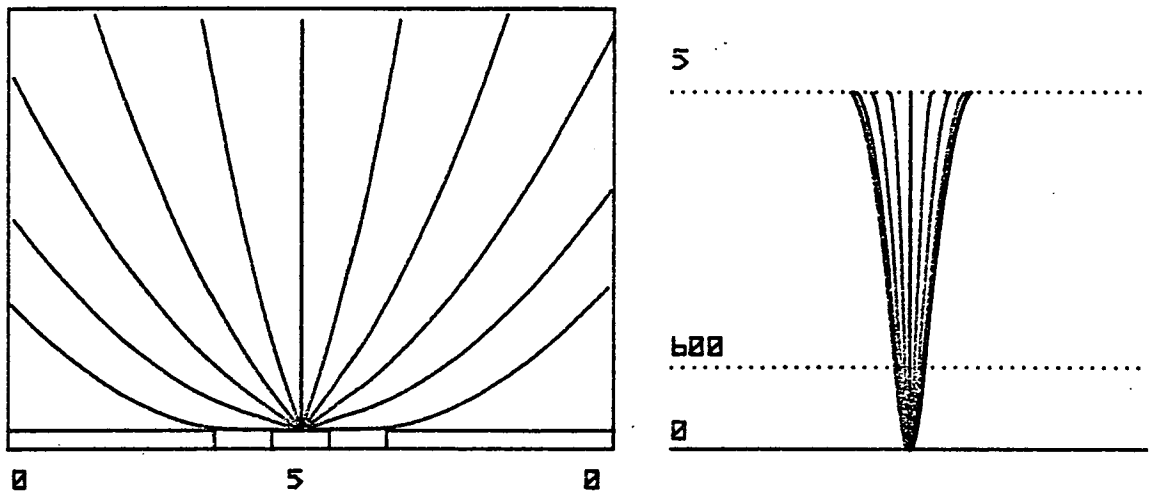


Figure 5.34(b)

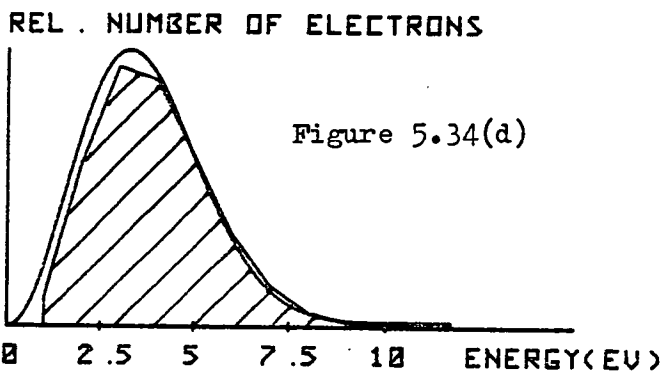
Trajectories at emitted energies of (a) 3eV
(b) 6eV

Trajectories for a positive track between two earthed conductors
and an emitted energy of 10eV



10 EU

Figure 5.34(c)

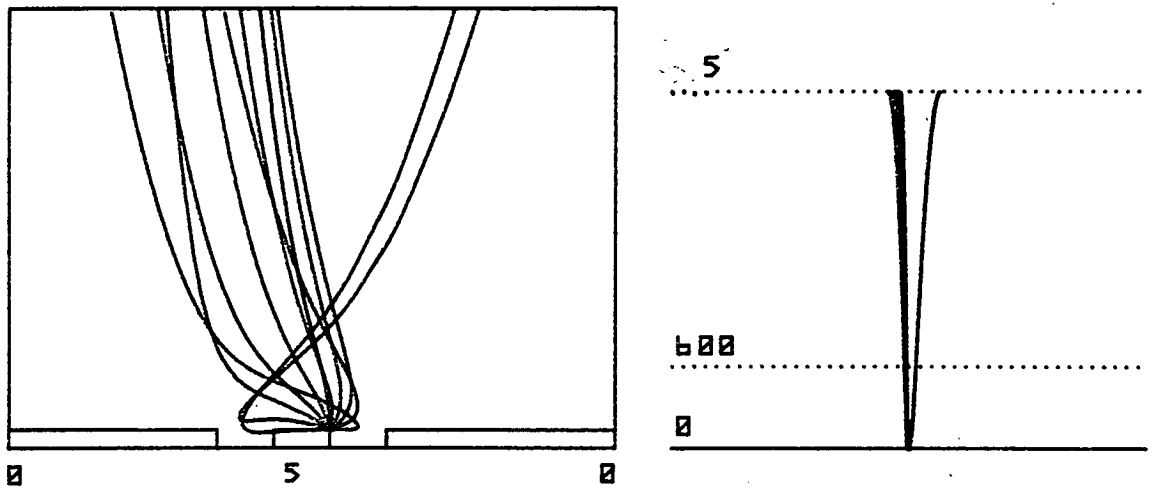


Transport Efficiency = 0.91

Energy analysis for a positive track between two earthed conductors

Trajectories leaving the gap edge of a positive track between two earthed conductors

Electrons are emitted with an energy of 3eV



3eV
(3 micron gaps)

Figure 5.35(a)

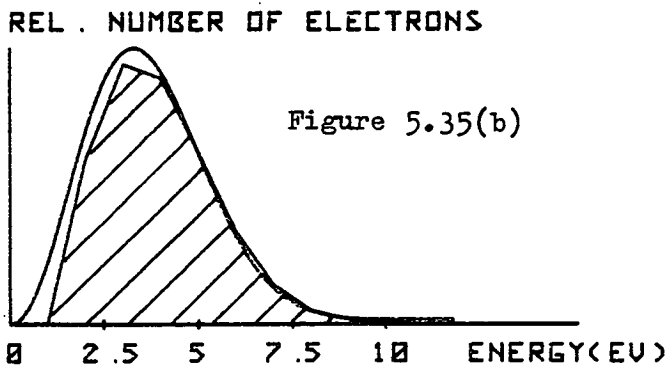


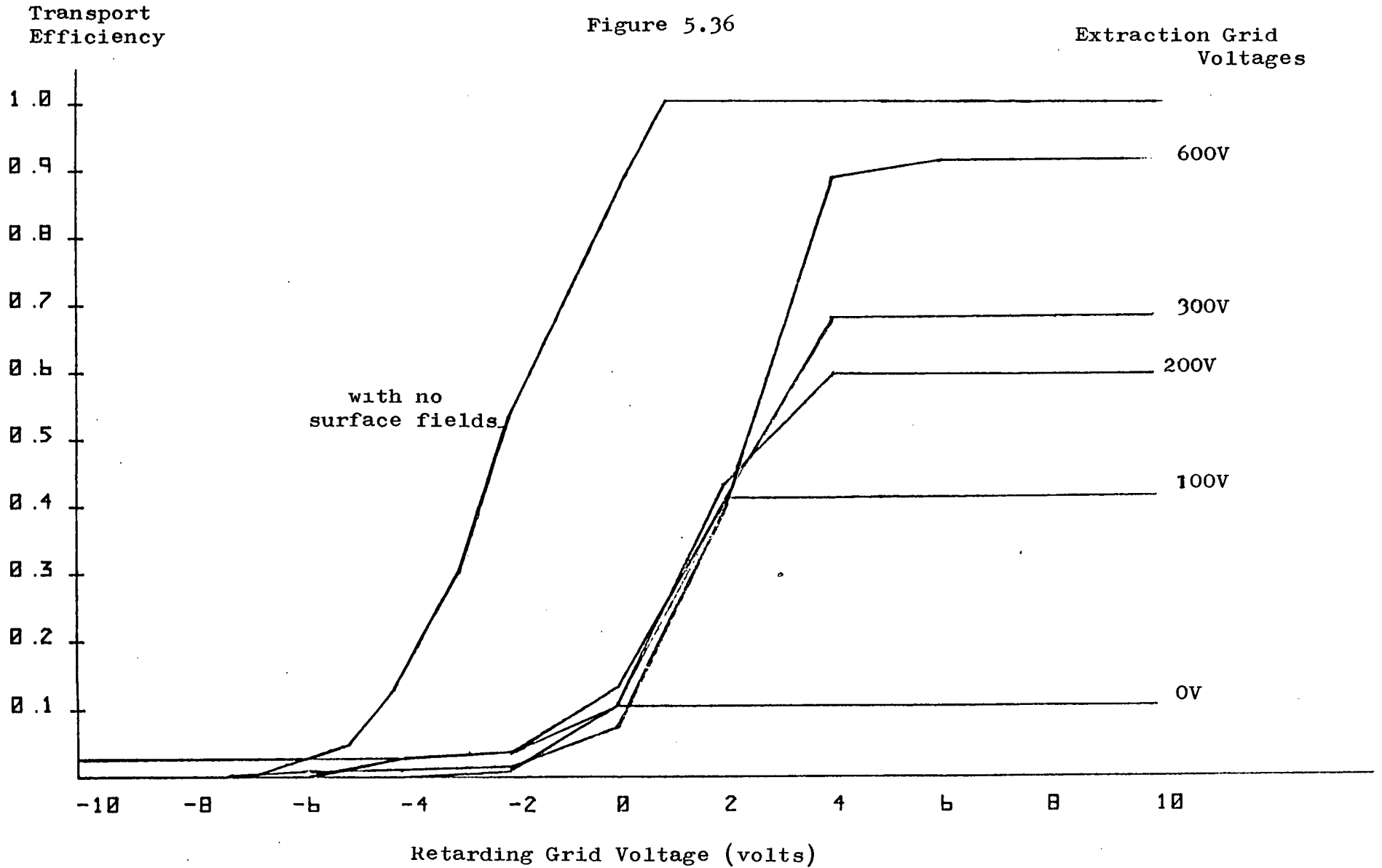
Figure 5.35(b)

Transport Efficiency = 0.88

Energy analysis for electrons leaving the gap edge of a positive track between two earthed conductors

S-curves for Different Extraction Grid Voltages above a 3 Conductor Layout

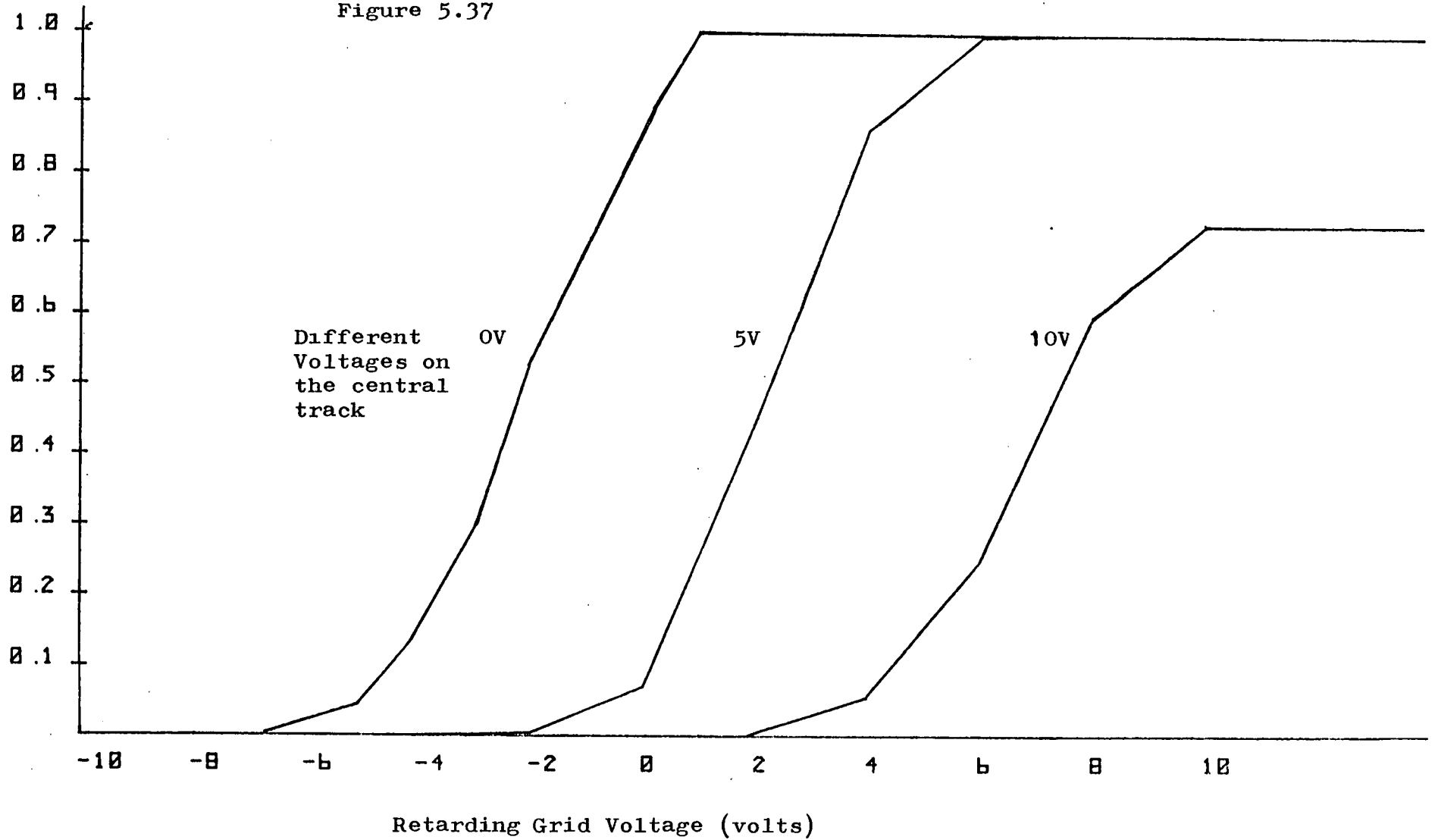
Figure 5.36



Transport Efficiency

S-curves for Different Voltages on a 90 micron Track with 0 volt Neighbouring Conductors

Figure 5.37

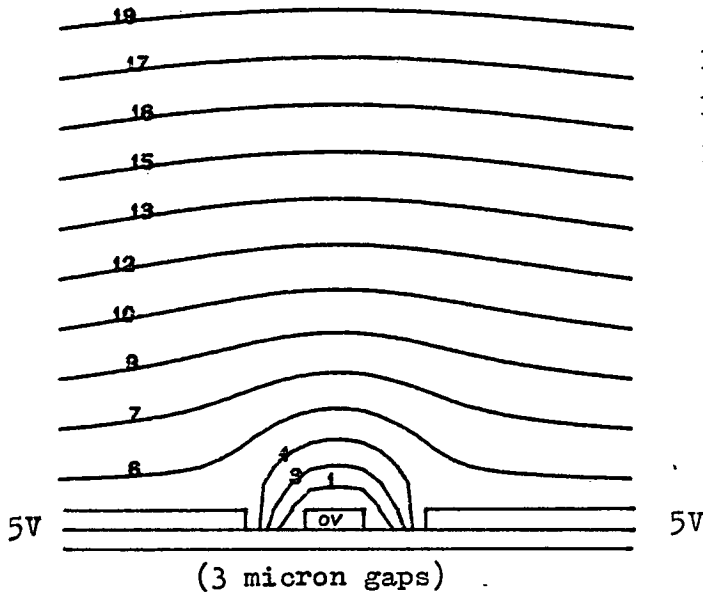


the extraction field.

At lower extraction fields, surface field effects can still be present for large gap sizes between a large track and its nearest neighbours. Figure 5.37 shows S-curves from the centre of a 90 micron track and with gap sizes of 90 microns to its 0 volt nearest neighbouring conductors. The voltage at the central track is changed to 0, 5 and 10 volts and a different S-curve is generated for each voltage. The 0 volt S-curve is as expected and corresponds to the 'normal' S-curve previously calculated. The 5 volt S-curve shifts from 4 to 5 volts away from the 0 volt S-curve, indicating the slight surface field effects from the neighbouring conductors. The 10 volt S-curve drops in height to 72% and shifts 4 to 5.2 volts away from the 5 volt S-curve. All S-curves were calculated for an extraction grid voltage of 80 volts. This result shows that surface fields can affect voltage measurements even on large conductor areas on a specimen, their effect can be reduced greatly however by increasing the extraction field.

5.4.13 An Earthed Track between Two Large Positive Conductors

Results have been obtained for an earthed track, 3 microns wide between two 5 volt infinitely wide conductors with gap sizes also 3 microns. Figure 5.38(a) shows equipotential lines for this configuration in which an extraction voltage of 600 volts was used. Electron trajectories at initial energies of 3eV were traced through the field with initial positions at the centre of the earthed track and the results are shown in Figure 5.38(b). Electrons leaving with



Equipotentials for an Earthed Track between Two Large Positive Conductors (Extraction grid voltage of 600 volts)

Figure 5.38(a)

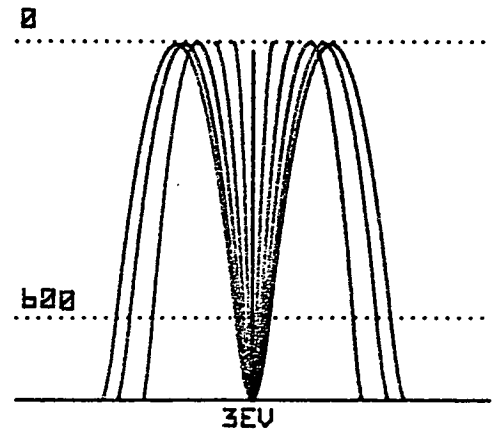
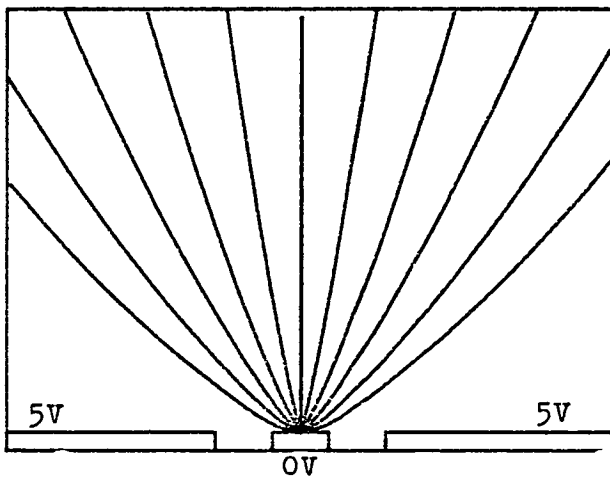


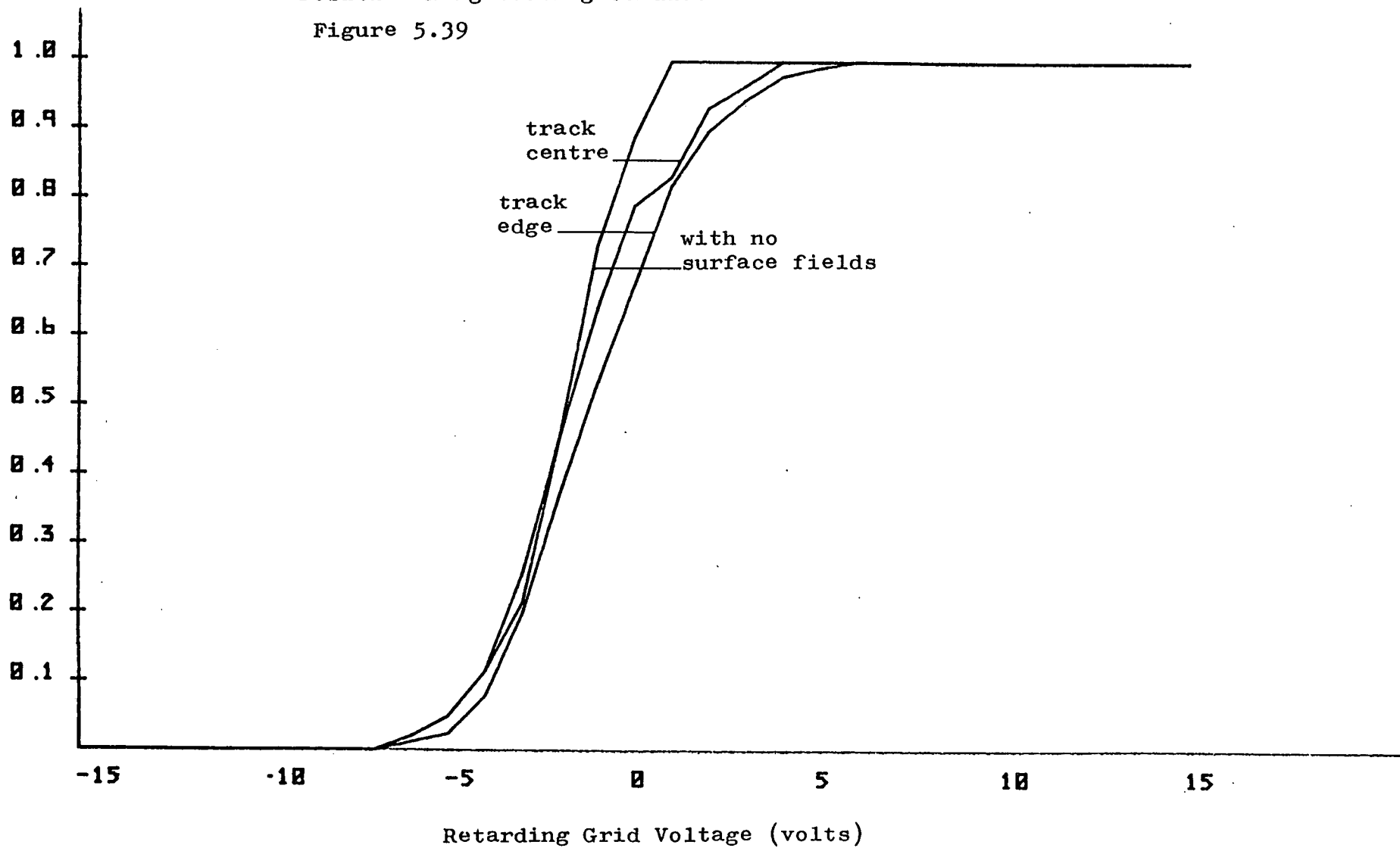
Figure 5.38(b)

Trajectories for an earthed track between two large positive conductors and an emitted energy of 3eV

Transport Efficiency

S-curves for Different Positions on a 3 micron Central Track with Positive Neighbouring Conductors

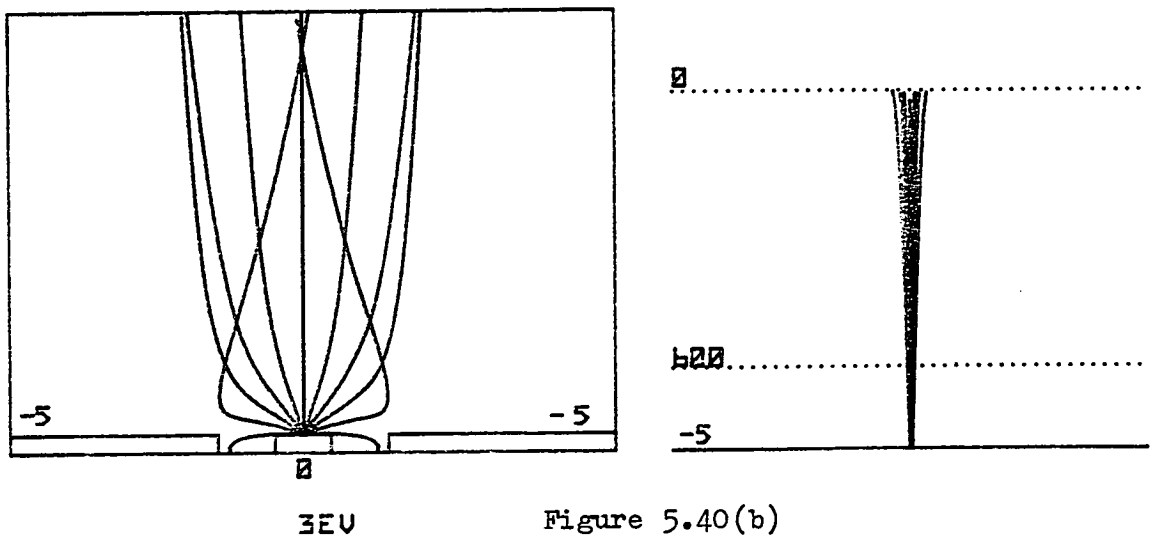
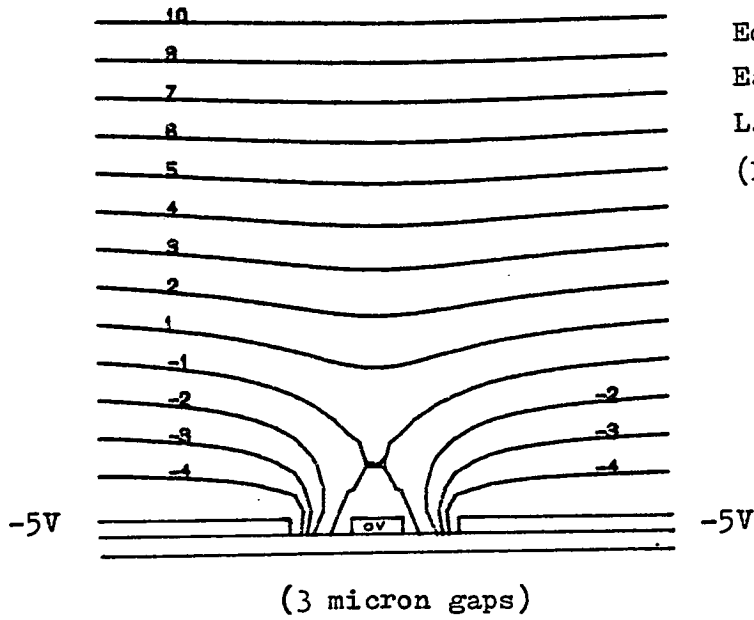
Figure 5.39



small angles to the specimen are seen to be attracted to the neighbouring conductors and 90% of the electrons reach the retarding grid. Figure 5.39 shows S-curves for electrons leaving the centre and edge of the middle track. Both the S-curves are close to the normal expected S-curve and have slight positive shifts of up to 1.5 volts in their linear regions. The S-curve for the track centre keeps a shift of 0.5 volts for most of its linear region while the S-curve from the track edge is larger—below 1 volt for most of its linear region. In this case as with the last layout, surface fields have been greatly reduced at an extraction voltage of 600 volts.

5.4.14 An Earthed Track between Two Negatively Biased Conductors

Figures 5.40(a) and 5.40(b) show equipotential lines and electron trajectories for electrons leaving the centre of a 3 micron track. The track lies between two infinitely wide conductors which are biased to -5 volts, both conductors lie 3 microns away from the central track. Figure 5.40(b) shows how electrons of an initial energy of 3eV undergo large deviations from their normal trajectory paths. This is particularly true for electrons close to the horizontal. However for most electrons, the surrounding conductors seem to have a focussing effect and most electrons reach the retarding grid. The extraction voltage was kept at 600 volts. An S-curve was plotted for this case and is compared to the normal 0 volt S-curve, both are shown in Figure 5.41. The S-curve generated from the central track seems to shift slightly negatively, 0.44 to 0.75 volts and also drops in height to 92%.

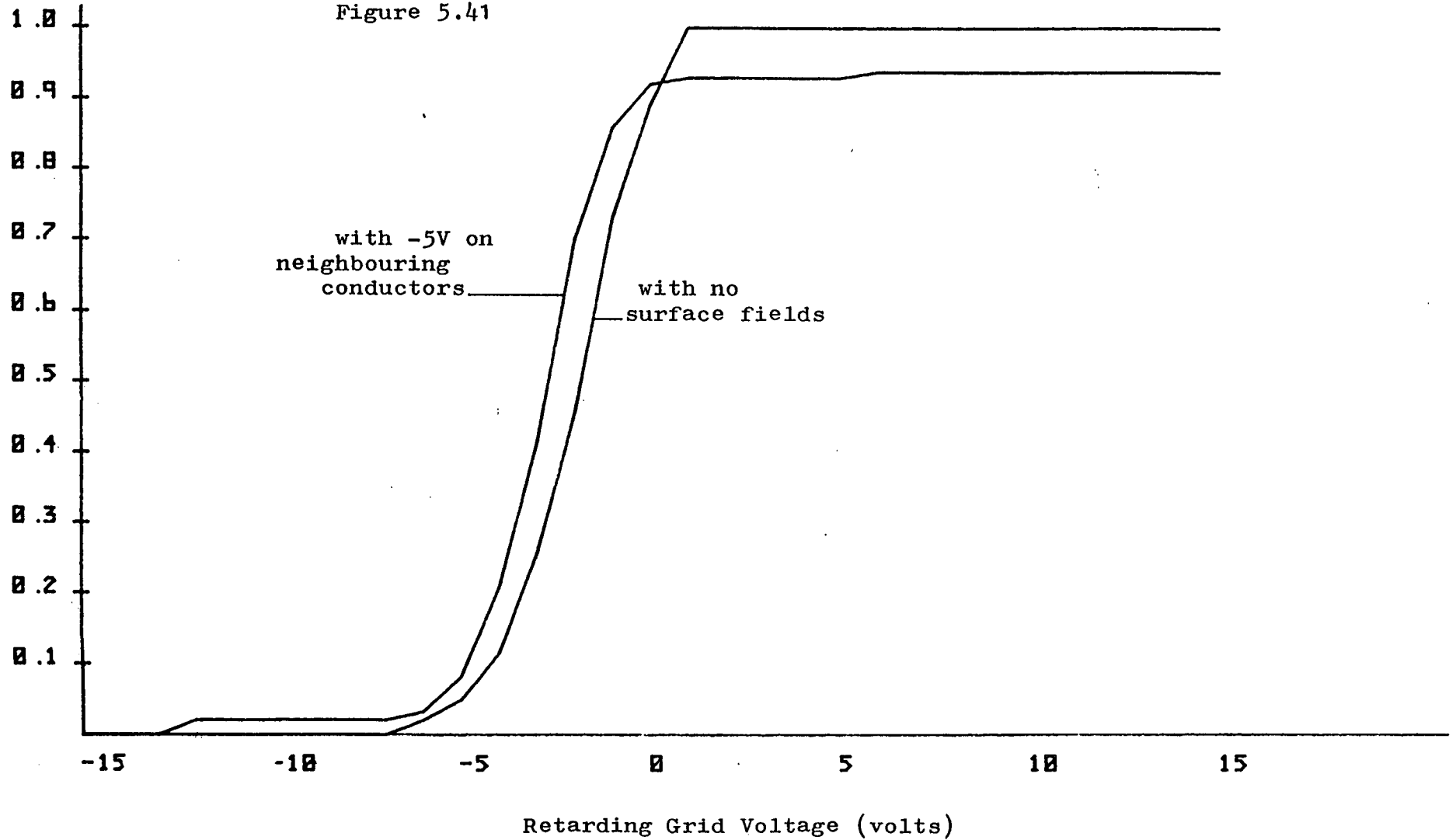


Trajectories for an earthed conductor between two large negative conductors and an emitted energy of 3eV

Transport Efficiency

S-curve for Electrons Leaving a 3 micron Central Track with Negative Neighbouring Conductors

Figure 5.41



5.5 Surface Fields in Hemispherical Detectors

5.5.1 Introduction

The surface field program for a linear retarding field was used to approximate the field variation within the first mesh above the specimen in Fentem's detector. The voltage at the top of this square as stated before was found to be 5.9 volts. This voltage was taken to be the extraction grid voltage in the normal surface field program. It corresponds to a position of 0.5mm above the specimen in Fentem's detector.

Electron trajectories were traced through the surface mesh F1 in the surface field program and their positions and velocities on traversing the surface mesh boundaries were noted and stored. This information was in turn used as initial conditions for plotting trajectories in Fentem's detector. Hence a single complete electron trajectory was made up of two parts; the first part is traced using the normal linear surface field program in surface mesh F1; the second part of the trajectory is traced in Fentem's detector. The retarding grid in Fentem's detector was initially set to -5 volts.

5.5.2 Results

A 3 micron track at 5 volts was specified between two infinitely wide 0 volt conductors, their separation gaps were chosen to be 3 microns. Figure 5.42(a) shows 3eV electron trajectories leaving the middle of the centre track. All these electrons are seen to be quickly attracted back to the track. Figure 5.42(b) shows that the

same is true for electrons leaving the track edge. This result is not unexpected when considering the low extraction field present above the surface layout—5.9 volts a distance of 0.5mm away from the specimen. The results from sections 5.12–5.14 show that such relatively low extraction fields greatly reduce the collection efficiency for the three conductor layout considered here. Figure 5.42(c) shows the energy transport efficiency curve for complete electron trajectories through the surface fields and Fentem's detector. Only 23% of all emitted electrons below 12eV reach the final collection electrode on Fentem's detector. A lower cut-off energy of 5eV is indicated in Figure 5.42(c) which implies the presence of a 5 volt retarding field directly above the central track on the specimen.

Figure 5.43(a) show final S-curves for different track and gap sizes on the three conductor surface layout. All S-curves are greatly reduced in height; 41%, 30% and 22% for track and gap sizes of 21mm, 9mm and 3mm respectively. The S-curves appear by their position to indicate a 0 volt central track, which implies that they have undergone a negative fictitious shift of 5 volts. Figure 5.43(b) shows similar curves for electrons leaving the central track edge; these S-curves, however, have slightly lower heights than those in Figure 5.43(a). Since Tee's detector has a similar low extraction field as that of Fentem's detector, it is predicted that Tee's detector will also produce S-curves like those in Figures 5.43(a) and 5.43(b) for the same specimen conditions. The above results show that the two hemispherical detectors considered are

Trajectories leaving a positive track between two earthed conductors in the Fentem detector

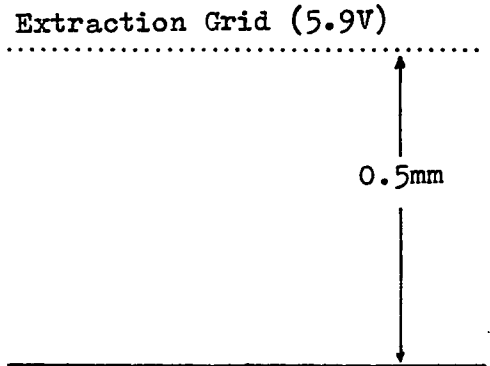
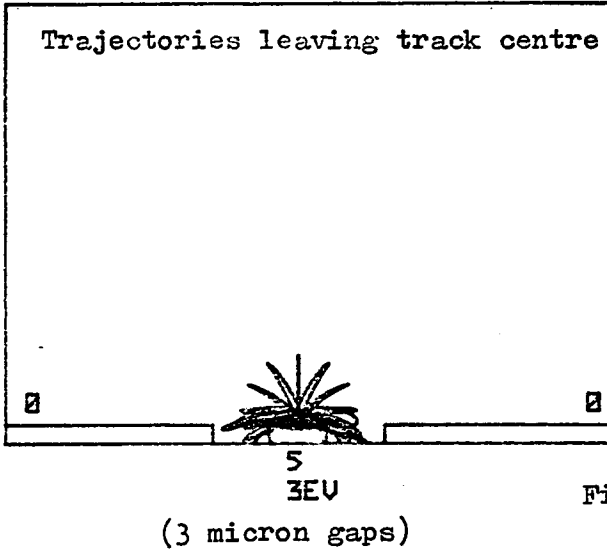


Figure 5.42(a)

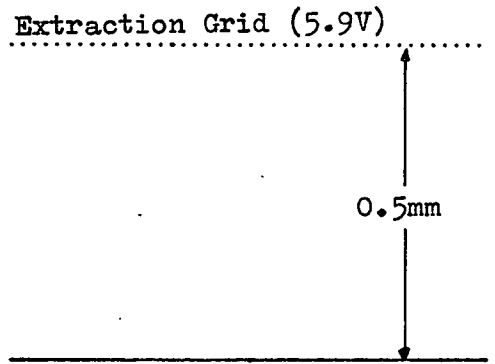
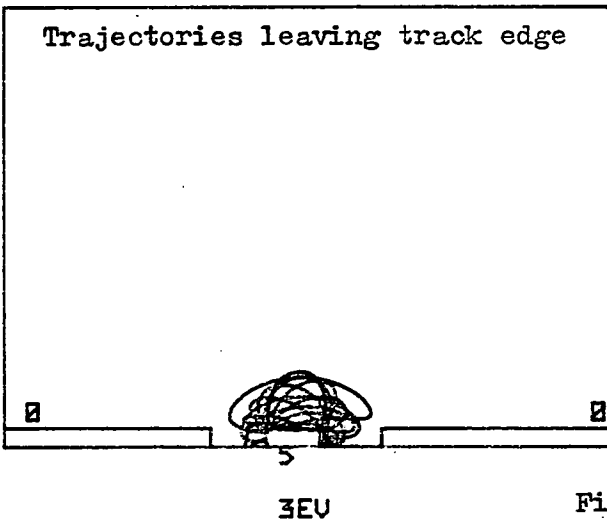
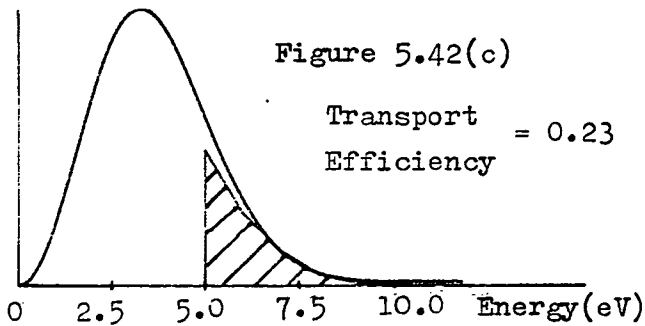


Figure 5.42(b)

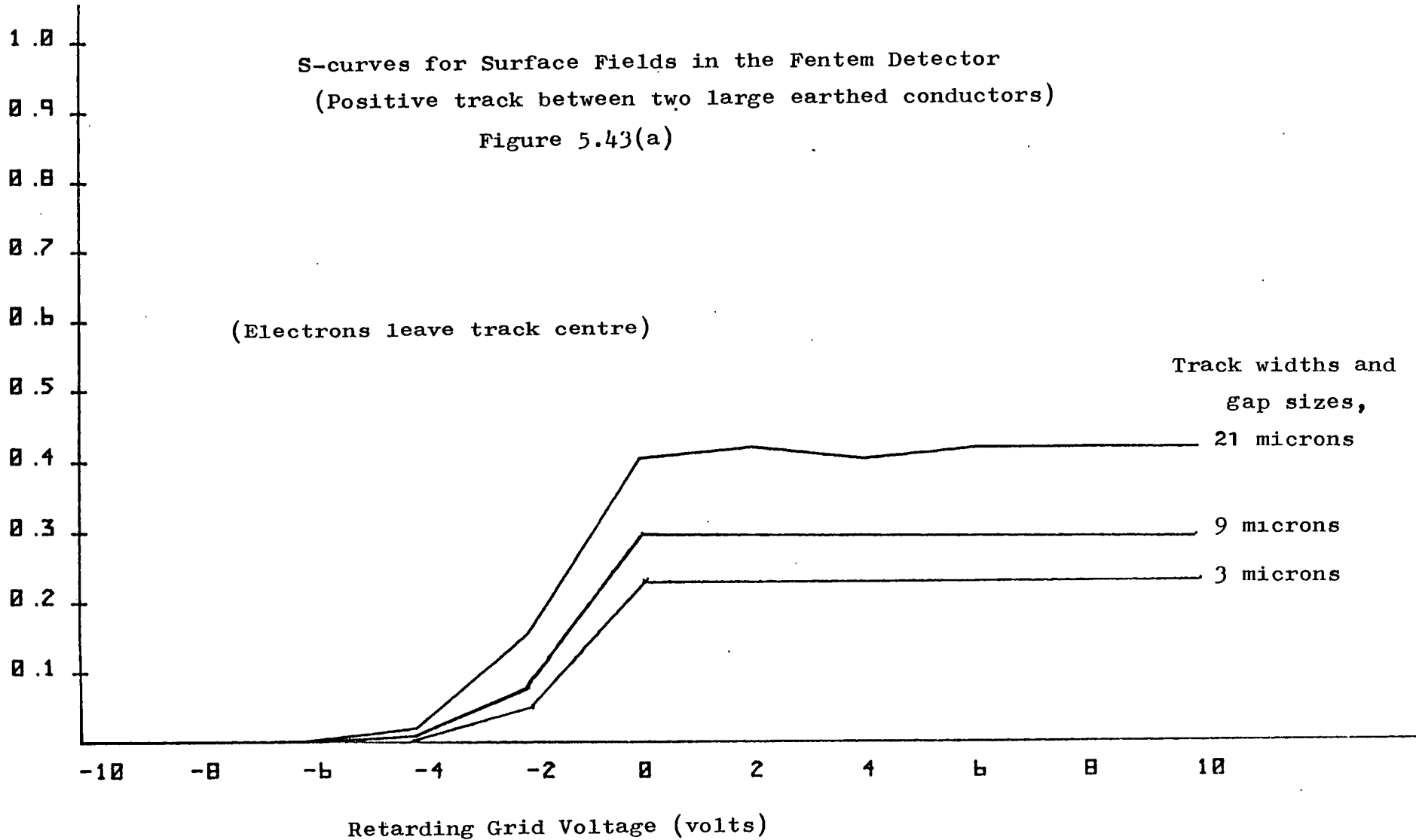
Relative number of electrons



Energy analysis for a positive track between two earthed conductors in the Fentem Detector

Transport
Efficiency

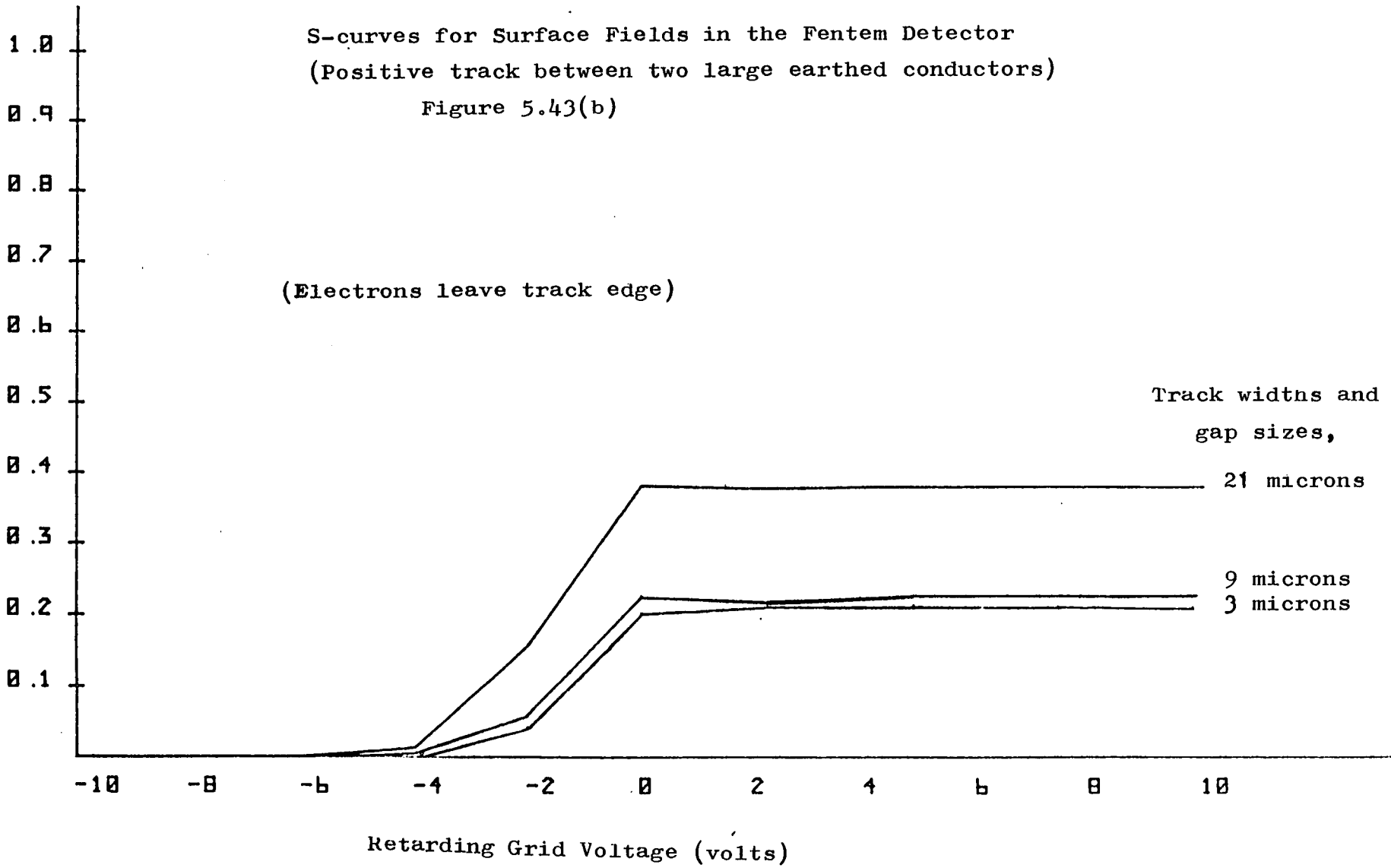
S-curves for Surface Fields in the Pentem Detector
(Positive track between two large earthed conductors)
Figure 5.43(a)



Transport
Efficiency

S-curves for Surface Fields in the Fentem Detector
(Positive track between two large earthed conductors)

Figure 5.43(b)



inadequately designed to cope with voltage measurements under strong surface field conditions.

5.6 Surface Fields In the Feuerbaum Detector

The surface field program was used to plot electron trajectories through the lower half of the Feuerbaum detector. This was done without writing extra programs, since the Feuerbaum detector is a linear retarding field detector and simple modifications were made to existing programs. The positions and velocities were stored for electrons that had reached the retarding grid in the surface field program. This information was used as initial conditions for the plotting of electron trajectories in the Feuerbaum detector.

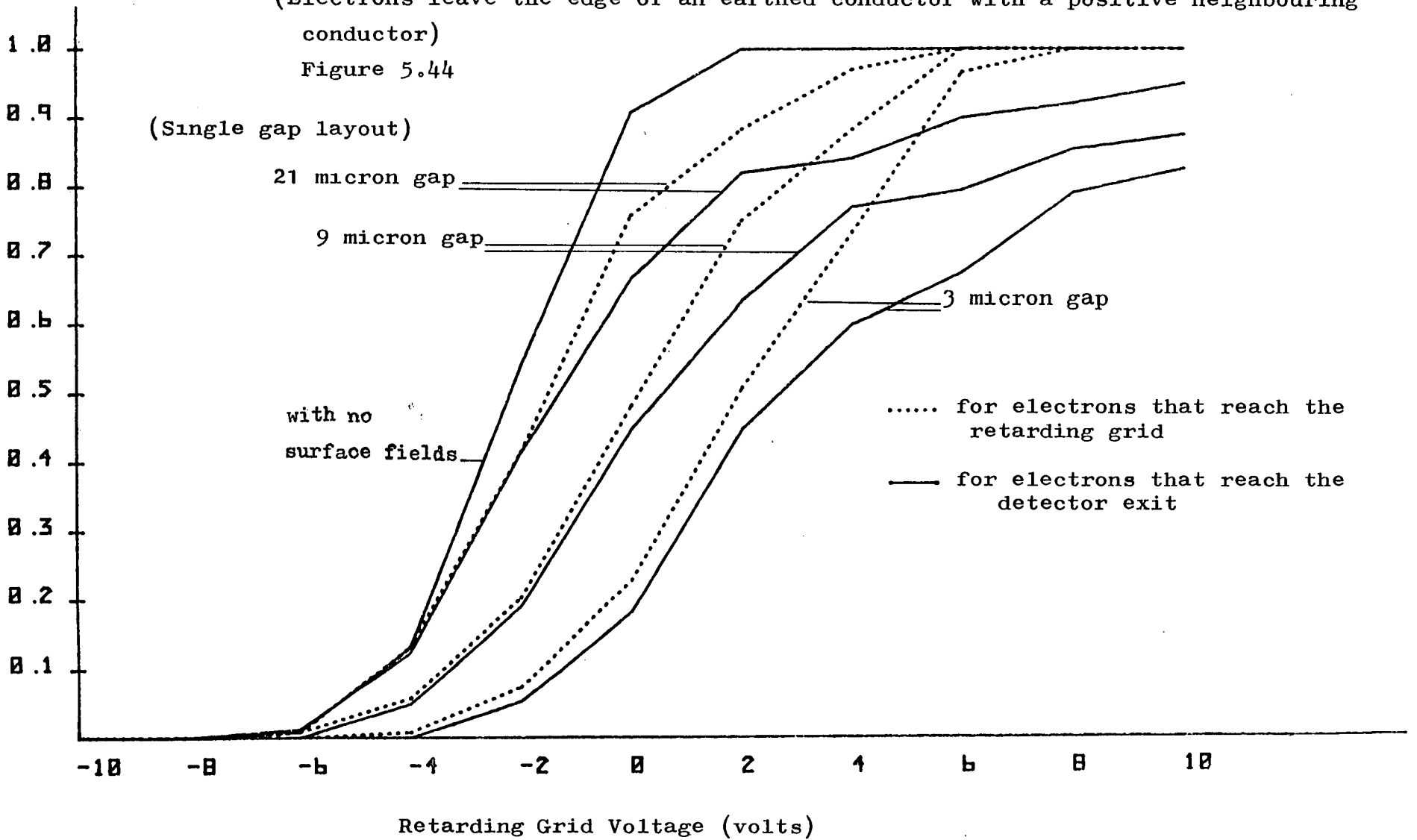
A single gap (Figure(5.3(b))) layout was specified in which electrons left the edge of an infinite 0 volt conductor, the neighbouring conductor was biased to 5 volts. Figure 5.44 shows S-curves for electrons reaching the retarding grid in the Feuerbaum detector, these S-curves were generated for the different gap sizes of 3, 9 and 21 microns on the specimen layout. The 3 micron curve has the greatest deviance from the normal S-curve, a fictitious shift of 2.8 to 4.6 volts is observed in its linear region. On the same graph is shown the final S-curves obtained on the collection gauze of the Feuerbaum detector. These final S-curves are more non-linear and less like an 'S' shape. They do not rise to a definite plateau and voltage measurements would be difficult to make from them. The final S-curves are also seen to drop in height at their final current values, 94%, 84% and 82% for gap sizes 21, 9, and 3 microns on the specimen. In the linear region for the 3 micron curve, fictitious shifts exceed 5 volts.

Transport Efficiency

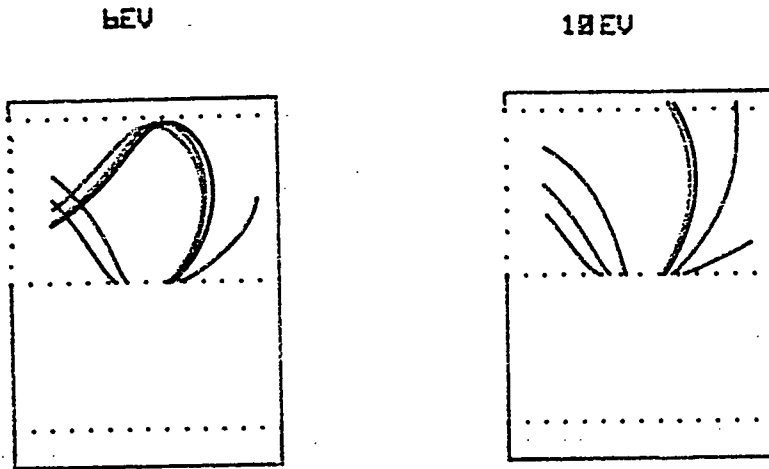
S-curves for Surface Fields in the Feuerbaum Detector

(Electrons leave the edge of an earthed conductor with a positive neighbouring conductor)

Figure 5.44



Effect of Surface Fields in the Feuerbaum Detector for a
Single Gap Layout



Electron Trajectories
for emission energies
of
3eV - (c), (f)
6eV - (a), (d), (g)
10eV - (b), (e), (h)

Figure 5.45(a) (3 micron gap) Figure 5.45(b)

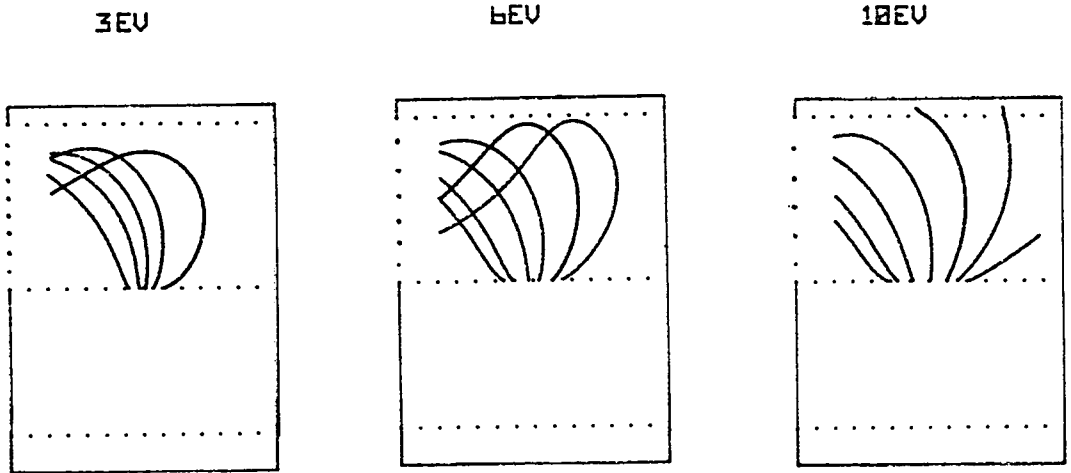


Figure 5.45(c)

Figure 5.45(d)
(9 micron gap)

Figure 5.45(e)

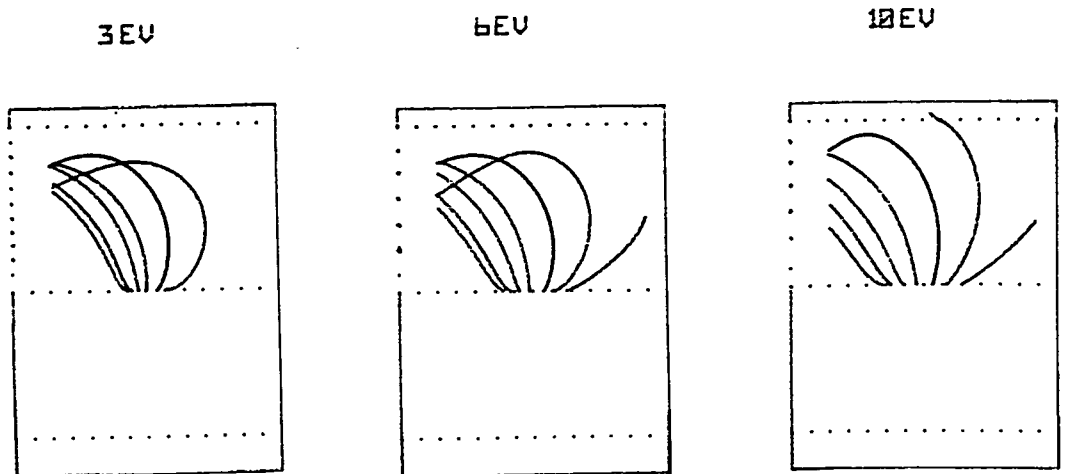


Figure 5.45(f)

Figure 5.45(g)
(21 micron gap)

Figure 5.45(h)

Figures 5.45(a-h) show electrons in the Feuerbaum detector after traversing the surface fields; no 3eV electrons were plotted since none of these electrons reached the retarding grid. Only a moderate percentage of electrons of initial energies higher than 6eV are deflected successfully by the deflection field in the Feuerbaum detector. However, electron collection is better in this respect for the 21 and 9 micron gaps than for the 3 micron gap. It is also apparent from Figures 5.45(a-h) that generally only 50% of emitted electrons in the Z-X plane for 21 and 9 micron gap sizes reach the retarding grid. From the above results it is seen that the linear retarding field of Feuerbaum's detector cannot cope with voltage measurements on conductors separated by a small gap. The deflection field also exhibits a non-linear response in the final collected S-curves in these cases.

Summary

Development of computer techniques to model surface fields was made. A method of graded meshes in finite-difference form was used and both single and double gap electrode layouts were analysed. A large percentage of electrons leaving a conductor near a single gap were affected by surface fields and were deflected back to the surface. Increasing the extraction grid voltage did not significantly reduce the effect of surface fields in this case. Increasing the extraction grid voltage in the double gap layout however, did significantly reduce the surface fields present. Electron trajectories in Fentem's detector were found to be affected by the surface fields created by a double gap layout while the same was

true in Feuerbaum's detector for a single gap layout.

CHAPTER 6DESIGN OF A NEW VOLTAGE CONTRAST DETECTOR6.1 Introduction

In the previous chapters the, Dinnis, Lintech, Fentem and Feuerbaum detectors have been analysed and of these the Feuerbaum detector gives the better performance. The aim of this chapter is to design a new voltage contrast detector which gives comparable or better performance than that of Feuerbaum's detector. The general requirements of a voltage contrast detector are:

- 1) That it produce S-curves which shift linearly with specimen voltage variations
- 2) It have a high transport efficiency giving an acceptable output signal/noise ratio
- 3) Backscattered electrons should be filtered from the collected secondary electrons
- 4) The effect of surface fields should be minimised
- 5) The detector must have low constructional height in order to give a moderate working distance in the S.E.M.

From Chapter 3 it was found that two curved grids provided an efficient deflection field, the lower grid was set to 100 volts while the upper grid was set to -5 volts. Figure 3.29 shows electron trajectories through such a system. The deflection field was placed on top of a normal planar retarding field. This detector model was analysed in two-dimensional rectilinear coordinates and did not simulate electrons in all directions. A three-dimensional model

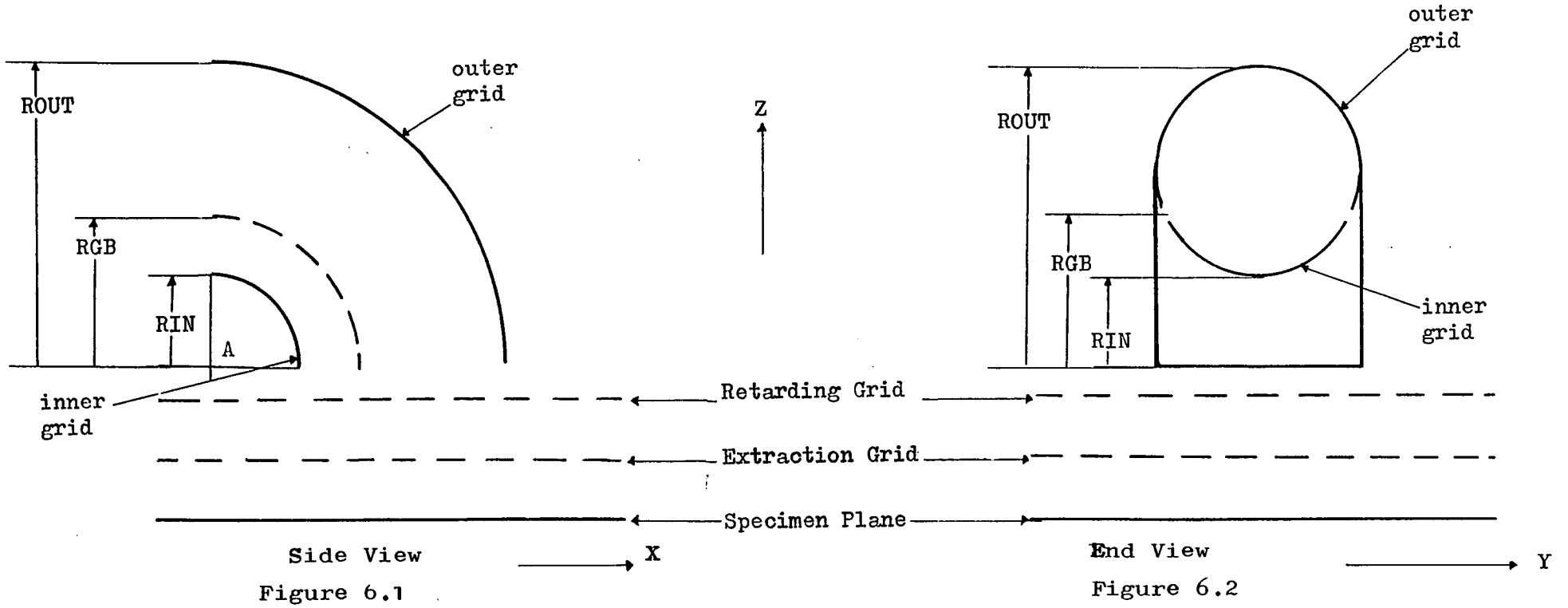
based on the two-dimensional curved grid model was made. The grids in this case were still curved but now were also made cylindrical, hence the deflecting field had a curved tube geometry. The curved tube arrangement consisted of two portions, a lower grid at 100 volts and an upper grid at -5 volts. Figures 6.1 and 6.2 show the side and end views of the detector. The retarding field remained unchanged. The purpose in having cylindrical symmetry in the deflection field was to collect electrons in all possible directions in the X-Y plane or with all possible angles in the azimuth direction.

Initial computer simulations were made on the proposed cylindrical tube detector and its design was optimised.

6.2 Program Model to Simulate a Curved-tube Detector

A program was written to simulate the performance of the suggested twin-grid curved tube detector. The program was based on a model in three-dimensional coordinates. Initial dimensions were given to the detector but these were later modified as the detector was optimised. The computer model was based upon the side and end views shown in Figures 6.1 and 6.2. R_{gb} defines the boundary between the upper and lower grids in the deflection field. The inner and outer dimensions of the curved cylinder are given by R_{in} and R_{out} respectively. These distances are given with respect to the point A, defining the position of the deflection grids with respect to the rest of the detector. All dimensions shown were interactively

New Detector



specified by the programmer.

6.2.1 The Potential Distribution in the Deflection Field

No readily available analytical solution to the potential distribution for the designed detector could be found. Its complex geometry only allowed the use of numerical methods. The finite-difference method was used and six-pointed asymmetrical stars were constructed on a three dimensional rectilinear mesh. Intersections between the curved tube boundary and all mesh lines had to be calculated before any asymmetrical stars could be constructed.

6.2.2 Boundary and Mesh Line Intersections

Mesh lines in a rectilinear three-dimensional coordinate system were put into three categories:

- 1) Mesh lines that were parallel to the X-axis and perpendicular to the Z-Y plane. The positions which these lines intersected the curved tube boundary were given by the functions $XB1(Y,Z)$ and $XB2(Y,Z)$
- 2) The second category consisted of mesh lines parallel to the Y-direction and perpendicular to the Z-X plane. The intersections with the two curved grid boundaries were denoted by the functions $YB1(X,Z)$ and $YB2(X,Z)$
- 3) The last category consisted of mesh lines parallel to the Z-direction and perpendicular to the Y-X plane. Their intersections with the deflecting grids were given by $ZB1(X,Y)$ and $ZB2(X,Y)$. If integer values of X,Y,Z are given by I,J,L respectively then the

mesh nodes in each of the Z-Y, Z-X and Y-X planes are scanned and the quantities $XB1(J,L)$, $XB2(J,L)$, $YB1(I,L)$, $YB2(I,L)$, $ZB1(I,J)$ and $ZB2(I,J)$ were calculated. From these arrays asymmetrical stars were computed. Trajectory calculations used the normal error-reducing routines that had been written for earlier programs.

6.3 Initial Detector Design

The detector was initially designed to have a curved tube geometry in its deflection field as already described in Section 6.1. The detector design was provisionally assigned an overall height of 10mm. The potential field of the detector was solved by using a 15 by 15 by 15 relaxation mesh size. Equipotential lines in the central Z-X plane are given in Figure 6.3 for the first detector design. As expected these lines show the presence of a large deflection field. Figure 6.4 shows that there is little variation in output current for trajectory step sizes of less than 0.5(SLT>2).

Electron trajectories for initial energies of 3eV, 6eV, 10eV and 50eV are shown in Figures 6.5(a-d) for the detector. Figure 6.5(e) shows the detector design to have a high transport efficiency, for all electrons under 12eV an overall transport efficiency of 99.7% was found. As Figures 6.5(a-d) show, all 3eV electrons are collected and almost all 6eV and 10eV electrons reach the detector exit. Approximately 25% of 50eV electrons are collected, hence it is predicted that most backscattered electrons will be filtered out of the final electron collection.

Equipotentials of the 'Curved Tube Detector'

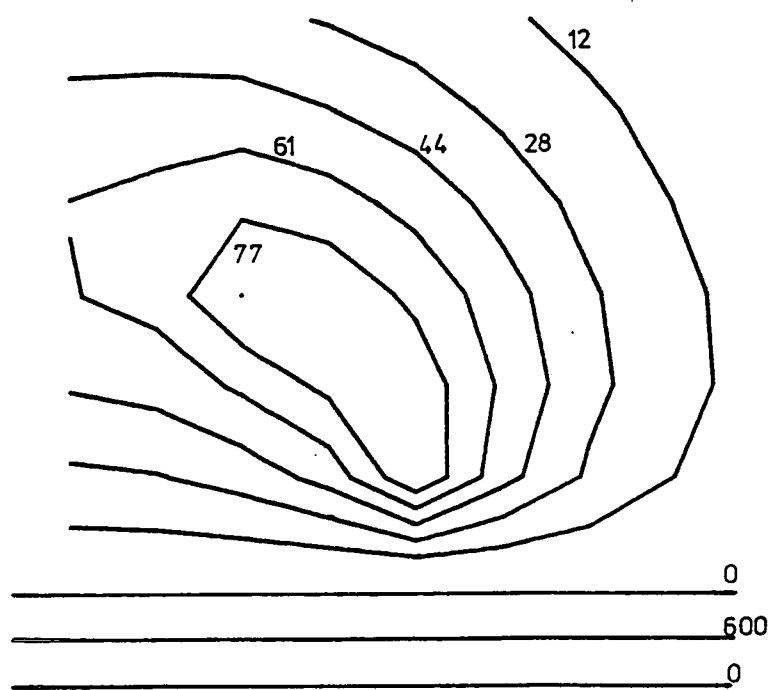
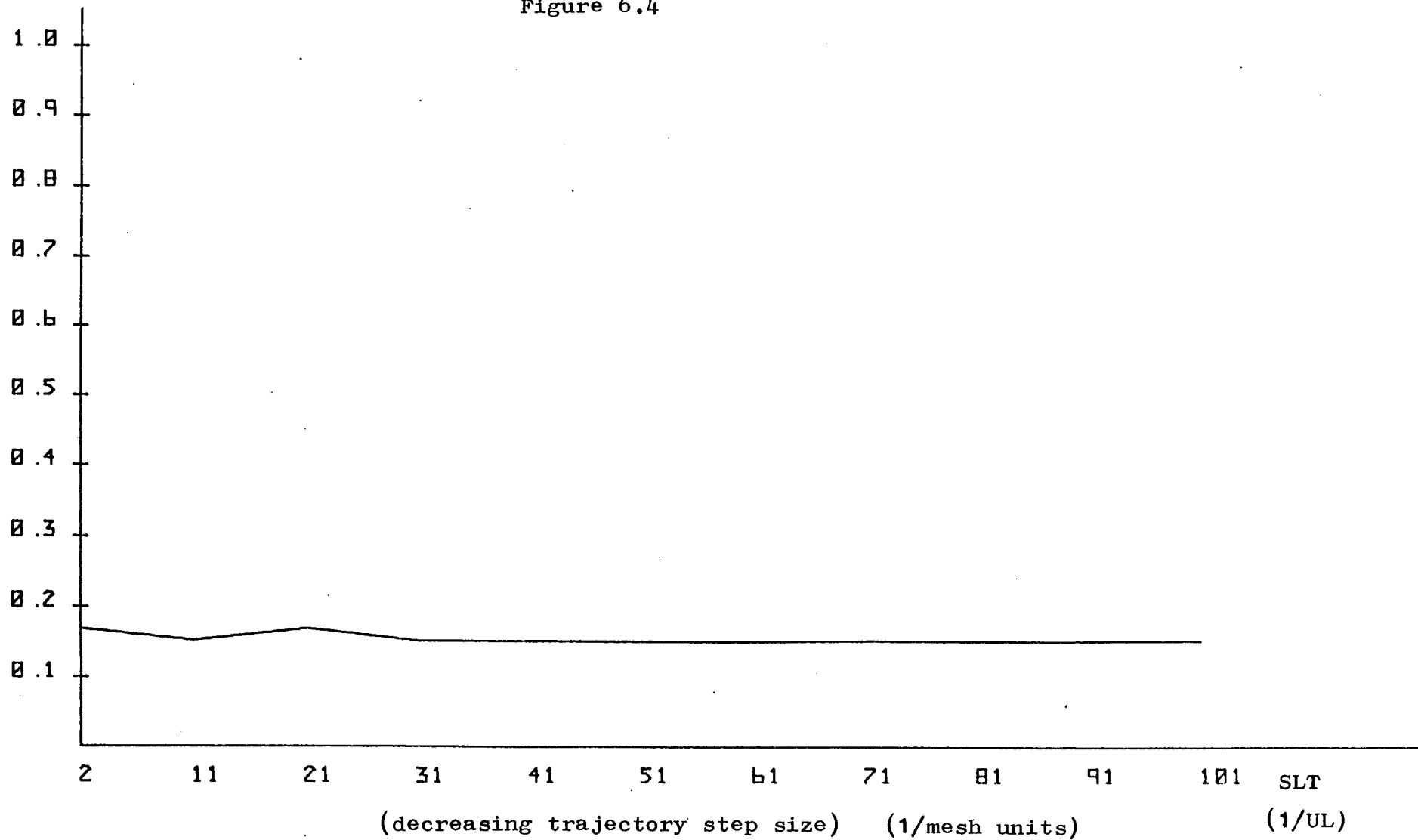


Figure 6.3

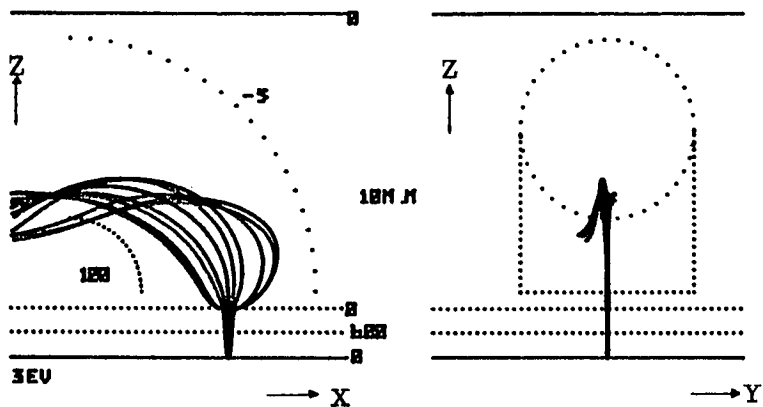
Transport
Efficiency

Error Option for the New Detector

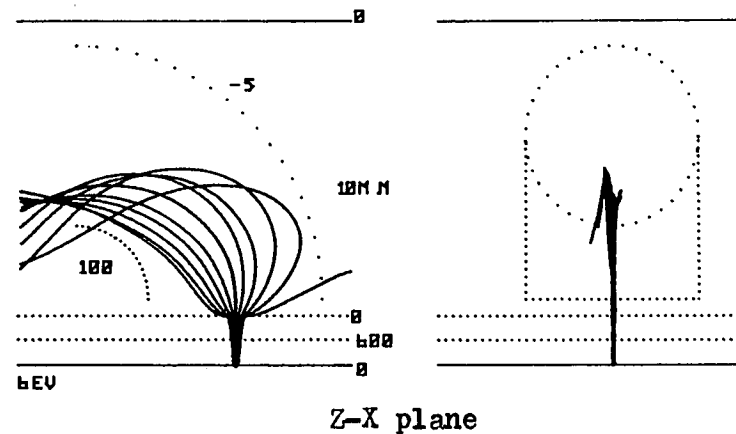
Figure 6.4



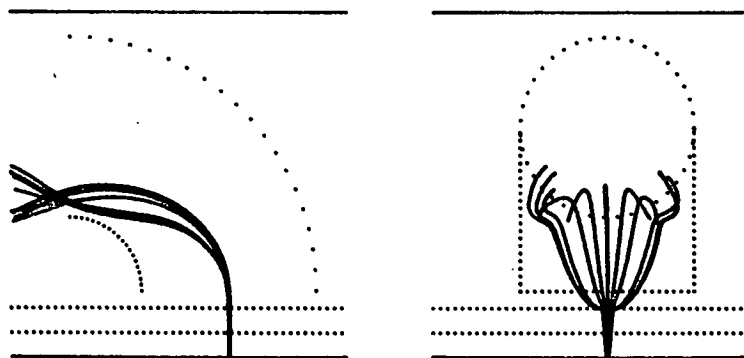
Trajectories for the initial design of the Curved-Tube Detector



Emission in the Z-X plane
Figure 6.5(a)

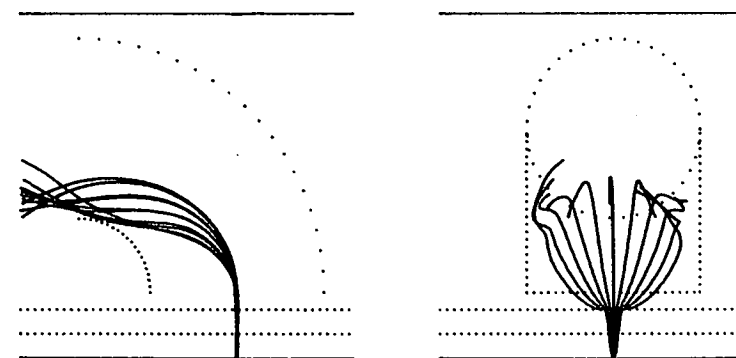


Z-X plane
Figure 6.5(b)



Emission in the Z-Y plane

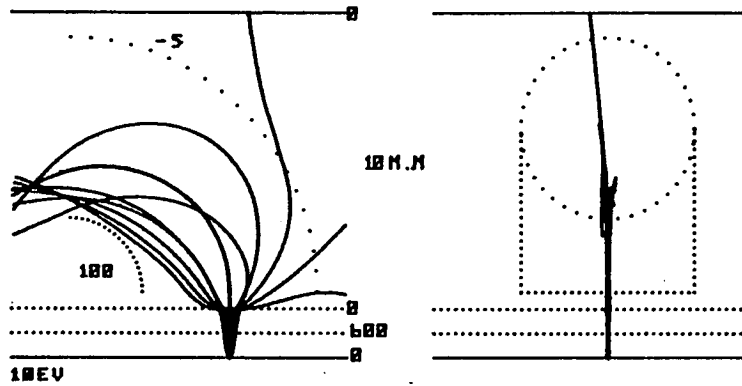
Trajectories with emitted energies
of 3eV



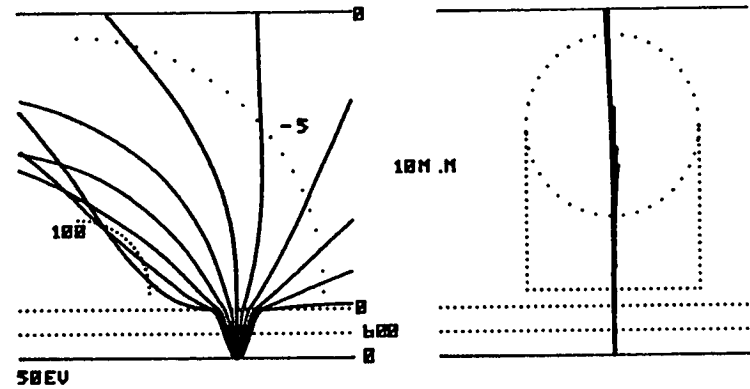
Z-Y plane

Trajectories with emitted energies
of 6eV

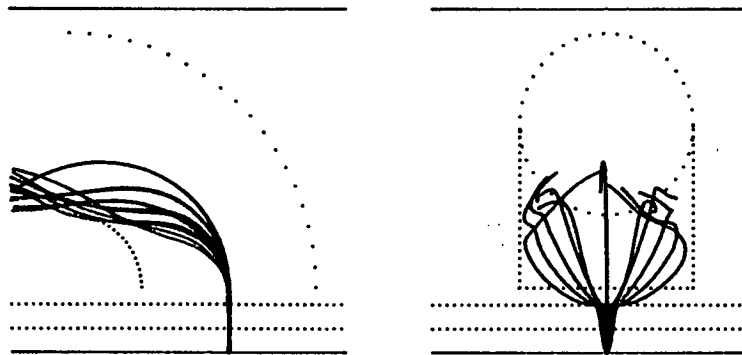
Trajectories for the initial design of the Curved-Tube Detector



Z-X plane
Figure 6.5(c)

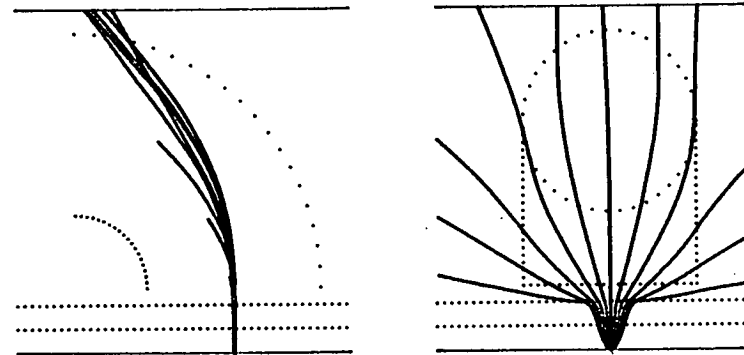


Z-X plane
Figure 6.5(d)



Z-Y plane

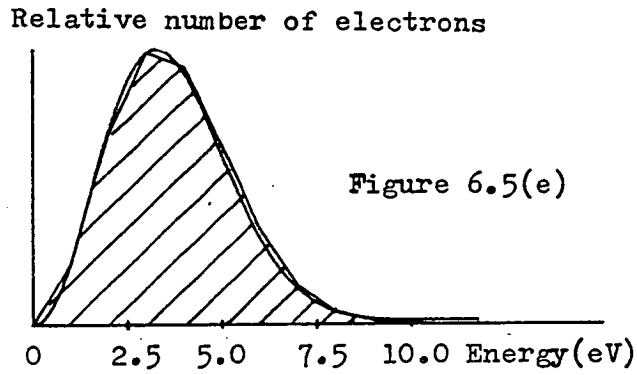
Trajectories with emitted energies
of 10eV



Z-Y plane

Trajectories with emitted energies
of 50eV

Energy analysis for the initial design of the
Curved-Tube Detector



Transport Efficiency = 0.997

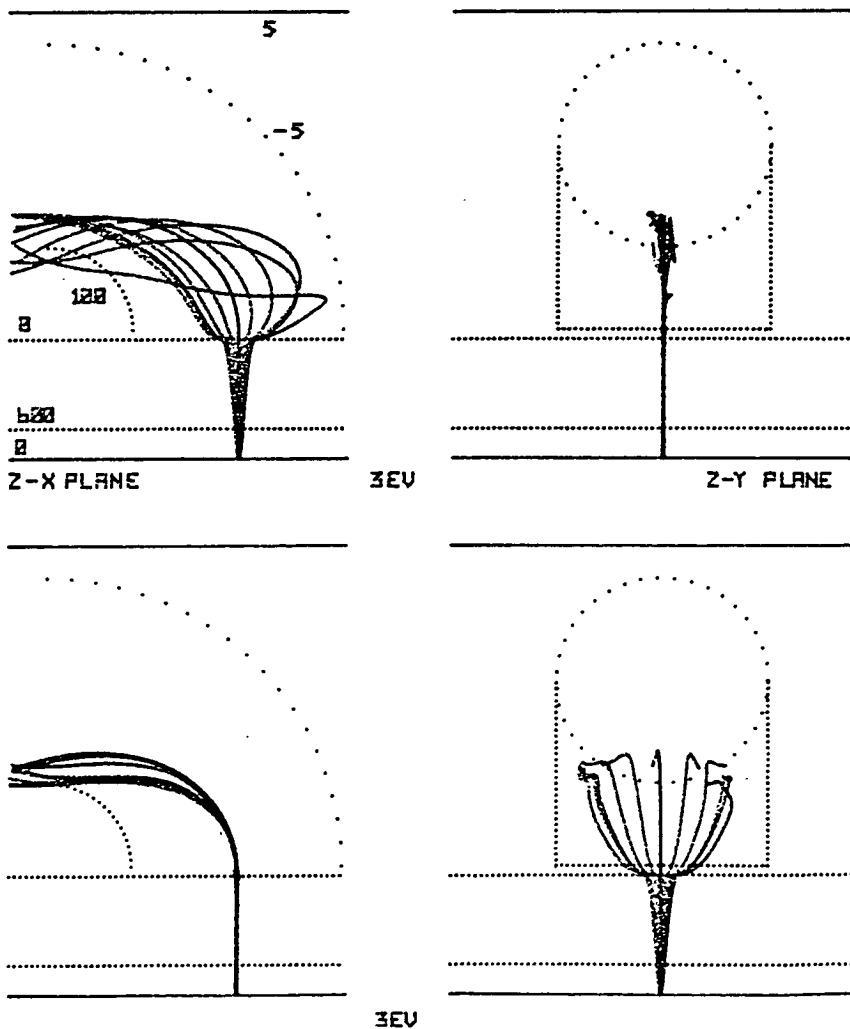


Figure 6.8(a)

Trajectories for the practical design of the Curved-Tube
Detector and an emitted energy of 3eV

6.4 Practical Construction of the 'Curved Tube' Detector

Practical construction of the 'curved tube' detector proved to be difficult for the dimensions of the initial detector design (height 10mm). More realistic dimensions for practical construction are shown in Figure 6.6. An overall height of 24mm was necessary, a distance of 1mm from the specimen to the extraction grid is included in this figure although in practice this distance was made variable. Figure 6.6 also shows the retarding and extracting grids were mounted into a dielectric material. Holes for the primary beam were made in the extraction, retarding and upper curved grids and the diameters of these are given in Figure 6.6. The grids were made of stainless steel and had an 80% optical transparency. The two curved grids in the deflection field were mounted on a stainless steel frame, as shown by the photographs in Figures 6.7(a-c). The detector was mounted on the normal scintillator/light pipe housing arrangement. The complete practical construction of the detector was carried out by British Telecom at their Martlesham Research Laboratories.

6.5 Computer Simulation of the Practical Design

Simulation of the practical design is shown in Figures 6.8(a) and 6.8(b) in this case the overall transport efficiency drops to 95% and slightly fewer electrons reach the exit of the detector. This slight drop in efficiency was considered to be an acceptable compromise for the realization of a practical design. Different S-curves were calculated for different surface voltages and are

Cross-section of 'Curved Tube Detector'

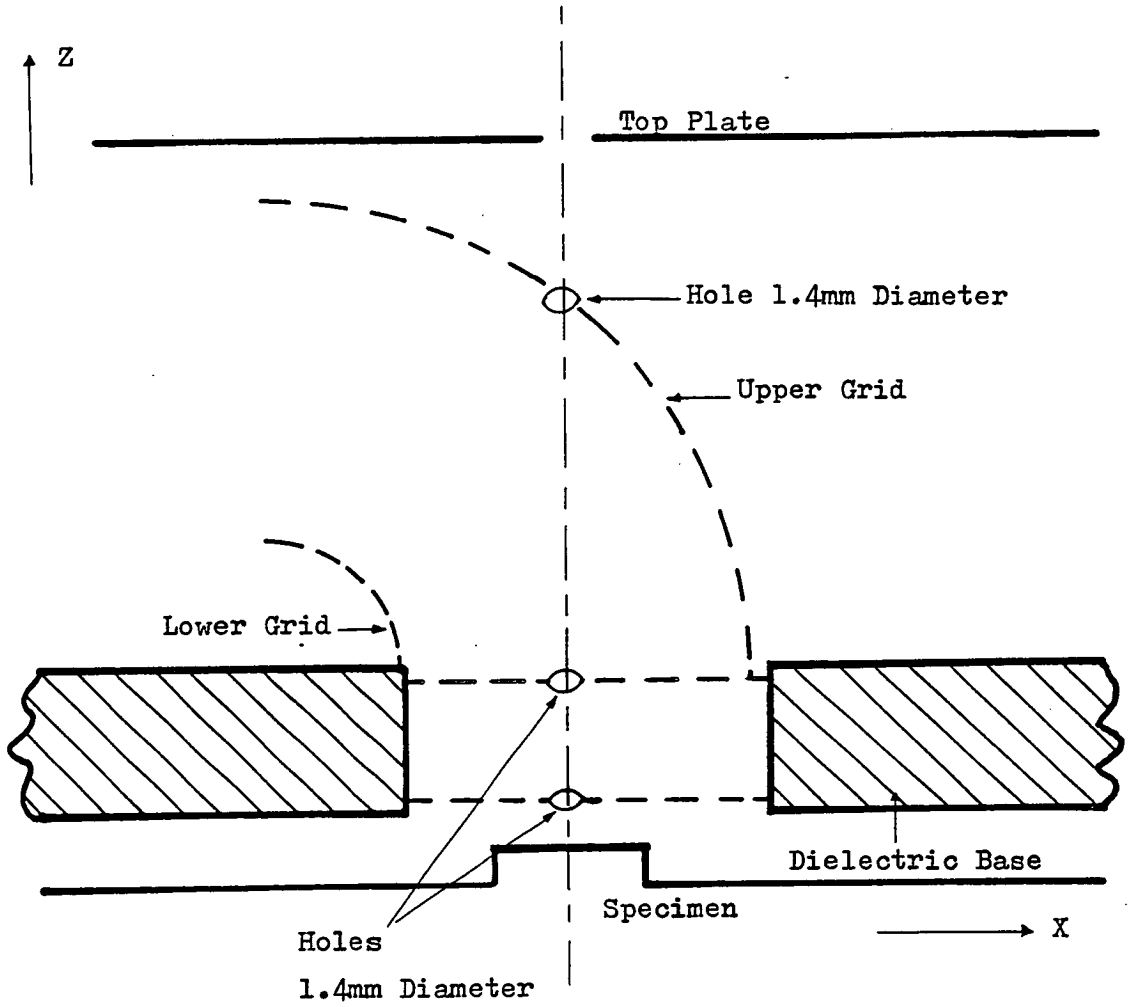


Figure 6.6

Scale: 

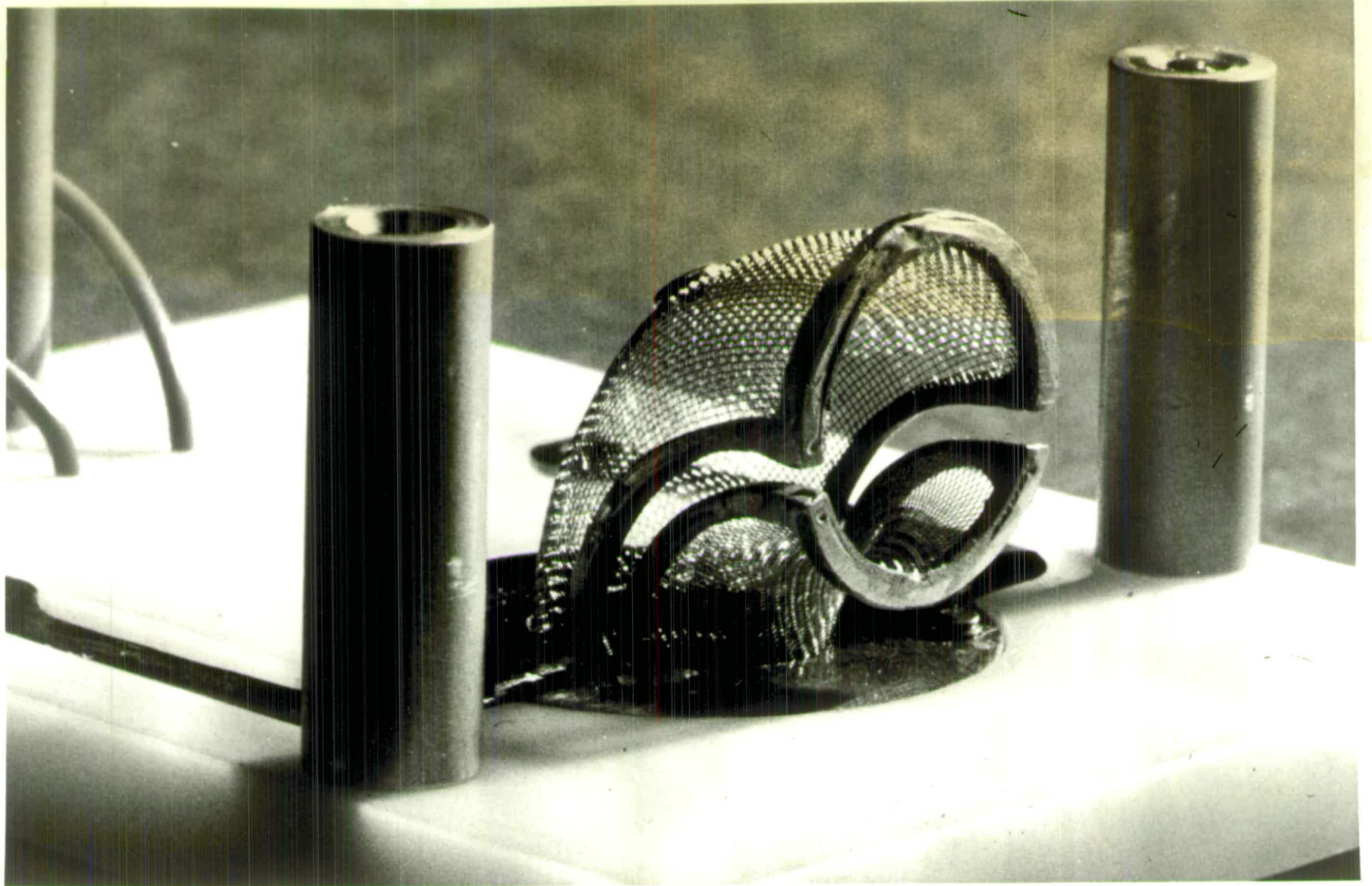


Figure 6.7(a)

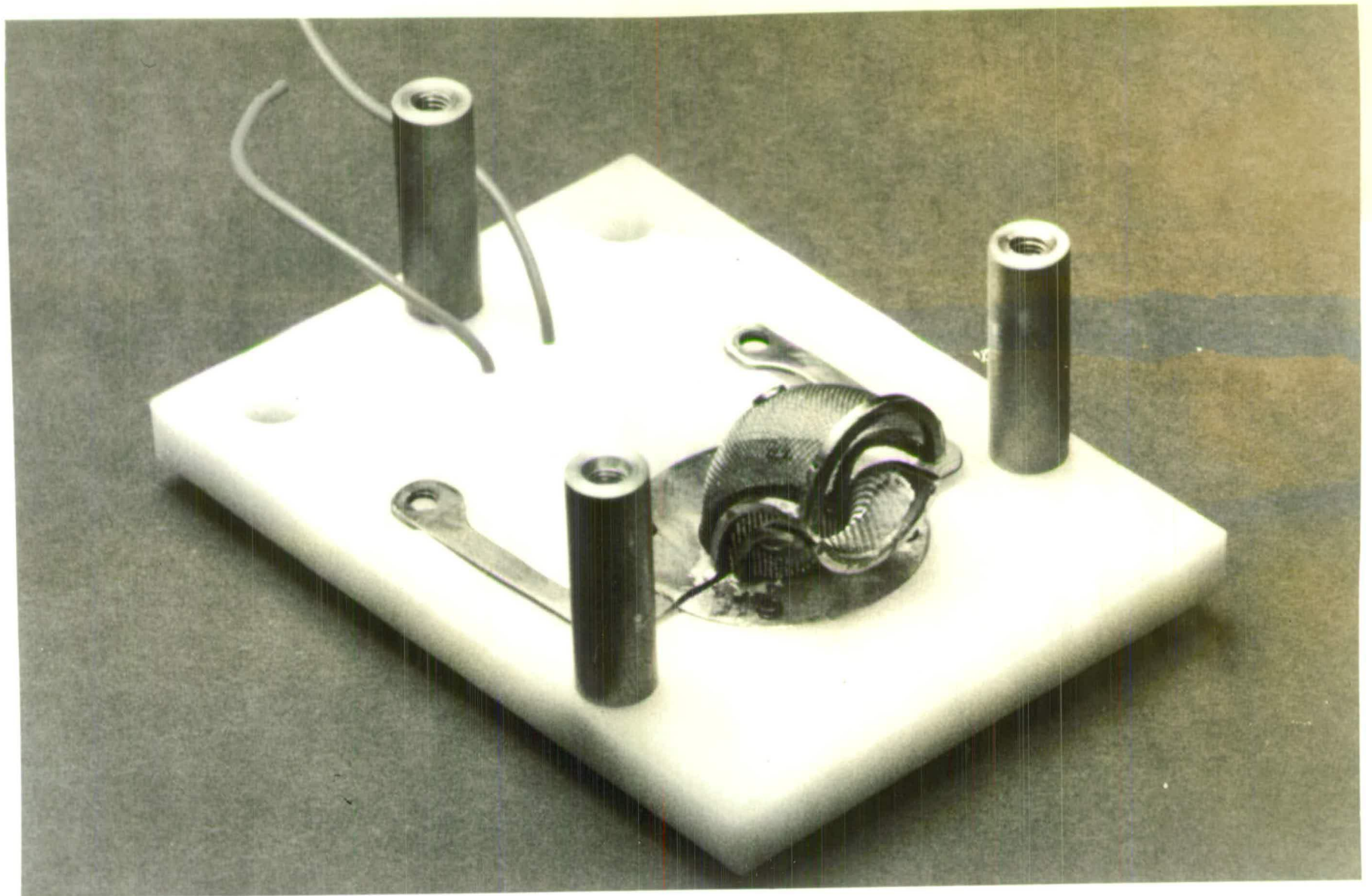


Figure 6.7(b)

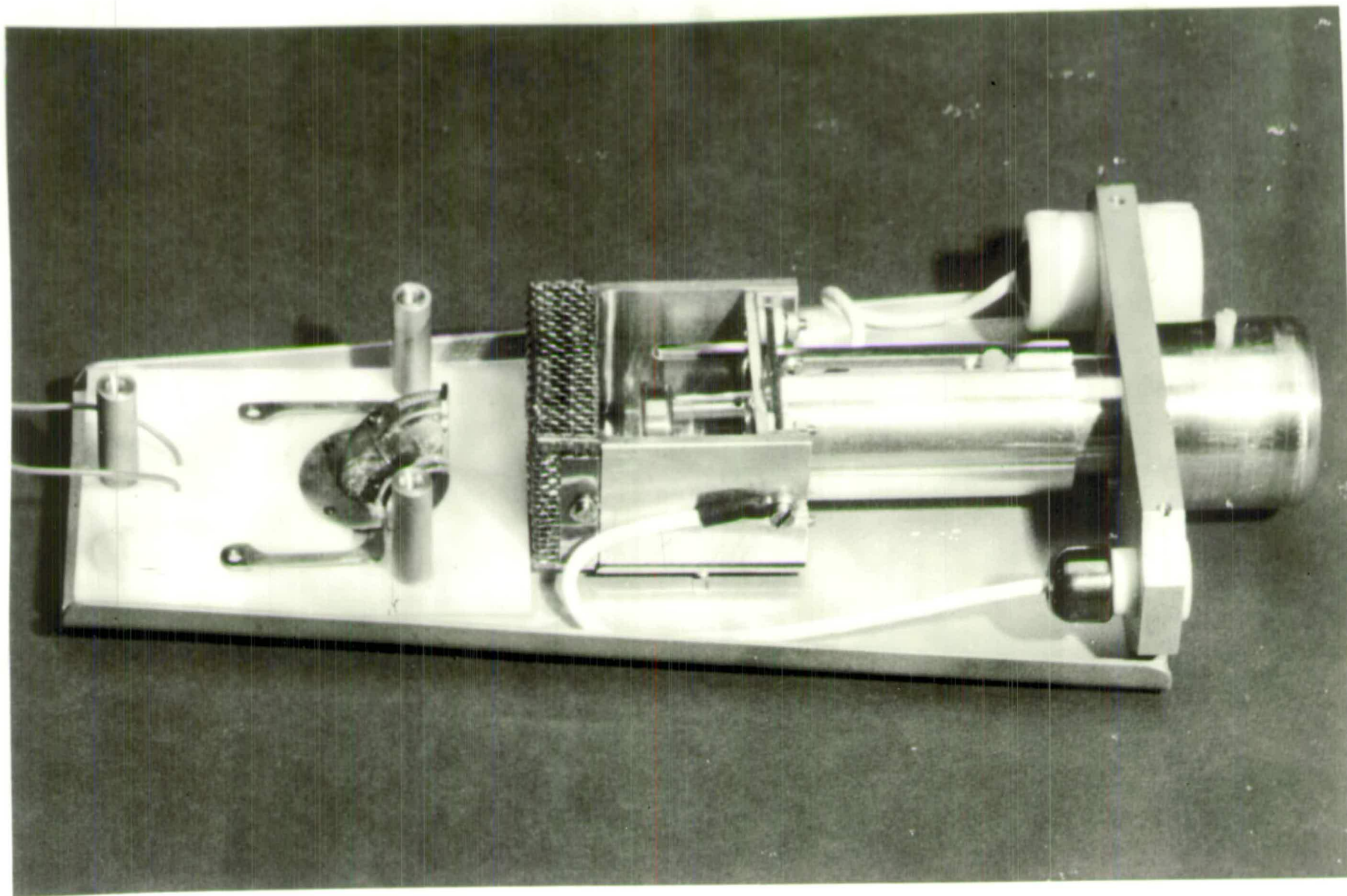
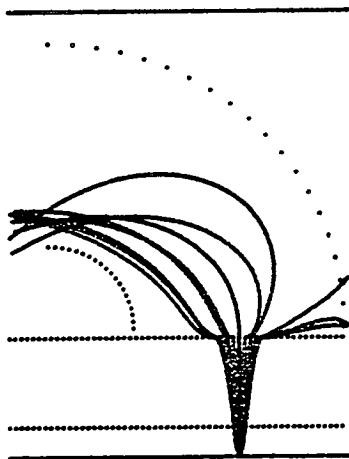


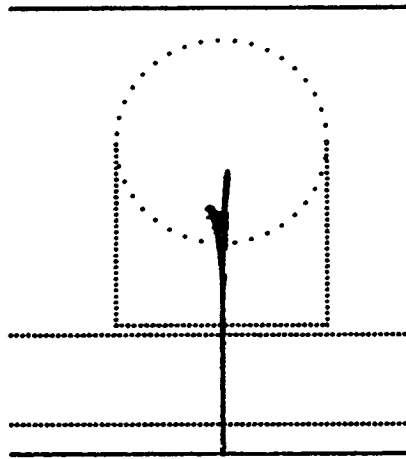
Figure 6.7(c)

Trajectories for the practical design of the Curved-Tube
Detector for an emitted energy of 6eV



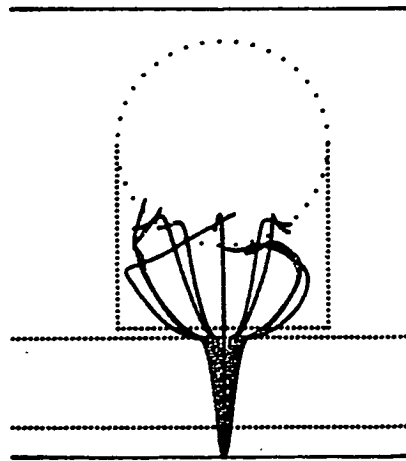
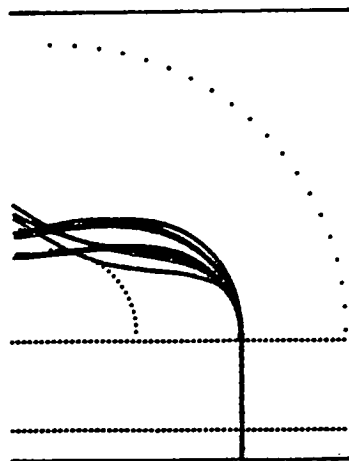
Z-X plane

6eV



Z-Y plane

Figure 6.8(b)



shown in Figure 6.9. They are seen to have ideal 'S' shapes and give linear shifts under the 5 volt specimen changes of -5 volts and 5 volts. Voltage shifts are given to within 0.5% accuracy in the linear regions of the S-curves.

6.5.1 Optimum Voltage Configuration

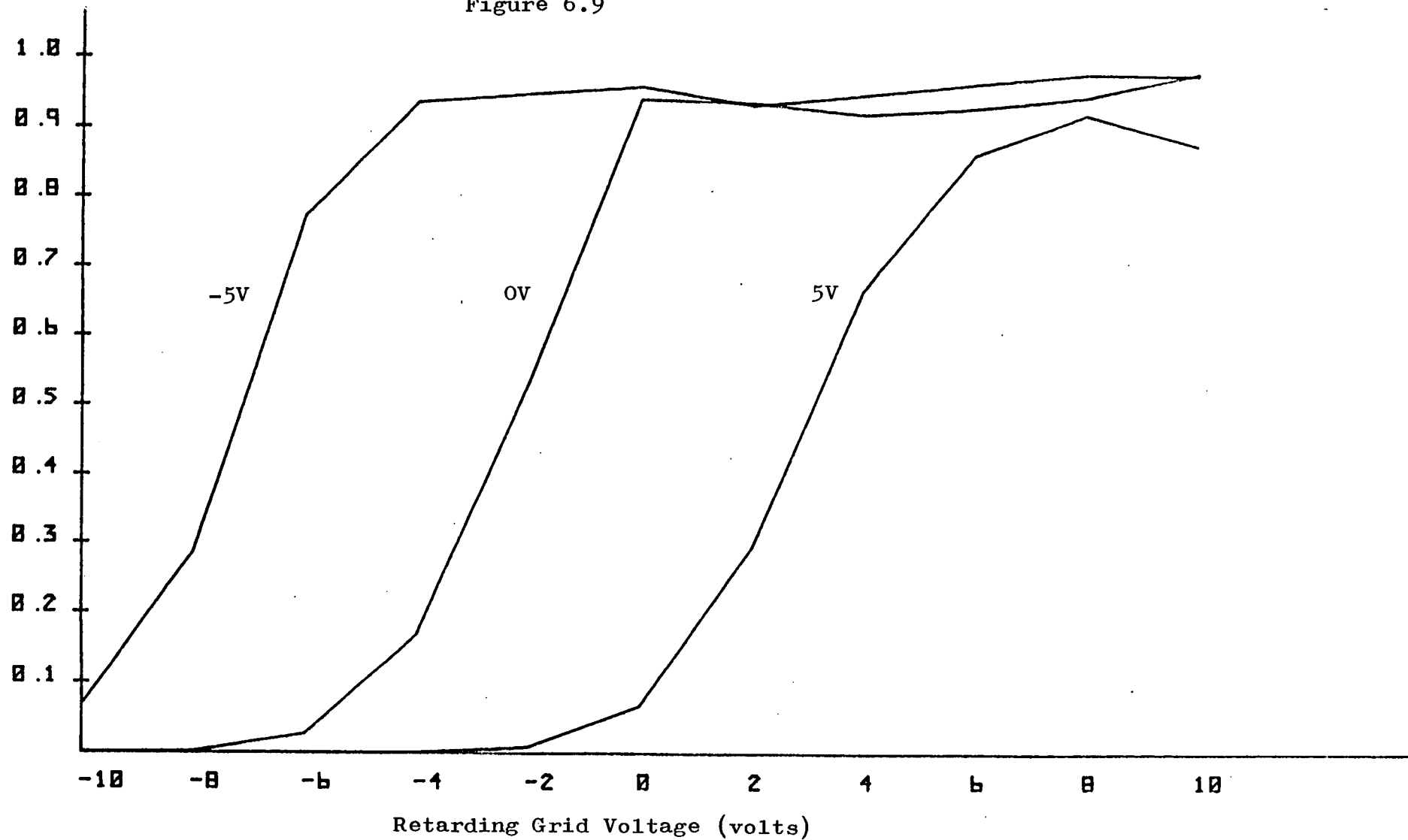
Potentials on each electrode in the detector were varied separately and the corresponding output current response was calculated. Figure 6.10 shows that the output current does not change significantly (<5%) above an extraction grid voltage of 100 volts but below this voltage it rises steeply from 56% at 0 volts to 92% at 100 volts extraction voltage.

Figure 6.11 shows that there is a peak value in the output current for variations in the upper curved grid, this occurs at a voltage of -5 volts and has a height of 95%. This graph confirms the initial voltage set for this grid. Figure 6.12 shows a steady rise in output current with variation of the voltage on the lower deflection grid. The output current rises from 6% at 0 volts to 97% at 110 volts. This results suggests that if the initial voltage of a 100 volts were increased to 110 volts a 2% increase in transport efficiency would result. From the above results all voltages were kept at their previous values except for the voltage on the lower deflection grid which was increased to 110 volts in the detector design.

Transport
Efficiency

S-curves for Different Specimen Voltages in the New Detector

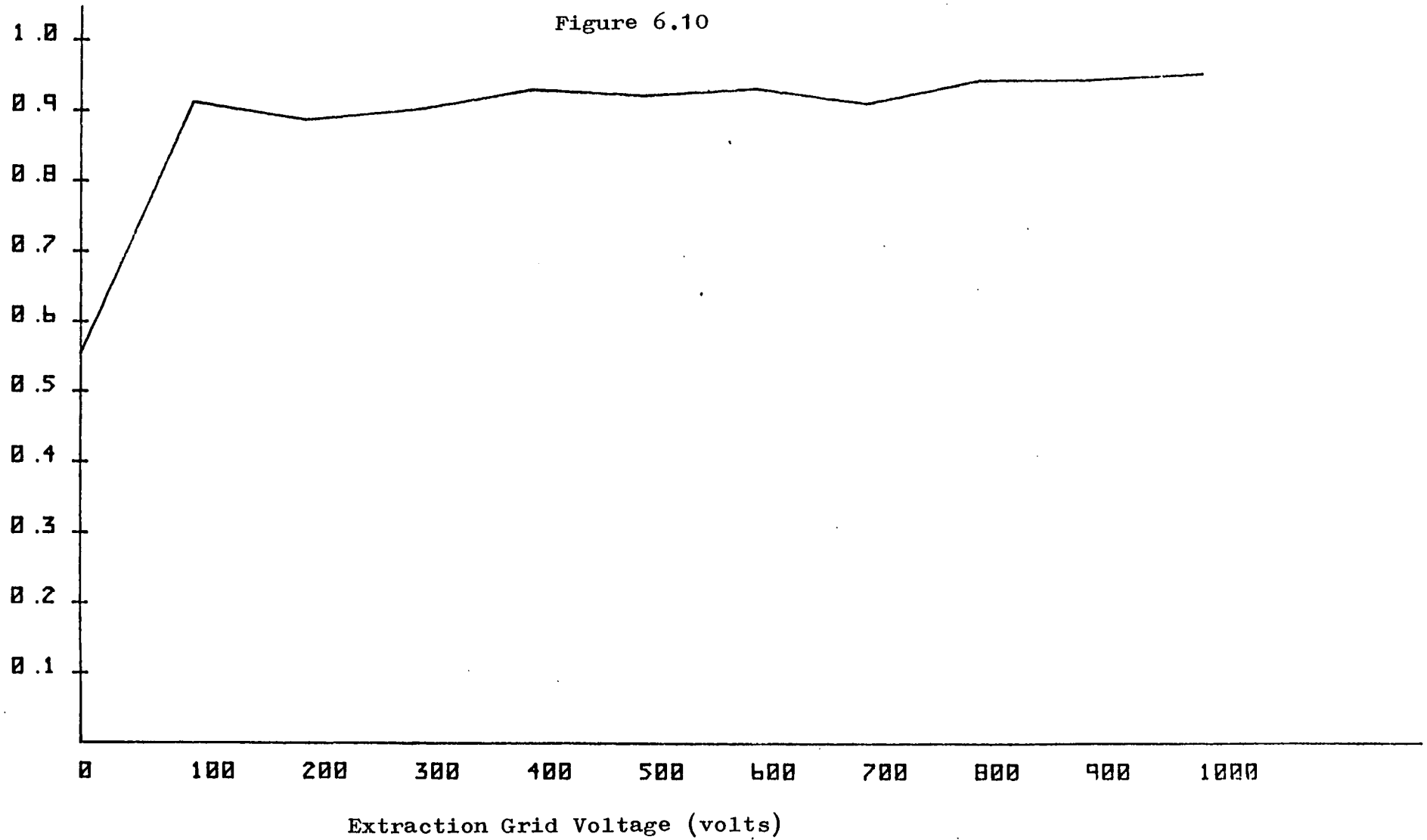
Figure 6.9



Transport
Efficiency

Variation in the Extraction Grid Voltage for the New Detector

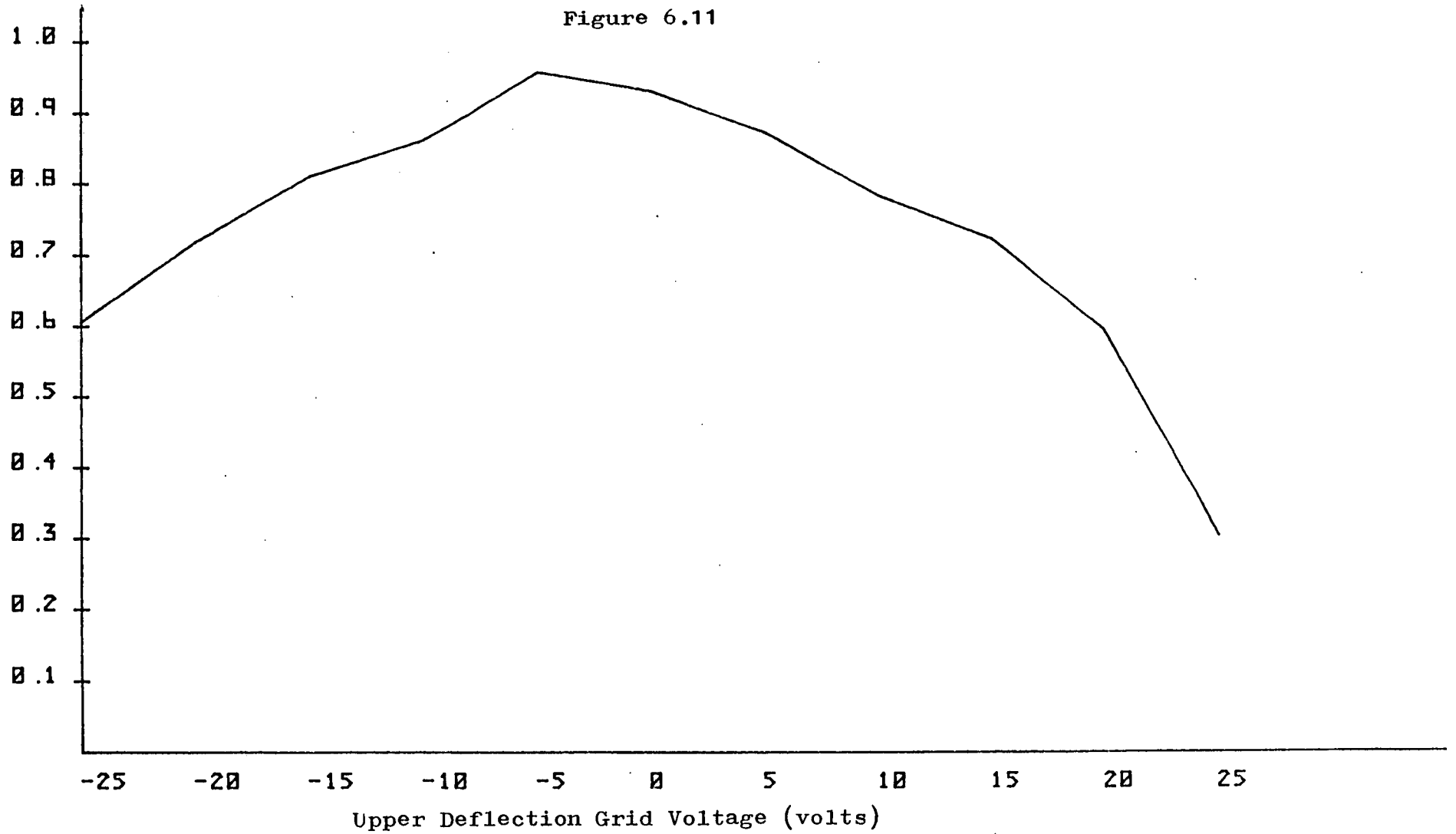
Figure 6.10



Transport
Efficiency

Variation in the Upper Deflection Grid Voltage for the New Detector

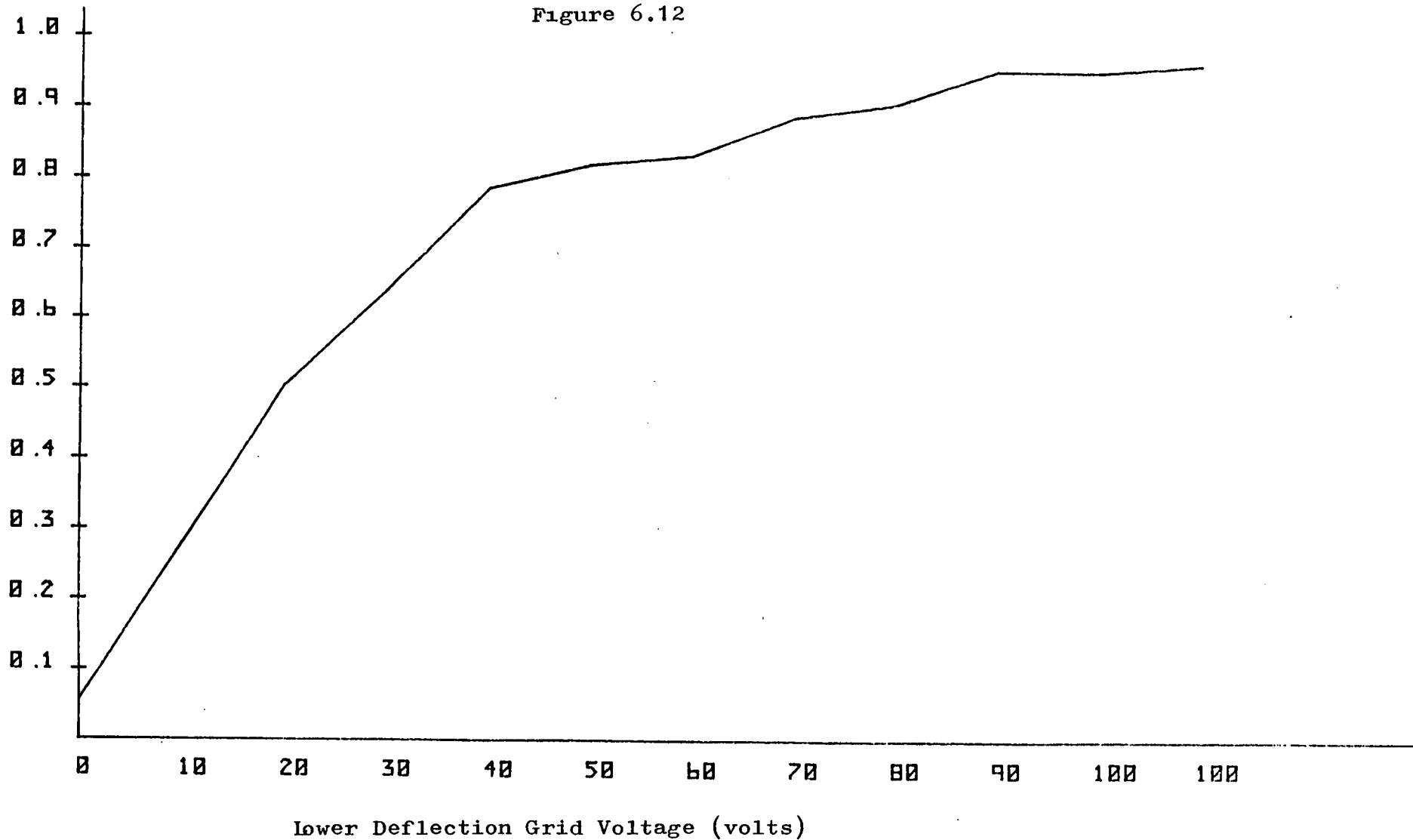
Figure 6.11



Transport
Efficiency

Variation in the Lower Deflection Grid Voltage for the New Detector

Figure 6.12



6.5.2 Off-Axis Positions

Figure 6.13 shows different off-axis positions on the specimen, positions 1, 2 and 3 are off-axis positions 1mm, 2mm and 3mm respectively along the positive X-axis. Positions 4, 5 and 6 are off-axis positions along the negative Y-axis and 7, 8 and 9 are such positions on the negative X-axis. Results from positions on the negative Y-axis are equivalent to those from positions on the positive Y-direction since the field is symmetrical about the X-axis.

Figure 6.14 shows S-curves for positions 1, 7 and 4, each position lies 1mm off-centre on the three afore-mentioned axis. The S-curves from positions 1 and 4 remain identical to the S-curve generated from the central axis shown in Figure 6.9, while the S-curve from position 7 indicates an improvement. The height for this latter S-curve is 100% at 0 volts on the retarding grid, showing an increase of 5% in the transport efficiency over the central axis S-curve. Figure 6.15 shows S-curves from positions 2, 5 and 8 which are 2mm off-centre. The S-curves from positions 8 and 2 remain the same as those from positions 1 and 7, while the S-curve from position 5 indicates a maximum drop of 6% in height from the central axis S-curve. Figure 6.16 shows S-curves from positions 9, 6 and 3, 3mm off-centre, S-curves along the X-axis (positions 9 and 3) remain the same as for previous off-centre positions 1mm and 2mm along this axis. The S-curve 3mm off-centre along the Y-axis becomes non-linear and drops in height by as much as 20% from the normal S-curve.

Specimen Plane of 'Curved Tube Detector'

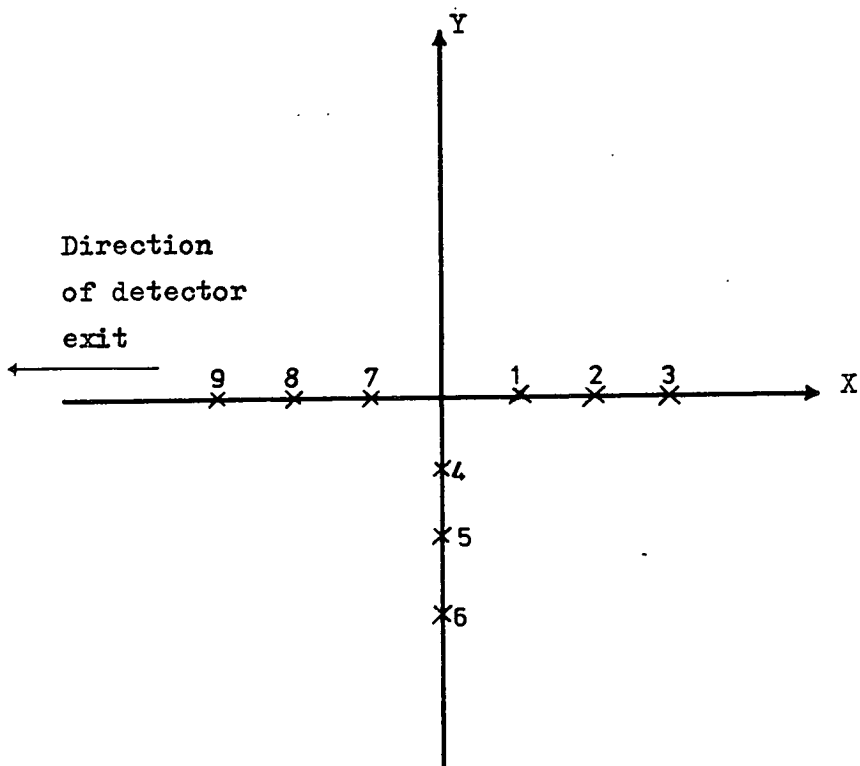



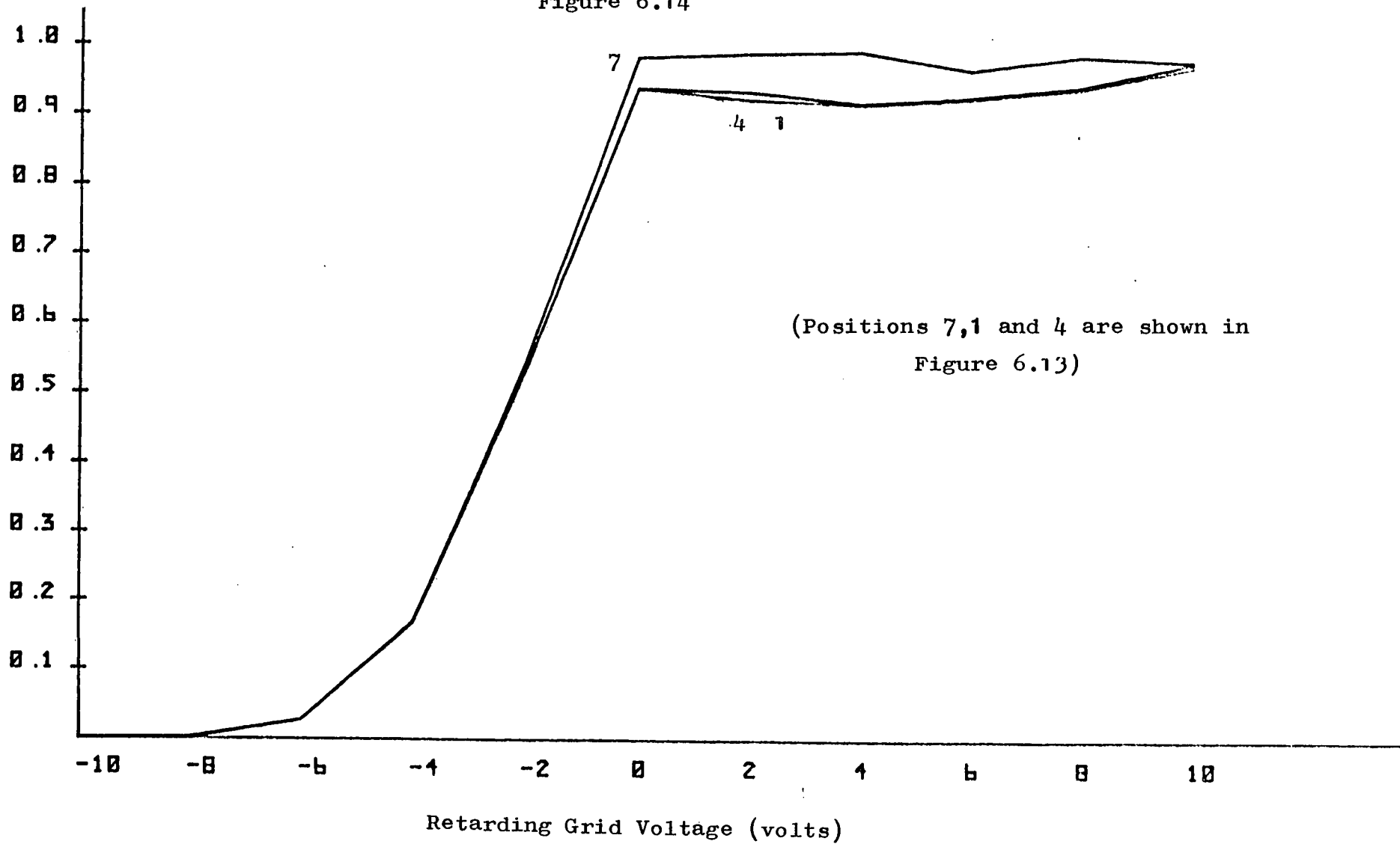
Figure 6.13

Scale: 
1mm

Transport
Efficiency

S-curves for 1mm Off-axis Positions in the New Detector

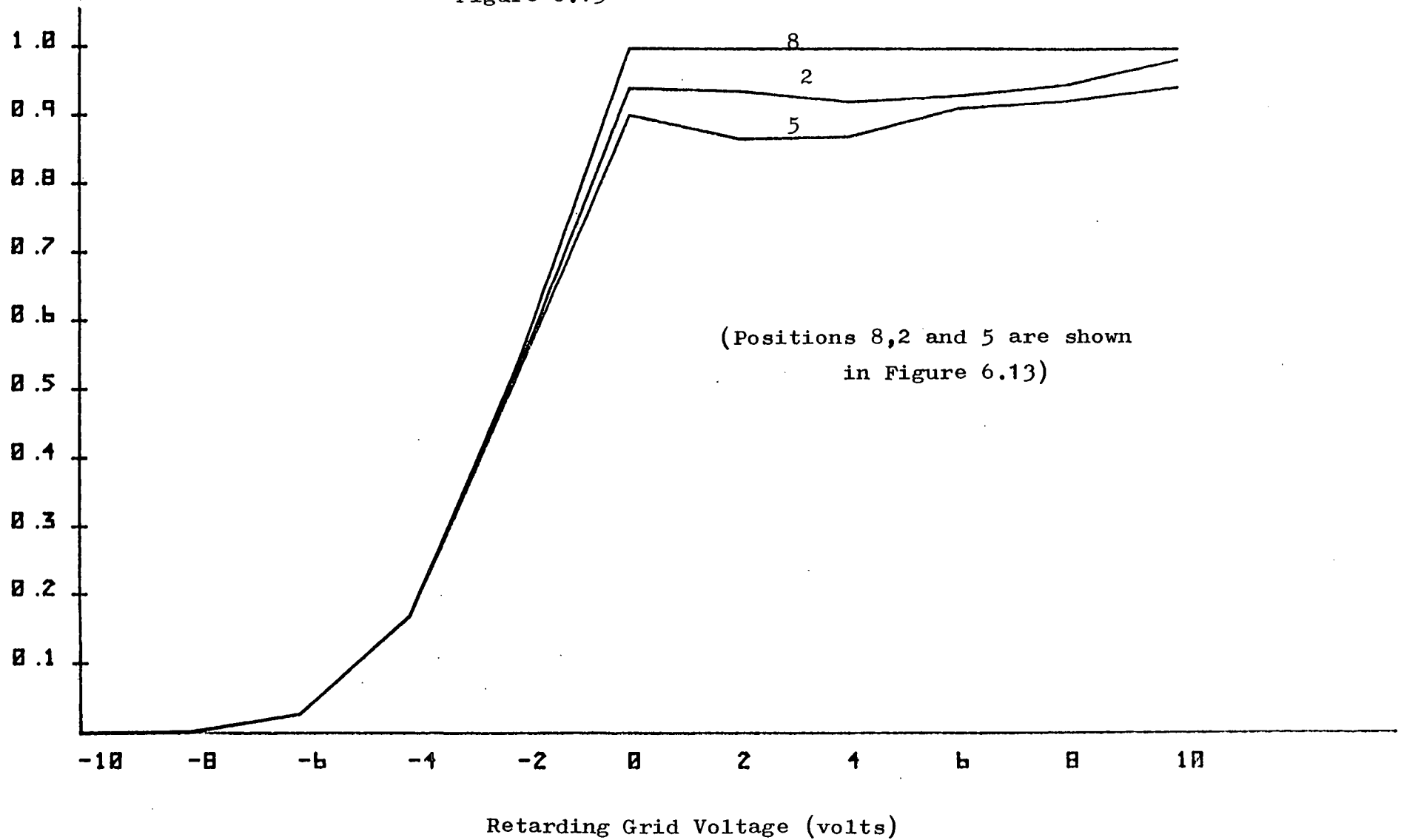
Figure 6.14



Transport
Efficiency

S-curves for 1mm Off-axis Positions in the New Detector

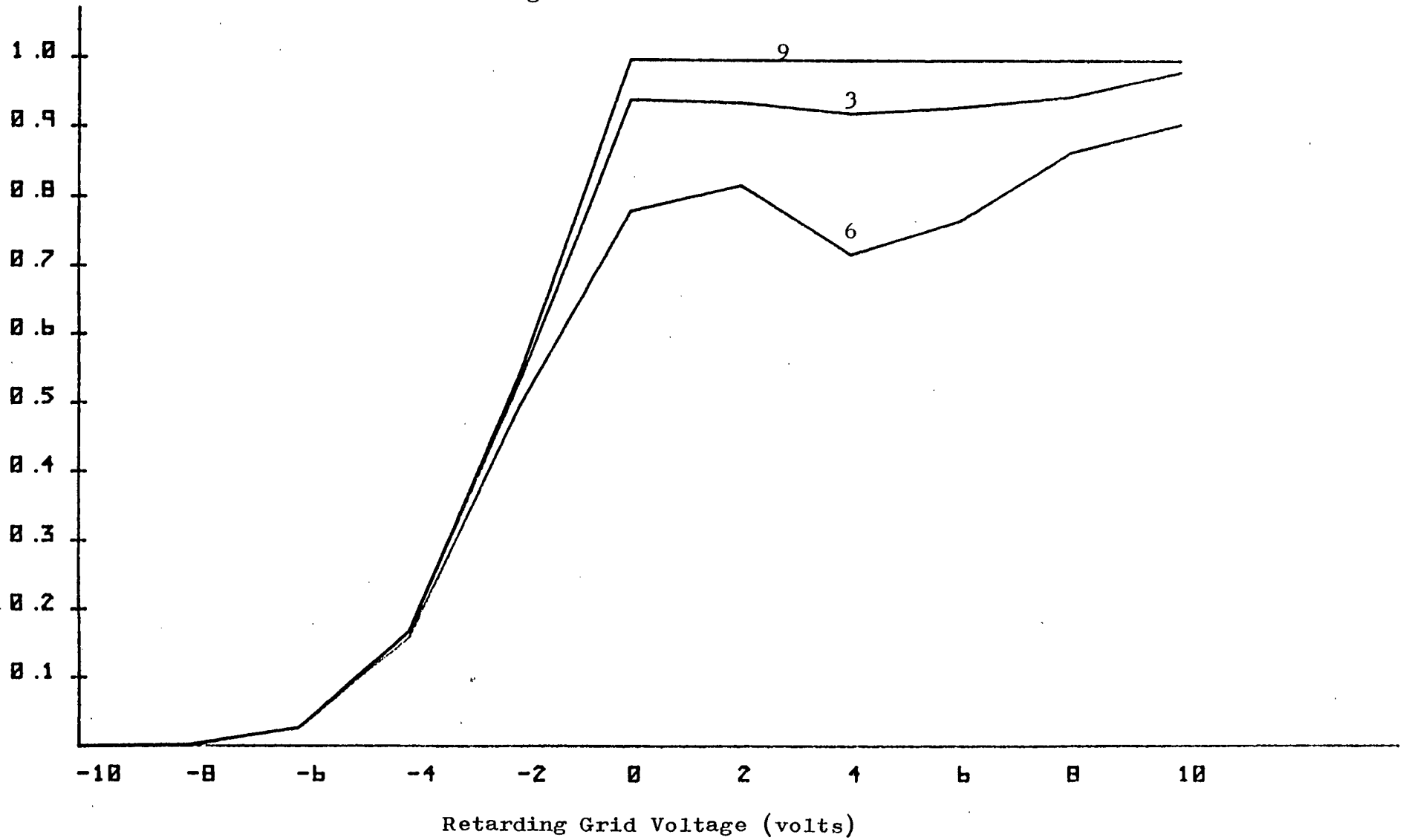
Figure 6.15



Transport
Efficiency

S-curves for 3mm Off-axis Positions in the New Detector

Figure 6.16



In summary S-curves from positions up to 3mm along the positive X-axis do not greatly differ from the normal central axis S-curve. S-curves from positions up to 3mm along the negative X-axis are better than those from the central axis. A 100% transport efficiency is obtained at 0 volts retarding grid for these curves. The field of view however is limited above 2mm in the negative and positive directions along the Y-axis. At 2mm the S-curve height falls 6% below the normal S-curve, but still remains linear. At 3mm however the S-curve becomes non-linear varying from overall transport efficiencies of 80%, 72% and 92% from respective retarding grid voltages of 0, 4 and 10 volts.

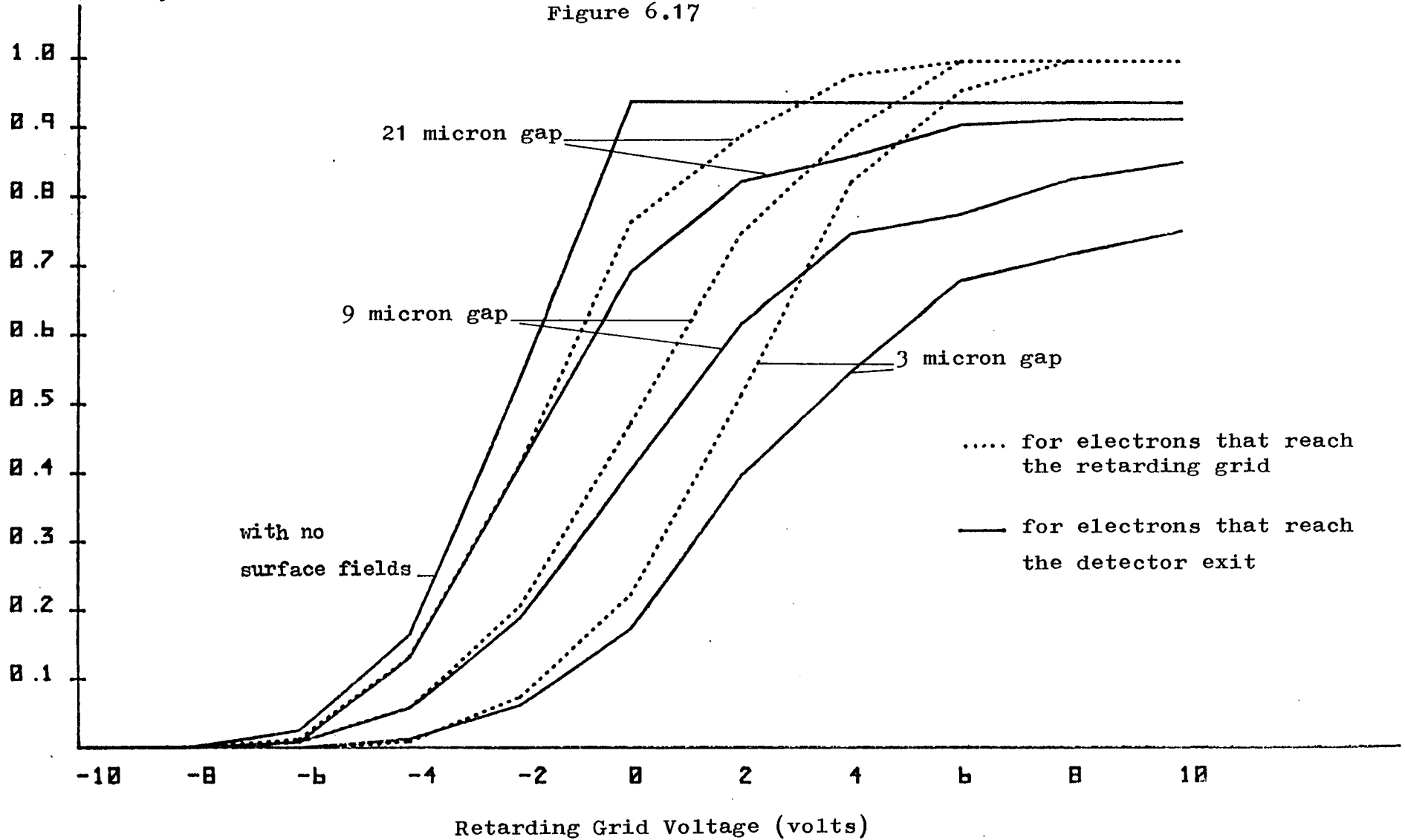
6.5.3 Surface Field Effects in the New Detector Design

The programs described in Chapter 5 were used to calculate the effect of surface fields in the new detector design. These programs were used to plot electron trajectories through the detector's extracting and retarding fields. Final electron velocities and positions were registered for electrons crossing the retarding grid. This information was input as initial conditions to another program which plotted electron trajectories through the detector's deflection field. Figure 6.17 shows S-curves for electrons at the detector's retarding grid and S-curves from electrons at the detector's exit, S-curves have been generated from a single gap surface layout with gaps 3, 9 and 21 microns for both cases. Electrons leave the edge of a 0 volt conductor and their trajectories are influenced by a neighbouring 5 volt conductor. The S-curves which represent electrons at the detector exit are similar to those at the

Transport Efficiency

S-curves for a Single Gap Surface Layout in the New Detector

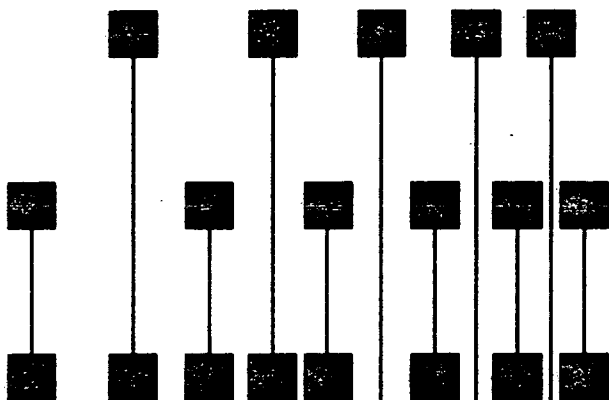
Figure 6.17



Feuerbaum detector exit for the same surface layout. S-curves drop in their final heights to 92%, 82% and 76% at gaps 21, 9 and 3 microns respectively, their 'S' shape also becomes non-uniform. Fictitious shifts of greater than 5 volts are found for the 3 micron case. The above results show that the detector's linear retarding field cannot cope with strong surface fields and the detector's deflection field also introduces large errors on voltage measurements under such conditions.

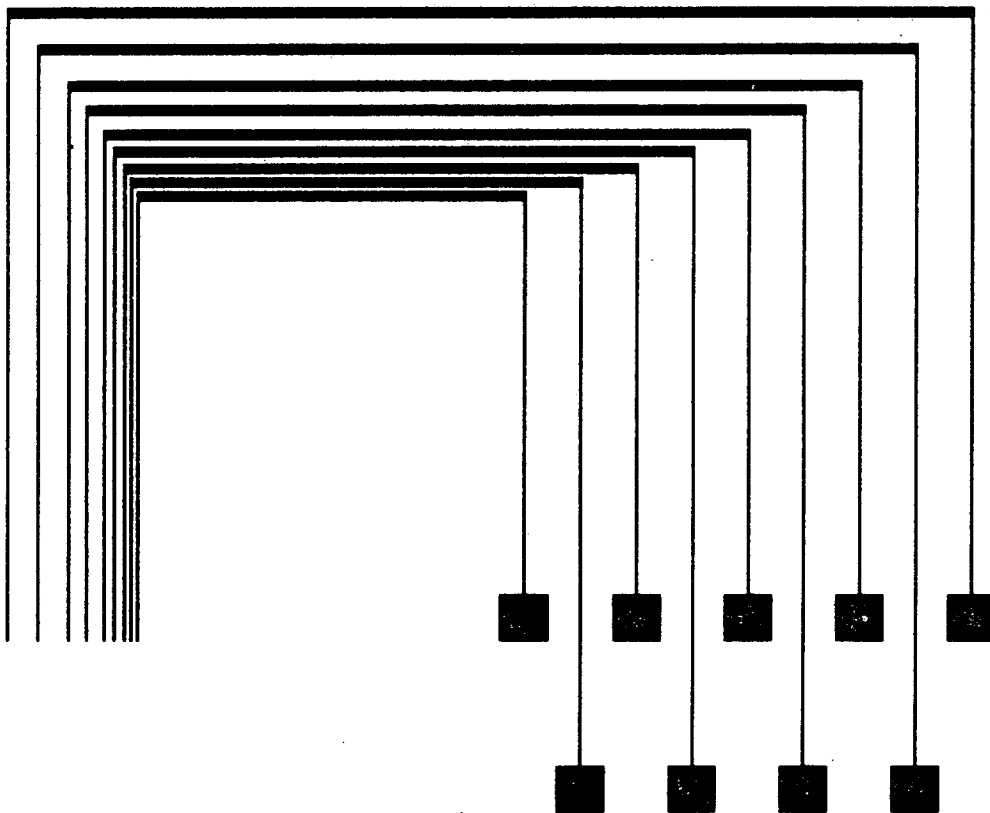
6.6 Design and Construction of a Test Specimen

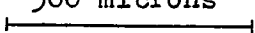
A test specimen was specially designed and made to investigate the effects of a wide range of surface field conditions on voltage measurements. The specimen could also be used to provide precise conditions for which practical results could be compared with computing predictions. The specimen was constructed to simulate real surface conditions on MOS devices and is made of aluminium conductors on a layer of silicon dioxide which in turn lies on an earthed silicon substrate. Figure 6.18 shows a layout diagram for the test specimen. Measurements can be made on aluminium pads with neighbouring pads, tracks with neighbouring pads and tracks between neighbouring tracks. Test pads were specified to be a 100 microns square and gap sizes were 3, 10, 25, 50 and 100 microns and two track widths of 10 and 25 microns were provided.



Test Specimen

Figure 6.18



Scale:  500 microns

6.7 Provisional Experimental Results from the New Detector

Due to the lack of available time only provisional experimental results are presented. All results were made on a copper stub specimen and a beam voltage of 2.5KV was used. The experimental results are divided into two parts; in the first case S-curves were obtained on an X-Y recorder; and in the second case S-curves were obtained on an oscilloscope.

As expected the S-curves obtained on the X-Y recorder (Figure 6.19) have more variations in the S-curve shifts than those in the oscilloscope trace (Figure 6.20). This is due to the inherent phase lag of the X-Y recorder yielding a 'hysteresis effect' which prevented any S-curves from being exactly reproduced. The relatively slow sweep voltage (a few seconds) on the retardation grid also allowed beam current variations to further add to non-linear changes in the output S-curves. The voltage configuration on the detector electrodes was set to 600 volts on the extraction grid, -5 volts on the upper deflection grid, and 100 volts on the lower deflection grid. The retardation grid varied from -40 to +40 volts for -20 to +20 volt changes (5 volt steps) on the specimen for the X-Y recorder S-curves (Figure (6.19)). While a -12 to +12 volt sweep voltage was used on the retardation grid for specimen changes of -7 to +7 volts (steps of 1 volt) for the S-curves on the oscilloscope trace (Figure 6.20). Both S-curves have ideal 'S' shapes and linear shifts which as a first approximation conform to theoretical predictions (Figure 6.9). The results also show a considerable

Experimental S-curves from the New Detector for Different Specimen Voltages

output
current from
S.E.M

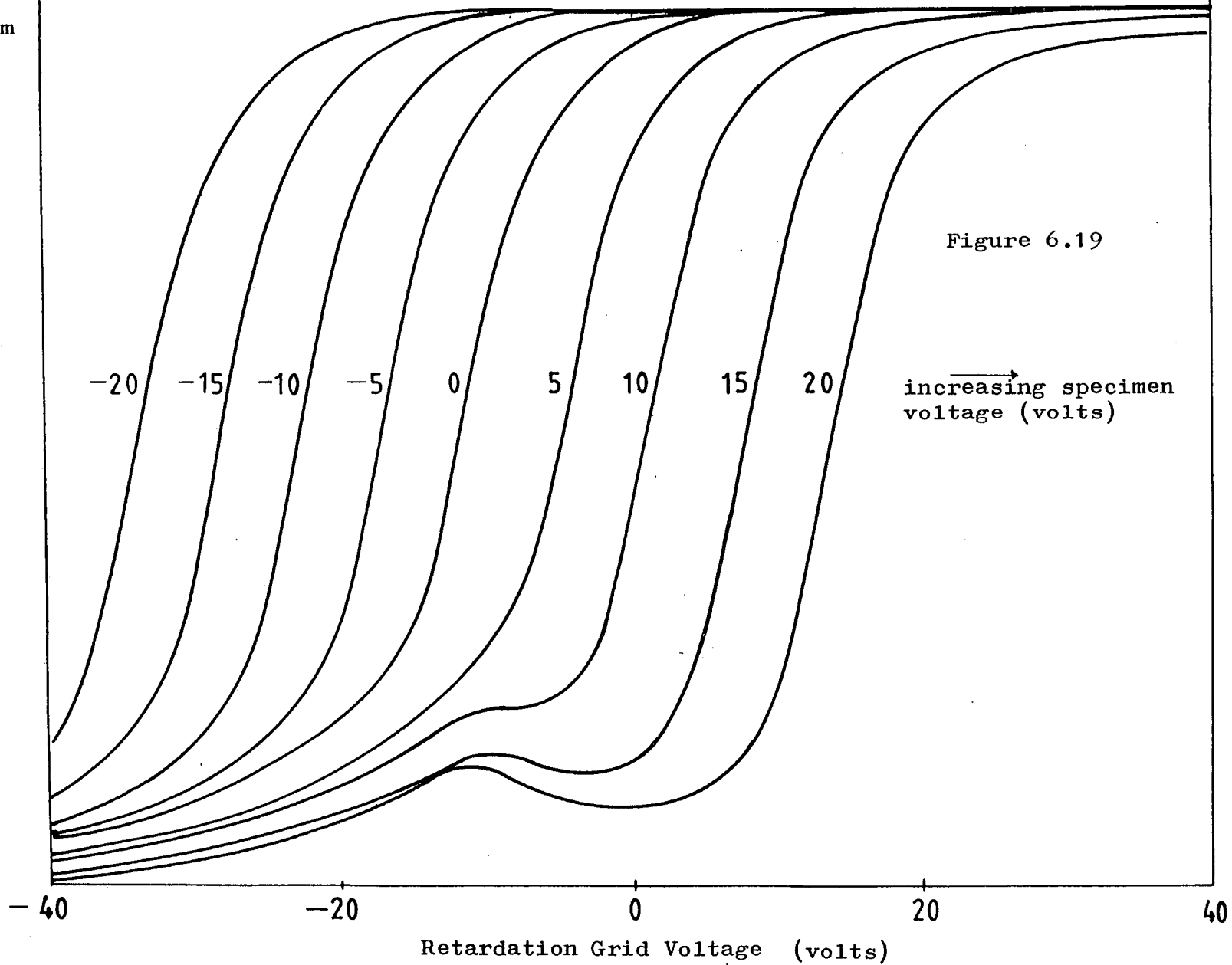
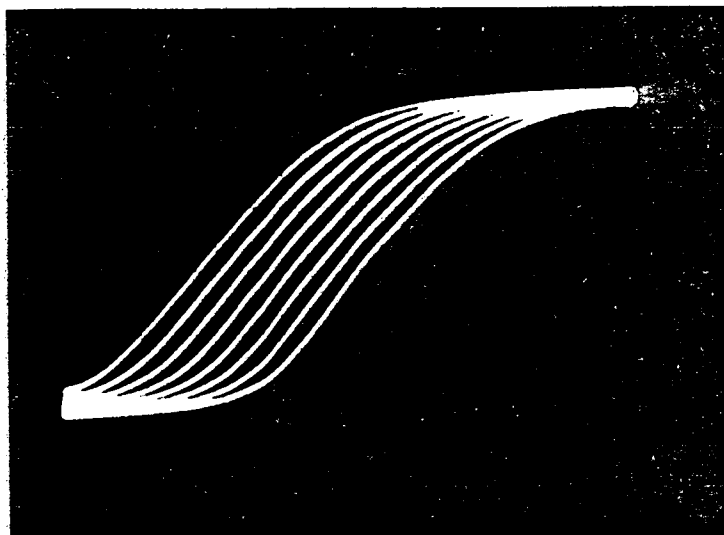


Figure 6.19

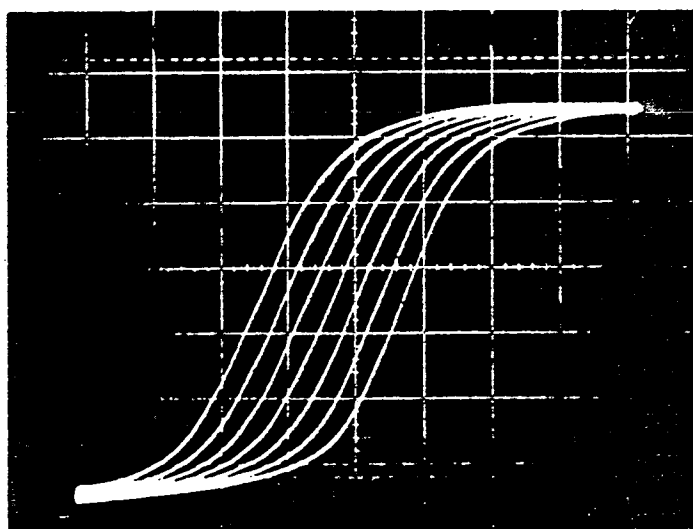
S-curves from the 'Curved Tube Detector'



Specimen Voltage varies from 0 to 7 volts
in Steps of 1 volt.

Both results were taken on a Copper-Stub with a
-12 to 12 volt sweep on the Retardation Grid.

Figure 6.20



Specimen Voltage varies from 0 to -7 Volts
in Steps of 1 Volt

improvement on the experimental detector curves from the Lintech detector(Figures 3.50 and 3.51). Very small beam shifts were found due to transverse fields generated above the retarding grid.This was easily corrected by pre-deflecting the beam.

Summary

A new detector design was based on results from the 2-D rectilinear design program described in Chapter 3. Programs were written to simulate its performance and found it to be comparable to the Feuerbaum detector. A practical design of the new detector was built and provisional experimental results were presented which indicate a first order correspondence with theoretical predictions.

CHAPTER 77.1 Conclusions

From Chapter 2 it was shown that past detectors had not been designed on a strong theoretical base and that comparisons of their performance were difficult to make from published experimental results. This was in part due to lack of information in published results but also to the non-uniform conditions in which each experiment was performed. It was concluded that simulation tools should be developed by which the performance of different detectors could be compared and a new detector designed. Chapter 2 also showed that little theoretical information in the subject of surface field effects on voltage contrast measurements existed. Development of theoretical aids in achieving knowledge in this area was also considered important.

Chapter 3 has described the development of computer design and simulation programs which aid design and analysis of detectors in two-dimensional coordinates. Techniques in interactive computer graphics greatly aided the specification of a detector's voltage and geometrical configuration and helped display a detector's performance. Certain parameters such as transport efficiency were defined and incorporated as program options which helped to assess a detector's performance. Special error-reducing techniques in plotting electron trajectories were written. These involved: modifying electric field steps near boundaries; avoiding errors in turning points in an electrons trajectory; preventing electrons from

'stepping' across grids; and developing detailed interpolation methods for calculating electric potential values near electrodes.

The programs described in Chapter 3 were used to analyse the performance of two existing detectors, the Dinnis detector (1981) and the Lintech detector (1981). Theoretical predictions for these detectors correspond well with experimental results of variations in output current from voltage changes on different electrodes in each detector. Electron trajectories were plotted through the Dinnis detector and showed it to have a low overall transport efficiency and suggestions for changes of the detector's design were made for the improvement of electron collection. The Lintech detector was shown to have non-linear S-curves and a low transport efficiency. Electron trajectories were plotted to show how electrons were lost in the detector.

Chapter 4 described the development of programs to analyse the Feuerbaum (1979), Fentem (1974) and Tee (1976) detectors in three-dimensional coordinates. An analytical expression for the electric field distribution inside Fentem's detector was developed and numerical techniques were also used. Special error techniques were developed to prevent electrons from incurring large errors across spherical grids. Electron trajectories were plotted for each detector and S-curves were given; little difference in performance was found between Fentem's and Tee's detector. The overall transport efficiency for each detector was found to be higher than 95%; however this figure was not taken as a measure of high performance for the

hemispherical detectors since they had an inefficient method of electron collection. Off-axis analysis of hemispherical detectors was made and at a distance of 2mm significant changes in the S-curves were found. The Feuerbaum detector was shown to have a high transport efficiency and linear S-curves. S-curves however were significantly changed at off-axis positions of greater than 1mm in the opposite direction to the collection gauze.

Chapter 5 describes the development of programs to analyse surface field effects in linear extracting and retarding fields. Different layouts were considered. Results show large errors in voltage measurements for strong surface fields of single gap layouts, typically errors of 5 volts can be experienced for measurements on a 0 volt conductor with a neighbouring 5 volt conductor 3 microns away. Results also show that under such surface field conditions increasing the extraction field strength does not significantly reduce the large errors in the voltage measurement. Different gap sizes in the single gap layout were considered and results show that a considerable improvement is found for a 21 micron gap, voltage errors are reduced to less than 1 volt in these cases. From an analysis of three conductor layouts, it was found that surface field effects can be significantly reduced by increasing the extraction field strength. Voltage errors of less than 1 volt were found from a central 3 micron track with 5 volt neighbouring tracks lying 3 microns away.

The response of the Feuerbaum and Fentem detectors to surface

fields were analysed. Fentem's detector was found to respond poorly to even moderate surface fields from a three electrode layout with gap and track widths of 21 microns. Negative voltage errors of 5 volts were obtained and the electron collection was reduced by over 50%. Results for the Feuerbaum detector show that it gives large errors under strong surface fields from single gap layouts. Most of these errors are attributed to the inability of the detector's linear retarding field to reduce surface field effects. The deflection field of the detector is also responsible for non-linearity in the detector's final S-curve.

Chapter 6 presents the development of a new detector design. An initial design was changed to a more practical design and its theoretical performance was simulated. Computer simulation shows this detector to have a transport efficiency of over 95% and to produce linear S-curves. The optimum voltage configuration of the detector electrodes was found. The detector's response to surface fields was predicted to be similar to the Feuerbaum detector's response and this is largely due to its linear retarding and extracting field. The detector responds better to off-axis positions than the Fentem or Feuerbaum detectors. Only distances greater than 3mm perpendicular to the detectors exit direction cause significant changes in measured S-curves. Practical construction of the detector was made and initial experimental results were given.

7.2 FUTURE WORK

There are a number of developments which can be made on the work described in this thesis. They basically fall into two categories; making the existing programs more comprehensive; and improving the practical design of the new curved tube detector.

Programs can be extended to cover the plotting of electron trajectories in electromagnetic fields and also specify and solve fields which include general dielectric configurations. It is suggested that the finite element method be adopted to provide the above extensions. The finite element method may also be used to solve field distributions above more complex surface layouts as already mentioned in section 5.2.1. The two-dimensional design programs can also be extended to three-dimensional programs. Also further investigation into different types of extraction fields should be made, since important limitations on linear retarding fields were found when considering surface fields.

The practical construction of the curved-tube detector can be improved by investigating ways of reducing the overall height. The holes in the detector grids made for the primary beam should also be shifted towards the detector exit, hence further optimising the detector's performance as concluded from section 6.5.2.

More work remains in the area of making experimental measurements under realistic surface field conditions. Measurements can be made

on the specially constructed test specimen described in section 6.6. These results can be compared to the theoretical predictions on surface fields from section 5.4.

APPENDIX 1Hemispherical Shell

A general solution to Laplace's equation in axially symmetric coordinates is given by,

$$V(r, \theta) = \sum_{n=0}^{\infty} (a_n r^n + b_n / r^{n+1}) \cdot P_n(\cos \theta) \quad (1A)$$

a_n and b_n must be found by substituting in the boundary conditions of the hemispherical shell shown in Figure 4.2. These boundary conditions are,

$$V(r, \theta) = V_0 \quad \text{for} \quad \theta = \pi/2 \quad \text{and} \quad r_1 < r < r_2 \quad (2A)$$

$$V(r, \theta) = V_1 \quad \text{for} \quad 0 \leq \theta \leq \pi/2 \quad \text{and} \quad r=r_1 \quad (3A)$$

$$V(r, \theta) = V_2 \quad \text{for} \quad 0 \leq \theta \leq \pi/2 \quad \text{and} \quad r=r_2 \quad (4A)$$

substituting these conditions in equation (1A) gives three different equations

$$V_0 = \sum_{n=0}^{\infty} (a_n r^n + b_n / r^{n+1}) \cdot P_n(0) \quad (5A)$$

$$V_1 = \sum_{n=0}^{\infty} (a_n r_1^n + b_n / r_1^{n+1}) \cdot P_n(\cos \theta) \quad (6A)$$

$$V_2 = \sum_{n=0}^{\infty} (a_n r_2^n + b_n / r_2^{n+1}) \cdot P_n(\cos \theta) \quad (7A)$$

Consider equation (5A)

$$\begin{aligned}
 P_n(0) &= 1 && \text{for } n=0 \\
 &= 0 && \text{for } n \text{ odd} \\
 &= (-1)^{n/2} \frac{(n-1)!!}{n!!} && \text{for } n \text{ even } \geq 1 \quad (\text{Arfken}(1970), p542)
 \end{aligned}$$

$$\therefore V_0 = \sum_{m=0}^{\infty} (a_{2m} r^{2m} + b_{2m}/r^{2m+1}) \cdot P_{2m}(0) \quad \forall \quad r_1 < r < r_2 \quad (8A)$$

To satisfy the boundary condition of (2A)

$$a_{2m} = 0 \quad \text{for } m \geq 1, \quad b_{2m} = 0 \quad \text{and} \quad a_0 = V_0$$

$$\therefore V(r, \theta) = V_0 + \sum_{\substack{m=1 \\ \text{ODD}}}^{\infty} (a_m r^m + b_m/r^{m+1}) \cdot P_m(\cos\theta) \quad (9A)$$

Equations (6A) and (7A) are modified to

$$V_1 - V_0 = \sum_{\substack{n=1 \\ \text{ODD}}}^{\infty} (a_n r_1^n + b_n/r_1^{n+1}) \cdot P_n(\cos\theta) \quad (10A)$$

$$V_2 - V_0 = \sum_{\substack{n=1 \\ \text{ODD}}}^{\infty} (a_n r_2^n + b_n/r_2^{n+1}) \cdot P_n(\cos\theta) \quad (11A)$$

Orthogonality conditions are required for the half interval $[0,1]$,

$$\int_0^1 P_m(x)P_n(x)dx = \frac{1}{2} \int_{-1}^{+1} P_m(x)P_n(x)dx = 0$$

$m \text{ odd}, n \text{ odd} \qquad \qquad \qquad m \text{ odd}, n \text{ odd}$

$$\text{since } P_m(-x) = (-1)^m P_m(x)$$

$$P_n(-x) = (-1)^n P_n(x)$$

making $P_n(x)P_m(x)$ an even function for m odd and n odd

Multiplying both sides of equation (10A),

$$\int_0^1 (V_1 - V_0) \cdot P_m(x) dx = \sum_{\substack{n=1 \\ \text{ODD}}}^{\infty} (a_n r_1^n + b_n / r_1^{n+1}) \int_0^1 P_m(x) P_n(x) dx$$

$$= (a_m r_1^m + b_m / r_1^{m+1}) \int_0^1 [P_m(x)]^2 dx$$

Hence equations (10A) and (11A) become,

$$(V_1 - V_0) \int_0^1 P_m(x) dx = (a_m r_1^m + b_m / r_1^{m+1}) \int_0^1 [P_m(x)]^2 dx \quad (12A)$$

$$(V_2 - V_0) \int_0^1 P_m(x) dx = (a_m r_2^m + b_m / r_2^{m+1}) \int_0^1 [P_m(x)]^2 dx \quad (13A)$$

$$\text{Let } \alpha_m = \int_0^1 P_m(x) dx / \int_0^1 [P_m(x)]^2 dx \quad (14A)$$

(12A) and 13A) become

$$\alpha_m (V_1 - V_0) = a_m r_1^m + b_m / r_1^{m+1} \quad (15A)$$

$$\alpha_m (V_2 - V_0) = a_m r_2^m + b_m / r_2^{m+1} \quad (16A)$$

For these two equations a_m can be eliminated by,

$$(15A) * r_2^m - (16A) * r_1^m,$$

$$\begin{aligned} \alpha_m r_2^m (V_1 - V_0) - \alpha_m r_1^m (V_2 - V_0) &= b_m \left(\frac{r_2^m}{r_1^{m+1}} - \frac{r_1^m}{r_2^{m+1}} \right) \\ &= b_m \left(\frac{r_2^{2m+1} - r_1^{2m+1}}{(r_1 r_2)^{m+1}} \right) \end{aligned}$$

$$b_m = \alpha_m \frac{[r_1^{m+1} r_2^{2m+1} (V_1 - V_0) - r_1^{2m+1} r_2^{m+1} (V_2 - V_0)]}{[r_2^{2m+1} - r_1^{2m+1}]} \quad (17A)$$

$$\text{find } a_m \text{ by } (15A) * r_1^{m+1} - (16A) * r_2^{m+1},$$

$$\alpha_m r_1^{m+1} (V_1 - V_0) - \alpha_m r_2^{m+1} (V_2 - V_0) = a_m (r_1^{2m+1} - r_2^{2m+1})$$

$$a_m = - \alpha_m \frac{[r_1^{m+1} (V_1 - V_0) - r_2^{m+1} (V_2 - V_0)]}{[r_2^{2m+1} - r_1^{2m+1}]} \quad (18A)$$

Calculating α_m

$$\int_0^1 P_{2r+1}(x) dx = P_{2r}(0) / (2r+2) \quad \therefore \int_0^1 P_m(x) dx = \frac{P_{m-1}(0)}{m+1}$$

0 ODD

(Arfken(1970), p552)

$$\text{since } [P_m(x)]^2 = [P_m(-x)]^2 \quad \forall m$$

$$\int_0^1 [P_m(x)]^2 dx = \frac{1}{2} \int_{-1}^{+1} [P_m(x)]^2 dx = \frac{1}{2} \frac{2}{2m+1} \quad \forall m \quad (\text{Arfken}(1970), \text{p}547)$$

$$\therefore \alpha_m = \frac{P_{m-1}(0)}{m+1} \frac{1}{\left(\frac{1}{2m+1}\right)} = \left(\frac{2m+1}{m+1}\right) P_{m-1}(0)$$

substituting for α_m in equations (17A) and (18A) and rearranging,

$$a_m = \left(\frac{2m+1}{m+1}\right) P_{m-1}(0) \frac{[(v_2 - v_0) - (v_1 - v_0)(r_1/r_2)^{m+1}](1/r_2^m)}{[1 - (r_1/r_2)^{2m+1}]} \quad (19A)$$

$$b_m = \left(\frac{2m+1}{m+1}\right) P_{m-1}(0) \frac{[(v_1 - v_0) - (v_2 - v_0)(r_1/r_2)^m]r_1^{m+1}}{[1 - (r_1/r_2)^{2m+1}]} \quad (20A)$$

Substituting a_m and b_m in equation (1A) the final solution is given

by

$$V(r, \theta) = V_0 + \sum_{\substack{m=1 \\ \text{ODD}}}^{\infty} \frac{(2m+1)P_{m-1}(0)P_m(\cos\theta)}{(m+1)[1 - (r_1/r_2)^{2m+1}]} \times \\ \left\{ [(v_2 - v_0) - (v_1 - v_0)(r_1/r_2)^{m+1}](r/r_2)^m \right. \\ \left. + [(v_1 - v_0) - (v_2 - v_0)(r_1/r_2)^m](r_1/r)^{m+1} \right\}$$

or

$$v(r, \theta) = v_0 + \sum_{\substack{m=1 \\ \text{ODD}}}^{\infty} \frac{(2m+1)P_{m-1}(0)P_m(\cos\theta)}{(m+1)[1-(r_1/r_2)^{2m+1}]} \times$$

$$\left\{ (v_2 - v_0) \left[(r/r_2)^m - (r_1/r_2)^m (r_1/r)^{m+1} \right] \right. \\ \left. - (v_1 - v_0) \left[(r_1/r_2)^{m+1} (r/r_2)^m - (r_1/r)^{m+1} \right] \right\}$$

APPENDIX 2The Inner Hemisphere ProblemProblem A

This problem consists of finding the potential distribution of a circular disc in an infinite plane as shown in Figure 4.4(a). The general solution of Laplace's equation in axially symmetric cylindrical coordinates is given by

$$V(\rho, z) = \int_0^{\infty} A(\xi) \cdot e^{-\xi z} J_0(\xi \rho) d\xi + B$$

The boundary conditions for this problem are,

$$\begin{aligned} V(\rho, z) &= V_s & 0 \leq \rho < a, z=0 \\ &= V_0 & \rho > a, z=0 \end{aligned}$$

$$\therefore \int_0^{\infty} A(\xi) \cdot J_0(\xi \rho) d\xi = \begin{aligned} &= V_s - B & 0 \leq \rho < a \\ &= V_0 - B & \rho \geq a \end{aligned}$$

It is convenient to use the property

$$\int_0^{\infty} \sin(a\xi) \cdot J_0(\xi \rho) d\xi = \begin{aligned} &= (a^2 - \rho^2)^{-\frac{1}{2}} & 0 \leq \rho < a \\ &= 0 & \rho \geq a \end{aligned}$$

(Bateman(1954), p99)

let $B=V_0$

$$\therefore A(\xi) = (V_s - V_0) (a^2 - \rho^2)^{\frac{1}{2}} \sin(a\xi)$$

$$V(\rho, z) = V_0 + (V_s - V_0) (a^2 - \rho^2)^{\frac{1}{2}} \int_0^{\infty} \sin(a\xi) \cdot e^{-\xi z} \cdot J_0(\xi \rho) d\xi$$

In terms of r, θ

$$v_A(r, \theta) = v_0 + (v_s - v_0)(a^2 - r^2 \sin^2 \theta)^{\frac{1}{2}} \int_0^{\infty} \sin(a\xi) \cdot e^{-\xi r \cos \theta} J_0(\xi r \sin \theta) d\xi$$

at r_1 ,

$$v_A(r_1, \theta) = v_0 + (v_s - v_0)(a^2 - r_1^2 \sin^2 \theta)^{\frac{1}{2}} \int_0^{\infty} \sin(a\xi) e^{-\xi r_1 \cos \theta} J_0(\xi r_1 \sin \theta) d\xi$$

APPENDIX 3The Inner Hemisphere ProblemProblem B

This problem is shown in Figure 4.4(b) and consists of a hemispherical surface on a 0 volt base. The boundary conditions of this problem are,

$$V_B(r, \pi/2) = 0.$$

$$\begin{aligned} V_B(r_1, \theta) &= V_G(\theta) = V_1 - V_A(r_1, \theta) \\ &= V_1 - V_0 - \tilde{V}(\theta) \end{aligned}$$

where $V_A(r_1, \theta)$ is given at the end of Appendix 2.

$$\begin{aligned} V_A(r_1, \theta) &= V_0 + (V_s - V_0)(a^2 - r_1^2 \sin^2 \theta)^{\frac{1}{2}} \int_0^\infty \sin(a\xi) \cdot e^{-\xi r_1 \cos \theta} J_0(\xi r_1 \sin \theta) d\xi \\ &= V_0 + \tilde{V}(\theta) \\ &= V_0 + (V_s - V_0) \cdot f(\theta) \end{aligned}$$

where

$$\begin{aligned} \tilde{V}(\theta) &= (V_s - V_0) \cdot f(\theta) \\ \text{and } f(\theta) &= (a^2 - r_1^2 \sin^2 \theta)^{\frac{1}{2}} \int_0^\infty \sin(a\xi) \cdot e^{-\xi r_1 \cos \theta} J_0(\xi r_1 \sin \theta) d\xi \end{aligned}$$

The general solution is given by,

$$V_B(r, \theta) = \sum_{m=0}^{\infty} (a_m r^m + b_m / r^{m+1}) \cdot P_m(\cos \theta)$$

applying the first boundary condition

$$V_B(r, \pi/2) = \sum_{m=0}^{\infty} (a_m r^m + b_m / r^{m+1}) \cdot P(0) = 0, \quad P_m(0) = 0 \text{ m odd}$$

substituting for $f(x)$ in terms of r and θ the full expression

using $V_G(\theta) = V_0 + (V_s - V_0)f(\theta)$ is,

$$\begin{aligned}
 V_B(r, \theta) = & (V_1 - V_0) \sum_{\substack{m=1 \\ \text{ODD}}}^{\infty} \frac{\alpha_m}{\beta_m} (r/r_1)^m \cdot P_m(\cos\theta) \\
 & - (V_s - V_0) \sum_{\substack{m=1 \\ \text{ODD}}}^{\infty} \frac{1}{\beta_m} (r/r_1)^m \left[\int_0^{\pi/2} P_m(\cos\theta') \cdot \sin\theta' \cdot (a^2 - r_1^2 \sin^2\theta')^{\frac{1}{2}} d\theta' \right. \\
 & \left. \int_0^{\infty} \sin(a\xi) \cdot e^{-\xi r_1 \cos\theta'} \cdot J_0(\xi r_1 \sin\theta') d\xi \right]
 \end{aligned}$$

θ' and ξ are dummy variables.

APPENDIX 4Analytical Solution to Potential FieldInside the Feuerbaum Detector

The deflection field of the Feuerbaum detector is similar to the field of the Banbury and Nixon(1970) detector whose potential distribution is given by Munro(p77,1971) to be

$$\begin{aligned}
 V(z,r,\theta) = & \sum_{n=1}^{\infty} a_n \sinh[k_n(z_1-z)] J_0(k_n r) \\
 & \sum_{n=1}^{\infty} c_n \sinh(k_n z) J_0(k_n r) \\
 & \sum_{n=1}^{\infty} b_n \sin(k_n^* z) I_0(k_n^* r) \\
 & \sum_{m=1}^{\infty} \sum_{n=1}^{\infty} d_{mn} \sin(k_n^* z) I_m(k_n^* r) \cos(m\theta)
 \end{aligned}$$

where J_m is the ordinary Bessel function of the first kind of order m , and I_m is its modified form,

$$k_n = x_n/r_1 \quad (x_n = \text{nth zero of } J_0(x)) \quad , \quad d_{mn} = \frac{8(V_D - V_B) \sin(m\theta_D)}{\pi k_n^* z_1^m I_m(k_n^* r_1)}$$

$$a_n = \frac{2}{\sinh(k_n z_1) r_1^2 J_1^2(k_n r_1)} \int_0^{r_1} V_A(r) r J_0(k_n r) \cdot dr$$

$$c_n = \frac{2}{\sinh(k_n z_1) r_1^2 J_1^2(k_n r_1)} \int_0^{r_1} V_C(r) r J_0(k_n r) \cdot dr$$

$$k_n^* = (2n-1)\pi/z_1 \quad , \quad b_n = \frac{4(V_D \theta_D + V_B(\pi - \theta_D))}{\pi k_n^* z_1 I_0(k_n^* r_1)}$$

where $V_A(r)$ and $V_C(r)$ are voltages on the retarding and suppressor grids respectively in the Feuerbaum detector (Figure 4.8), V_D denotes the potential of the deflection gauze and θ_D is the angle it subtends, for the Feuerbaum detector $\theta_D = \pi/2$ (semi-circle), V_B is the voltage on the cylindrical walls.

APPENDIX 5Residual Equation at a Silicon Dioxide/Air Interface

The relaxation star at a silicon dioxide/air interface is shown in Figure 5.3(c) in which medium B represents air and medium A represents silicon dioxide. The two boundary conditions at the interface are that the tangential field at the interface is continuous and that the normal component of flux to the boundary is continuous. These conditions imply the following

$$V_{3a} = V_{3b} = V_3$$

$$V_{1a} = V_{1b} = V_1$$

$$V_{0a} = V_{0b} = V_0$$

and from the normal flux conservation

$$D_a = D_b$$

where D_a and D_b represent the normal components of flux in mediums A and B respectively.

$$\epsilon_a (V_{4a} - V_{2a}) = \epsilon_b (V_{4b} - V_{2b})$$

let

$$S = \epsilon_a / \epsilon_b \quad (\text{in this case } S=3.8)$$

so

$$V_{2b} = V_{4b} - S(V_{4a} - V_{2a})$$

ϵ_a and ϵ_b are the permittivities of regions A and B. V_{2b} and V_{4a} are fictitious and must be eliminated. Laplace's equation in finite-difference form for region A is

$$V_3 k_1 + V_1 k_2 + V_{2a} k_3 + V_{4a} k_4 - V_0 k_5 = 0 \quad (1)$$

where

$$k_1 = \frac{2D1}{D3D1(D3+D1)}, \quad k_2 = \frac{2D3}{D3D1(D3+D1)}$$

$$k_3 = \frac{2D4}{D4D2(D2+D4)}, \quad k_4 = \frac{2D2}{D4D2(D4+D2)}$$

$$k_5 = 2 \left(\frac{1}{D1D3} + \frac{1}{D2D4} \right)$$

$D1, D2, D3$ and $D4$ define points 1, 2, 3 and 4 on the asymmetrical star shown in Figure 5.3(c). Laplace's equation in medium B is given by

$$V_3 k_1 + V_1 k_2 + V_{2b} k_3 + V_{4b} k_4 - V_0 k_5 = 0 \quad (2)$$

substituting in for V_{2b} in (2)

$$V_3 k_1 + V_1 k_2 + k_3 (V_{4b} - S(V_{4a} - V_{2a})) + V_{4b} k_4 - V_0 k_5 = 0$$

$$V_3 k_1 + V_1 k_2 + V_{4b} (k_3 + k_4) - k_3 S V_{4a} + k_3 S V_{2a} - V_0 k_5 = 0 \quad (3)$$

eliminate V_{4a} by calculating $(3)k_4 + k_3 S(1)$

so (3) becomes

$$V_3 k_1 k_4 + V_1 k_2 k_4 + V_{4b} (k_3 + k_4) k_4 - k_3 k_4 S V_{4a} + k_3 k_4 S V_{2a} - V_0 k_5 k_4 = 0 \quad (4)$$

equation (1) becomes

$$V_3 k_1 k_3 S + V_1 k_2 k_3 S + V_{2a} k_3^2 S + V_{4a} k_4 k_3 S - V_0 k_5 k_3 S = 0 \quad (5)$$

add (4) + (5) and finally

$$V_3 (k_4 + k_3 S) k_1 + V_1 (k_4 + k_3 S) k_2 + V_{2a} k_3 S (k_3 + k_4) + V_{4b} (k_3 + k_4) k_4 - V_0 k_5 (k_3 S + k_4) = 0$$

This is the residual equation used at the silicon dioxide/air interface.

REFERENCES

ALLEN D.N. de G, 'Relaxation Methods', Magraw-Hill Publishing Company LTD, London,1954

ARFKEN G., 'Mathematical Methods for Physicists', Academic Press Inc. (London) LTD, second edition,1970

BANBURY J.R. and NIXON W.C., 'Voltage Measurements in the Scanning Electron Microscope', IITRI, SEM, 1970,pp473-480

BALK L.J., FEUERBAUM H.P., KUBALEK E. and MENZEL E., 'Quantitative Voltage Contrast at High Frequencies in the SEM', IITRI, SEM, 1976,pp615-624

BATEMAN MANUSCRIPT PROJECT, 'Tables of Integral Transforms', California Institute of Technology,Vol.1,p99,1954

BRUINING H., 'Physics and Applications of Secondary Electron Emission', Pergamon Press, London,1954

BUCKINGHAM R.A., 'Numerical Methods', Sir Isaac Pitman and Sons Ltd, p249,1957

DINNIS A.R., KHURSHEED A. and NYE P.D., 'Quantitative Voltage Contrast in the SEM', Electron Microscopy and Analysis,61,1981,p527-530

EVERHART T.E., 'Reflections on Scanning Electron Microscopy', IITRI, SEM, 1968,pp3-12

FLEMMING J.P. and WARD E.W., 'A Technique for Accurate Measurement and Display of Applied Potential Distributions using the Scanning Electron Microscope', IITRI, SEM, pp467-472,1970

FENTEM P.J. and GOPINATH A., 'Voltage Contrast Linearization with a Hemispherical Retarding Analyzer', J.Physics E:Sci Instr. 1,pp930-933,1974

FEUERBAUM H.P., 'VLSI Testing Using the Electron Probe', IITRI, SEM, 1979,pp285-296

FEUERBAUM H.P., KANTZ D., WOLFGANG E. and KUBALEK E., 'Quantitative Measurement with High Time Resolution of Internal Waveforms on MOS RAMS', Using a Modified Scanning Electron Microscope', IEEE Journal of Solid-State Circuits, Vol. sc-13, No. 3, June 1978

FUJIOKA H., NAKAME K. and URA K., 'Local Field Effects on Voltage Measurement using a Retarding Field Analyser in the SEM', Scanning Electron Microscopy(IITRI SEM), 1981, Vol 1

GIBBS W.J., 'Conformal Transformations in Electrical Engineering', Chapman and Hall Ltd, London, 1958

GOPINATH A., 'Estimate of Minimum Measurable Voltage Change in the SEM', Journal of Physics E; Sci. Intr., 10, 911-13, 1977

GOPINATH A., GOPINATHAN K.G. and THOMAS P.R., 'Voltage Contrast: A Review', IITRI, SEM, Vol. 1, pp375-380, 1978

GOPINATH A., and SANGER C.C., 'A Technique for the Linearization of Voltage Contrast in the SEM', J. Sci. Inst. (J. Phys. E), 4, 334-336, 1971

HANNAH J.M., 'Scanning Electron Microscope Applications to Integrated Circuit Testing', PhD Thesis, University of Edinburgh, 1974

HARDY W.R., BEHERA S.K. and CAVAN D., 'A Voltage Contrast Detector for the SEM', Journal of Physics E: Sci. Instruments, 8, 789-793, 1975

HAWKES P.W., 'Electron Optics and Electron Microscopy', Taylor and Francis Ltd, London, 1972

HAWKES P.W., 'Image Processing and Computer-Aided Design in Electron Optics', Academic Press Inc. Ltd, London, 1973

KHURSHEED A., 'Voltage Contrast Detector for the SEM', Patent Application No 8308329

KHURSHEED A. and DINNIS A.R. 'Computation of Trajectories in Voltage Contrast Detectors', to be published in a 1983 edition of Scanning (International Journal of Scanning Microscopy and Related Methods).

KLEMPERER , 'Electron Optics', University Press, Cambridge, 1953(2nd Edition)

MACDONALD N.C., 'Potential Mapping using Auger Electron Spectroscopy', IITRI, SEM, 1970,p481-487

MENZEL E., 'Electronic Test System for the Functional Failure Analysis of Integrated Circuits', PhD Thesis, University of Duisburg, 1982

MOON and SPENCER, 'Field Theory for Engineers', Princeton, 1961

MULVEY T. and WALLINGTON M.J., 'Electron Lenses', Rep. Prog. Phys., 36, 347-416, 1973

MUNRO E., 'Computer-Aided Design Methods in Electron Optics', PhD Thesis, University of Cambridge, 1971

OATLEY C.W. and EVERHART T.E., 'The Examination of P-N Junctions with the Scanning Electron Microscope', J. Electron, 2, 568-570, 1957

PASZKOWSKI B., 'Electron Optics', Iliffe Books, London, 1968

PLOWS G.S., 'Spec. of Stroboscopic SEM System', Lintech Instruments Ltd, Cambridge Science Park, Milton Road, Cambridge CB4 4BN

RANASINGHE D.W. and KHURSHEED A. 'Design of a High Efficiency Secondary Electron Detector', to be published in the conference proceedings of the Microscopy of Semiconducting Materials, The Institute of Physics, March 1983

RAU E.E.I. and SPIVAK G.V., 'On the Visualization and Measurements of Surface Potentials in the SEM', IITRI, SEM, 1979, Vol I, p325-332

SANGER C.C., 'Emissive Mode Operation of the Scanning Electron Microscope', PhD Thesis, University College of North Wales, 1980

SHA' F.S., 'Relaxation Methods', Dover, New York, 1953

THOM A., APELT C.J. and TEMPLE G.F.J., 'Field Computations in Engineering and Physics', D. Van Nostrand Company Inc. , London, 1961

TEE W.J. and GOPINATH A., 'A Voltage Measurement Scheme for the SEM using a Hemispherical Retarding Analyser', IITRI, SEM,1976, Vol. I,p595-602

URA K., FUJIOKA H. and YOKOBAYASHI T., 'Calculation of Local Field Effect on Voltage Contrast of SEM', Proc. 7th European Cong. on Electron Microscopy, Vol. 1,1980,pp330-331

VITKOVITCH D., 'Field Analysis:Experimental and Computational Methods', D. Van Nostrand Company Ltd,London, 1966

VERSTER J.L., 'On the Use of Gauzes in Electron Optics', Philips Research Laboratories, Philips Research Reports 18,pp465-605, December,1963

WELLS O.C., 'Scanning Electron Microscopy', McGraw-Hill Inc,1974

WELLS O.C. and BREMER C.G., 'Voltage Measurement in the Scanning Electron Microscope', Journal of Scientific Instruments,1968 Series 2,,1,902-906

WOLFGANG E., OTTO J., KANTZ D., LINDER R., 'Stroboscopic Voltage Contrast of Dynamic 4096 MOS RAM: Failure Analysis and Function Testing', IITRI, SEM,1976, Vol. I,pp625-32

YAKOWITZ H., BALLANTYNE J.P., MUNRO E., NIXON W.C., 'The Cylindrical Secondary Electron Detector as a Voltage Measuring Device in the Scanning Electron Microscope', IITRI, SEM,1972, pp33-40

PATENT APPLICATION NO 8308329

Voltage Contrast Detector for SEM

Anjam Khursheed

INTEGRATED CIRCUIT TESTING ARRANGEMENTS

This invention relates to integrated circuit testing and is concerned with the examination of integrated circuits by measurement of voltage contrast.

05 With the increasingly small size and closer packing density of integrated circuits it has become more difficult to test and examine such circuits, whether for flaws or for other purposes, by conventional microscope techniques. One technique that has been suggested is to examine the circuit in normal operation and observe the pattern of voltage contrast by the use of a scanning electron
10 microscope. One form of this technique involves bombarding the surface of the circuit with a focused primary electron beam and collecting secondary electrons which are emitted as a result of such bombardment. The secondary electrons will have varying energies depending on the potential of the point from which they
15 were emitted. A retarding electrode is provided the potential of which can be varied cyclically. The field produced by the retarding electrode causes the rejection of those secondary electrons of energy below a value determined by the potential on the retarding electrode. The secondary electron current that passes the retarding
20 electrode represents an integration of the secondary electron energy distribution at the surface of the specimen above that value. The retarding field thus acts as a low-pass energy filter. Electrons that pass through the retarding field are deflected away from the axis of the primary beam and are detected in a suitable
25 electron detector, for example, a scintillator.

It is important that as high a proportion as possible of the secondary electrons are deflected and that the deflecting structure does not affect the primary beam or allow back scattered electrons to reach the detector.

30 It is an object of the invention to provide an arrangement in which the deflecting electrode structure has a high degree of efficiency.

According to the invention an integrated circuit testing arrangement for use with a scanning electron microscope to obtain

voltage contrast imaging comprises an extractor electrode for secondary electrons emitted from the surface of a circuit being examined on bombardment of the surface by a primary electron beam provided by the microscope, a retarding electrode for filtering
05 out those secondary electrons of energies below a value determined by the instantaneous voltage applied to the retarding electrode, means for varying the voltage applied to the retarding electrode, deflection means for generating a deflected field to deflect
10 filtered secondary electrons, and an electron detector for electrons deflected by the deflection means characterised in that the deflection means comprises a grid structure in the shape of a section of a bent tube having an input end facing the retarding electrode and an output end facing the electron detector, the grid structure being in two parts insulated from each other and separated
15 along lines generally parallel to the axis of the tube, and means for applying different potentials to the two parts of the grid structure to generate a deflecting and focussing field for secondary electrons that pass the retarding electrode.

In order that the invention may be more fully understood
20 reference will now be made to the accompanying drawings in which:-

Figure 1 and Figure 2 show diagrammatically an embodiment of the invention in side view and in plan respectively, and

Figure 3 shows a family of curves explanatory of the invention.

Figure 1 and Figure 2 show part of a scanning electron micro-
25 scope and in particular an electrode system designed to extract secondary electrons from a specimen. The primary electron beam 1 of the microscope passes the final lens 2 and traverses a short distance of the order of say 25 mm to impinge upon a specimen 3. Specimen 3 may be an integrated circuit which it is desired to
30 examine or test. The circuit is used normally and it is the operating potentials which will be indicated. To this end secondary electrons generated by bombardment of the primary electron beam are examined. The energy distribution of the secondary electrons depends on the voltage of the joint on the
35 surface of the circuit under examination from which they were emitted.

To provide for the efficient extraction of the secondary electrons and reject backscattered primary electrons the electrode system shown in the figures comprises an extractor grid 4, a retarding grid 5 and a deflecting grid which is in two sections 6 and 7. The deflecting grid also acts to focus the secondary electrons. To measure the intensity of secondary electrons a scintillator 8 is provided positioned within a collector cage 9.

The deflecting grid is in the shape of a bent tube having an input end facing retarding electrode 5 and an output end facing scintillator 8. The general shape of the bent tube comprising the two sections 6 and 7 is that of a ship's cowl or ventilator. The two sections of the tube are separated along lines generally parallel to the axis of the tube to enable different potentials to be applied to the two sections.

In the construction of the electrode system an insulating plate 10 is provided having a generally cylindrical cut-out positioned to allow electron beam 1 to pass axially therethrough. Grids 4 and 5 are secured to opposite surfaces of plate 10. Sections 6 and 7 of the deflecting tube are secured to the top surfaces of plate 10 in insulating relationship to each other and to retarding grid 5. Extraction grid 4 and retarding grid 5 are respectively connected to external terminals 11 and 12. Likewise the two sections 6 and 7 of the deflecting electrode are connected to respective terminals 13 and 14.

To allow free passage of electron beam 1 a small hole is cut out of the top section 6 of the deflecting electrode and there are similar holes in the grids 4 and 5 in line with each other.

In operation of the arrangement the extraction electrode 4 has a potential of up to 1 kV applied to it. The potential of the retarding electrode 5 has a ramp waveform applied to it. The range of variation of voltage of the retarding grid may be between -40V and +40V. Section 6 of the deflecting electrode has a potential of -5V while section 7 of the deflecting electrode is given a potential of +100V.

The retarding grid allows passage of secondary electrons which have energies above a value determined by the instantaneous potential

applied to it. The resulting relationship between collected secondary electron current and retarding grid voltage is approximately S-shaped and is known as an S-curve. The application of a ramp waveform to the retarding grid will produce an output current corresponding to such an S-curve. The S-curve, and thus the current output when a ramp waveform is applied, will be displaced for different values of surface voltage. A family of S-curves for various surface voltages is shown in Figure 3. With a deflecting grid structure as shown in Figure 1 and Figure 2 the S-curves are uniform in shape and are displaced linearly with surface voltage.

The effect of the deflecting electrode structure is such as to ensure extraction of practically all secondary electrons emitted from the specimen and all these extracted electrons are deflected away from the axis of the primary beam to impinge on scintillator 8. The output of scintillator 8 can be displayed on an oscilloscope against the ramp waveform applied to the retarding grid. An S-curve will be displayed which will be displaced in accordance with the voltage of the point under examination.

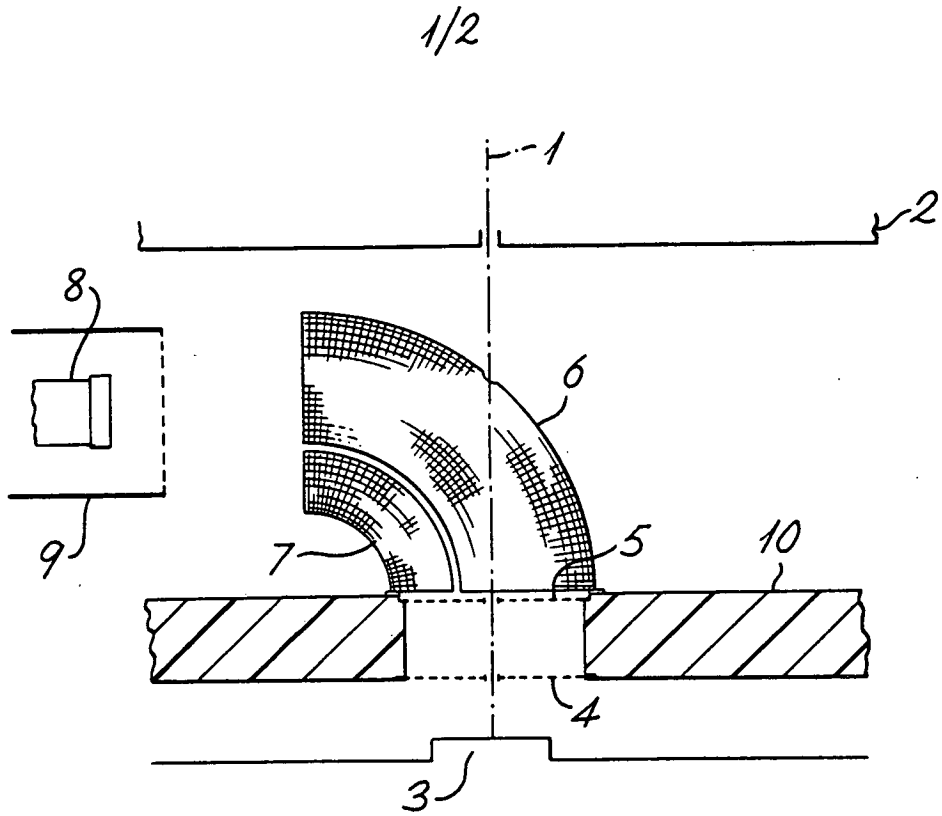


Fig. 1

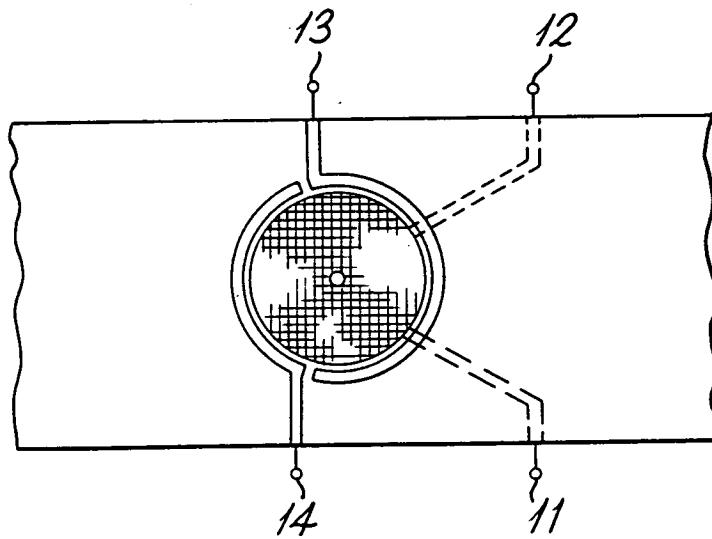


Fig. 2

2/2

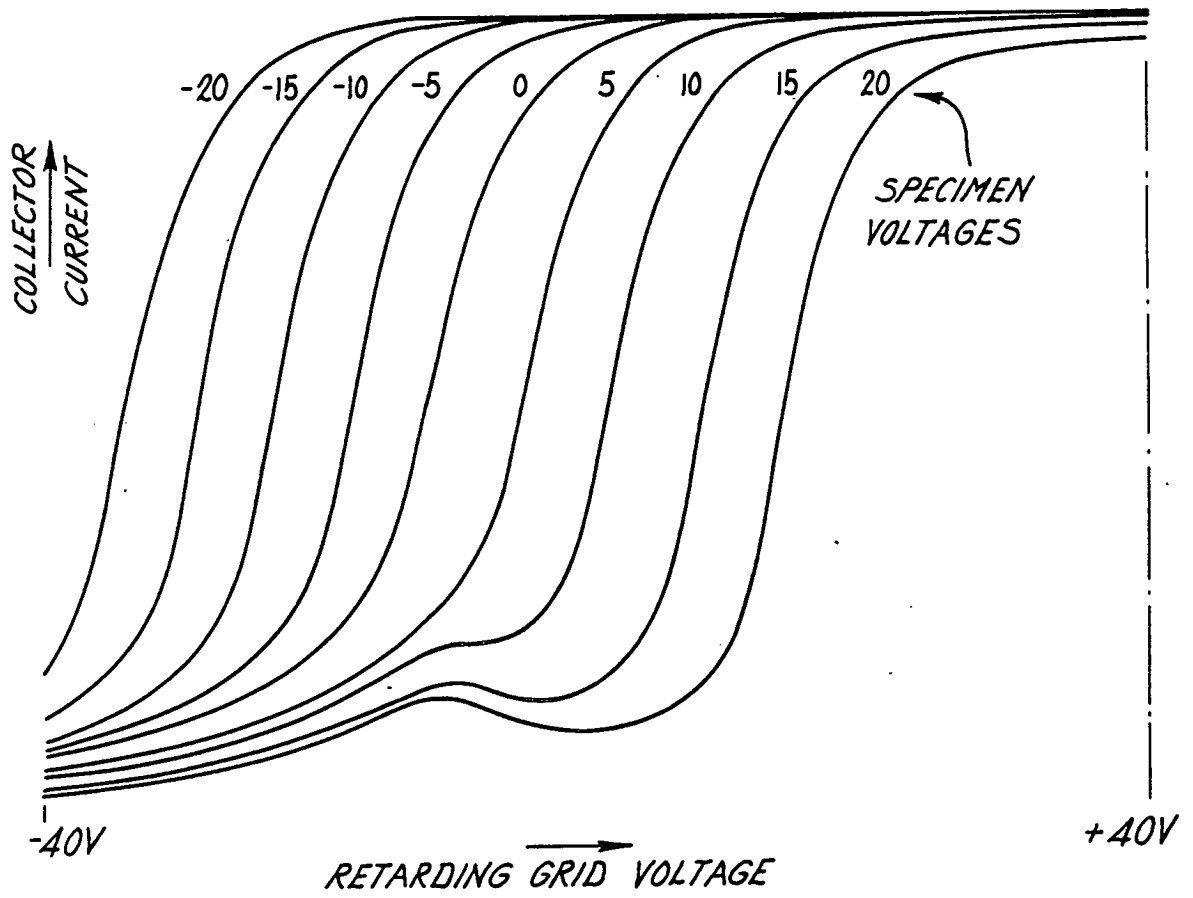


Fig. 3